PROCEEDINGS OF THE
INTERNATIONAL SYMPOSIUM ON

TOPOLOGICAL ASPECTS OF CRITICAL SYSTEMS AND NETWORKS

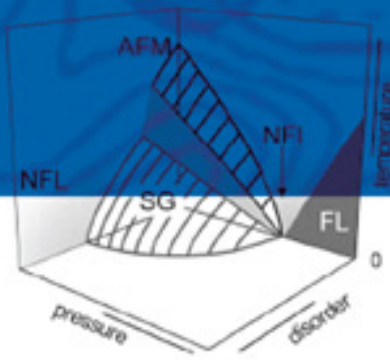

EDITORS

KOUSUKE YAKUBO

HIROSHI AMITSUKA

GOO ISHIKAWA

NOZOMI KICHIJI

KAZUO MACHINO

TOSHIYUKI NAKAGAKI

SATOSHI TANDA

HIDETO YAMADA

with CD-ROM

PROCEEDINGS OF THE
INTERNATIONAL SYMPOSIUM ON

TOPOLOGICAL ASPECTS OF CRITICAL SYSTEMS AND NETWORKS

This page intentionally left blank

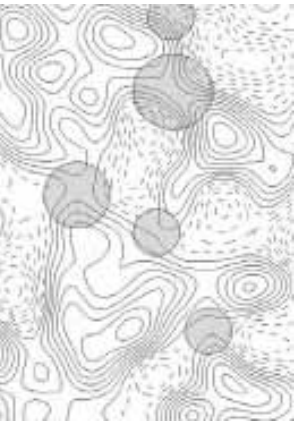

PROCEEDINGS OF THE
INTERNATIONAL SYMPOSIUM ON

TOPOLOGICAL ASPECTS OF CRITICAL SYSTEMS AND NETWORKS

Sapporo, Japan

13 – 14 February 2006

EDITORS

KOUSUKE YAKUBO

HIROSHI AMITSUKA

GOO ISHIKAWA

KAZUO MACHINO

TOSHIYUKI NAKAGAKI

SATOSHI TANDA

HIDETO YAMADA
Hokkaido University, Japan

NOZOMI KICHIJI
Asahikawa University, Japan

World Scientific

NEW JERSEY • LONDON • SINGAPORE • BEIJING • SHANGHAI • HONG KONG • TAIPEI • CHENNAI

Published by

World Scientific Publishing Co. Pte. Ltd.

5 Toh Tuck Link, Singapore 596224

USA office: 27 Warren Street, Suite 401-402, Hackensack, NJ 07601

UK office: 57 Shelton Street, Covent Garden, London WC2H 9HE

British Library Cataloguing-in-Publication Data
A catalogue record for this book is available from the British Library.

TOPOLOGICAL ASPECTS OF CRITICAL SYSTEMS AND NETWORKS (with CD-ROM)

ISBN-13 978-981-270-736-0
ISBN-10 981-270-736-9

Printed in Singapore.

PREFACE

The complexity in the world around us results, in many cases, from finely balanced systems in a state known as criticality. This is the case not only for substantial but also insubstantial structures such as networks not involving the concept of distance. In order to reveal the universal features and mechanisms in such a wide range of complex structures and dynamical processes, it is important to study their topological aspects. The International Symposium on "Topological Aspects of Critical Systems and Networks", sponsored by The 21st Century COE Program "Topological Science and Technology", which was held at Hokkaido University in Sapporo, Japan, February 13-14, 2006, provided an interdisciplinary forum on the topological aspects of general networks and critical systems for physicists, chemists, biologists, mathematicians, medical scientists, social scientists, and other related researchers. This book is the proceedings of this International Symposium. A total of 57 papers, including 23 invited papers, were presented at the Symposium, that was attended by 103 participants. Out of these this book records 37 papers from a wide area of science and technology related to "Topological Aspects of Critical Systems and Networks", representing subjects as diverse as the general properties of complex networks, complexity in social science, patterns in biological objects, and criticality in pure and applied physics.

We hope that the proceedings will be useful to many researchers in related fields. Finally we would like to thank reviewers for their careful reading of the submitted papers and all participants in the Symposium for fruitful and exciting discussions throughout the Symposium.

Kousuke Yakubo
(Chief editor of the proceedings)

Hokkaido University, Japan
April 2007

This page intentionally left blank

CONTENTS

Preface v

International Symposium on *Topological Aspects of Critical Systems and Networks* xi

Group Photo xiii

I. General Properties of Networks

Physics of Network Security 3
Y.-C. Lai, X. Wand and C. H. Lai

Multi-State Interacting Particle Systems on Scale-Free Networks 11
N. Masuda and N. Konno

Homotopy Reduction of Complex Networks 18
Y. Hiraoka and T. Ichinomiya

Analysis of the Susceptible-Infected-Susceptible Model on Complex Network 24
T. Ichinomiya

II. Complexity in Social Science

Innovation and Development in a Random Lattice 33
J. Lahtinen

Long-Tailed Distributions in Biological Systems: Revisit to Lognormals 40
N. Kobayashi, K. Kohyama, O. Moriyama, Y. Sasaki, M. Matsushita and S. Matsushita

Two-Class Structure of Income Distribution in the USA: Exponential Bulk and Power-Law Tail 49
V. M. Yakovenko and A. Christian Silva

Power Law Distributions in Two Community Currencies 59
N. Kichiji and M. Nishibe

III. Patterns in Biological Objects

Stoichiometric Network Analysis of Nonlinear Phenomena in a Reaction Mechanism for TWC Converters 67
M. Marek, O. Hadač, I. Schreiber, M. Schejbal and M. Kubíček

Collective Movement and Morphogenesis of Epithelial Cells 82
H. Haga and K. Kawabata

Indecisive Behavior of Amoeba Crossing an Environmental Barrier 86
S. Takagi, Y. Nishiura, T. Nakagaki, T. Ueda and K.-I. Ueda

Effects of Amount of Food on Path Selection in the Transport Network of an Amoeboid Organism 94
T. Nakagaki, T. Saigusa, A. Tero and R. Kobayashi

Light Scattering Study in Double Network Gels 101
M. Fukunaga, M. Takesada, A. Onodera, R. Kuwadara, J. P. Gong, Y. Osada and T. Yagi

Blood Flow Velocity in the Choroid in Punctate Inner Choroidopathy and Vogt–Koyanagi–Harada Disease; and Multifractal Analysis of Choroidal Blood Flow in Age-Related Macular Degeneration 106
K. Yoshida, W. Saito, H. Fujii and K. Yakubo

Topological Analysis of Placental Arteries: Correlation with Neonatal Growth 114
H. Yamada and K. Yakubo

IV. Criticality in Pure and Applied Physics

Droplets in Disordered Metallic Quantum Critical Systems 125
A. H. Castro Neto and B. A. Jones

Importance of Static Disorder and Inhomogeneous Cooperative Dynamics in Heavy-Fermion Metals 135
O. O. Bernal

Competition between Spin Glass and Antiferromagnetic Phases in Heavy Fermion Materials 143
S. Süllow

Emergent Phases via Fermi Surface Reconstruction near the Metamagnetic Quantum Critical Point in $U(Ru_{1-x}Rh_x)_2Si_2$ 151
K. H. Kim, Y. S. Oh, N. Harrison, P. A. Sharma, M. Jaime, H. Amitsuka and J. A. Mydosh

Continuous Evolution of the Fermi Surface of $CeRu_2Si_2$ Across the Metamagnetic Transition 159
R. Daou, C. Bergemann and S. R. Julian

Phase Transition between the Itinerant and the Localized f-electron States in Heavy Fermion Antiferromagnet $Ce(Ru_{0.9}Rh_{0.1})_2(Si_{1-y}Ge_y)_2$ 166
Y. Tabata, C. Kanadani, R. Yamaki, T. Taniguchi and S. Kawarazaki

Relation between Magnetism and Metal-Insulator Transition in Mn-Doped $SrRuO_3$ 172
M. Yokoyama, C. Satoh, K. Fujita, Y. Nishihara, H. Kawanaka and H. Bando

Magnetization Study of Pairing and Vortex States in Sr_2RuO_4 178
K. Tenya, R. Yamahana, A. Ishii, H. Amitsuka, M. Yokoyama, K. Deguchi and Y. Maeno

Single-Site Effects of Pr Ions Doped in $ThRu_2Si_2$ 184
A. Morishita, Y. Saito, K. Matsuda, T. Wakabayashi, I. Kawasaki, K. Tenya and H. Amitsuka

^{51}V-NMR Studies of Heisenberg Triangular System V15 Cluster 190
Y. Furukawa, Y. Nishisaka, K. Kumagai and P. Kögerler

Menger Sponge-like Fractal Body Created with a Designed Template Method 195
H. Mayama and K. Tsujii

Nonlinear Lattice Relaxation Mechanism for Photoexcited Dimetal-Hallide Chain Compounds 202
J. Ohara and S. Yamamoto

Real Space Renormalization Group Analysis with the Replica Method for the Two-Dimensional Ising Spin Glass 208
T. Hasegawa and K. Nemoto

Quantum Network Models and Their Symmetry Properties 214
T. Ohtsuki and K. M. Slevin

Fractality of Critical Percolation Networks 220
M. Mitobe and K. Yakubo

Ising Phase Transition on Curved Surfaces 226
Y. Sakaniwa, I. Hasegawa and H. Shima

Quantum Confinement in Deformed Cylindrical Surfaces 233
H. Taira and H. Shima

Topological Spin Currents due to Nonadiabatic Quantum Pumping 239
K. Yakubo and M. Morikawa

Charge Density Wave State in Topological Crystal 245
T. Nogawa and K. Nemoto

Spatiotemporal Mapping of Symmetrical Surface Acoustic Fields on Crystals and Periodic Microstructures 249
T. Tachizaki, O. B. Wright, O. Matsuda and Y. Sugawara

Clean Optical Vortex Beam Generation for Large Topological Charge 253
J. Hamazaki, Y. Mineta and R. Morita

Spherically Symmetric Black Hole in a Topological Universe: A Toy Model 258
K. Konno, T. Matsuura, S. Tanda and T. Matsuyama

Author Index 265

International Symposium on Topological Aspects of Critical Systems and Networks

Date & Place

February 13–14, 2006, Sapporo, Japan

Sponsor

Hokkaido University, The 21st Century COE Program
"Topological Science and Technology"

Invited Speakers

(Alphabetical order)

O. O. Bernal (California State Univ., USA)
A. H. Castro Neto (Boston Univ., USA)
R. Daou (Univ. Sherbrooke, Canada)
S. Dorogovtsev (Univ. de Aveiro, Portugal)
Y. Hiraoka (Hokkaido Univ., Japan)
H. Haga (Hokkaido Univ., Japan)
Y. Hoshi (Tokyo Inst. Psychiatry, Japan)
K. H. Kim (Seoul National Univ., Korea)
J. Lahtinen (Eternum Consulting, Finland)
Y.-C. Lai (Arizona State Univ., USA)
M. Marek (Inst. Chemical Technology, Prague, Czech Republic)
N. Masuda (Tokyo Univ., Japan)
M. Matsushita (Chuo Univ., Japan)
T. Ohtsuki (Sophia Univ., Japan)
S. Süllow (Technical Univ. Braunschweig, Germany)
Y. Tabata (Osaka Univ., Japan)
H. Takayasu (Sony Computer Science Lab., Japan)
N. Tamaki (Hokkaido Univ., Japan)
R. Tsuji (Meiji Gakuin Univ., Japan)
V. M. Yakovenko (Univ. Maryland, USA)
H. Yamagami (Kyoto Sangyo Univ., Japan)
Y. Yasuda (Center for the Network Analysis Co. Ltd., Japan)
K. Yoshida (Hokkaido Univ., Japan)

Organizing Committee

Chairperson:

K. Yakubo (Hokkaido Univ., Japan)

H. Amitsuka (Hokkaido Univ., Japan)
G. Ishikawa (Hokkaido Univ., Japan)
N. Kichiji (Asahikawa Univ., Japan)
K. Machino (Hokkaido Univ., Japan)
T. Nakagaki (Hokkaido Univ., Japan)
H. Yamada (Hokkaido Univ., Japan)

Number of Presentations: 57
Number of Invited Talks: 23
Number of Participants: 103
Number of participating countries: 8


ATIONAL SYMPOSIUM ON
GICAL ASPECTS OF
STEMS AND NETWORKS
FEBRUARY 13-14, 2006
NCE HALL, HOKKAIDO UNIVERSITY
SAPPORO, JAPAN

I

General Properties of Networks

This page intentionally left blank

PHYSICS OF NETWORK SECURITY

Y.-C. LAI *

Department of Electrical Engineering,
Department of Physics and Astronomy,
Arizona State University
Tempe, AZ 85287, USA
E-mail: yclai@chaos1.la.asu.edu

X. WANG and C. H. LAI

Department of Physics,
National University of Singapore, Singapore 117542

In a scale-free network, there is a small subset of nodes with linkages far heavier than those of others in the network. Intentional attack on one or a few nodes in this group can trigger a *cascade* of node failures, leading to potential breakdown of the network on a large scale. This typically occurs for situations where the capacities of nodes in the network are small and overload results in node failure. Breakdown of the network can be understood as a phase transition that occurs when the node capacity parameter is decreased through a critical point. However, when the node capacities are sufficiently large, the network can be robust against cascading breakdown. A physical theory to account for these phenomena is reviewed. In situations where overload does not cause node failure but generate traffic congestion, attack can induce persistent oscillations of the network in the sense that its characterizing quantities, such as the diameter, oscillate in time and are never able to restore to their original values. This remarkable phenomenon of *network oscillation* is also discussed.

1. Introduction

Complex networks arising in many natural and man-made systems are scale-free in that their connectivity (or degree) distributions follow an algebraic law.[1,2] In such a network, a small subset of nodes can be far more important than others in that the numbers of links, or the degrees, of these nodes can be significantly larger than those of the rest of the nodes in the network.

*Work partially supported by NSF under Grant No. ITR-0312131 and by AFOSR under Grant No. F49620-01-1-0317.

From the standpoint of security, this means attacks on nodes in this group can have a devastating effect on the overall integrability and function of the network.[3] Assuming that the node capacity is finite and a node functions normally only when its load is smaller than the capacity, there are two distinct situations concerning the effect of attack: (1) overload causes a node to fail completely, and (2) overload does not cause node failure but instead generate traffic congestion at the node. A typical example of the former is electrical power grid, while examples of the latter include the internet and air transportation networks. The purpose of this article is to address the physics and dynamics of the security of scale-free networks mainly for the first case. [The second case will be discussed only briefly as the research is still ongoing at the National University of Singapore (NUS).]

In a scale-free network, since nodes with the higher degrees in the network typically handle more loads necessary for the normal operation of the network, an attack to disable one or few of these nodes means that their loads will be redistributed to other nodes. Because the amount of the redistributed loads can be large, this can cause other nodes in the network to fail, if their loads exceed their capacities, which in turn causes more loads to be redistributed, and so on. This cascading process can continue until the network becomes totally disintegrated. Indeed, simulations show, for instance, that for a realistic power-grid network, attack on a single node can disable more than half of the nodes, essentially shutting down the network.[4]

In Sec. 2, we describe a prototype model for attack-induced cascades on scale-free networks. In Sec. 3, we review a physical theory in terms of phase transition to understand the dynamical mechanism underlying the cascading process. In Sec. 4, we discuss a practical strategy to prevent cascading breakdown and derive theoretical criteria for designing networks that are immune to cascades. Summary and a discussion of network oscillations are presented in Sec. 5.

2. Model of cascades in complex networks

A prototype model based on load dynamics for cascading in complex networks is proposed recently.[4] The load (or the betweenness[6]) at a node is defined as the total number of shortest paths passing through this node. The capacity of a node is the maximum load that the node can handle, which is assumed[4] to be proportional to its initial load,

$$C_i = (1+\alpha)L_0(i) \equiv \lambda L_0(i), \tag{1}$$

where $\alpha \geq 0$ is the capacity parameter. For a particular node, if the load on it increases and becomes larger than the capacity, the node fails. Any failure leads to a redistribution of loads over the network and, as a result, subsequent failures can occur. The failures can stop without affecting too much the network connectivity but it can also propagate and shutdown a considerable fraction of the whole network. Cascading failures can be conveniently quantified by the relative size of the largest connected component $G = N'/N$, where N and N' are the numbers of nodes in the component before and after the cascade, respectively. The integrity of the network is maintained if $G \approx 1$, while breakdown at a global scale occurs if $G \approx 0$.

It is demonstrated[4,7] that global cascades can occur if (1) the network exhibits a highly heterogeneous distribution of loads, (2) the removed node is among those with higher load, and (3) the capacity parameter is around or below a critical value. It is further demonstrated[7] that, when the capacity parameter α is viewed as a control parameter, the occurrence of global cascades can be regarded as the consequence of a phase transition. In particular, as α is decreased through a critical value α_c, global cascades are highly probable.

Given a scale-free network, how to obtain theoretical estimate of the critical capacity-parameter value α_c for phase transition becomes an interesting issue. A formula is obtained[7] that relates α_c to several basic quantities characterizing the network. The main idea leading to the formula will be presented in the next Section. Another interesting question concerns the robustness of the network against cascading breakdown. In particular, for sufficiently large value of α, global cascades are unlikely. The issue is to determine the lower bound α_s, where cascades are not possible for $\alpha > \alpha_s$. This may be important for network design under the constraint of limited resource, where one wishes to have networks that are immune to global cascades but at the same time do not wish to employ nodes with unnecessarily large capacities. These considerations are schematically illustrated in Fig. 1. Theoretical determination of α_s has been obtained recently,[8] which will be discussed in Sec. 4.

3. Formula for phase-transition point α_c

It is convenient to consider the situation[7] where cascading failures are caused by attack on the node with the largest number of links and the failures lead to immediate breakdown of the network. That is, the quantity G becomes close to zero after one redistribution of the load. For a node in the network, its load is a function of the degree variable k. For

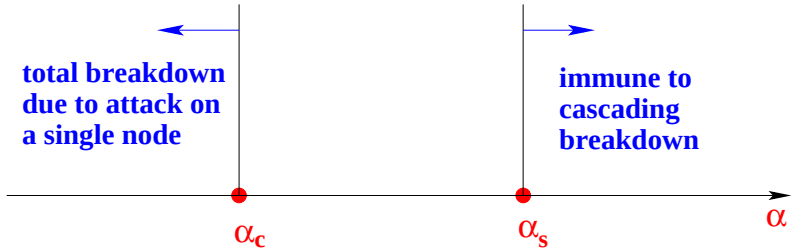

Fig. 1. Schematic illustration of the key capacity-parameter values α_c and α_s, the phase-transition point for global cascades and the lower bound for cascade-free networks, respectively.

scale-free networks, we have,[5,9,10] $L(k) \sim k^{\eta}$, where $\eta > 0$ is a scaling exponent. More formally, the degree and the load distribution can be written as $P(k) = ak^{-\gamma}$ and $L(k) = bk^{\eta}$, respectively, where a and b are positive constants. Let k_{max} be the largest degree in the network. Before the attack, we have $\int_1^{k_{max}} P(k)dk = N$ and $\int_1^{k_{max}} P(k)L(k)dk = S$, where S is the total load of the network. Evaluating the integrals yields

$$a = \frac{(1-\gamma)N}{[k_{max}^{1-\gamma} - 1]} \quad \text{and} \quad b = \frac{\beta S}{a(1-k_{max})^{-\beta}}, \tag{2}$$

where $\beta \equiv \gamma - \eta - 1$. After the removal of the highest degree node, the degree and the load distribution become $P'(k) = a'k^{-\gamma'}$ and $L'(k) = b'k^{\eta'}$, respectively. Since only a small fraction of nodes is removed from the network, we expect the changes in the algebraic scaling exponents of these distributions to be negligible. We thus write $P'(k) \approx a'k^{-\gamma}$ and $L'(k) \approx b'k^{\eta}$, where the proportional constants a' and b' can be calculated in the same way as for a and b. We obtain $a' = (1-\gamma)(N-1)/[k_{max}^{1-\gamma} - 1]$ and $b' = \beta S'/a'(1-k_{max})^{-\beta}$, where S' is the total load of the network after the attack. For nodes with k links, the difference in load before and after the attack can be written as $\Delta L(k) \approx (b' - b)k^{\eta} = (b'/b - 1)L(k)$. Given the capacity $C(k)$, the maximum load increase that the nodes can handle is $C(k) - L(k) = \alpha L(k)$. A node still functions if $\alpha > (b'/b - 1)$ but it fails if $\alpha < (b'/b - 1)$. The critical value α_c of the tolerance parameter is then

$$\alpha_c = \frac{b'}{b} - 1 \approx \left\{ 1 - {k_{max'}}^{-\beta} \left(-1 + \left(\frac{k_{max}}{k_{max'}} \right)^{-\beta} \right) \right\} \left(\frac{S'}{S} \right) - 1, \tag{3}$$

where the fact $({k_{\max'}}^{1-\gamma} - 1)/({k_{\max}}^{1-\gamma} - 1) \approx 1$ has been used. This is so because both ${k_{max'}}^{1-\gamma}$ and ${k_{max'}}^{1-\gamma}$ approach zero for $N \to \infty$ and $\gamma > 1$. In the limit $N \to \infty$, we have $k_{\max'}^{-\beta} \sim 0$, $k_{max}/k_{max'} \sim$ constant, and

$S'/S \to 1$, so $\alpha_c \approx 0$, indicating that an infinite scale-free network cannot be brought down by a single attack if $\alpha > 0$. For a finite-size network, since $k_{\max'}^{-\beta} > 0$, we have $\alpha_c > 0$, suggesting that breakdown can occur for $\alpha < \alpha_c$. The practical usage of Eq. (3) is that it provides a way to monitor the state of (finite) network to assess the risk of cascading breakdown. In particular, the critical value α_c can be computed in time and comparison with the pre-designed capacity-parameter value α can be made. If α_c shows a tendency of increase and approaches α, early warning can be issued to signal an immediate danger of network breakdown. The validity of Eq. (3) has been established through extensive numerical computations.[7]

4. Determination of α_s: criterion for designing cascade-free networks

Theoretical determination of α_s is made possible by considering the parallel problem of how to prevent catastrophic cascades caused by attacks. A simple and intuitive method is to lower the average loads present in the network. This can be achieved by removing a small set of nodes that contribute to the loads in the network but they themselves otherwise process little load.[11] Removal of these nodes and all links connected to them will not affect the functioning of the network but will help enhance the load tolerance for each remaining node. When an intentional attack occurs to disable one or few influential nodes in the network, the load to each remaining node will increase but, because of the extra capacity gained through control, failure is less likely. For scale-free networks, cascades can be prevented or their sizes can be reduced significantly by intentionally removing carefully selected, a few percent of the nodes.[11]

To formulate the problem quantitatively, we let ρ be the fraction of intentionally removed nodes. As ρ is increased from zero, the network becomes more robust against global cascading. However, this trend cannot continue indefinitely, for the network will become disintegrated (even without any attack) if ρ is too large. There exists then a critical value ρ_c for which the network's ability to sustain attack-induced cascading breakdown reaches maximum. By hypothesizing the equivalence of the cascade-control problem to the problem of designing cascade-free network, both α_s and ρ_c can be obtained in a single theoretical framework.[8]

The starting point of the analysis is again the observation that, for a scale-free network, its load distribution obeys[5,7,10] algebraic scaling with the degree variable k. $L(k) \sim k^{\eta}$, where η and b are positive constants. After removing a small fraction ρ of low-degree nodes, the average connectivity

of the network changes little. Moreover, the degree distribution remains to be algebraic with approximately the same scaling exponent. The next step is to determine the relation between the load distributions before and after removing ρ fraction of low-degree nodes. For convenience, all nodes in the network are labeled by integers from 1 to N, while the removed nodes are labeled by $(1-\rho)N$ to N. The total load before the removal can be written as $S = \sum_{i=1}^{(1-\rho)N} L_i + \sum_{i=N(1-\rho)}^{N} L_i \equiv S_0 + S_1$, where S_0 is the sum of loads of the remaining nodes before the removal and S_1 is the total load of the removed nodes. Because the removed nodes have relatively low degrees, we have $S_0 \gg S_1$ and, hence, $S \approx S_0 = \sum_{i=1}^{N(1-\rho)} L_i$. After the removal, the total load of the network is $S' = \sum_{i=1}^{N(1-\rho)} L'_i \approx \sum_{i=1}^{N(1-\rho)} \sigma L_i$, where $0 < \sigma < 1$ is a shifting constant. Since $S = N(N-1)D \approx N^2 D$, $S' = N(1-\rho)[N(1-\rho)-1]D' \approx (1-\rho)^2 N^2$ and $D \approx D'$, where D and D' are the diameters of the networks before and after the removal, respectively, we have $\sigma \approx (1-\rho)^2 \approx 1-2\rho$. Thus, on average, the difference between the loads of node i before and after the removal is $\Delta L_i = L_i - L'_i \approx 2\rho L_i$, which is indepenent of the parameter λ. Since, initially, the load tolerance of node i is $(\lambda-1)L_i$ and the process of removal results in equivalently an extra amount of load tolerance $2\rho L_i$, the node will not fail unless the load increment due to an attack exceeds $(\lambda-1+2\rho)L_i$. Controlled removal of ρ percent of low-degree nodes is thus equivalent to increasing the parameter λ to $\lambda+2\rho$ in the original network.

The effect on G of removing a ρ fraction of low-degree nodes can be analyzed by noting that, in general, G depends on both λ and ρ: $G \equiv G(\lambda,\rho)$. However, without the controlled removal, G depends on λ only and we write $G(\lambda,0) \equiv G^0(\lambda)$. Note that $G^0(\lambda)$ can be calculated one the network configuration is given. A detailed analysis of the relation between $G(\lambda,\rho)$ abd $G^0(\lambda)$ yields[8] the following formulas for estimating λ_s and ρ_c:

$$\frac{dG^0}{d\lambda}|_{\lambda_s} \approx \frac{G^0(\lambda_s)}{2} \quad \text{and} \quad \rho_c \approx (\lambda_s - \lambda_0)/2, \tag{4}$$

where λ_0 is the initial value of the network capacity. The formulas have been verified numerically.[8]

5. Discussions

Studying attacks on complex networks can help identify the vulnerabilities of real-world networks, which can be used either for protective or destructive purposes. Examples of the former include critical infrastructural networks such as the internet and the power grid, while an example of the latter is

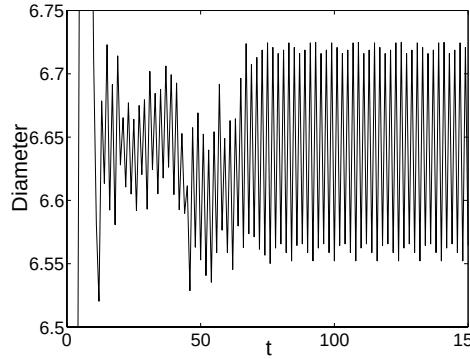

Fig. 2. An example of periodic oscillations of a scale-free network of 1000 nodes and of average degree $\langle k \rangle = 4$. To generate the oscillations, the node that handles the largest amount of load is identified and a ten-fold, sudden increase of load is applied to this node (*e.g.*, due to an attack). The diameter of the network in steady state is $D_0 \approx 5.4$. Shown are the persistent oscillations of the network diameter about a higher average value, indicating that the network is *never* able to return to its original steady state.

malfunctioned biological networks to be targeted and cured by drugs. This review article presents a theoretical approach for understanding the basic physics associated with the security of scale-free networks. In particular, we have presented a theoretical formula for estimating the critical phase-transition point with respect to the network capacity parameter, around and below which total disintegration of the network due to attack even on a single node is highly likely. We have also discussed what it takes for a scale-free network to be robust against global cascading breakdown as caused by attacks on a single node. Analyzing the dynamics of load redistribution as a result of selectively removing a small set of low-degree nodes yields a criterion that allows the lower bound of the capacity parameter for cascades-free scale-free networks and the optimal fraction of intentionally removed nodes to be determined.

An ongoing research project at NUS concerns situations in complex networks where overload does not necessarily lead to failures and an attack typically causes a large perturbation to the network. An example is the denial-of-service type of attacks on the internet, where the load of the attacked node suddenly increased to the extent that the excessive load cannot be handled in reasonable amount of time, leading to traffic congestion at the node. When this occurs, packets (or more generally, information flow) must find alternative paths in the network to reach their destinations in the fastest possible way. This can effectively change the fundamental quantities

characterizing the network, such as its diameter and betweenness centrality.[5] The congested nodes, by design, try to process the excessive loads within their capacities by routing packets to other nodes in the network as fast as possible. Since packets are continuously generated, processed, and delivered on the network as required by its operation, routing of a large amount of excessive loads can cause other nodes in the network to be jammed. As a result, quantities such as the network diameter starts to oscillate in time and, the *network oscillates* in this sense. A remarkable recent finding at NUS is that the oscillation can be persistent in that, due to the attack, the network will never relax to its normal state prior to the attack. Depending on the specifics of the attack and the network state, the oscillation can be periodic or completely random. An example of the oscillation of a scale-free network is shown in Fig. 2. The striking feature is that the oscillations, periodic or random, are caused solely by the interplay between the network topology and the traffic flow protocol, regardless of the local node dynamics. In fact, no apparent node dynamics, linear or nonlinear, is assumed, except for the simple rule that it "holds" and causes the traffic to wait when overloaded. This may have wide implications. For instance, it can provide an alternative explanation for the recently observed chaotic oscillations in real internet traffic flow.[12] From the point of view of security, persistent oscillations the network away from its normal state could cause serious disruption to its function and therefore could be of significant concern.

References

1. A.-L. Barabási and R. Albert, *Science* **286**, 509 (1999).
2. R. Albert and A.-L. Barabási, *Rev. Mod. Phys.* **74**, 47 (2002).
3. R. Albert, H. Jeong, and A.-L. Barabási, *Nature* **406**, 378 (2000).
4. A. E. Motter and Y.-C. Lai, *Phys. Rev. E* **66**, 065102(R) (2002).
5. K.-I. Goh, B. Kahng, and D. Kim, *Phys. Rev. Lett.* **87**, 278701 (2001).
6. M. E. J. Newman, *Phys. Rev. E* **64**, 016132 (2001).
7. L. Zhao, K. Park, and Y.-C. Lai, *Phys. Rev. E* **70**, 035101(R) (2004).
8. L. Zhao, K. Park, Y.-C. Lai, and N. Ye, *Phys. Rev. E* **72**, 025104(R) (2005).
9. K.-I. Goh, C.-M. Ghim, B. Kahng, and D. Kim, *Phys. Rev. Lett.* **91**, 1898041 (2003).
10. K. Park, Y.-C. Lai, and N. Ye, *Phys. Rev. E* **70**, 026109 (2004).
11. A. E. Motter, *Phys. Rev. Lett.* **93**, 098701 (2004).
12. J.-B. Gao, N. S. V. Rao, J. Hu, and J. Ai, *Phys. Rev. Lett.* **94**, 198702 (2005).

MULTI-STATE INTERACTING PARTICLE SYSTEMS ON SCALE-FREE NETWORKS

N. MASUDA*

RIKEN Brain Science Institute, Wako, Saitama 351-0198, Japan
**E-mail: masuda@brain.riken.jp*

N. KONNO

Faculty of Engineering, Yokohama National University,
Yokohama, Kanagawa 240-8501, Japan
E-mail: konno@ynu.ac.jp

In this paper, after reviewing some known results, we extend the analysis of epidemic thresholds for complex networks to more general epidemic dynamics with more than two states. The fact that the epidemic threshold is extinguished for highly heterogeneous networks is transferred to most of these generalized models. However, in some types of models, additional constraints associated with pathogen mutation are needed for the epidemic threshold to disappear.

Keywords: Complex networks; Scale-free netweorks, Epidemic spreading, SIS model

1. Introduction

Real networks are complex and not similar to conventional graphs such as lattices, regular trees, or classical random graphs. Many networks own the small-world and scale-free properties.[2,17] In small-world networks, the mean distance between a pair of vertices is fairly small on average. The scale-free network is defined by the vertex degree k distributed according to the power law: $p_k \propto k^{-\gamma}$.

The critical infection rates above which epidemics can occur scale as $\langle k \rangle / \langle k^2 \rangle$ in the percolation,[1,5,16] the SIS model,[7,18,19] and the SIR models.[3,14,15] Scale-free networks with $\gamma \leq 3$ have epidemic thresholds equal to 0 because $\langle k^2 \rangle$ diverges as the number of vertices increases.

Realistic epidemic processes are complex both in terms of networks and interactions. Particularly, multi-state models in which each vertex changes its state at properly designed rates of, for example, birth, death, infection,

recovery, and mutation better correspond to real infectious diseases such as gonorrhoea and HIV/AIDS.[3,4,6,7,9,23] Multi-state models considered on networks may serve to understand relevance of complex networks to real epidemics. In this direction, there are just a few analyses. Liu and coworkers performed complex-network analysis of the SIRS model and the so-called household model to show the $\langle k \rangle / \langle k^2 \rangle$-dependence of the critical infection rates.[10,11] In this paper, we start with reviewing the analysis of the SIS model and the SIRS model in populations with heterogeneous contact rates. Then, we present the analysis of models with multiple possible states on complex networks.

2. SIS model

Let us start with the SIS model on complex networks, or in heterogeneous populations.[3,7,18,19] In the SIS model, an agent on each vertex takes either state 0 (susceptible) or state 1 (infected). As schematically shown in Fig. 1, a susceptible vertex is infected at a rate proportional to the infection rate λ and the number of infected vertices in its neighborhood. An infected vertex spontaneously becomes healed after a random time, whose mean is set 1 without losing generality. The cured individual is not assumed to acquire immunity. On lattices and regular trees, there are nontrivial critical infection rates, denoted by λ_c, only above which vertices of state 1 persist in infinite time with a positive probability. This situation corresponds to the endemic state in which the states 0 and 1 can coexist.

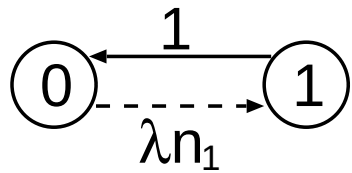

Fig. 1. The transition rule of the SIS model. The solid line represents transition independent of states of neighbors, whereas the dashed line represents the neighbor-dependent transition. The values indicate the transmission rates, where n_i ($i = 1$ here) is the number of vertices in state i in the neighborhood.

Let us denote by p_k the probability that a vertex has degree k. Obviously, $\sum_{k=1}^{\infty} p_k = 1$, and the mean degree $\langle k \rangle \equiv \sum_{k=1}^{\infty} k p_k$. We denote by $\rho_{1,k}$ the probability that a vertice with degree k takes state 1. The portion

of vertices with state 0 among those with degree k is equal to $1-\rho_{1,k}$. The meanfield dynamics are

$$\dot{\rho}_{1,k} = \lambda k \left(1-\rho_{1,k}\right) \Theta_1 - \rho_{1,k}, \quad (k = 1, 2, \dots) \tag{1}$$

where the first and second terms of Eq. (1) represent the mean transition rates from 0 to 1 and from 1 to 0, respectively. The probability that a neighborhood located on the end of a randomly chosen edge takes state 1, denoted by Θ_1, becomes

$$\Theta_1 = \frac{\sum_k k p_k \rho_{1,k}(t)}{\langle k \rangle}. \tag{2}$$

In the equilibrium, we obtain

$$\rho^*_{1,k} = \frac{\lambda k \Theta^*_1}{1+\lambda k \Theta^*_1}, \tag{3}$$

where $*$ indicate the steady state. Plugging Eq. (3) into Eq. (2) leads to

$$\Theta^*_1 = \frac{1}{\langle k \rangle} \sum_k \frac{\lambda \Theta^*_1 k^2 p_k}{1+\lambda \Theta^*_1 k}. \tag{4}$$

Equation (4) holds when $\Theta^* = 0$, corresponding to the disease-free state denoted by $\{0\}$. When $0 < \Theta^* < 1$, two states coexist ($\{0,1\}$). Since the RHS of Eq. (4) is equal to (smaller than) the LHS when $\Theta^* = 0$ ($\Theta^* = 1$),

$$\frac{\partial}{\partial \Theta^*_1} \left(\frac{1}{\langle k \rangle} \sum_k \frac{\lambda \Theta^*_1 k^2 p_k}{1+\lambda \Theta^*_1 k} \right) \Bigg|_{\Theta^*_1 = 0} > 1 \tag{5}$$

is a sufficient condition for the $\{0,1\}$ phase. Equations (5) guarantees that

$$\lambda_c = \frac{\langle k \rangle}{\langle k^2 \rangle} \tag{6}$$

divides $\{0\}$ and $\{0,1\}$. When $p_k \propto k^{-\gamma}$ ($\gamma \leq 3$), we have $\lambda_c = 0$.

3. SIRS-type Models

Figure 2 is the transition rule of a variant of the SIRS model. The states 0, 1, and 2 respectively represent susceptible, infected, and recovered. After recovery at rate μ, immunity persists for a random time with mean 1 before coming back to the susceptible state. The state 2 can be also considered as empty, if the birth process ($2 \to 0$) is roughly independent of the neighbors' states, as for forest trees. This model extends the SIS model, which corresponds to $\mu = 0$ and $\delta = 1$.

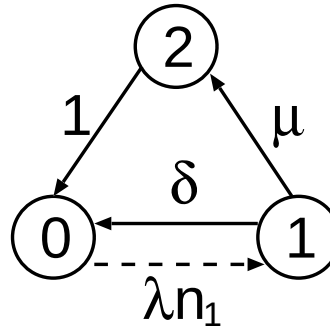

Fig. 2. The rule of the SIRS model.

The meanfield analysis predicts that two phases $\{0\}$ and $\{0,1,2\}$ are separated by $\lambda = \mu + \delta$. On regular lattices, the critical infection rate λ_c rigorously exists for $\delta = 0$ and $\mu > 0$,[4,6,23] and λ quantitatively influences the survival probability more than μ does.[8,9]

With heterogeneous contact rates, λ_c behaves essentially in the same manner as Eq. (6).[10] Let us briefly review the analysis; denote the proportion of vertices with state i ($i = 0, 1, 2$) and degree k by $\rho_{i,k}$. Noting that $\rho_{0,k} + \rho_{1,k} + \rho_{2,k} = 1$, the meanfield dynamics are given by

$$\begin{aligned} \dot{\rho}_{1,k} &= \lambda(1 - \rho_{1,k} - \rho_{2,k})k\Theta_1 - (\mu + \delta)\rho_{1,k}, \\ \dot{\rho}_{2,k} &= \mu\rho_{1,k} - \rho_{2,k}, \end{aligned} \tag{7}$$

whose steady state is

$$\rho^*_{1,k} = \frac{\rho^*_{2,k}}{\mu} = \frac{\lambda k\Theta^*_1}{\mu + \delta + \lambda(\mu + 1)\Theta^*_1 k}. \tag{8}$$

The $\{0,1,2\}$ phase requires $\Theta^*_1 > 0$. With Eqs. (2) and (8), we derive

$$\Theta^*_1 = \frac{1}{\langle k \rangle} \sum_k \frac{\lambda\Theta^*_1 k^2 p_k}{\mu + \delta + \lambda(\mu + 1)\Theta^*_1 k}, \tag{9}$$

and

$$\lambda_c = (\mu + \delta) \langle k \rangle / \langle k^2 \rangle . \tag{10}$$

The result has also been extended[11] to another variant called the household model.[22]

4. Multi-state Epidemic Dynamics

Actual contagion processes are more complex than these simple dynamics. We analyze several multi-state epidemic models in heterogeneous populations, in which each vertex of a graph takes a state among more than two types. These states correspond to, for example, susceptible, infected, recovered, superspreader, and empty states, whereas a state transition means, for example, birth, death, infection, recovery, or mutation (see 12 for details). The epidemic thresholds mostly become extinct as $\langle k^2 \rangle \to \infty$, but with a couple of interesting exceptions. The upshot of introducing complex networks seems to be determined by gross organizations of the transition rules. The exceptions can be classified into two types.

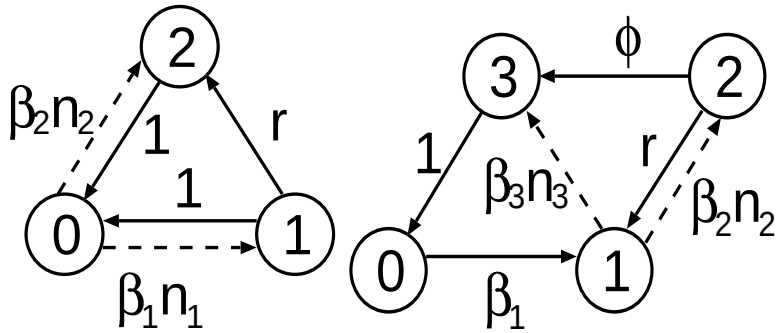

Fig. 3. Transition rules of two models with competing pathogens. The states are denoted by 0, 1, 2, and 3. Solid lines mean transition rates independent of the neighbors' states. Dashed lines indicate neighbor-dependent ones. The number of the vertices with state i in the neighborhood of a vertex is denoted by n_i.

One is when multiple pathogens with mutation compete against each other.[20,21] In this case, coexistence of different types of strains requires a meanfield-type condition on mutation rates. Even though $\langle k \rangle / \langle k^2 \rangle = 0$ results in the coexistence of all kinds of states (including the infectious states) in the simple models, examples shown in Fig. 3 require network-independent conditions, namely, $\beta_1 > \beta_2(r+1)$ (left) or $\beta_2/(r+\phi) > \beta_3$ (right) for full coexistence.

The second class consists of the rock-scissors-paper game and the voter model, in which all the transition rates depend on the states of the neighborhood. In such models, steady states are independent of degree distributions and the same as the meanfield solutions. However, we note that the stabil-

ity of steady states is affected by networks. Dispersed degree distributions stabilize the coexistence equilibria.[13]

References

1. R. Albert, H. Jeong, A.-L. Barabási. Error and attack tolerance of complex networks. *Nature* **406**, 378–382 (2000).
2. R. Albert, A.-L. Barabási. Statistical mechanics of complex networks. *Rev. Mod. Phys.* **74**, 47–97 (2002).
3. R. M. Anderson, R. M. May. *Infectious diseases of humans* (Oxford University Press, Oxford, 1991).
4. E. Andjel, R. Schinazi. A complete convergence theorem for an epidemic model. *J. Appl. Prob.* **33**, 741–748 (1996).
5. R. Cohen, K. Erez, D. ben-Avraham, S. Havlin. Resilience of the Internet to random breakdowns. *Phys. Rev. Lett.* **85**, 4626–4628 (2000).
6. R. Durrett, C. Neuhauser. Epidemics with recovery in $D = 2$. *Ann. Appl. Prob.* **1(2)**, 189–206 (1991).
7. H. W. Hethcote, J. A. Yorke. Gonorrhea: transmission and control. Lect. Notes Biomath. 56, 1–105. (1984).
8. J. Joo, J. L. Lebowitz. Pair approximation of the stochastic susceptible-infected-recovered-susceptible epidemic model on the hypercubic lattice. *Phys. Rev. E* **70**, 036114. (2004).
9. M. Kobayashi, K. Sato, N. Konno. Phase diagrams and correlation inequalities for epidemic models. *Trans. Materials Res. Soc. Jpn.* **26(1)**, 365–368 (2001).
10. J. Liu, Y. Tang, Z. R. Yang. The spread of disease with birth and death on networks. *J. Stat. Mech.* P08008 (2004).
11. J. Liu, J. Wu, Z. R. Yang. The spread of infectious disease on complex networks with household-structure. *Physica A* **341**, 273–280. (2004).
12. N. Masuda, N. Konno. Multi-state Epidemic Processes on Complex Networks, *J. Theor. Biol.*, in press (2006). Preprint: cond-mat/0504329
13. N. Masuda, N. Konno. Heterogeneity in connectivity of habitat networks saves stable coexistence of competing species. Preprint:cond-mat/0603114
14. R. M. May, A. L. Lloyd. Infection dynamics on scale-free networks. *Phys. Rev. E* **64**, 066112 (2001).
15. Y. Moreno, R. Pastor-Satorras, A. Vespignani. Epidemic outbreaks in complex heterogeneous networks. *Eur. Phys. J. B* **26**, 521–529 (2002).
16. M. E. J. Newman. Spread of epidemic disease on networks. *Phys. Rev. E* **66**, 016128 (2002).
17. M. E. J. Newman. The structure and function of complex networks. *SIAM Rev.* **45**, 167–256 (2003).
18. R. Pastor-Satorras, A. Vespignani. Epidemic spreading in scale-free networks. *Phys. Rev. Lett.* **86**, 3200–3203 (2001).
19. R. Pastor-Satorras, A. Vespignani. Epidemic dynamics and endemic states in complex networks. *Phys. Rev. E* **63**, 066117 (2001).
20. R. B. Schinazi, J. Stat. Phys. **97(1/2)**, 409–417 (1999).

21. R. B. Schinazi, Balance between selection and mutation in a spatial stochastic model. *Markov Processes Relat. Fields* **7**, 595–602 (2001).
22. R. B. Schinazi. On the role of social clusters in the transmission of infectious diseases. *Theor. Pop. Biol.* **61**, 163–169 (2002).
23. J. van den Berg, G. R. Grimmett, R. B. Schinazi. Dependent random graphs and spatial epidemics. *Ann. Appl. Prob.* **8(2)**, 317–336 (1998).

HOMOTOPY REDUCTION OF COMPLEX NETWORKS

Y. HIRAOKA

Hiroshima University,
Kagamiyama 1-7-1, Higashihiroshima, Hiroshima, Japan
E-mail: hiraoka@mis.hiroshima-u.ac.jp

T. ICHINOMIYA

Hokkaido University
Kita 12, Nishi 6, Kita-ku, Sapporo, Japan
E-mail: miya@nsc.es.hokudai.ac.jp

In this paper, the notion of homotopy reductions is presented to derive a skeleton structure focusing on loops in complex networks. The main result is to show scale-free networks as skeleton structures of random networks under some rules. In addition, homotopy reductions are applied to scale-free real networks(WWW and protein interaction networks[1]). The potential of homotopy reduction techniques is also discussed in detail.

In recent years, structures of complex networks have been discovered in many areas and much effort to understand their properties such as topology, dynamics, and so forth, has been focused on this attractive and huge research topics.[2,3] Above all, random networks and scale-free networks have played crucial roles for the progress of this research field due to the difference of the respective topological structures. As is well known, a degree distribution for a random network forms the Poisson distribution determined by its average degree $\langle k \rangle$, which has a rapid declining tail with respect to degree k faster than exponential decays. On the other hand, one of the totally dissimilar properties for scale-free networks is asymptotical tail behaviors of degree distributions exhibiting power laws. These tail behaviors cause spatial inhomogeneity of scale-free networks and make spatial network structures different from random networks, which are regarded as homogeneous networks.

Although these two networks are different from each other in the sense of spatial connections, a natural question relating to the topology arises. That is to say, the question is whether it is possible to derive a mean-

ingful skeleton structure of complex networks. In this paper, we introduce a homotopy reduction approach in order to reduce complex networks to skeleton structures focusing on loops and discuss its properties, especially relationship between random networks and scale-free networks. One of the main results of this paper is that a random network can be reduced to a scale-free network by the homotopy reduction. In other words, initial random structure of networks obtains spatial inhomogeneity with the scale-free property through this shrinking process which preserves loops during deformations. Thus, this approach is different from the usual viewpoint which requires growth and preferential attachment for emergences of scale-free networks.[4,5]

Let us give the precise definition of homotopy reductions of networks. Suppose that X is a network with nodes $n_i, i = 1, \cdots N_n$ and edges $e_i, i = 1, \cdots N_e$. Then a network Y is called a homotopy reduction of the original network X if Y is derived by the following two rules(see also Fig. 1):

($r1$) An endpoint n_i(degree one node) and the edge adjacent to n_i are removed.
($r2$) Two nodes $n_i, n_j (i < j)$ of an edge e_l are reduced to one node n_i by shrinking e_l and removing n_j if e_l is not an edge of any triangles constructed by three edges of the network.

In addition, a network Y is defined as a minimal homotopy reduction of X if Y is a homotopy reduction of X and Y can not be reduced anymore by ($r1$) and ($r2$). Hence, homotopy reductions are considered as homotopy deformations preserving network structures.

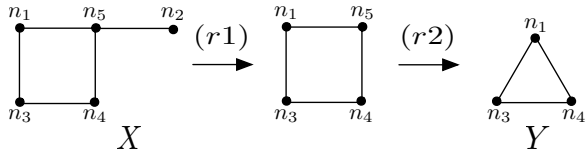

Fig. 1. homotopy reduction.

The definition of homotopy reductions leads to the following properties. The reduction makes networks shrink, preserves loop structures of networks, and is not unique. The nonuniqueness means that reduced networks depend on orders of ($r1$) and ($r2$) to the nodes of the original network. Precisely speaking, although all reduced networks derived by the same original

network is homotopic to each other, the nonuniqueness corresponds to the freedom to choose one representative in a homotopy class of the original network.

In order to remove this ambiguity, let us consider the following prescribed order of homotopy reductions called the preferential homotopy reduction algorithm. The preferential homotopy reduction algorithm consists of five steps:

($pr1$) Execute ($r1$) to all endpoints of the original network.
($pr2$) Set $* = i$, where i is the smallest number of the remaining nodes.
($pr3$) Repeat ($r2$) to the node n_* and all possible edges $e_{\ell_1}, \cdots, e_{\ell_s}$ adjacent to n_*, where $\ell_1 < \ell_2 < \cdots < \ell_s$. First reduce e_{ℓ_1} by ($r2$), then reduce e_{ℓ_2} by ($r2$). Repeat ($r2$) in this order till all possible edges are reduced.
($pr4$) Take the smallest number j of the remaining nodes larger than $*$ such that ($r2$) can be performed to n_j, and renew $* = j$. If no such nodes exist, finish the algorithm.
($pr5$) Return to ($pr3$).

We also add an additional rule such that subnetworks which are homotopic to one point are removed, since our main interest is to focus on loop structures of the original networks.

First of all, let us apply the preferential homotopy reduction algorithm to random networks. Here, we investigate two examples: (i) 1000 nodes with the probability 0.005 (ii) 10000 nodes with the probability 0.0005. The degree distributions of the reduced networks are described in Fig. 2. For both cases, the degree distributions are obtained by the ensemble averages for 10 times trials of different random networks.

It should be noted that scale-free networks appear as the skeleton structures of random networks. The power exponents for these two examples are approximately 2.7 for (i) and 2.9 for (ii). The reason for the emergence of scale-free networks through homotopy reductions is summarized as follows. Obviously, the process ($r1$) does not increase degree distributions due to just shrinking endpoints. However, in general, the process ($r2$) creates a node with degree $k_i + k_j - 2$ by two nodes with degrees k_i and k_j, respectively, which are linked and can be reduced. By this mechanism together with the preferential choice effect, scale-free networks appear as reductions of random networks.

Let us mention that tail parts of degree distributions decrease slowly if we also take degrees of nodes into account for the prearranged order as

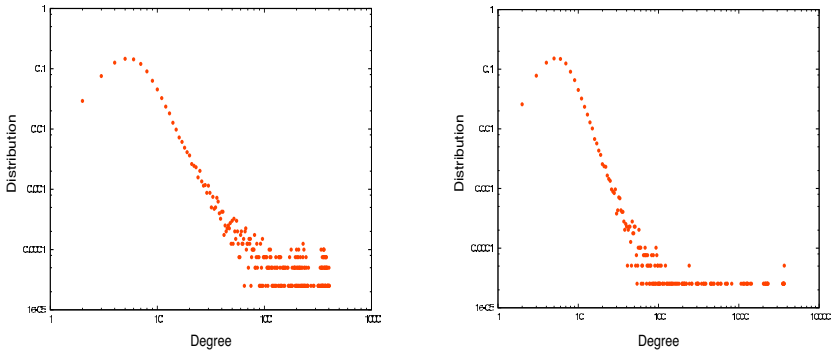

(i) (ii)

Fig. 2. Degree distributions of the reduced networks of random networks.

well as the original Barabási-Albert model, although we just successively perform ($r2$) from nodes with smaller number in the preferential homotopy reduction algorithm. It should be also mentioned that the larger the average degree is in the original random network, the more difficult the reduced network possesses the power law decay. This is related that the properties of random networks with large average degrees are similar to those of complete graphs. Since all edges in complete graphs form triangles with three nodes, no edges can be removed by the reduction process.

On the other hand, this result is also interesting from the viewpoint of self-organizing process. The original random networks gradually shrink in view of loops and form spatial inhomogeneity with the scale-free property.

Next, let us apply the preferential homotopy reduction algorithm to scale-free networks. We study two real data listed in Barabási's website:[1] (i) World Wide Web,[6] (ii) protein interaction network.[7] In the WWW case, we performed the reductions to three networks derived by the nodes with numbering less than 10000, 30000, 50000. Figure 3 shows the degree distributions of the original networks(red points) and the reduced networks(green points). As is easily observed, the power exponents of the original networks and the reduced networks are almost same. In this sense, the reduced networks preserve the structure of spatial connections. The degree distributions of the protein interaction network and its reduced network are described in Fig. 4. Again, it can be observed that the power exponent is preserved through the reduction process. We list in Table 1 the changes of total number of nodes and edges through the homotopy reductions for each case.

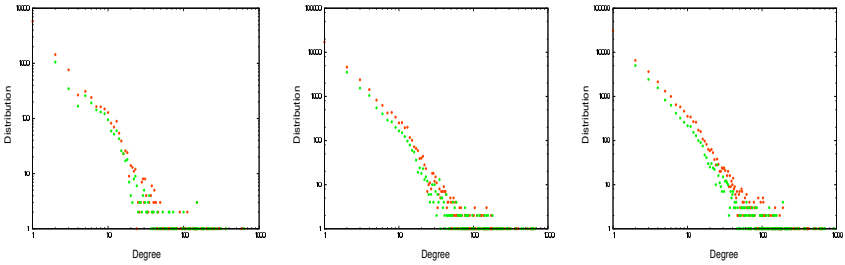

10000 nodes 30000 nodes 50000 nodes

Fig. 3. Degree distributions of WWW. Red points and green points correspond to degree distributions of the original networks and the reduced networks, respectively.

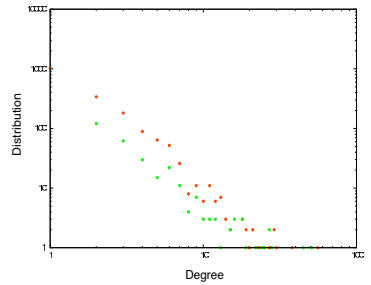

Fig. 4. Degree distributions of a protein interaction network. Red points and green points correspond to degree distributions of the original network and the reduced network, respectively.

Table 1. Changes of total number of nodes and edges.

	WWW(10000)	WWW(30000)	WWW(50000)	Protein
node	10000 → 2940	30000 → 8946	50000 → 12993	2114 → 300
edge	19305 → 12245	51727 → 30673	80621 → 43614	2203 → 797

Finally, let us summarize the paper and discuss future works. We have presented a notion of homotopy reductions to derive skeleton structures by focusing on loops in complex networks. The main result is to show the emergence of scale-free networks as reduced networks of random networks.

The result here is based on numerical simulations, so the power laws in degree distributions of reduced networks should be mathematically shown. Although it is not an easy problem since it is also related to the global topology of complex networks, the analysis is now in progress. We can also raise two questions to the notion of homotopy reductions. The first question is whether it is related to natural phenomena or not. As we mentioned before, if there exist some processes which take similar behavior to homotopy reductions, it corresponds that original random networks gradually shrink in view of loops and form spatial inhomogeneity with the scale-free property. It seems to be interesting from the viewpoints of self-organizing process. On the other hand, the second question is related to the applications of reduction techniques to the analysis of dynamical systems on complex networks. For example, it can be useful to study semi-conjugacy between the dynamics on the original networks and that on the reduced networks. In this case, we need to study which properties in dynamics on original networks are lifted down to the dynamics on reduced networks. The relationship between synchronizations and semi-conjugacy will be studied in the paper.[8]

References

1. http://www.nd.edu/~alb/
2. R. Albert and A.-L. Barabási, *Rev. Mod. Phys.* **74**, 47(2002).
3. S. N. Dorogovstev and J. F. F. Mendes, *Evolution of Networks*, (Oxford University Press, Oxford, 2003).
4. A.-L. Barabási and R. Albert, *Science* **286**, 509 (1999).
5. K. Klemm and V. M. Eguíluz, *Phys. Rev. E* **65**, 036123 (2002).
6. R. Albert, H. Jeong and A.-L. Barabási, *Nature* **401**, 130 (1999).
7. H. Jeong, S. Mason, A.-L. Barabási and Z. N. Oltvai, *Nature* **411**, 41 (2001).
8. Y. Hiraoka and T. Ichinomiya, in preparation.

ANALYSIS OF THE SUSCEPTIBLE-INFECTED-SUSCEPTIBLE MODEL ON COMPLEX NETWORK

T. ICHINOMIYA

Laboratory of Nonlinear Studies and Computation,
Research Institute of Electronic Science,
Hokkaido University,
Kita 12 Nishi 6, Kita-ku, Sapporo 060-0812, JAPAN
E-mail: miya@nsc.es.hokudai.ac.jp

We investigate the susceptible-infected-susceptible(SIS) model on complex network. By counting the number of paths from one node to another, we show that the epidemic threshold K_c must satisfy the relation $K_c \geq \ln(1 + 1/\lambda_0)$, where λ_0 represents the largest eigenvalue of the adjacent matrix of network. We also propose the new strategy for the immunization on complex networks.

It is widely believed that the divergence of the average of k^2, where k represents the degree of each node, causes the pathological behavior of scale-free network. It is well known that real complex networks often show the scale-free degree distribution, $P(k) \propto k^{-\gamma}$, where $P(k)$ represents the degree distribution function.[1] In many cases, the exponents γ is smaller than 3, which means the divergence of $\langle k^2 \rangle$ on the thermodynamical limit, where $\langle \cdots \rangle$ represents the average over all nodes.

In case of the random scale-free network with $\gamma \leq 3$, many pathological behavior appear. The typical example in this regard is the absence of the epidemic threshold of the susceptible-infected-susceptible(SIS) model on random scale-free networks. Pastor-Satorras and Vespignani[2] carried out the mean-field analysis of the SIS model on random scale-free networks and showed that the threshold of the epidemic spreading becomes 0 when $\gamma \leq 3$. Their analysis shows that the threshold K_c is proportional to $\langle k \rangle / \langle k^2 \rangle$, and the absence of threshold is due to the divergence of $\langle k^2 \rangle$. If the infection rate K, defined in later part of this paper, is smaller than K_c, the number of the infected nodes decreases exponentially as the time increases, and the disease is eradicated. On the other hand, if $K > K_c$, the disease can persist.

However, the divergence $\langle k^2 \rangle$ does not always lead to the absence of

the threshold if the network is not random scale-free network. For example, Eguíluz and Klemm showed that the SIS model on the deactivate scale-free network has a finite threshold, while $\langle k^2 \rangle$ diverges.[3] They explained that this is due to the finiteness of $\langle k_{nn} \rangle$, average of the degree of the neighbour nodes. In case of random scale-free network, $\langle k_{nn} \rangle$ is proportional to $\langle k^2 \rangle$ and diverges if $\gamma \leq 3$. However, they didn't clearly show the relation between the threshold and $\langle k_{nn} \rangle$.

In this paper, we show that the "topological" analysis of the complex network sheds light on the dynamics of the SIS model. First we define the SIS model used in the rest of this paper. In the SIS model, each node has the variable s. If $s_i = 1$, the node i is infected, and if $s_i = 0$, the node i is susceptible. If node i is susceptible at time t, it becomes infected with probability $K\Delta t n_i$ at time $t+\Delta t$, where n_i represents the number of infected neighbors of node i. This probability can be written as $K\Delta t \sum_j a_{i,j} s_j$, where $A = (a_{i,j})$ represents the adjacent matrix: $a_{i,j} = 1$ if the node i and j are connected by an edge, and 0 otherwise. On the other hand, if the node i is infected at time t, it becomes susceptible with probability Δt at time $t + \Delta t$.

The key idea of our analysis is to consider the "path of infection". First we assume that only one node i_0 is infectious, while all the other nodes are susceptible at time $t = 0$. Then the disease will propagate to the neighbor of i_0, and new infected nodes will also make their neighbors infectious. Here we note that we can always define the "path of infection" from the infected node to i_0. By estimating the probability that the disease propagates through every path, we can estimate the probability that each node becomes infectious. We present the two application of this idea.

First, we make an intuitive discussion that the epidemic threshold K_c satisfies that $K_c > \ln\left(1 + \frac{1}{\lambda_0}\right)$, where λ_0 represents the largest eigenvalue of the adjacent matrix. First, we estimate the probability that the disease at the node i_0 propagates to the other node i_l, through the path $i_0 \to i_1 \to i_2 \to \cdots \to i_l$. If $l = 1$, the probability is simply given by $r = 1 - \exp(-K)$. In case of $l = 2$, this probability seems r^2, but it is incorrect. The probabilities that the disease propagates from node i_0 to i_1, i_1 to i_2 are both given by r. However, if the propagation from the node i_1 to i_2 failed, i_1 can be infectious again if node i_0 is still infectious. In this case, we can show the probability of propagation from i_0 to i_2 is smaller than $\frac{r^2}{1-r}$. Using the mathematical reduction, it is easy to show the probability is smaller than $\frac{r^l}{(1-r)^{l-1}}$. On the other hand, the number of paths from node i

to node j whose lengths are l is given by $(A_{i,j})^l$, and can be approximated as $\lambda_0^l(\mathbf{v_0})_i$ for large l, where $\mathbf{v_0}$ represents the largest eigenvector of A. If $\frac{r}{1-r}\lambda_0 < 1$, the probability that the disease propagates from node i to j through a path whose length is l decreases exponentially. This discussion suggests that if $\frac{r}{1-r}\lambda_0 < 1$ the disease will be eradicated. Therefore we obtain the result that $K_c > \ln\left(1+\frac{1}{\lambda_0}\right)$. This is not the exact proof, but is consistent with the result that Massoilié and Towsley recently proved by different approach, $K_c \geq 1/\lambda_0$.[5]

Another important application of our idea is the estimation of the "importance" of each node. In the SIS model on inhomogeneous networks, we can prevent the spread of disease by immunizing "important" nodes. In case of random scale-free networks, it is found that the immunization of the high-degree node will efficiently stop the spreading of the disease.[6] Such a targeted immunization works well for some network models, however, it is not versatile. For example, we consider the network depicted in Fig. 1. In this network, the node A has the largest degree, while the immunization of node B is more efficient than immunizing the node A. If there exist many "stars" just like node A, the strategy of the immunization of the highest-degree nodes becomes inefficient. The network depicted in this figure is too artificial, however, there are many real networks in which the immunization of the highest-degree nodes is not efficient. For example, there are networks in which large-degree nodes tend to be connected with small-degree nodes. In such a network, the immunization of the high-degree nodes can be ineffective.

Such a failure of the targeted immunization can be recovered by considering the correction from the long "path of infection". From the viewpoint of our approach, the immunization of the highest degree nodes implies that the "importance" of each node is proportional to its degree. Because the degree of node i is given by $\sum_j (A)_{i,j}$, this implication means that the number of paths whose length is 1 is important. However, when we consider the propagation of disease from one node to another, we should also consider the contribution from paths whose length are larger than 1. From the discussion we have made, one of the suitable value that represents the importance of node i is $\sum_{l,j} \frac{r^l}{(1-r)^l}(A^l)_{i,j}$. However, this value depends on the infection rate K through $r = 1-\exp(-K)$. It is difficult to evaluate K from emphirical data, and we would like to find the value to estimate the "importance" of each node, independent of the infection rate K. In this paper, we propose to use $(\mathbf{v}_0)_i$, the i-th component of the largest eigenvector, as the "importance" of the node i. This value is proportional to $\sum_j (A^l)_{i,j}$

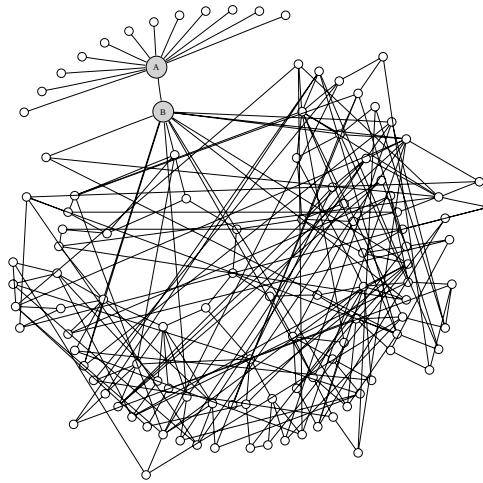

Fig. 1. An example of network in which the immunization of high-degree node does not work.

for large l. By immunizing the node i where $(\mathbf{v}_0)_i$ is large, we will be able to enhance the threshold K_c more efficiently than the immunization of the high-degree nodes.

From the discussion above, we propose the following procedure to determine the targets to be immunized.

(1) First we calculate the largest eigenvector $\mathbf{v}_0$ of the adjacent matrix A.
(2) We define the "importance" of the node i as $(\mathbf{v}_0)_i$, the i-th component of the largest eigenvector.
(3) Immunize the node that has the largest importance.
(4) Remove the immunized node from the adjacent matrix, and go to (1).

By repeating these procedures, we determine the target nodes to be immunized. In the following simulation, we invesitigate the SIS model on the complex networks including 10000 nodes. In this case, we need 2-4 hours to determine the 100 targets of immunization, using personal computer whose CPU is Pentium 4, 2.4 GHz.

In Fig. 2, we show the population of the infected nodes in the non-immunized and immunized cases for the random scale-free network with

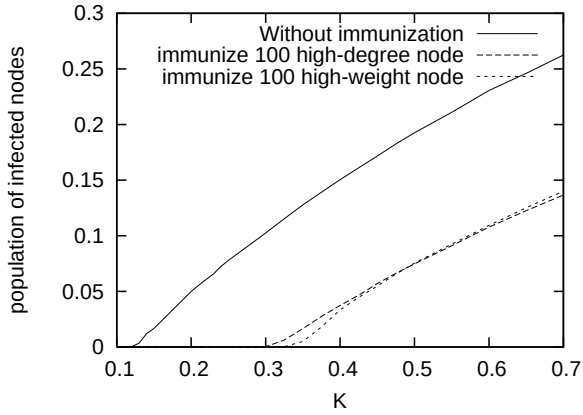

Fig. 2. Population of infected nodes at $t = 100$ for random scale-free network.

$\gamma = 2.3$. When we don't immunize any nodes, the epidemic threshold is about 0.12. The targeted immunization quickly enhances this threshold. In case of the highest-degree immunization represented by long-dashed line, the epidemic threshold is enhanced to 0.30 by immunizing 100 nodes. On the other hand, in case of our immunization strategy shown as dashed line, the epidemic threshold is enhanced to 0.32. The difference of the threshold is small, but our strategy seems as good or better than the the immunization of the highest-degree nodes. Here we note that the "importance" of the node we use has close relation to the degree of each node. The nodes which have large degrees tend to have large "importance" in random networks, and the smallness of the difference between two strategy is due to this correlation.

Figure 3 shows the another example which represents the efficiency of our strategy. In this case, we applied targeted immunization to the network which has many "stars". The network consists of scale-free network including 8000 nodes and 20 stars including 2000 nodes. The immunization to the highest-degree nodes is ineffective in this network, because the immunized nodes are at the center of stars. This figure clearly shows that the immunization of the highest-degree nodes does not stop the epidemic spreading. The population of infected the nodes doesn't differ between the non-immunized network and the network in which the high degree nodes are immunized. On the other hand, our immunization strategy enhances the threshold very well. This result suggests that our strategy can be applied to many networks, including the networks in which the high-degree immunization fails to prevent the epidemic spreading of disease.

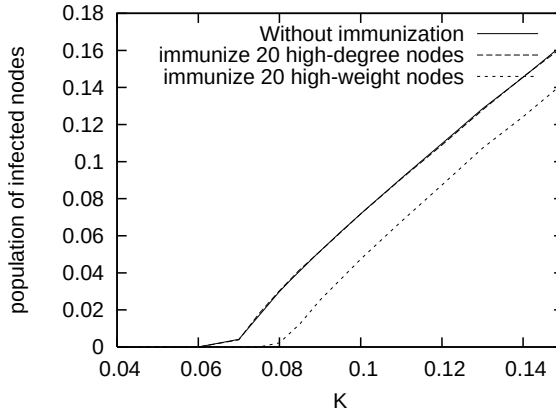

Fig. 3. Population of infected nodes at $t = 100$ in networks which includes many stars.

In summary, we presented the analysis of the SIS model based on topological approach. By considering the number of paths from node to node, we can obtain the lower limit of the epidemic threshold and the efficient strategy for the targeted immunization.

We acknowledge to Y. Hiraoka, M. Iima, T. Yanagita, and Y. Nishiura for fruitful discussion.

References

1. R. Albert and A.-L. Barabási, *Rev. Mod. Phys.* **74**, 47 (2002).
2. R. Pastor-Satorras and A. Vespignani, *Phys. Rev. Lett.* **86**, 3200 (2001).
3. V. M. Eguíluz and K, Klemm, *Phys. Rev. Lett.* **89**, 108701 (2002).
4. H. Chen, H. Jin, J. Sun and Z. Han, *Lecture note in computer science*, **3296**, 232 (2004).
5. A. J. Ganesh and L. Massoulié and D. Towsley, *Proceeding of IEEE Infocom(2005)*.
6. Z. Denzö and A. -L. Barabási, *Phys. Rev. E* **65**, 055103 (2002).

This page intentionally left blank

II

Complexity in Social Science

This page intentionally left blank

INNOVATION AND DEVELOPMENT IN A RANDOM LATTICE

J. LAHTINEN

Eternum Consulting,
Helsinki, 00100, Finland
E-mail: jani@eternum-consulting.com

The intellectual property rights and their effect to the field where they are applied is an important issue especially in the software industry. In this paper we inspect a simple dynamic model of innovation in a lattice of dependencies of a pair of agents that can either collaborate or do not. We use a graph where we add some short– and long–range connections. We inspect a quantity we call *mixing*, which refers to the proportion of the histories of sites first visited by agents overlap. We show that the mixing of the progression of non–cooperative agents makes a rapid transition from zero when we add connections. Also when the number of long–range connections increases the non–cooperative agents initially mix faster than non–cooperative agents.

Keywords: Complex systems, networks, critical systems, effort estimation

1. Introduction

The problem of innovation and development is both about copyrights as well as about collective effort. Many innovations come about as a derivation of other existing innovations. The conundrum of the patents especially in the United States is that many software patents is that instead of promoting innovation as originally intended they are actually preventing it.[1] Similar problems come also about when estimating the development cost of project, and thus estimating the needed effort.[2–4] The standard models used in effort estimation do not take into account the dependencies of the development items, which is what we are now inspecting. Also in a large organization inevitably there will be people repeating the same work simply because they are unaware of it having been done before. Here we introduce a simple dynamical model of agents acting on a small–world lattice, and demonstrate their behavior in different topologies. We change the lattice by adding random links. We do the addition by two means: either by adding

local links to the nearest neighbors or so called long–range links that can span across the field.

Previous work on the field includes the works on spreading and epidemics on small–world networks,[5,6] but especially close to this study is the work Bessen and Maskin who analyzed a simple system of sequential innovations and imitation.[7] We intend to further their analysis by modeling not only a linear sequence of innovation but also their dependencies in a network. Also of relevance is the author's paper on sand piles on Watts–Strogatz graphs where we have shown that subtle changes in the topology of the networks has critical effects to the system's behavior.[8]

This paper is structured so that we first introduce the model we have used. We specifically focus on one key characteristic of this model which captures the fashion in which the agents paths overlap. We then simulate this system and present the results.

2. Model

As a simplification of the situation we take a system of two agents that perform a walk on an essentially 2–dimensional directed lattice with added random links. At each turn the agents will proceed by visiting a new *enabled* site that is in the neighborhood of a site that they have previously visited. By enabled we mean that the agent has already visited all the sites that have a link pointing to the site in question. Also, the agents begin from a given set of initial states that are freely accessibly.

Our model is a 2–dimensional lattice with nodes $\{(i,j)|i \in \mathbb{Z}, j \in \{0,1,\ldots,n-1\}\}$. We denote with $y \to x$ if there is a directed connection between the nodes x and y, and we call the site y as the *premise*, and x as the *dependent*. We also denote with $P(x) = \{y|y \to x\}$ the set of premises of x.

In this lattice for all sites $x = (i,j)$ we always have the connections $x \to (i+1,j)$ and with probability p to one of its immediate neighbors $x \to (i+1, i-1 \mod n)$ or $x \to (i+1, i+1 \mod n)$ but now both, each case with equal probability. Furthermore with probability q there is a link to one more long-range site $x \to (i,k)$, where $k \in \{0,1,\ldots,i-2,i+2,\ldots,n-1\}$.

At time $t = 0$ we assign 2 agents to random sites $(0,k_i)$ such that $k_1 \neq k_2$, *i.e.*, the agents begin from separate states. We then simulate the actions of the agents so that at time t the first agent visits one enabled site, and at time $t + 1/2$ the second agent does the same. There are two alternative definitions of activity: either the agents are *cooperative* or *non–cooperative*. If the agents are non-cooperative a site x is enabled for an

agent a iff the agent has visited all premises y of x. If in turn the agents are cooperative a site x is enabled iff for all premises y of x either agent has already visited y. Furthermore, if there are no enabled sites for the agent, the agent visits with equal probability a site $(0, L_a - 1 \mod n)$ or $(0, R_a + 1 \mod n)$, where initially $L_a = R_a = k_a$.

The model of Bessen and Maskin assumed that each agent had only a single trial to attempt a transition.[7] In their model an agent can try to visit an enabled site with a predefined probability, and should that one try fail the agent is never able to make the transition. Our criticism is that no innovation is truly a single attempt. If a discovery is there eventually it will be discovered given enough time and effort, only its eventual cost will increase. It would be more realistic to make the probability of firing a transition exponentially distributed and make the cost dependent on the time of the transition. However, this would make the analysis much more complicated.

When an agent a visits a site x before the other agent has visited it we label it with a, and denote this with $\ell(x) = a$. A site yet unvisited is labeled zero. Let us then define the *mixing* for node x and agent a with aid of the following counting function:

$$\chi_a(x) = \begin{cases} \sum_{y \in P(x)} \chi_a(y), & \text{if } \ell(x) \neq a \\ \sum_{y \in P(x)} \chi_a(y) + 1, & \text{if } \ell(x) = a \end{cases} \tag{1}$$

In other words we count the number of premises of x that agent a has visited first before the other agent. Here we rather use the normalized inverse count:

$$\mu_a(x) = 1 - \frac{\chi_a(x)}{\sum_b \chi_b(x)}, \tag{2}$$

which is a quantity in the range $[0, 1]$ and when $p = q = 0$, for both agents a, $\mu_a(x) = 0$. The cooperative agents reach the perfect mixing on the limit $\lim_{t \to \infty} \mu_a(x) \to 1/2$ when either $p > 0$ or $q > 0$. The mixing, μ, then is defined as the average:

$$\mu = E_a\big\{E_x\{\mu_a(x) | \ell(x) = a\}\big\}. \tag{3}$$

This quantity is interesting because it captures the characteristics of how the agents' development overlap.

3. Simulations

We simulated the system of two agents with $n = 16$. The width of the system, n, does not essentially effect the qualitative phenomena that we

are interested in. We simulated the system for 500 steps and repeated this procedure for 800 times to ensure reliable statistics. In the following plots the solid curves represent the non-cooperative system and the dashed curve the cooperative one. In Fig. 1 we have plotted the values of μ as a function of t, where p varies over $\{0, 0.1, \ldots, 1\}$ with $q = 0$. It can be seen that the system of cooperative agents mixes faster in all cases.

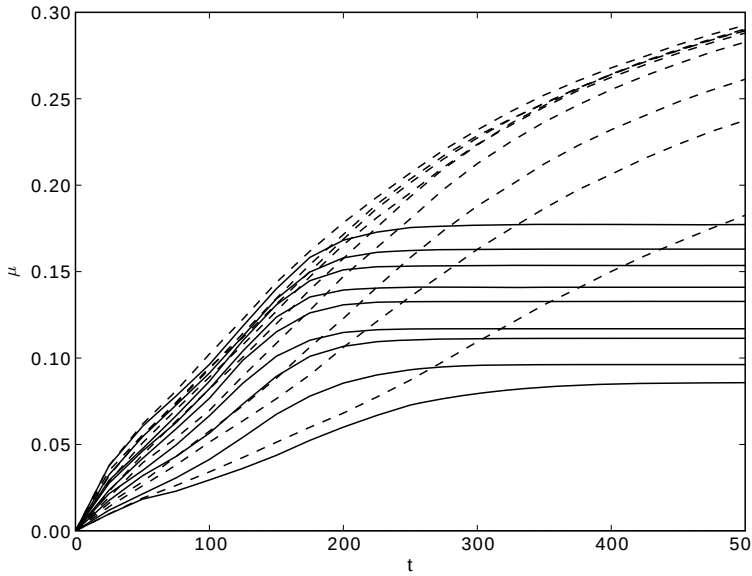

Fig. 1. A plot of the system over different values of p when $q = 0$.

The Fig. 2 in turn shows plots of μ over t when $p = 0$. The values of q are in the same range as with p, *i.e.*, $\{0, 0.1, \ldots, 1\}$. Here, however, we can see that the system of cooperative agents mixes initially slower than the non-cooperative one. This happens because the agents initially do not need to spread their fields when they can use each others sites while making new steps.

With the non-cooperative agents we can see that the system stabilizes eventually to specific value of mixing. In Fig. 3 we have plotted values of this stable state as a function of p with a different curve for each q in $\{0, 0.1, \ldots, 1\}$. The solid lines are linear fits to the respective points. We

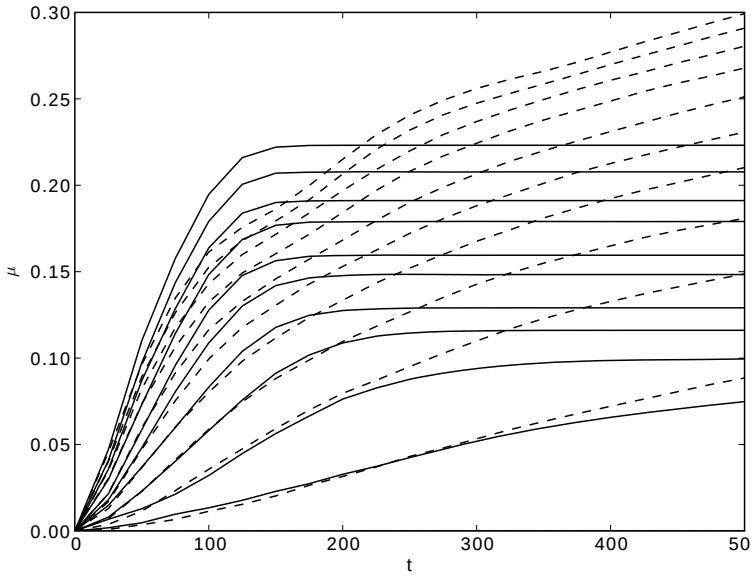

Fig. 2. A plot of the system over different values of q when $p = 0$.

can see that, aside from the near singular transition from the origin, when $p = q = 0$, this follows simple linear dynamics, $\mu \sim \alpha p + \beta q$, plus a constant, with slopes $\alpha = 0.10$ and $\beta = 0.16$.

In case of cooperative agents the mixing of the system approaches the perfect mixing as time approaches infinity, but in Fig. 4 simply for interest we have plotted the values of μ as a function of p at the end of the observation period, which was 500. Different curves again correspond to different values of q. We can see that the cooperative agents do not have a similar singular behavior at the origin.

4. Conclusions

In this paper we have shown that the effect of the dependencies on the system are magnified in a situation where the innovation not only follows a sequence but the dependencies span across the field. We can see that the spreading of the dependencies, *i.e.*, the parameters p and q increase the mixing likewise increases. We have observed that the cooperative agents mix initially slower than non-cooperative ones in case of added long–range

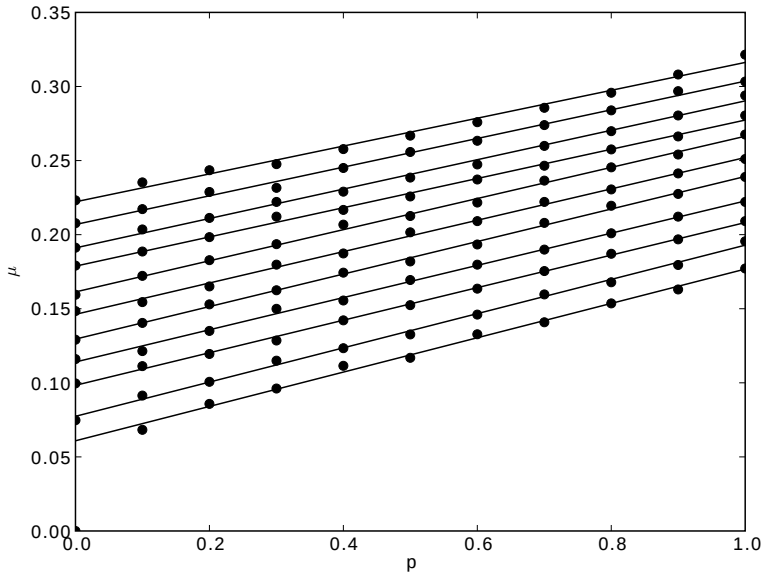

Fig. 3. A plot of the stable mixings of the cooperative agents as a function of p over different values of q.

connections. This we attribute to their lesser need of extending their field when they can take support of each others results.

The simulations presented in this paper were done with Python with NumPy module. The source codes can be found from the author's webpage http://eternum-consulting.com.

Acknowledgments

The author would like to thank prof. K. Yakubo the other organizers for the invitation to join this symposium.

References

1. A. Jaffe and J. Lerner, *Innovation and Its Discontents* (Princeton University Press, Princeton, 2004).
2. O. Benediktsson, D. Dalcher, K. Reed and M. Woodman, *Software Quality Journal* , 265 (2003).
3. B. Boehm, *Software Engineering Economics* (Prentice Hall, 1981).

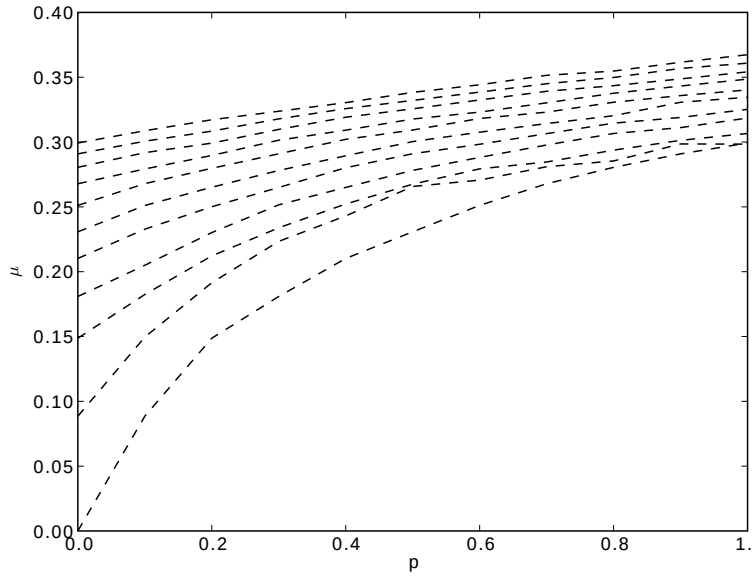

Fig. 4. A plot of the distance of the mixings at the end of the simulation period ($t = 500$) of the cooperative agents as a function of p over different values of q.

4. F. Brooks, *The Mythical Man-Month: Essays on Software Engineering* (Addison Wesley Longman, 1975).
5. S. Watts and S. Strogatz, *Nature* **393**, 440 (1998).
6. A. Barabasi and R. Albert, *Science* **286**, 509 (1999).
7. J. Bessen and E. Maskin, Sequential innovation, patents, and imitation (2002), `http://www.researchoninnovation.org/online.htm#ip2`.
8. J. Lahtinen, J. Kertész and K. Kaski, *Physica A* **349**, 535 (2004).

LONG-TAILED DISTRIBUTIONS IN BIOLOGICAL SYSTEMS: REVISIT TO LOGNORMALS*

N. KOBAYASHI* and K. KOHYAMA

Food Function Division, National Food Research Institute,
2-1-12 Kannondai, Tsukuba, 305-8642, Japan
**E-mail: knaoki@affrc.go.jp*

O. MORIYAMA, Y. SASAKI and M. MATSUSHITA*

Department of Physics, Chuo University,
Kasuga, Bunkyo-ku, Tokyo, 112-8551, Japan
**E-mail: matusita@chuo-u.ac.jp*

S. MATSUSHITA

Tokyo Metropolitan Geriatric Hospital,
Sakae-cho, Itabashi-ku, Tokyo, 173-0015, Japan

Long-tailed distributions in biological systems have been studied. First, we found that lognormal distributions show excellent fit with various data for the duration distribution of disability in aged people, irrespective of their severity and gender. The robust lognormal distribution of disability implies that the incidence of diseases can be completed by many independent subprocesses in succession. Next, we studied food fragmentation by human mastication. A lognormal distribution well fits to the entire region for masticated food fragments for a small number of chewing strokes. Furthermore, the tail of the fragment-size distribution changes from the lognormal distribution to a power-law one as the chewing stroke number increases. The good data fitting by the lognormal and power-law distribution implies that two functions of mastication, a sequential fragmentation with cascade and randomness and a lower threshold for fragment size, may affect the size distribution of masticated food fragments.

1. Introduction

Long-tailed distributions such as power-law and lognormal distributions have been observed in various complex phenomena. The fragmentation with

*A part of this work was supported by the Program for Promotion of Basic Research Activities for Innovative Biosciences (PROBRAIN).

high impact energy usually exhibits the power-law distribution. Fragment-mass distribution of brittle materials[1,2] and mass distribution of asteroids[3] are typical examples known to exhibit the power-law distribution. Another example is self-organized critical systems,[4] such as the Gutenberg-Richter law for earthquakes.[5]

Just as the power-law, the lognormal distribution has been observed in various complex systems, too. The general formula for the probability density function of lognormal distributions is given as follows:

$$n(t) = \frac{1}{\sqrt{2\pi\sigma^2}t} \exp[-\frac{(\log(t/T))^2}{2\sigma^2}], \tag{1}$$

where σ and T are the fitting parameters meaning the dispersion and the average, respectively. The formula for cumulative form of the lognormal distribution is as follows :

$$N(t) = \frac{N_{\mathrm{T}}}{2}(1 - \mathrm{erf}(\frac{\log(t/T)}{\sqrt{2}\sigma})). \tag{2}$$

Here N_T is the total number and $\mathrm{erf}(x)$ is the error function defined as $\mathrm{erf}(x) = \frac{2}{\pi^{1/2}} \int_0^x \exp(-y^2)dy$.

When a complex process requires the completion of many independent and sequential subprocesses, the probability of success or failure for the primary process is considered to show a lognormal distribution due to the central limit theorem.[6] That is why the lognormal distribution has been used to describe various phenomena such as the productivity of scientists publishing research papers,[7] income distributions,[6] the life span of animals,[8] the population distribution of prefectures in post-World War II Japan,[8] the fragment-size distribution with low impact energy.[1,2]

In this paper, we report results of two studies for long-tailed distribution. One is the distribution of duration of life for disability in aged people,[8–10] and the other is the fragment-size distribution by human mastication.[11] It turns out that both show the long-tailed structure and fit the lognormal distributions very well.

2. Long-tailed Distribution of Duration of Disability for Aged People

Disability and the resulting lowered quality of life are serious problems accompanying increased longevity. Curiously, despite its potential contribution to aging theory,[12] complete statistical and etiological structures of this common and unwelcome aging phenotype before death have not been well studied. The consequences of aged people's diseases are not only very

important to the aged people themselves but also young people as well because of the financial and social problems such as payment of various kinds of pensions and nursing of the aged.

Here we analyze characteristic long tails of duration distributions for disability in the aged. The duration means a period from the onset of disability until the death of an aged patient. In this study, we investigate the duration of disability based on datasets capturing from the case records of Tokyo Metropolitan Geriatric Hospital (TMGH) between 1987 and 1989. We classify and analyze two types of disability. The one type is the duration of *disability in transfer*, where patients are disabled in terms of transfer, dressing and bathing by themselves. The other is the duration of *disability in voiding*, where patients are disabled in voiding and eating by themselves. The latter is more severe conditions than the former. The total number of patients is 1017 each. The average duration of disability are 2.04 and 1.39 years for transfer and voiding, respectively. The average age at death is 79.3 ± 9.0.

In data analysis, we sorted data in descending order and made a histogram, *i.e.*, the cumulative number. Figure 1 shows the cumulative number of patients with disability in voiding. The fitted curve is the lognormal distribution (2). In Fig. 1, we found that the fit of a log-normal distribution

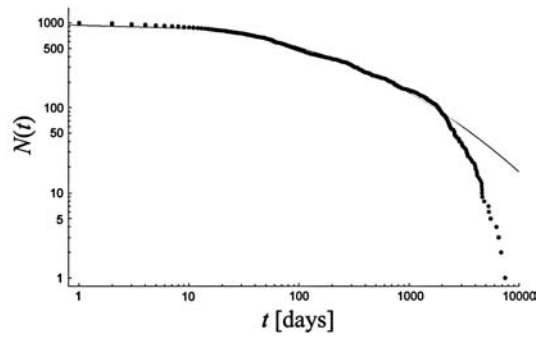

Fig. 1. Log-log plots of the cumulative number $N(t)$ versus the duration t in voiding. Fitting parameters are $N_T = 1017, T = 106.0$ and $\sigma = 2.15$.

is extremely good up to 2000 days for disability in voiding. The distribution for the duration of disability in transfer also shows almost the same tendency. Figures 2 and 3 show the cumulative number of male and female patients with disability in voiding, respectively. We also found that the lognormal distributions fit excellently with the respective data of male

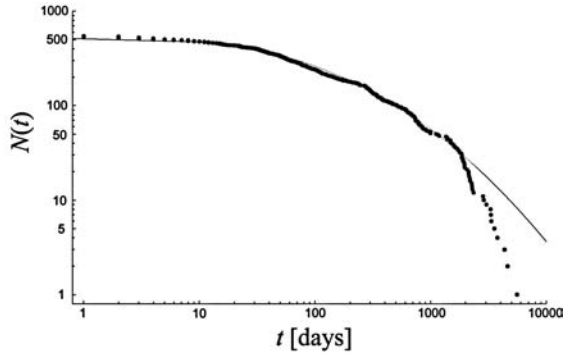

Fig. 2. Log-log plots of the cumulative number $N(t)$ versus the duration t in voiding for male. Fitting parameters are $N_T = 543, T = 90.0$ and $\sigma = 1.90$.

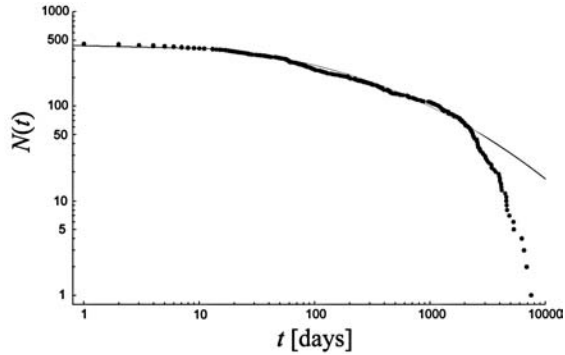

Fig. 3. Log-log plots of the cumulative number $N(t)$ versus the duration t in voiding for female. Fitting parameters are $N_T = 457, T = 160.0$ and $\sigma = 2.30$.

Table 1. Values of fitting parameters for distributions of duration of disabilities by lognormal distribution. This table was distinguished from the severity and gender.

	N_{T}	T	σ
transfer	1017	200	2.15
voiding	1017	106	2.15
transfer for male	543	170	1.95
voiding for male	543	90	1.90
transfer for female	457	280	2.40
voiding for female	457	160	2.30

and female patients. Moreover, the distribution of disability in transfer is roughly the same as in voiding.

Table 1 shows values of parameters obtained for data fitting by lognormal distribution. As shown in Table 1, the dispersion σ depends on not the severity (transfer or voiding) but the gender (male or female). On the other hand, the dependence of T is in accordance with the severity of disability. There is also significant difference between male and female for transfer and voiding, *i.e.*, nearly twofold difference, respectively. In any case, very good fit with other available data strongly suggests that the lognormal distribution is robust for the duration of disability in the aged.

The excellent data fitting by lognormal distribution implies that many subprocesses are involved in disability. In fact, aging itself causes the aged to have a weak constitution such as musculoskeletal inactivity, cardiorespiratory depression and the risk of compromised immune function. Because of that, unlike young people, once aged people suffer from one disease and become disabled, it tends to entail other potential diseases, such as pneumonia, cerebral hemorrhage, heart disease and cancer. Recent medical statistics tells us that cancer and heart attack increase progressively as a cause of death for the aged as the life expectancy becomes longer. Therefore, aged people sustain multiple diseases, as is commonly observed in geriatric practice. It is a plausible scenario for the robust lognormal distribution of disability, irrespective of the difference of severity or gender, that the incidence of diseases of the aged can be considered as many independent subprocesses in succession, namely, random multiplicative stochastic processes.

In Figs. 1, 2 and 3 the tail end of the observed distributions deviates from the lognormal. We consider that the deviation is due to the natural limitation of the human life span. As aged people grow older, the rate of death follows exponential increase.[13,14] Consequently, the tail end of distribution of disability may follow the exponential decay.

3. Food Fragmentation by Human Mastication

Mastication is in-mouth fragmentation process in which food is broken, ground or crushed by the teeth to prepare for swallowing and digestion.[15] Hutchings and Lillford suggested that there are two thresholds, the size breakdown and enough lubrication, and both of them must be satisfied before swallowing.[16] At least as the first approximation, we propose that the mastication by teeth is the sequential fragmentation in the oral cavity. Therefore, we have investigated the fragment-size distribution produced by

human mastication.

Experimental procedure was simple as follows. We chose raw carrot ($23 \times 23 \times 4$ mm, *ca.* 2 g) as masticated sample. After chewing as naturally as possible with a specified number of strokes, the subject expectorated food bolus into a beaker. In order to expectorate entirely, the subject rinsed their mouth with water. The food fragments and water were carefully stirred in a beaker and dropped onto a sieve with a mesh size of 0.5 mm, since the resolution of our image analysis is about 10^{-1} mm. It is possible to employ another instrument in order to investigate fragments below the mesh size, such as laser diffraction analysis.[17] However, we believe that our results are not influenced by the smaller fragments, because the weight loss through the mesh was less than 0.1 per cent. After removing smaller fragments and water, the fragments on the sieve were placed on white color paper without overlap. Then, we took pictures of the bolus by a digital camera (CANON, TOKYO) and digitized the snapshots of masticated food fragments with a suitable resolution (*ca.* 0.13 mm/pixel). Five subjects with a healthy dentition participated in the experiments. It should be noticed that the following results of mastication experiments were obtained from one of these subjects. But the macroscopic structure in size distributions such as the form of the curves was more or less the same as for other subjects.

In 1941 Kolmogorov suggested that fragment-distribution produced by sequential and random fragmentation follows lognormal distribution.[18] Let us apply a lognormal distribution to fit a curve to data in the case of fragmentation by mastication. Figure 4 shows the cumulative number of masticated food fragments of raw carrot chewed 5 strokes. We found that the fit of a lognormal distribution is extremely good up to almost the entire region. As the result of experiments with 5 chewing strokes, we have found that a single lognormal distribution fits to almost 99 % data points for food fragments. Consequently, the fragmentation by human mastication is characterized by the effect of random multiplicative stochastic processes. It should be noted that the tail end of the observed fragment-size distributions deviates from the lognormal.

Figure 5 shows the cumulative number of food-fragments for the threshold number of chewing strokes, when each subject required for normal swallow (*ca.* 15-25). Increasing the number of chewing strokes, the deviation became larger, as seen in Fig 5. The majority of distribution belongs to the small size region characterized by the lognormal distribution, while the large particles were fitted to a power-like behavior, *i.e.* $N(s) \sim s^{-\alpha}$.

In order to explain the power-law behavior in larger fragment group, we

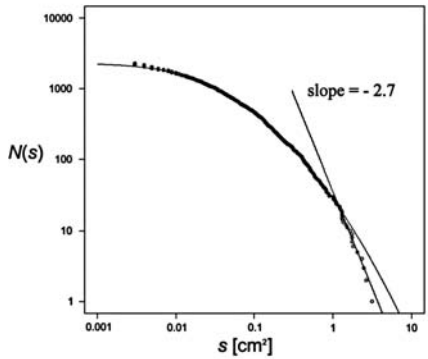

Fig. 4. Log-log plots for the cumulative number of masticated food fragments of raw carrot chewed 5 strokes, $N(s)$, versus their size s. Addition data over 10 trials are shown. The curve indicates a lognormal distribution with $N_T = 2277$, $\bar{s} = 0.0255$ and $\sigma = 0.488$.

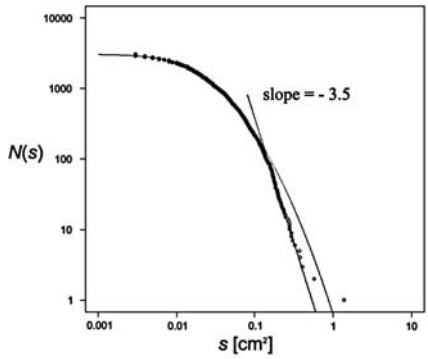

Fig. 5. Log-log plots for the cumulative number of masticated food fragments of raw carrot chewed by the threshold number of strokes (about 16 strokes), $N(s)$, versus their size s. Addition data over 5 trials are shown. The curve indicates a lognormal distribution with $N_T = 3000$, $\bar{s} = 0.0209$ and $\sigma = 0.349$.

assume that the mastication has a lower limit (threshold) for fragment size. We can imagine that as the food fragments become smaller, they become softer and more difficult to be fragmentized due to diverse factors such as saliva in the oral cavity and moisture contained in the food. Matsushita and Sumida proposed simple stochastic models to better understand the one-dimensional brittle fracture such as very thin and fragile glass rods.[19]

Their models yield the fragment-size distribution close to the lognormal because their models have dynamics like cascade fracture, *i.e.*, random multiplicative stochastic processes. They extended one simple cascade model which leads to the lognormal distribution. They put a lower threshold for fragment-size. If any fragments happen to become smaller than the lower threshold, they never break any more. It was found that the lower threshold changes the fragment-size distribution from the lognormal to the power-law behavior. In the case of the present mastication experiments we think that the similar effect as in the Matsushita-Sumida model happens.

4. Conclusion

In this paper we have studied long-tailed distribution of biological systems. We have found that the lognormal distribution is characteristic of the statistics of the duration distribution of life for disability. We believe that the main lesson from the argument of the duration distribution for disability in aged people is that any hospital for the aged must be a polyclinic which can cope with various diseases simultaneously in a coordinated fashion, because diseases in aged people usually proceed multiplicatively.

Next, we have studied the fragment-size distribution of masticated raw carrot. Just as the duration distribution for disability, we found that lognormal distribution is characteristic of the statistics of food fragmentation by human mastication for early stage of mastication. Especially, it is important that the fragment-size distribution changes from the lognormal to a double-size-group structure of lognormal with power-law tail, as the number of chewing strokes increases. In order to explain this structure, we suggested that the mastication has a lower threshold for fragment size. We believe that this behavior is described by the Matsushita-Sumida model with a lower threshold.

In various complex networks recently discussed extensively, the typical distribution function is power-law one.[20] The successive growth phenomena dominated by a mechanism of preferential attachment lead to the power-law distribution, such as the World Wide Web.[21] On the other hand, the duration of disability and the masticatory fragmentation are also successive growth phenomena. According to our present study, however, they lead to lognormal distribution, not the power-law. One of the reasons may be that the randomness is more dominant than the preferential attachment for both of the present cases.[22] In case of the duration of disability in the aged, they do not have mechanism of the preferential attachment since diseases in the aged develop not only sequentially but also randomly. It is

a matter of course that mechanism of masticatory fragmentation does not include the preferential attachment. In conclusion, we think that the events involved in these cases are multiplicative stochastic processes with strong randomness, whose distribution is, at least as the first approximation, a lognormal distribution.

References

1. T. Ishii and M. Matsushita, *J. Phys. Soc. Jpn.* **61**, 3474 (1992).
2. H. Katsuragi, D. Sugino, and H. Honjo, *Phys. Rev. E* **70**, 065103(R) (2004).
3. A. Fujiwara, *Icarus* **52**, 434 (1982).
4. P. Bak, C. Tang, K. Wiesenfeld, *Phys. Rev. Lett.* **59**, 381 (1987).
5. B. Gutenberg and C. F. Richter, *Ann. Geofis.* **9**, 1 (1956).
6. E. W. Montroll and M. F. Shlesinger, *J. Stat. Phys.* **32**, 209 (1983).
7. W. Shockley, *Proc. IRE* **45**, 279 (1957).
8. N. Kobayashi, Y. Sasaki, O. Moriyama, S. Matsushita, and M. Matsushita, accepted for publication in *Nonlinear Phenomena in Complex Systems* (2006).
9. O. Moriyama, H. Itoh, S. Matsushita, and M. Matsushita, *J. Phys. Soc. Jpn.* **72**, 2409 (2003).
10. S. Matsushita, M. Matsushita, H. Itoh, K. Hagiwara, R. Takahashi, T. Ozawa and K. Kuramoto, *Geriatr. Gerontol. Int.* **3**, 189 (2003).
11. N. Kobayashi, K. Kohyama, Y. Sasaki and M. Matsushita, *J. Phys. Soc. Jpn.* **75**, 083001 (2006).
12. C. E. Finch and T. B. L. Kirkwood. *Chance, Development and Aging.* (Oxford University Press, New York, 2000).
13. B. Gompertz, *Philos. Trans. Roy. Soc. Lond. A* **115**, 513 (1825).
14. D. Stauffer, "The Complexity of Biological Ageing" in *Thinking in Patterns*, Edited by M. M. Novak (World Scientific, Singapore, 2004) 131.
15. M. Bourne, *Food Texture and Viscosity, 2nd ed.* (Academic Press, London, 2003).
16. J. B. Hutchings and P. J. Lillford, *J. Texture Stud.* **19**, 103 (1988).
17. M.-A. Peyron, A. Mishellany and A. Woda, *J. Dent. Res.* **83**, 578 (2004).
18. A. N. Kolmogorov, *Dokl. Akad. Nauk SSSR.* **31**, 99 (1941).
19. M. Matsushita and K. Sumida, *Bull. Facul. Sci.& Eng. Chuo Univ.* **31**, 69 (1988).
20. R. Albert and A.-L. Barabási, *Rev. Mod. Phys.* **74**, 47 (2002).
21. A.-L. Barabási and R. Albert, *Science* **286**, 509 (1999).
22. S. Redner, *Phys. Today* **58**(June), 49 (2005).

TWO-CLASS STRUCTURE OF INCOME DISTRIBUTION IN THE USA: EXPONENTIAL BULK AND POWER-LAW TAIL

V. M. YAKOVENKO and A. CHRISTIAN SILVA

Department of Physics, University of Maryland, College Park, MD 20742-4111, USA
http://www2.physics.umd.edu/~yakovenk/econophysics.html

Personal income distribution in the USA has a well-defined two-class structure. The majority of population (97–99 %) belongs to the lower class characterized by the exponential Boltzmann-Gibbs ("thermal") distribution, whereas the upper class (1–3 % of population) has a Pareto power-law ("superthermal") distribution. By analyzing income data for 1983–2001, we show that the "thermal" part is stationary in time, save for a gradual increase of the effective temperature, whereas the "superthermal" tail swells and shrinks following the stock market. We discuss the concept of equilibrium inequality in a society, based on the principle of maximal entropy, and quantitatively show that it applies to the majority of population.

Keywords: Econophysics, social inequality, income distribution, Boltzmann-Gibbs distribution, Pareto law

Attempts to apply the methods of exact sciences, such as physics, to describe a society have a long history.[1] At the end of the 19th century, Italian physicist, engineer, economist, and sociologist Vilfredo Pareto suggested that income distribution in a society is described by a power law.[2] Modern data indeed confirm that the upper tail of income distribution follows the Pareto law.[3–7] However, the majority of population does not belong there, so characterization and understanding of their income distribution remains an open problem. Drăgulescu and Yakovenko[8] proposed that the equilibrium distribution should follow an exponential law analogous to the Boltzmann-Gibbs distribution of energy in statistical physics. The first factual evidence for the exponential distribution of income was found in Ref. 9. Coexistence of the exponential and power-law parts of the distribution was recognized in Ref. 10. However, these papers, as well as Ref. 11, studied the data only for a particular year. Here we analyze temporal evolution of

the personal income distribution in the USA during 1983–2001.[12] We show that the US society has a well-defined two-class structure. The majority of population (97–99 %) belongs to the lower class and has a very stable in time exponential ("thermal") distribution of income. The upper class (1–3 % of population) has a power-law ("superthermal") distribution, whose parameters significantly change in time with the rise and fall of stock market. Using the principle of maximal entropy, we discuss the concept of equilibrium inequality in a society and quantitatively show that it applies to the bulk of population. Most of academic and government literature on income distribution and inequality[13–16] does not attempt to fit the data by a simple formula. When fits are performed, usually the log-normal distribution[17] is used for the lower part of the distribution.[5–7] Only recently the exponential distribution started to be recognized in income studies,[18,19] and models showing formation of two classes started to appear.[20,21]

Let us introduce the probability density $P(r)$, which gives the probability $P(r)\,dr$ to have income in the interval $(r, r + dr)$. The cumulative probability $C(r) = \int_r^\infty dr' P(r')$ is the probability to have income above r, $C(0) = 1$. By analogy with the Boltzmann-Gibbs distribution in statistical physics,[8,9] we consider an exponential function $P(r) \propto \exp(-r/T)$, where T is a parameter analogous to temperature. It is equal to the average income $T = \langle r \rangle = \int_0^\infty dr' r' P(r')$, and we call it the "income temperature." When $P(r)$ is exponential, $C(r) \propto \exp(-r/T)$ is also exponential. Similarly, for the Pareto power law $P(r) \propto 1/r^{\alpha+1}$, $C(r) \propto 1/r^\alpha$ is also a power law.

We analyze the data[22] on personal income distribution compiled by the Internal Revenue Service (IRS) from the tax returns in the USA for the period 1983–2001 (presently the latest available year). The publicly available data are already preprocessed by the IRS into bins and effectively give the cumulative distribution function $C(r)$ for certain values of r. First we make the plots of $\log C(r)$ *vs.* r (the log-linear plots) for each year. We find that the plots are straight lines for the lower 97–98 % of population, thus confirming the exponential law. From the slopes of these straight lines, we determine the income temperatures T for each year. In Fig. 1, we plot $C(r)$ and $P(r)$ *vs.* r/T (income normalized to temperature) in the log-linear scale. In these coordinates, the data sets for different years collapse onto a single straight line. (In Fig. 1, the data lines for 1980s and 1990s are shown separately and offset vertically.) The columns of numbers in Fig. 1 list the values of the annual income temperature T for the corresponding years, which changes from 19 k$ in 1983 to 40 k$ in 2001. The upper horizontal axis in Fig. 1 shows income r in k$ for 2001.

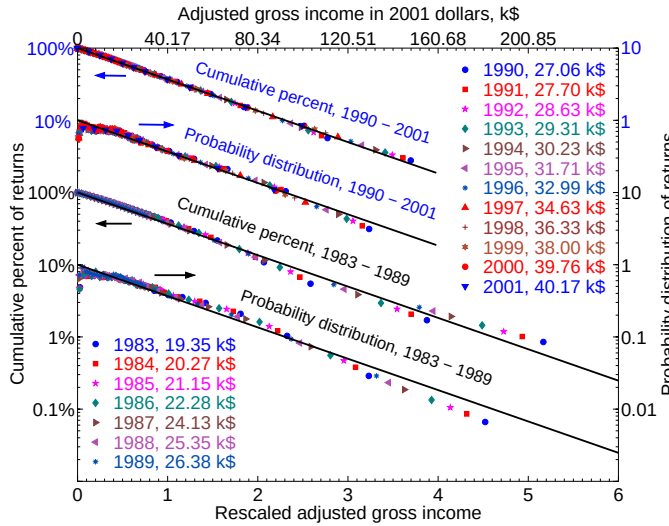

Fig. 1. Cumulative probability $C(r)$ and probability density $P(r)$ plotted in the log-linear scale *vs.* r/T, the annual personal income r normalized by the average income T in the exponential part of the distribution. The IRS data points are for 1983–2001, and the columns of numbers give the values of T for the corresponding years.

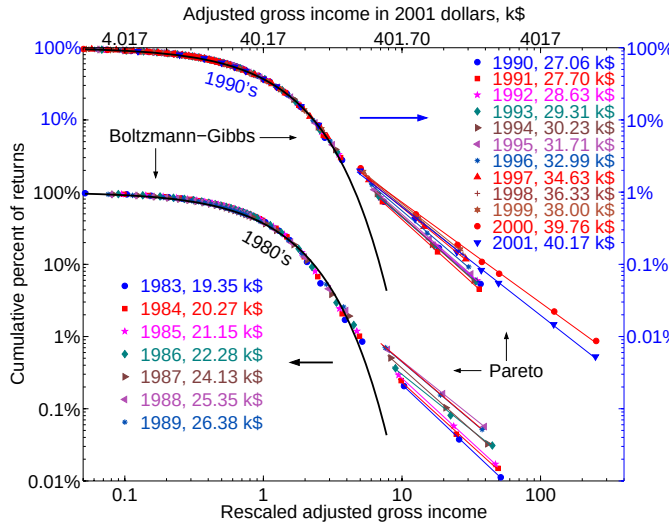

Fig. 2. Log-log plots of the cumulative probability $C(r)$ *vs.* r/T for a wider range of income r.

In Fig. 2, we show the same data in the log-log scale for a wider range of income r, up to about $300T$. Again we observe that the sets of points for different years collapse onto a single exponential curve for the lower part of the distribution, when plotted *vs.* r/T. However, above a certain income $r_* \approx 4T$, the distribution function changes to a power law, as illustrated by the straight lines in the log-log scale of Fig. 2. Thus we observe that income distribution in the USA has a well-defined two-class structure. The lower class (the great majority of population) is characterized by the exponential, Boltzmann-Gibbs distribution, whereas the upper class (the top few percent of population) has the power-law, Pareto distribution. The intersection point of the exponential and power-law curves determines the income r_* separating the two classes. The collapse of data points for different years in the lower, exponential part of the distribution in Figs. 1 and 2 shows that this part is very stable in time and, essentially, does not change at all for the last 20 years, save for a gradual increase of temperature T in nominal dollars. We conclude that the majority of population is in statistical equilibrium, analogous to the thermal equilibrium in physics. On the other hand, the points in the upper, power-law part of the distribution in Fig. 2 do not collapse onto a single line. This part significantly changes from year to year, so it is out of statistical equilibrium. A similar two-part structure in the energy distribution is often observed in physics, where the lower part of the distribution is called "thermal" and the upper part "superthermal".[23]

Temporal evolution of the parameters T and r_* is shown in Fig. 3A. We observe that the average income T (in nominal dollars) was increasing gradually, almost linearly in time, and doubled in the last twenty years. In Fig. 3A, we also show the inflation coefficient (the consumer price index CP0I from Ref. 24) compounded on the average income of 1983. For the twenty years, the inflation factor is about 1.7, thus most, if not all, of the nominal increase in T is inflation. Also shown in Fig. 3A is the nominal gross domestic product (GDP) per capita,[24] which increases in time similarly to T and CPI. The ratio r_*/T varies between 4.8 and 3.2 in Fig. 3A.

In Fig. 3B, we show how the parameters of the Pareto tail $C(r) \propto 1/r^{\alpha}$ change in time. Curve (a) shows that the power-law index α varies between 1.8 and 1.4, so the power law is not universal. Because a power law decays with r more slowly than an exponential function, the upper tail contains more income than we would expect for a thermal distribution, hence we call the tail "superthermal".[23] The total excessive income in the upper tail can be determined in two ways: as the integral $\int_{r_*}^{\infty} dr' r' P(r')$ of the power-law distribution, or as the difference between the total income in the system

and the income in the exponential part. Curves (c) and (b) in Fig. 3B show the excessive income in the upper tail, as a fraction f of the total income in the system, determined by these two methods, which agree with each other reasonably well. We observe that f increased by the factor of 5 between 1983 and 2000, from 4 % to 20 %, but decreased in 2001 after the crash of the US stock market. For comparison, curve (e) in Fig. 3B shows the stock market index S&P 500 divided by inflation. It also increased by the factor of 5.5 between 1983 and 1999, and then dropped after the stock market crash. We conclude that the swelling and shrinking of the upper income tail is correlated with the rise and fall of the stock market. Similar results were found for the upper income tail in Japan in Ref. 4. Curve (d) in Fig. 3B shows the fraction of population in the upper tail. It increased from 1 % in 1983 to 3 % in 1999, but then decreased after the stock market crash. Notice, however, that the stock market dynamics had a much weaker effect on the average income T of the lower, "thermal" part of income distribution shown in Fig. 3A.

For discussion of income inequality, the standard practice is to construct the so-called Lorenz curve.[13] It is defined parametrically in terms of the two coordinates $x(r)$ and $y(r)$ depending on the parameter r, which changes from 0 to ∞. The horizontal coordinate $x(r) = \int_0^r dr' P(r')$ is the fraction of population with income below r. The vertical coordinate $y(r) = \int_0^r dr' r' P(r') / \int_0^\infty dr' r' P(r')$ is the total income of this population, as a fraction of the total income in the system. Fig. 4 shows the data points for the Lorenz curves in 1983 and 2000, as computed by the IRS.[16] For a purely exponential distribution of income $P(r) \propto \exp(-r/T)$, the formula $y = x + (1-x)\ln(1-x)$ for the Lorenz curve was derived in Ref. 9. This formula describes income distribution reasonably well in the first approximation,[9] but visible deviations exist. These deviations can be corrected by taking into account that the total income in the system is higher than the income in the exponential part, because of the extra income in the Pareto tail. Correcting for this difference in the normalization of y, we find a modified expression[11] for the Lorenz curve

$$y = (1-f)[x + (1-x)\ln(1-x)] + f\Theta(x-1), \tag{1}$$

where f is the fraction of the total income contained in the Pareto tail, and $\Theta(x-1)$ is the step function equal to 0 for $x < 1$ and 1 for $x \geq 1$. The Lorenz curve (1) experiences a vertical jump of the height f at $x = 1$, which reflects the fact that, although the fraction of population in the Pareto tail is very small, their fraction f of the total income is significant. It does not

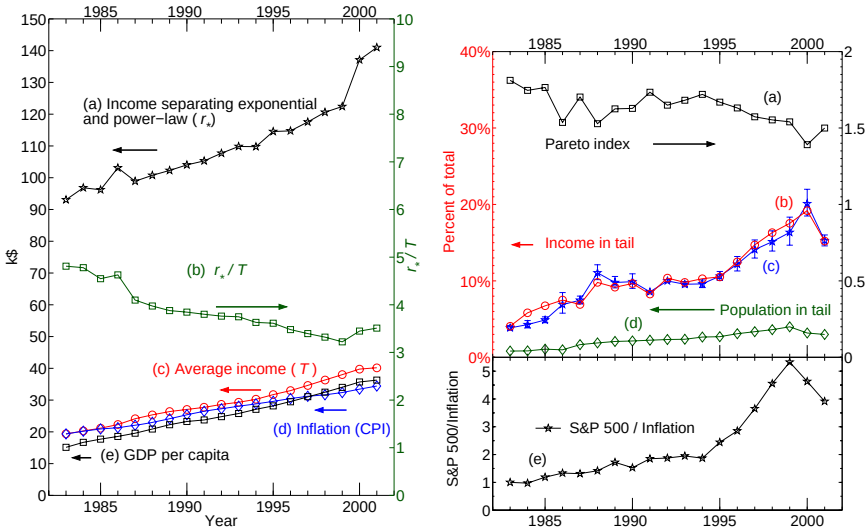

Fig. 3. Left panel A: Temporal evolution of various parameters characterizing income distribution. Right panel B: (a) The Pareto index α of the power-law tail $C(r) \propto 1/r^{\alpha}$. (b) The excessive income in the Pareto tail, as a fraction f of the total income in the system, obtained as the difference between the total income and the income in the exponential part of the distribution. (c) The tail income fraction f, obtained by integrating the Pareto power law of the tail. (d) The fraction of population belonging to the Pareto tail. (e) The stock-market index S&P 500 divided by the inflation coefficient and normalized to 1 in 1983.

matter for Eq. (1) whether the extra income in the upper tail is described by a power law or another slowly decreasing function $P(r)$. The Lorenz curves, calculated using Eq. (1) with the values of f from Fig. 3B, fit the IRS data points very well in Fig. 4.

The deviation of the Lorenz curve from the diagonal in Fig. 4 is a certain measure of income inequality. Indeed, if everybody had the same income, the Lorenz curve would be the diagonal, because the fraction of income would be proportional to the fraction of population. The standard measure of income inequality is the so-called Gini coefficient $0 \leq G \leq 1$, which is defined as the area between the Lorenz curve and the diagonal, divided by the area of the triangle beneath the diagonal.[13] It was calculated in Ref.[9] that $G = 1/2$ for a purely exponential distribution. Temporal evolution of the Gini coefficient, as determined by the IRS,[16] is shown in the inset of Fig. 4. In the first approximation, G is quite close to the theoretically calculated value $1/2$. The agreement can be improved by taking into account the Pareto tail, which gives $G = (1 + f)/2$ for Eq. (1). The inset in Fig.

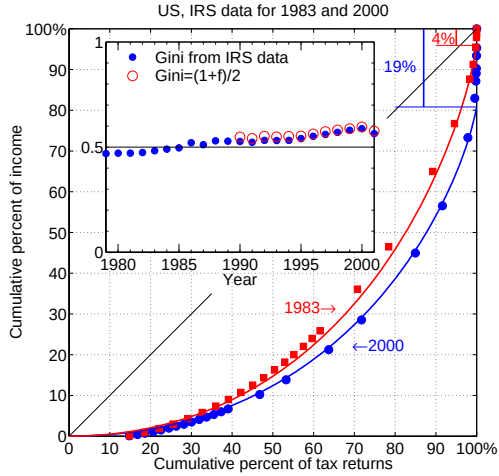

Fig. 4. Main panel: Lorenz plots for income distribution in 1983 and 2000. The data points are from the IRS,[16] and the theoretical curves represent Eq. (1) with f from Fig. 3. Inset: The closed circles are the IRS data[16] for the Gini coefficient G, and the open circles show the theoretical formula $G = (1 + f)/2$.

4 shows that this formula very well fits the IRS data for the 1990s with the values of f taken from Fig. 3B. We observe that income inequality was increasing for the last 20 years, because of swelling of the Pareto tail, but started to decrease in 2001 after the stock market crash. The deviation of G below $1/2$ in the 1980s cannot be captured by our formula. The data points for the Lorenz curve in 1983 lie slightly above the theoretical curve in Fig. 4, which accounts for $G < 1/2$.

Thus far we discussed the distribution of individual income. An interesting related question is the distribution of family income $P_2(r)$. If both spouses are earners, and their incomes are distributed exponentially as $P_1(r) \propto \exp(-r/T)$, then

$$P_2(r) = \int_0^r dr' P_1(r') P_1(r - r') \propto r \exp(-r/T). \tag{2}$$

Equation (2) is in a good agreement with the family income distribution data from the US Census Bureau.[9] In Eq. (2), we assumed that incomes of spouses are uncorrelated. This assumption was verified by comparison with the data in Ref. 11. The Gini coefficient for family income distribution (2) was found to be $G = 3/8 = 37.5$ %,[9] in agreement with the data. Moreover, the calculated value 37.5 % is close to the average G for the developed capitalist countries of North America and Western Europe, as

determined by the World Bank.[11]

On the basis of the analysis presented above, we propose a concept of the *equilibrium inequality* in a society, characterized by $G = 1/2$ for individual income and $G = 3/8$ for family income. It is a consequence of the exponential Boltzmann-Gibbs distribution in thermal equilibrium, which maximizes the entropy $S = \int dr\, P(r) \ln P(r)$ of a distribution $P(r)$ under the constraint of the conservation law $\langle r \rangle = \int_0^\infty dr\, P(r)\, r = \text{const}$. Thus, any deviation of income distribution from the exponential one, to either less inequality or more inequality, reduces entropy and is not favorable by the second law of thermodynamics. Such deviations may be possible only due to non-equilibrium effects. The presented data show that the great majority of the US population is in thermal equilibrium.

Finally, we briefly discuss how the two-class structure of income distribution can be rationalized on the basis of a kinetic approach, which deals with temporal evolution of the probability distribution $P(r,t)$. Let us consider a diffusion model, where income r changes by Δr over a period of time Δt. Then, temporal evolution of $P(r,t)$ is described by the Fokker-Planck equation[25]

$$\frac{\partial P}{\partial t} = \frac{\partial}{\partial r}\left(AP + \frac{\partial}{\partial r}(BP) \right), \quad A = -\frac{\langle \Delta r \rangle}{\Delta t}, \quad B = \frac{\langle (\Delta r)^2 \rangle}{2\Delta t}. \qquad (3)$$

For the lower part of the distribution, it is reasonable to assume that Δr is independent of r. In this case, the coefficients A and B are constants. Then, the stationary solution $\partial_t P = 0$ of Eq. (3) gives the exponential distribution[8] $P(r) \propto \exp(-r/T)$ with $T = B/A$. Notice that a meaningful solution requires that $A > 0$, *i.e.* $\langle \Delta r \rangle < 0$ in Eq. (3). On the other hand, for the upper tail of income distribution, it is reasonable to expect that $\Delta r \propto r$ (the Gibrat law[17]), so $A = ar$ and $B = br^2$. Then, the stationary solution $\partial_t P = 0$ of Eq. (3) gives the power-law distribution $P(r) \propto 1/r^{\alpha+1}$ with $\alpha = 1 + a/b$. The former process is additive diffusion, where income changes by certain amounts, whereas the latter process is multiplicative diffusion, where income changes by certain percentages. The lower class income comes from wages and salaries, so the additive process is appropriate, whereas the upper class income comes from investments, capital gains, *etc.*, where the multiplicative process is applicable. Reference 4 quantitatively studied income kinetics using tax data for the upper class in Japan and found that it is indeed governed by a multiplicative process. The data on income mobility in the USA are not readily available publicly, but are accessible to the Statistics of Income Research Division of the IRS. Such data would allow to verify the conjectures about income kinetics.

The exponential probability distribution $P(r) \propto \exp(-r/T)$ is a monotonous function of r with the most probable income $r = 0$. The probability densities shown in Fig. 1 agree reasonably well with this simple exponential law. However, a number of other studies found a nonmonotonous $P(r)$ with a maximum at $r \neq 0$ and $P(0) = 0$. These data were fitted by the log-normal[5–7] or the gamma distribution.[19,20,26] The origin of the discrepancy in the low-income data between our work and other papers is not completely clear at this moment. The following factors may possibly play a role. First, one should be careful to distinguish between personal income and group income, such as family and household income. As Eq. (2) shows, the later is given by the gamma distribution even when the personal income distribution is exponential. Very often statistical data are given for households and mix individual and group income distributions (see more discussion in Ref. 9). Second, the data from tax agencies and census bureaus may differ. The former data are obtained from tax declarations of all taxable population, whereas the later data from questionnaire surveys of a limited sample of population. These two methodologies may produce different results, particularly for low incomes. Third, it is necessary to distinguish between distributions of money,[8,26,27] wealth,[20,28] and income. They are, presumably, closely related, but may be different in some respects. Fourth, the low-income probability density may be different in the USA and in other countries because of different social security policies: see the study of income distribution in Australia.[30] All these questions require careful investigation in future work. We can only say that the data sets analyzed in this paper and our previous papers are well described by a simple exponential function for the whole lower class. This does not exclude a possibility that other functions can also fit the data.[29] However, the exponential law has only one fitting parameter T, whereas log-normal, gamma, and other distributions have two or more fitting parameters, so they are less parsimonious.

References

1. P. Ball, *Critical Mass* (Farrar, Straus, and Giroux, New York, 2004).
2. V. Pareto, *Le Cours d'Economie Politique* (Macmillan, London, 1897).
3. D. G. Champernowne, *The Distribution of Income between Persons* (Cambridge University Press, 1973).
4. Y. Fujiwara, W. Souma, H. Aoyama, T. Kaizoji, and M. Aoki, *Physica A* **321**, 598 (2003); H. Aoyama, W. Souma, and Y. Fujiwara, *Physica A* **324**, 352 (2003).
5. W. Souma, Fractals 9 (2001) 293.
6. F. Clementi and M. Gallegati, *Physica A* 350 (2005) 427.

7. T. Di Matteo, T. Aste, and S. T. Hyde, in *The Physics of Complex Systems*, eds. F. Mallamace and H. E. Stanley, (IOS Press, Amsterdam, 2004, p. 435.)
8. A. A. Drăgulescu and V. M. Yakovenko, *Eur. Phys. J. B* **17**, 723 (2000).
9. A. A. Drăgulescu and V. M. Yakovenko, *Eur. Phys. J. B* **20**, 585 (2001).
10. A. A. Drăgulescu and V. M. Yakovenko, *Physica A* **299**, 213 (2001).
11. A. A. Drăgulescu and V. M. Yakovenko, in *Modeling of Complex Systems: Seventh Granada Lectures*, eds. P. L. Garrido and J. Marro (AIP Conference Proceedings **661**, New York, 2003), p. 180.
12. A. C. Silva and V. M. Yakovenko, *Europhys. Lett.* **69**, 304 (2005).
13. N. Kakwani, *Income Inequality and Poverty* (Oxford University Press, Oxford, 1980).
14. D. G. Champernowne and F. A. Cowell, *Economic Inequality and Income Distribution* (Cambridge University Press, Cambridge, 1998).
15. *Handbook of Income Distribution*, eds. A. B. Atkinson and F. Bourguignon (Elsevier, Amsterdam, 2000).
16. M. Strudler and T. Petska, *An Analysis of the Distribution of Individual Income and Taxes, 1979–2001* (IRS, Washington DC, 2003), http://www.irs.gov/pub/irs-soi/03strudl.pdf.
17. R. Gibrat, *Les Inégalités Economiques* (Sirely, Paris, 1931).
18. M. Nirei and W. Souma, working paper (2004), http://www.santafe.edu/~makoto/papers/income.pdf.
19. J. Mimkes, Th. Fruend, and G. Willis, cond-mat/0204234; G. Willis and J. Mimkes, cond-mat/0406694.
20. N. Scafetta, S. Picozzi, and B. J. West, *Quantitative Finance*, **4**, 353 (2004).
21. I. Wright, *Physica A* **346**, 589 (2005)
22. *Individual Income Tax Returns, Pub. 1304* (IRS, Washington DC, 1983–2001).
23. A. Hasegawa, K. Mima, and M. Duong-van, *Phys. Rev. Lett.* **54**, 2608 (1985); M. I. Desai *et al.*, *Astrophysical Journal* **588**, 1149 (2003); M. R. Collier, *Advances in Space Research* **33**, 2108 (2004).
24. *How Much is That?* http://eh.net/hmit/.
25. E. M. Lifshitz and L. P. Pitaevskii, *Physical Kinetics* (Pergamon Press, Oxford, 1981).
26. J. C. Ferrero, *Physica A* **341**, 575 (2004).
27. A. Chatterjee, B. K. Chakrabarti, and S. S. Manna, *Physica Scripta* **T106**, 36 (2003).
28. J.-P. Bouchaud and M. Mézard, *Physica A* **282**, 536 (2000); S. Solomon and P. Richmond, *Physica A* **299**, 188 (2001); A. Y. Abul-Magd, *Phys. Rev. E* **66**, 057104 (2002).
29. A. A. Drăgulescu, Ph. D. Thesis (2002), Sec. II H, cond-mat/0307341.
30. A. Banerjee, V. M. Yakovenko, and T. Di Matteo, physics/0601176, *Physica A* in press.

POWER LAW DISTRIBUTIONS IN TWO COMMUNITY CURRENCIES

N. KICHIJI

Department of Engineering, Hokkaido University, Kita 13, Nishi 8, Kita-ku, Sapporo, Hokkaido 060-8628, Japan,
E-mail: kichiji@topology.coe.hokudai.ac.jp
www.topology.coe.hokudai.ac.jp/

M. NISHIBE

Graduate School of Economics, Hokkaido University, Kita 9, Nishi 7, Kita-ku, Sapporo, Hokkaido 060-0809, Japan
E-mail: nishibe@econ.hokudai.ac.jp

The purpose of this paper is to highlight certain newly discovered social phenomena that accord with Zipf's law, in addition to the famous natural and social phenomena including word frequencies, earthquake magnitude, city size, income[1] *etc.* that are already known to follow it. These phenomena have recently been discovered within the transaction amount (payments or receipts) distributions within two different Community Currencies (CC) that had been initiated as social experiments. One is a local CC circulating in a specific geographical area, such as a town. The other is a virtual CC used among members who belong to a certain community of interest (COI) on the Internet. We conducted two empirical studies to estimate the economic vitalization effects they had on their respective local economies. The results we found were that the amount of transactions (payments and receipts) of the two CCs was distributed according to a power-law distribution with a unity rank exponent. In addition, we found differences between the two CCs with regard to the shapes of their distribution over a low-transaction range. The result may originate from the difference in methods of issuing CCs or in the magnitudes of the minimum-value unit; however, this result calls for further investigation.

Keywords: Power law; Zipf's law; Community Currencies; Social Experiment.

1. Introduction

After the full liberalization of capital movements in the early 1980s, free capital flows have generated new risks of instability. Because of this situ-

ation, Community Currencies (CCs)[a] have spread over the world, particularly in Western countries since the 1980s-the second CC boom after the first one in the 1930s. However, little research and few studies have been carried out to quantify how much these CCs vitalize local economies. Since the two communities of the CC cooperated, we were able to conduct two empirical studies in which we quantitatively estimated the economic effects of those two CCs. We discovered that Zipf's law applies to the distribution of the transaction amounts within those CCs; the results indicate that economic transactions create Zipf's law[2–4] without considering the type of CCs, because it is well known that income and wealth distribution with legal tender (*e.g.*, dollars or yen) follow Zipf's law. Section 2 deals with two CCs. Section 3 explains Zipf's law. Finally, we briefly comment on future research in this area.

2. Two Community Currencies

We conducted two empirical studies to estimate the economic vitalization effects of two different CCs on local economies. One of these CCs is a local one that circulates in a specific geographical area, and the other is a virtual CC that is used between members who belong to a certain community of interest (COI) on the Internet. The first CC is called Tomamae-cho ("town" in Japanese) Chiiki-Tuka ("Community Currency")[b]. Tomamae-cho is a small town in the northern part of Hokkaido in Japan with a population of about 4300 people. Its main industries are fishing, forestry, and commerce. Tomamae-cho has recently been faced with problems such as scarcity of job opportunities and spillover of purchasing power to relatively large neighboring towns (with population of 8000), in addition to long-term depopulation and aging, as in other rural areas in Japan. In 2004, the Tomamae-cho Commerce and Industry Association decided on an experimental introduction of a CC for the purpose of both economic activation and community revitalization, in collaboration with the Tomamae-cho Municipal Government.

The Tomamae-cho CC, called "P," has a linear equivalence to "yen," and the circulation works in two ways: (1) units are issued by the Commerce

[a]Community Currencies are also called Local Currencies or Complementary Currencies, with slightly different connotations. For example, Local Currencies often means the CCs that circulate in confined local areas such as towns or villages. However, we will use only the term Community Currency to avoid any confusion in terminology.

[b]This is legally a Gift Certificate redeemable into yen, so that shoppers may use it again to others or refund it with money when they receive it from their customers.

and Industry Association and the Municipal Government of Tomamae-cho when participants buy CC with yen[c], (2) participants get paid with CC for the service or goods they supply to others.

We have participated in the CC experiment and investigated its circulation flow in a unique way. Before the experimental circulation in 2004, our investigation team requested the issuing agents to devise an entry space on the back of each CC note for its recipients to record transaction dates, their names and addresses, and the purposes of use, for a maximum of five recipients. We also asked the participants to agree to cooperate in our investigation. After the circulation experiment of the Tomamae-cho CC, we collected all the currency notes that had returned to the issuing agents in exchange for yen, and we then created the adjacent matrix from the acquired data to analyze the circulation flow of the notes of the CC by using a social network theory.

The virtual CC is called LETS-Q[d]. Q is the "monetary" unit of LETS-Q; although it is not exchangeable with yen, it is equivalent to yen. The CC system was initiated in Japan in November 2001 and is managed by an administrative committee called Q-hive, comprising individuals such as professors, teachers, farmers, students, artists, and musicians. One of the authors, Makoto Nishibe, is the initiator of LETS-Q and an ex-representative of Q-hive. Coffee shops and bakeries are also members of LETS-Q apart from individual members, and are scattered all over the world. Some of them are in Tokyo and Osaka, and others in Hokkaido and even in New York. The other author, Nozomi Kichiji, is also a member of LETS-Q.

The characteristic feature of LETS-Q lies in the realization of the same type of multilateral settlement of accounts in the Internet as in the case of usual LETS systems[e]. Using this technique, participants are relieved of the constraints of geographically localized communities such that they can involve in LETS-Q irrespective of their location. Therefore, we call this type of online LETS "open communities" or "glocal" currency. Since LETS-Q was implemented on the Internet, and all related data are stored in the

[c]500 'Yen' can buy 500 'P' note and 10 'P' stamps as its 2 percent premium.

[d]LETS stands for a Local Exchange Trading System. This system embodies the most popular type of Community Currency; it was initiated in 1983 by Michael Linton in Comox Valley, Vancouver Island, Canada, and is now utilised in more than 2000 districts worldwide.

[e]All participants in LETS start from zero in their account and cumulatively record plus and minus transactions within their accounts when they offer and receive goods or services from other participants. It is a characteristic feature of the LETS system that the summation of all accounts remains constantly at zero.

LETS-Q server, we have been able, with the help of Q-hive, to access the LETS-Q data; these data contain only the ID numbers of participants, the transaction amount, and the time stamps of settlement on the web. It does not include personal data such as name, address, and age. Using this data, we can analyze economic phenomena at the meso level of a small-sized group.

3. Zipf's Law

Zipf's law, named after the Harvard linguistic professor George Kingsley Zipf, is the observation that frequency of occurrence of a certain event(P), as a function of the rank (i) when the rank is determined by the above frequency of occurrence, is a power-law function $P_i \sim \frac{1}{i^a}$ with the exponent close to unity (1). It is widely known that Zipf's law applies to city size, income, word frequency, and earthquake magnitude. However, the mechanism of Zipf's law has not been clarified enough; accordingly, it is desirable to find more events to which Zipf's law applies. In this paper, we have presented four such events. We examined the distribution of payments and receipts of Tomamae-cho CC and LETS-Q over a certain period. The results are illustrated in Fig. 1 and Fig. 2. All figures show the rank-size relationships of the transaction amounts, the x axis is the rank, and y axis is the size. These relationships are approximately linear on a log-log plot; in other words, the ranked slopes in both the cases are nearly -1, which makes them Zipf. Thus, we discovered Zipf's law distributions in the transaction amounts within the two different CCs (local and virtual). These results indicate that transaction amounts follow Zipf's law irrespective of the type of CCs.

However, the slope of the line of best fit of the Tomamae-cho CC (-1.13) is steeper than that of LETS-Q (-1.00). This indicates that the LETS-Q is slightly more level and even than the Tomamae-cho CC in terms of transaction amounts. Moreover, the ways the two graphs fit to linear lines, as is clear from the comparison between Fig. 1 and Fig. 2, are quite different. The distribution of transaction amounts of the Tomamae-cho CC almost perfectly fits a straight line, but that of the LETS-Q deviates from it after rank 100. It can be seen that the overall Gini coefficients[f] of the Tomamae-

[f]The Gini coefficient is a measure of inequality of a distribution, defined as the ratio of area between the Lorenz curve of the distribution and the curve of the uniform distribution, to the area under the uniform distribution.

cho CC are smaller than those of the LETS-Q[g]. However, when calculating the Gini coefficients for LETS-Q for the range of rank 1 to 100, we obtain results smaller than those for Tomamae-cho CC[h]. These results indicate that the Tomamae-cho CC is more equal than the LETS-Q on the whole but LETS-Q is more equal than the Tomamae-cho CC under rank 100; this twist is caused by the aforementioned deviation of the distribution of transaction amounts with LETS-Q from the line of best fit over a low-transaction range.

The subject of concern is the reason for such a deviation in the case of LETS-Q. There are two possible explanations for this. The first is due to the differing rules under which the CCs are issued. The Tomamae-cho CC can be bought and redeemed with yen, although the same is neither permitted nor possible for LETS-Q. This creates the difference of constraints on the boundary conditions of the two CCs. The other reason is more technical; in the Tomamae-cho CC, the minimum value unit is 500 P, because only 500 P notes are issued, but for LETS-Q it is just 1Q, because transaction amounts with arbitrary numbers can be recorded in the participants' accounts. This seems to make the lower-right tail of the LETS-Q longer than that of the Tomamae-cho CC. It would appear that the two types of fit of the distributions to Zipf's law reflect the differences between the inner mechanisms and the dynamics of these two CC systems.

4. Summary

It is widely recognized that Zipf's law applies to income and wealth distribution of individuals or corporations with legal tenders. In this paper, it has been shown that Zipf's law applies to different kinds of socio-economic phenomena, such as transactions in CCs. The results suggest that a generic economic transaction can create Zipf's law, regardless of the type of currency. Moreover, we also refer to the difference with regard to how well the distributions fit Zipf's law, signifying the difference of inner mechanisms and dynamics of the two CC systems. We observe that the distributions of transaction amounts of both CCs evolve over time, but further study is required on the relation between the evolution of distributions and Zipf's law.

[g]The overall Gini coefficients for receipts/payments with Tomamae-cho CC are 0.757641/0.719131, and those for LETS-Q are 0.772328/0.735642, respectively.

[h]The Gini coefficients for receipts/payments with LETS-Q for the range of ranks 1-100 are 0.62885/0.558051.

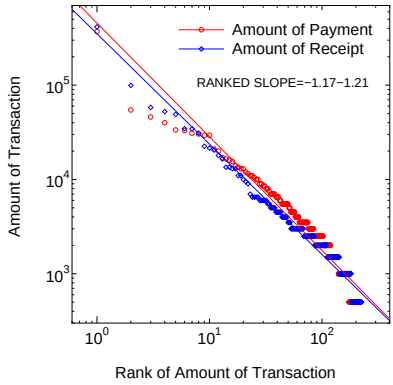

Fig. 1. Individual Rank by its transaction amount in Tomamae-cho CC. Rank of amount of transactions and the amount of transactions are plotted in the log-log scale. The plotted data are for Nov.2004-Feb.2005. The total amount of transactions is 1,385,500 P. The ranked slopes are from -1.17 to -1.21.

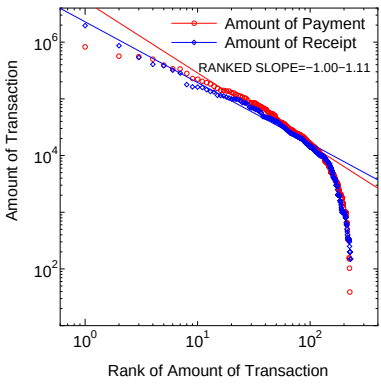

Fig. 2. Individual Rank by its transaction amount in LETS-Q. The rank of amount of transactions and the amount of transactions are plotted in the log-log scale. The plotted data are for Dec.2001-Oct.2002. The total amount of transactions is 10,220,305Q. The ranked slopes are from -1.00 to -1.11.

Acknowledgments

We like to express our appreciation to LETS-Q, Q-hive, Tomamae-cho Commerce and Industry Association and Tomamae-cho Municipal Government for their support and cooperation in our research; and to Takayoshi Kusago, Ippei Hozumi, Kenichi Kurita, Kenichi Yamamoto, Masayuki Yoshida, and Satoshi Yoshii for their collaborations in Tomamae-cho CC experiments. We also thank Satoshi Tanda and Victor M. Yakovenko for their advice and comments. This work was supported by Hokkaido University's 21st century COE program "Topological Science and Technology."

References

1. V. Pareto, *Le Cours d'Économie Politique* (Macmillan, London, 1897).
2. G. Zipf, *Human Behavior and the Principles of Least Effort* (Addison-Wesley, Cambridge, 1949).
3. L. Adamic and B. Huberman, *Glottometrics* **3**, 143 (2002).
4. L. A. Adamic, Zipf, power-laws and pareto - a ranking tutorial (2002), `http://www.hpl.hp.com/research/idl/papers/ranking/ranking.html`

III

Patterns in Biological Objects

This page intentionally left blank

STOICHIOMETRIC NETWORK ANALYSIS OF NONLINEAR PHENOMENA IN A REACTION MECHANISM FOR TWC CONVERTERS

M. MAREK*, O. HADAČ, I. SCHREIBER and M. SCHEJBAL

Department of Chemical Engineering, Center for Nonlinear Dynamics of Chemical and Biological Systems
Institute of Chemical Technology, Prague, Technická 5, 166 28 Prague 6, Czech Republic
** E-mail: Milos.Marek@vscht.cz*

M. KUBÍČEK

Department of Mathematics, Center for Nonlinear Dynamics of Chemical and Biological Systems
Institute of Chemical Technology, Prague, Technická 5, 166 28 Prague 6, Czech Republic

Experimental observations of oscillations and chaotic dynamics in the CO catalytic combustion on supported catalysts were reported more than fifteen years ago. Recently, a detailed reaction mechanism including over 20 reaction steps has been proposed for the catalytic CO oxidation, NO_x reduction and hydrocarbons oxidation taking place in a three-way catalytic converter (TWC), the most common reactor for detoxification of automobile exhaust gases. For an unforced lumped model, we report results of stoichiometric network analysis of several reaction subnetworks determining feedback loops, which cause oscillations within certain ranges of parameters.

Keywords: CO oxidation; C_2H_2 oxidation; TWC converter; Reaction network; Stoichiometric network analysis

1. Introduction

Catalytic oxidation of CO is the most often studied oscillatory heterogeneous catalytic reaction. Two decades ago, it was determined experimentally that periodic and chaotic oscillations can occur in the CO oxidation on noble metal catalysts. It was also found that the transition to chaos takes place via a period-doubling route. Oscillations in the course of CO oxidation on a porous platinum catalyst and on CuO/Al_2O_3 were reported more

than three decades ago.[1,2] Under low-pressure conditions, the CO oxidation on platinum single-crystal surfaces proceeds via a Langmuir-Hinshelwood mechanism.[3] The catalytic oxidation of CO on Pt(110) represents the best studied example among single-crystal oscillatory surface reactions.[4] Temporal oscillations are possible due to an adsorbate-driven phase transition in the top substrate layer[5] and are explained in terms of an oscillatory Langmuir-Hinshelwood network.[6,7]

The most common reactor, where the catalytic CO oxidation on a supported catalyst with Pt and other noble metals (Pd, Rh *etc.*) takes place, is a catalytic monolith used for automobile emission control, particularly the three-way catalytic converter (TWC).[8] The reactor consists of parallel channels, where the catalyst is deposited as a thin washcoat layer (10 – 50 μm thick). The reacting fluid contains CO and hydrocarbons, which are oxidized and nitrogen oxides, which are reduced. The inflow of air containing oxygen is controlled so that the reactor is operated close to stoichiometric composition, mostly under unsteady conditions as inlet flow-rate, temperature and concentrations of the reactants vary. The variation of oxygen content in the inlet gas is controlled by an oxygen λ-sensor. Due to a time lag, the control leads to a nearly periodic variation of the inlet oxygen concentration around the stoichiometric value with a frequency of the order of 1 Hz.

Recently, a detailed kinetic scheme for reactions in the TWC has been proposed.[9,10] This mechanism consists of over 20 elementary reaction steps and includes subnetworks for oxidation of carbon monoxide and hydrocarbons, and reduction of nitrogen oxides. We use the stoichiometric network analysis for identification of feedbacks and autocatalytic loops leading to oscillations. When choosing acetylene as a typical hydrocarbon, we present results for the reaction subsets involving CO oxidation, simultaneous CO and C_2H_2 oxidation, and simultaneous CO oxidation and NO_x reduction. The oscillatory subnetworks found by our analysis are then used to explain the structure of calculated bifurcation diagrams for a lumped model of the catalytic converter.

2. Mathematical Model

For a preliminary analysis of nonlinear phenomena (oscillations, multiple steady states, *etc.*), we have chosen a lumped model providing a simplified description in the bulk gas phase, in the pores of the catalyst and on the catalyst surface. It consists of two isothermally operated continuous stirred tank reactors (CSTRs) with mass exchange between them. The model is

described[11] by the mass balances in the bulk gas (1), in the pores of the catalyst (2) and on the catalyst surface (3)–(5),

$$\frac{\mathrm{d}c_i(t)}{\mathrm{d}t} = u\frac{T}{T^{\mathrm{std}}}(c_i^{\mathrm{in}} - c_i^{\mathrm{out}}) + \frac{k_{\mathrm{c}}a}{\varepsilon^{\mathrm{g}}}(c_i^{\mathrm{s}} - c_i), \tag{1}$$

$$\frac{\mathrm{d}c_i^{\mathrm{s}}(t)}{\mathrm{d}t} = \frac{1}{\varepsilon^{\mathrm{s}}}\sum_{j=1}^{J}\nu_{i,j}R_j - \frac{k_{\mathrm{c}}a}{\varepsilon^{\mathrm{s}}(1-\varepsilon^{\mathrm{g}})}(c_i^{\mathrm{s}} - c_i), \tag{2}$$

$$\frac{\mathrm{d}\theta_k(t)}{\mathrm{d}t} = \frac{1}{L_{\mathrm{NM}}}\sum_{j=1}^{J}\nu_{k,j}R_j, \tag{3}$$

$$\frac{\mathrm{d}\xi_m(t)}{\mathrm{d}t} = \frac{1}{L_{\mathrm{OSC}}}\sum_{j=1}^{J}\nu_{m,j}R_j, \tag{4}$$

$$\frac{\mathrm{d}\chi_q(t)}{\mathrm{d}t} = \frac{1}{L_{\mathrm{SUP}}}\sum_{j=1}^{J}\nu_{q,j}R_j, \tag{5}$$

where c is the concentration in the bulk gas, c^{s} is the concentration in the washcoat, θ is the coverage of noble metal sites (Pt), ξ is the coverage of oxygen storage sites (Ce), χ is the coverage of support sites (γ-Al_2O_3), k_{c} is the mass transfer coefficient, a is the specific external surface area, R is the reaction rate, ν denotes the stoichiometric coefficient, L_{NM} is the concentration of noble metal sites (Pt), L_{OSC} is the concentration of oxygen storage sites (Ce), L_{SUP} is the concentration of support sites (γ-Al_2O_3), ε^{g} is the macroscopic porosity (void fraction) of the reactor, ε^{s} is the porosity

Table 1. Parameters used in the lumped model.

Parameter	Value
u	20.8 s^{-1}
ε^{w}	0.8
ε^{g}	0.917
$k_{\mathrm{c}}a$	2067.0 s^{-1}
L_{NM}	80 $\mathrm{mol\,m}^{-3}$
L_{OSC}	0.1 $\mathrm{mol\,m}^{-3}$
$y^{\mathrm{in}}_{\mathrm{CO}}$	1.22 mol %
$y^{\mathrm{in}}_{\mathrm{CO_2}}$	20.0 mol %
$y^{\mathrm{in}}_{\mathrm{C_2H_2}}$	680 ppm
$y^{\mathrm{in}}_{\mathrm{NO}}$	1000 ppm
$y^{\mathrm{in}}_{\mathrm{NO_2}}$	1 ppm

Note: The value of u is evaluated at T^{std}=273.15 K ("standard space velocity").

Table 2. Microkinetic reaction scheme used in the model of TWC.

No.	Reaction step	Kinetic expression
1	$CO + * \rightleftharpoons CO^*$	$R_1 = k_1^{\mathrm{f}} L_{\mathrm{NM}} c_{\mathrm{CO}}^{\mathrm{s}} \theta_* - k_1^{\mathrm{b}} L_{\mathrm{NM}} \theta_{\mathrm{CO}^*}$
2	$O_2 + 2* \rightarrow 2O^*$	$R_2 = k_2 L_{\mathrm{NM}} c_{\mathrm{O_2}}^{\mathrm{s}} \theta_*$
3	$CO^* + O^* \rightarrow CO_2 + 2*$	$R_3 = k_3 L_{\mathrm{NM}} \theta_{\mathrm{CO}^*} \theta_{\mathrm{O}^*}$
4	$CO + O^* \rightleftharpoons OCO^*$	$R_4 = k_4^{\mathrm{f}} L_{\mathrm{NM}} c_{\mathrm{CO}}^{\mathrm{s}} \theta_{\mathrm{O}^*} - k_4^{\mathrm{b}} L_{\mathrm{NM}} \theta_{\mathrm{OCO}^*}$
5	$OCO^* \rightarrow CO_2 + *$	$R_5 = k_5 L_{\mathrm{NM}} \theta_{\mathrm{OCO}^*}$
6	$C_2H_2 + * \rightleftharpoons C_2H_2^*$	$R_6 = k_6^{\mathrm{f}} L_{\mathrm{NM}} c_{\mathrm{C_2H_2}}^{\mathrm{s}} \theta_* - k_6^{\mathrm{b}} L_{\mathrm{NM}} \theta_{\mathrm{C_2H_2^*}}$
7	$C_2H_2^* + 2* \rightleftharpoons C_2H_2^{***}$	$R_7 = k_7^{\mathrm{f}} L_{\mathrm{NM}} \theta_{\mathrm{C_2H_2^*}} \theta_*^2 - k_7^{\mathrm{b}} L_{\mathrm{NM}} \theta_{\mathrm{C_2H_2^{***}}}$
8	$C_2H_2^* + 3O^* \rightarrow 2CO^* + H_2O + 2*$	$R_8 = k_8 L_{\mathrm{NM}} \theta_{\mathrm{C_2H_2^*}} \theta_{\mathrm{O}^*}$
9	$C_2H_2^{***} + 3O^* \rightarrow 2CO^* + H_2O + 4*$	$R_9 = k_9 L_{\mathrm{NM}} \theta_{\mathrm{C_2H_2^{***}}} \theta_{\mathrm{O}^*}$
10	$C_2H_2 + O^* \rightleftharpoons C_2H_2O^*$	$R_{10} = k_{10}^{\mathrm{f}} L_{\mathrm{NM}} c_{\mathrm{C_2H_2}}^{\mathrm{s}} \theta_{\mathrm{O}^*} - k_{10}^{\mathrm{b}} L_{\mathrm{NM}} \theta_{\mathrm{C_2H_2O^*}}$
11	$C_2H_2O^* + 2O^* \rightarrow 2CO^* + H_2O + *$	$R_{11} = k_{11} L_{\mathrm{NM}} \theta_{\mathrm{C_2H_2O^*}} \theta_{\mathrm{O}^*}$
12	$O_2 + 2\mathrm{s} \rightarrow 2O^{\mathrm{s}}$	$R_{12} = k_{12} L_{\mathrm{OSC}} c_{\mathrm{O_2}}^{\mathrm{s}} \xi_{\mathrm{s}}$
13	$CO^* + O^{\mathrm{s}} \rightarrow CO_2 + * + \mathrm{s}$	$R_{13} = k_{13} L_{\mathrm{NM}} \theta_{\mathrm{CO}^*} \xi_{\mathrm{O^s}}$
14	$C_2H_2^* + 3O^{\mathrm{s}} + * \rightarrow 2CO^* + H_2O + 3\mathrm{s}$	$R_{14} = k_{14} L_{\mathrm{NM}} \theta_{\mathrm{C_2H_2^*}} \xi_{\mathrm{O^s}}$
15	$CO_2 + \gamma \rightleftharpoons CO_2^{\gamma}$	$R_{15} = k_{15}^{\mathrm{f}} L_{\mathrm{SUP}} c_{\mathrm{CO_2}}^{\mathrm{s}} \chi_{\gamma} - k_{15}^{\mathrm{b}} L_{\mathrm{SUP}} \chi_{\mathrm{CO_2^{\gamma}}}$
16	$NO + * \rightleftharpoons NO^*$	$R_{16} = k_{16}^{\mathrm{f}} L_{\mathrm{NM}} c_{\mathrm{NO}}^{\mathrm{s}} \theta_* - k_{16}^{\mathrm{b}} L_{\mathrm{NM}} \theta_{\mathrm{NO}^*}$
17	$NO^* + * \rightarrow N^* + O^*$	$R_{17} = k_{17} L_{\mathrm{NM}} \theta_{\mathrm{NO}^*} \theta_*$
18	$NO^* + N^* \rightarrow N_2O^* + *$	$R_{18} = k_{18} L_{\mathrm{NM}} \theta_{\mathrm{NO}^*} \theta_{\mathrm{N}^*}$
19	$N_2O^* \rightarrow N_2O + *$	$R_{19} = k_{19} L_{\mathrm{NM}} \theta_{\mathrm{N_2O^*}}$
20	$N_2O^* \rightarrow N_2 + O^*$	$R_{20} = k_{20} L_{\mathrm{NM}} \theta_{\mathrm{N_2O^*}}$
21	$N^* + N^* \rightarrow N_2 + 2*$	$R_{21} = k_{21} L_{\mathrm{NM}} \theta_{\mathrm{N}^*}^2$
22	$NO + O^* \rightleftharpoons NO_2^*$	$R_{22} = k_{22}^{\mathrm{f}} L_{\mathrm{NM}} c_{\mathrm{NO}}^{\mathrm{s}} \theta_{\mathrm{O}^*} - k_{22}^{\mathrm{b}} L_{\mathrm{NM}} \theta_{\mathrm{NO_2^*}}$
23	$NO_2^* \rightleftharpoons NO_2 + *$	$R_{23} = k_{23}^{\mathrm{f}} L_{\mathrm{NM}} \theta_{\mathrm{NO_2^*}} - k_{23}^{\mathrm{b}} L_{\mathrm{NM}} c_{\mathrm{NO_2}}^{\mathrm{s}} \theta_*$

Note: The reaction subsystems for CO and C_2H_2 oxidation on noble metal (*), O_2 storage and release on cerium (s), CO_2 storage on γ-Al_2O_3 (γ) and NO_x transformation on noble metal (*) are separated by horizontal lines. For values of the kinetic parameters see Refs. 10, 12, 13 and 15.

of the washcoat, u is the space velocity, T is the temperature and t is the time.

The model includes the description of mass transfer from the bulk to the catalyst surface (Eq. (1)), the reaction in the porous space (Eq. (2)) and the balances on the catalyst surface, using reaction rates described by the detailed kinetic reaction scheme represented in Table 2 (*cf.* also 10,12,13).

To be able to compare the results of the analysis with the previously cited experimental results for the CO oxidation,[14] we mainly studied the subsystem of reactions for the CO oxidation, consisting of eight reaction steps (reactions 1–5, 12, 13 and 15 in Table 2). The balance equations (1)–(5) form the system of eleven ODE's. The corresponding parameters are given in Table 1. The mathematical model is then formed by 11 ODE's together with algebraic equations for gas phase concentrations and the fractions of occupied centers on the Pt, CeO_2 and γ-Al_2O_3 surface.

3. Stoichiometric Network Analysis and Classification of Oscillatory Dynamics

A preliminary analysis of possible sources of oscillatory behavior in the TWC reaction mechanism given in Table 2 has been made in Ref. 11. Here we focus on the identification of these mechanistic sources of oscillatory instabilities with various modes of oscillatory dynamics displayed by the model. The analysis begins with determining a set of reaction rate vectors of major (or extreme) subnetworks from stoichiometric constraints imposed on steady states of the TWC reaction mechanism assumed to take place in a flow-through stirred reactor and a subsequent stability analysis.[16] Any steady state reaction rate vector in the network is a linear combination of the rate vectors of the extreme subnetworks, which form a basis of simplest or elementary pathways defining characteristic modes available in the network. In geometrical terms, the space of all admissible (*i.e.*, non-negative) rate vectors is an open cone with the extreme subnetworks forming its edges (1-faces). Certain pairs of edges span 2-faces, *etc.*, until full dimension of the cone is reached, spanned by all the edges. The edges and the faces constitute a natural hierarchy of increasingly complex subnetworks that are examined as potential sources of oscillatory behavior. Stability of a steady state (sub)network (not necessarily an edge or an n-face) is given in terms of principal minors of a matrix closely related to the Jacobian matrix.[16] The sign of the relevant minor determines whether the (sub)network is stable for any choice of kinetic parameters or may become unstable. In the latter case, the species associated with the unstable minor play a decisive role in the instability in the sense that their steady state values must be sufficiently small. By choosing the steady state values accordingly, the full Jacobian matrix is obtained. If there is a pair of pure imaginary eigenvalues of the Jacobian, the instability gives rise to periodic oscillatory dynamics via a Hopf bifurcation. In this way, the set of the simplest topologically distinct subnetworks that provide a Hopf bifurcation is found. At this point, a classification and determination of the role of species in oscillations[17] can be done, for example, by calculating mutual phase shifts of oscillating species,[18] or by other methods.[19,20]

As a first step, let us examine the catalytic oxidation of CO alone. This subsystem is represented by chemical reactions 1–5, 12, 13 and 15. In our previous work[11] we introduced two major subnetworks that are potential sources of oscillations. In fact, there are three extreme subnetworks and altogether five different assignments of the role of the species within these subnetworks that may potentially lead to oscillatory dynamics for a suit-

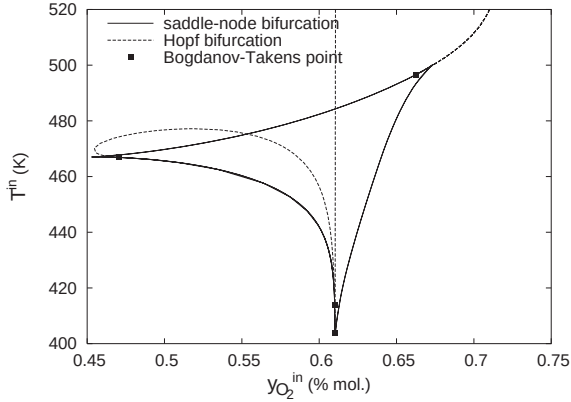

Fig. 1. Bifurcation diagram for CO oxidation, T^{in} - inlet temperature, $y^{\text{in}}_{\text{O}_2}$ - inlet oxygen concentration.

able choice of kinetic parameters. However, all these distinct oscillators may not correspond to realistic values of kinetic parameters. Within the context of this work it is therefore necessary to determine, which of them underlie the oscillatory behavior displayed by the model equations Eqs. (1)–(5) with a set of kinetic parameters according to Refs. 10, 12 and 13. The ultimate goal, of course, would be to determine which of them fit best the experimental observations. By taking the inflow molar percent of oxygen $y^{\text{in}}_{\text{O}_2}$ and the temperature T as free parameters, the bifurcation diagram in Fig. 1 shows two regions of oscillatory dynamics associated with curves of a Hopf bifurcation connected via Bogdanov-Takens points to a closed curve of a saddle-node bifurcation delineating a central region of multiple steady states. The curve of the saddle-node bifurcation contains three cusps rather than two. The cusp pointing down corresponds precisely to the stoichiometric amount of oxygen (0.61 mol%). This peculiar situation indicates that two different unstable subnetworks leading to multiple steady states are involved and associated with the left (negatively tilted sub-stoichiometric) and right (positively tilted super-stoichiometric) parts. The instabilities are nonoscillatory and involve a saddle steady state, but become oscillatory in the two adjacent regions delineated by the Hopf bifurcation curves.

According to the classification system of chemical oscillators,[17] each of the two oscillatory regions is tied up with a particular topologically distinct oscillatory subnetwork. An identification of these subnetworks—and simultaneously determination of the role of species in the mechanism—

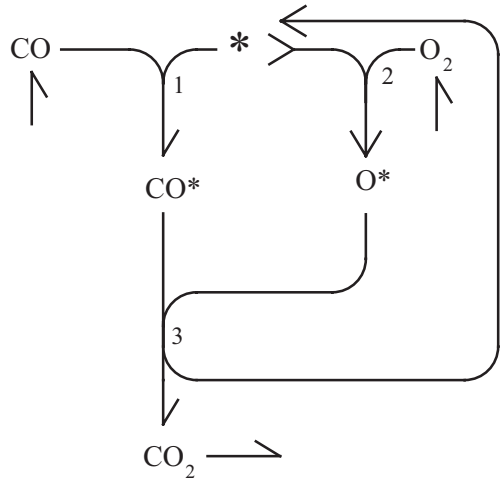

Fig. 2. Network diagram of the dominant subnetwork in the oscillatory region at sub-stoichiometric inlet oxygen compositions in the bifurcation diagram for CO oxidation in Fig. 1.

can be done in several ways.[19–21]

In the present case, we have used the method of mutual phase shifts of oscillating species. The phase shifts remain qualitatively the same throughout an oscillatory domain governed by a given unstable subnetwork and can be conveniently determined at or near the Hopf bifurcation point, where the waveform is sinusoidal.

Using the eigenvectors associated with the pair of pure imaginary eigenvalues of the Jacobian, we have calculated mutual phase shifts of all species for the oscillators where a particular unstable extreme subnetwork found before plays a dominant role. These phase shifts were then compared with those obtained by integrating the model equations (1)–(5) near the Hopf bifurcation. In this way, we can conclude that the occurrence of the two oscillatory regions in the bifurcation diagram in Fig. 1 is accounted for by the two unstable subnetworks shown in Fig. 2 and Fig. 3. Here and in the following reaction networks, each reaction is represented as a multi-tail/multi-head arrow, where the number of feathers/barbs determine the stoichiometric coefficients of reactants/products and the number of left feathers determine the reaction order. The first one corresponds to the case of less than stoichiometric amount of oxygen fed into the converter, the second one corresponds to the surplus of oxygen.

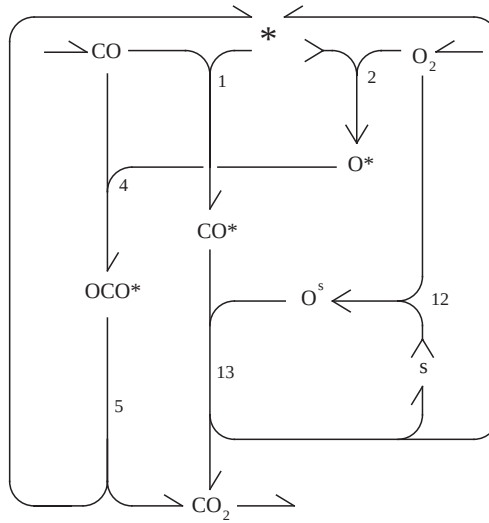

Fig. 3. Network diagram of the dominant subnetwork in the oscillatory region for near-to- or larger-than-stoichiometric inlet oxygen compositions in the bifurcation diagram for CO oxidation in Fig. 1.

The subnetwork in Fig. 2 involves the classical Langmuir-Hinshelwood mechanism whereby both O_2 and CO adsorb first, and the adsorbed forms react to produce CO_2 and regenerate active catalytic sites. The autocatalytic cycle involves reactions 2 and 3 and the species O^* and $*$, which are correspondingly called autocatalytic. The reaction order of these species in the reactions 2 and 3 is one and it is equal to their order in any reactions removing them from the cycle (here reaction 1). In this situation, an unstable steady state is achieved only if there exists an exit reaction, *i.e.*, a reaction of a non-cycle species with a cycle species removing that species.[16] This is provided by reaction 1 and CO is then called the exit species. The autocatalytic and exit species are readily indicated by the instability determining minor as those, having small steady state concentrations. Finally, the oscillatory instability is made possible by the presence of O_2 and its flow-controlled availability.

There is a negative cycle feedback exerted by O_2 upon itself via the path through O^* and $*$ implying that the autocatalysis depletes the supply of O_2, which must be replenished by the feed at a later time. During the autocatalytic phase CO is consumed, and as the autocatalysis reaches its peak, CO becomes depleted due to reaction 1. The overall effect is an os-

cillatory regime with the negative feedback species O_2 advancing the two autocatalytic species $*$ and O^*, which are mutually in-phase, and the exit species CO being antiphase relative to the autocatalytic species. All the above species are thus essential for oscillations. These qualitative considerations are corroborated by calculating mutual phase shift relations from the eigenvectors at the Hopf bifurcation point and are in agreement with phase shifts calculated from the lumped model, *cf.* Eqs. (1)–(5). Interestingly, there is another possible oscillator in the network in Fig. 2, where the roles of O_2 and CO are exchanged, but it is not supported by the phase shifts observed in the model.

On the other hand, the subnetwork shown in Fig. 3 is dominant in the oscillatory region in Fig. 1 where the amount of oxygen is just stoichiometric or in excess. Not surprisingly, the subnetwork involves the oxygen storage sites s. Here the assignment of species is as follows: the instability determining minor indicates that the species $*$, CO^*, s and O_2 should have small steady state concentrations and thus are likely to be of autocatalytic or exit type. Near the Hopf bifurcation, the species $*$, CO^* and s are in-phase. The cycle pathway is made by reactions 1 and 13, and involves only $*$ and CO^* as the autocatalytic species. Oxygen is antiphase correlated with respect to the autocatalytic species and plays the role of the exit species (via the exit reaction 2). The species s branches off the autocatalytic cycle and reacts with excess oxygen to store it (via reaction 12) and subsequently release it (via reaction 13) to feed the autocatalytic cycle. The role of s is to help promote the autocatalysis. Finally, the role of the negative feedback species is adopted by the inflowing carbon monoxide, which advances the autocatalytic species. The instability is also based on the Langmuir-Hinshelwood mechanism, but the flow-controlled species is now CO rather than oxygen. As in the sub-stoichiometric case, there is another possible oscillator within the network in Fig. 3 with the autocatalytic cycle passing through $*$, O^* and OCO^*, and the exit and the negative feedback species being CO and O_2, respectively. However, this arrangement does not agree with the phase shifts displayed by the model.

The complete TWC mechanism involves also nitrogen oxides reduction and acetylene oxidation. It is therefore interesting to see what effects on the oscillators we have just described the additional reactions would exert.

First, we mention the effect of simultaneous CO and C_2H_2 oxidation. The mechanism involves now reactions 1–15. The bifurcation diagram in the same free parameters as before is shown in Fig. 4. The region of multiple steady states still has a complex shape but without the cusp pointing

downward indicating the stoichiometric composition of oxygen (0.814 mol%, which is higher than in Fig. 1 because acetylene contained in the inflow gas must be counted in). There are two regions of stable oscillatory dynamics indicating that two different oscillatory subnetworks may be operational, one in the less than stoichiometric region and the other in the stoichiometric and excess region.

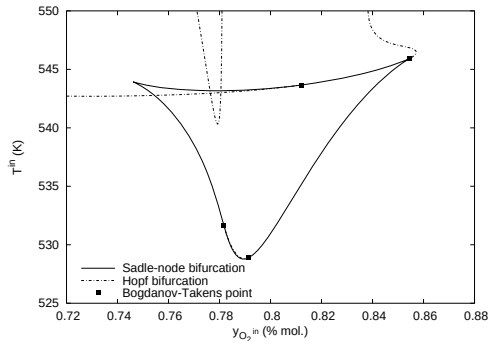

Fig. 4. Bifurcation diagram for CO – C_2H_2 system ($y^{\text{in}}_{C_2H_2}$=680 ppm), T^{in} - inlet temperature, $y^{\text{in}}_{O_2}$ - inlet oxygen concentration.

The identification of the potential oscillatory subnetworks with the oscillatory dynamics found in the regions of stable oscillations in the bifurcation diagram was done by the same methods as above. The two dominant oscillatory subnetworks identified are formally the same as for the CO oxidation, see Fig. 2 and Fig. 3. However, they are related differently to the lack or excess of oxygen, and the role of species in these subnetworks is quite different. The subnetwork in Fig. 3 corresponds to the sub-stoichiometric oscillator. The autocatalytic cycle passes through $*$, O^* and OCO^*; the exit and the negative feedback species are CO and O_2, respectively. Thus the topology of the subnetwork corresponds to the classical Eley-Rideal mechanism: oxygen is adsorbed on an active site and subsequently reacts with gaseous CO to provide an adsorbed carbon dioxide species OCO^*.

On the other hand, the subnetwork in Fig. 2 corresponds to oscillations in the super-stoichiometric region. There are two autocatalytic species $*$ and CO^* that form the autocatalytic loop, and the exit and the negative feedback species being O_2 and CO, respectively. Therefore this subnetwork involves the Langmuir-Hinshelwood mechanism.

Finally, we describe the effects of simultaneous NO_x reduction and CO

oxidation. The mechanism involves reactions 1-5, 12, 13, 15 and 16-23. The bifurcation diagram in the same free parameters as before is shown in Fig. 5. Again, the region of multiple steady states has a complex shape, the stoichiometric amount of oxygen (0.56 mol%, some oxygen is now provided by NO) is slightly less than the value corresponding to the downward cusp. There are three curves of the Hopf bifurcation indicating the existence of only two regions of stable oscillations, since the curve entirely enclosed in the region of multiple steady states does not provide stable oscillations. The remaining two Hopf bifurcation curves enclose regions neighboring the multiple steady state region, where the oscillations are stable and readily observed.

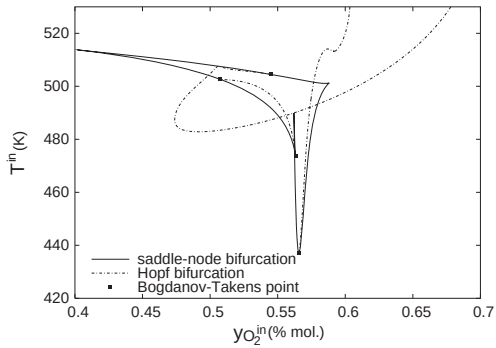

Fig. 5. Bifurcation diagram for CO – NO_x system ($y^{\text{in}}_{\text{NO}}$=1000 ppm), T^{in} - inlet temperature, $y^{\text{in}}_{\text{O}_2}$ - inlet oxygen concentration.

Two different oscillatory subnetworks are expected to operate, one in the less than stoichiometric region and near the stoichiometric point and the other with excess of oxygen. The stoichiometric network analysis indicates that there are altogether 15 different potential oscillatory subnetworks formed by edges or 2-faces of the corresponding reaction network that might explain the oscillations. Moreover, within those subnetworks the species may play different role. We focused on the NO reduction pathway since this species is present in much higher concentrations than NO_2. The identification of the potential oscillators with the ones found in the regions of stable oscillations in the bifurcation diagram was done by the phase shifts as above.

Three contributing oscillatory subnetworks identified as extreme ones are shown in Fig. 6, Fig. 7 and Fig. 8. The subnetwork in Fig. 6 corresponds

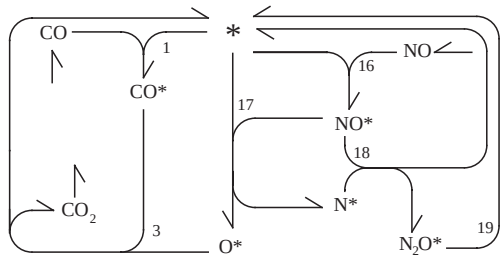

Fig. 6. Network diagram of the dominant subnetwork in the oscillatory region for sub- and near-to-stoichiometric inlet oxygen compositions in the bifurcation diagram for CO – NO_x system in Fig. 5

to the sub-stoichiometric and slightly super-stoichiometric oscillations (up to 0.59 mol% of oxygen). An unstable minor indicates that there is an autocatalytic pathway connecting autocatalytic species $*$ and N^* through reactions 17 and 21. Within this network, there is a negative feedback species NO^* that advances the autocatalytic species. The network shows that catalytic reactions for sub- and slightly super-stoichiometric amount of oxygen effectively reduce NO_x without formation of N_2O. Furthermore, CO^* and NO are also indicated as essential species. Thus there is a synergic effect of the loop of CO^* on the autocatalysis via reactions 1 and 3; at low concentrations of CO^* the autocatalysis is promoted and this species plays a role of a recovery species.[17] NO is an exit species.

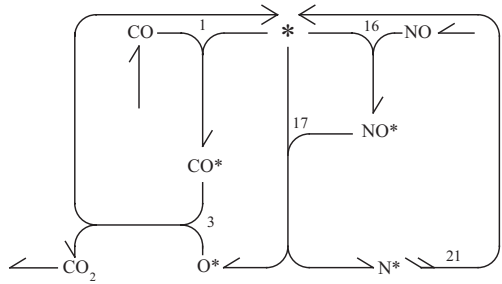

Fig. 7. Network diagram of the dominant subnetwork in the oscillatory region for super-stoichiometric inlet oxygen compositions in the bifurcation diagram for CO – NO_x system in Fig. 5.

By exceeding the concetration of oxygen 0.59 %mol., the mode of os-

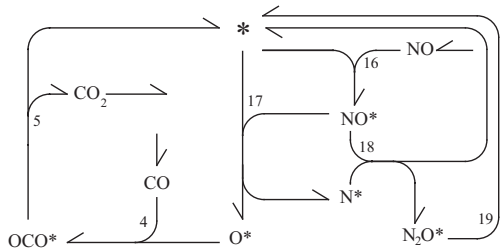

Fig. 8. Network diagram of the minor subnetwork in the oscillatory region for super-stoichiometric inlet oxygen compositions in the bifurcation diagram for CO – NO_x system in Fig. 5.

cillatory dynamics is changed. There are two oscillatory subnetworks, a dominant one in Fig. 7 and a minor one in Fig. 8. The topology of both subnetworks differ in the mechanism of CO oxidation. In the subnetwork shown in Fig. 7, there are two autocatalytic pathways formed by autocatalytic species $*$, N^* and CO^*; the first loop consists of reactions 1 and 3, and the other involves reactions 17 and 18. NO^* and CO are the necessary negative feedback species to provide autocatalysis. NO has the same role as above, the exit species. Here CO reacts according to the Langmuir-Hinshelwood mechanism. The minor subnetwork in Fig. 8 also involves two autocatalytic loops via reactions 17 and 18, and 17, 18 and 19, respectively. The autocatalytic species are $*$, N^* and N_2O^*, the exit species is NO and the negative feedback species is NO^*. On the other hand, CO is burned by the Eley-Rideal mechanism via reaction 4. Unfortunately, the essential species N_2O, a dangerous green-house gas, may be formed by the reaction 18 in substantial amounts and subsequently released into a passing fluid. Hence it is necessary to operate the three-way catalytic converter near the stoichiometric composition of oxygen strictly.

4. Conclusions

A systematic approach to the analysis of complex chemical reaction networks and reactor dynamics was applied to a realistic detailed mechanism of simultaneous oxidation of carbon monoxide and hydrocarbons (here represented by acetylene) and reduction of nitrogen oxides occurring in a three-way catalytic reactor. The stoichiometric network analysis was used to find positive and negative feedbacks that may cause oscillations of reaction components in the lumped isothermal model of the reactor. The phase shift analysis helps to identify which of the oscillatory subnetwork actually

cause the oscillations observed in the model. The results of the stoichiometric network analysis were used to explain the structure of the bifurcation diagrams obtained by applying numerical continuation techniques.[22,23] In earlier work,[11] periodic variations of the inlet oxygen concentration in the lumped reactor model revealed the periodic-doubling route to chaos, in agreement with earlier experimental observations of chaotic oscillations of CO oxidation on Pt catalysts.[24] Chaotic dynamics were also observed in the lumped model using the full TWC mechanism.[11] Based on the results of the stoichiometric network analysis and the following discussion of bifurcation diagrams presented in this work, we can interpret nonlinear dynamic features both for forced and unforced system. In general, the composition of the reaction mixture at the inlet to the converter should be maintained close to the stoichiometric composition, which means that mostly the Langmuir-Hinshelwood mechanism takes part in the oscillatory dynamics.

Acknowledgements

This work has been partially supported by the Grants GAČR 104/06/P301, GAČR 203/06/1269, GAČR 104/05/2616 of the Czech Science Foundation and by the project MSM 6046137306 from the Ministry of Education of Czech Republic.

References

1. H. Beusch, P. Fieguth and E. Wicke, *Advances in chemistry series* **109**, 615 (1972).
2. E. Eckert, V. Hlaváček, M. Marek, *Chem. Eng. Commun.* **1**, 89 (1973), ibid **1**, 95 (1973).
3. T. Engel and G. Ertl, *Adv. Catal.* **28**, 1 (1979).
4. R. Imbihl and G. Ertl, *Chem. Rev.* **95**, 697 (1995).
5. T. Gritsch, D. Coulman, R. Y. Behm and G. Ertl, *Phys. Rev. Lett.* **63**, 1086 (1989).
6. M. Eiswirth, chapter 6 in *Chaos in Chemistry and Biochemistry*, edited by R. J. Field and L. Györgyi, World Scientific, Singapore, (1993).
7. M. Eiswirth, J. Bürger, P. Strasser and G. Ertl, *J. Phys. Chem.* **100**, 19118 (1996).
8. R. M. Heck and R. J. Farrauto, *Applied Catalysis A: General* **221**, 443 (2001).
9. J. M. Harmsen, J. H. Hoebink and J. C. Schouten, *Ind. Eng. Chem. Res.* **39**, 599 (2000).
10. J. M. Harmsen, J. H. Hoebink and J. C. Schouten, Catal. Letters **71**, 81 (2001).
11. P. Kočí, V. Nevoral, M. Záhrubský, M. Kubíček and M. Marek, *Chem. Eng. Sci.* **59**, 5597 (2004).

12. R. H. Nibbelke, A. J. Nievergeld, J. H. Hoebink and G. B. Marin, *Applied Catalysis B: Env.* **19**, 245 (1998).
13. J. M. Harmsen, J. H. Hoebink and J. C. Schouten, *Chem. Eng. Sci.* **56**, 2019 (2001).
14. J. Kapička and M. Marek, *J. Catalysis* **229**, 508 (1989).
15. P. Kočí, M. Kubíček and M. Marek, *Chem. Eng. Res. Des.* **82**, 284 (2004).
16. B. L. Clarke, *Adv. Chem. Phys.* **43**, 1 (1980).
17. M. Eiswirth, A. Freund and J. Ross, *Adv. Chem. Phys.* **80**, 127 (1991); *J. Phys. Chem.* **95**, 1294 (1991).
18. T. Chevalier, I. Schreiber and J. Ross, *J. Phys. Chem.* **97**, 6776 (1993).
19. J. D. Stemwedel, I. Schreiber and J. Ross, *Adv. Chem. Phys.* **89**, 327 (1995).
20. J. Ross, I. Schreiber and M. O. Vlad, *Determination of Complex Reaction Mechanisms*, (Oxford University Press, New York, 2006).
21. I. Schreiber and J. Ross, *J. Phys. Chem. A* **107**, 9846 (2003).
22. M. Kubíček and M. Marek, *Computational methods in bifurcation theory and dissipative structures*, (Springer Verlag, New York, 1983).
23. M. Marek and I. Schreiber, *Chaotic Behaviour of Deterministic Dissipative Systems* (Cambridge Univ. Press, Cambridge, 1991, 1995).
24. J. Kapička and M. Marek, *Surf. Sci.* **222**, 885 (1989).

COLLECTIVE MOVEMENT AND MORPHOGENESIS OF EPITHELIAL CELLS

H. HAGA* and K. KAWABATA

Division of Biological Sciences, Graduate School of Science, Hokkaido University, Sapporo, Japan
**E-mail: haga@sci.hokudai.ac.jp*

We found that epithelial cells (Madin-Darby canine kidney cells) migrated collectively on a collagen gel substrate. Time-lapse images of MDCK cells cultured on type-I collagen gels and glass substrates were captured by phase contrast microscopy equipped with an incubation system. On the gel substrate, the directions of cell movement gradually converged on one direction as the number of cells increased, whereas the cells moved randomly on the glass substrate. We also observed "leader" cells, which extended large lamellae and were accompanied by many "follower" cells, migrating in the direction of oriented collagen fibers. Moreover, we found that epithelial cells exhibit wave-like collective movement during formation of an epithelial sheet on a collagen gel substrate. We name this "cellular wave". The cellular wave is categorized as a longitudinal wave, since the cells elongated their anterior edges and contracted their posterior parts alternately in a portion of the epithelial sheet. The morphological changes propagated to the neighboring cells through the cell-cell adhesions. The cellular wave always appeared when the cell density was getting saturated. Therefore, appearance of the cellular wave depends on both the cellular density and the substrate stiffness. We found new phenomena indicating how epithelial sheets organize a cyst structure when embedded in a collagen gel. Turnup of the periphery of the cellular sheet appeared at first, and then collective cell migration occurred until the cyst was formed.

1. Collective Cell Movement

Multicellular movement is essential for many physiological processes, including tissue regeneration, early embryogenesis, and metastasis of tumor cells. Epithelial cells play a central role in the morphogenesis as forming many kinds of organic structures, including sheets, cysts, and tubules.[1,2] The crucial factors for the morphogenesis are regulation of cell movement and cell-cell adhesion. From the phenomenological observation, these factors seem to be harmonized spatiotemporally by a self-organized matter. However, the molecular mechanism of the collective cell movement has not

been elucidated.

Our recent studies have shown that Madin-Darby canine kidney (MDCK) cells moved collectively as a massive stream along one direction on a soft gel substrate, whereas such collective movement was not observed on a stiff substrate.[3] Using the cell trajectories obtained from the time-lapse data, the mean squared displacement (MSD), $< \rho^2(\Delta t) >$, was calculated as a function of time interval Δt as described previously.[4] In general, the MSD has the asymptotic power-law form:

$$< \rho^2(\Delta t) > \propto \Delta t^{\alpha}, \tag{1}$$

where $\alpha = 1$ and 2 represent a random walk and ballistic movement, respectively. The exponent α can also be $1 < \alpha < 2$, corresponding to the anomalous diffusion induced by temporal and/or spatial correlations. All data of the cell trajectories indicate asymptotic power-law behavior, where the exponents are always larger in the gel than the glass substrate; the averaged values of the exponent are 1.7 and 1.4 in the gel and the glass, respectively. These results indicate that cellular movement of epithelia is described by the anomalous diffusion system.

We found that there was a role assignment among epithelial cells on the collagen gel. The "leader" cells, which extended large lamellae and being accompanied by many "follower" cells, migrated in the direction of oriented collagen fibers. In order to characterize the leader and the follower cells, we transfected MDCK cells with GFP-tagged myosin regulatory light chain (GFP-MRLC), and cultured them on type-I collagen gels.[5] Temporal sequence of GFP-MRLC fluorescent images were captured by confocal laser scanning microscopy equipped with an incubational system. The leader cells had stress fibers and migrated like mesenchymal cells, whereas the typical follower cells did not have stress fibers and showed amoeboid-like migration like leukocytes. Namely, the leader cell moved actively, whereas follower cells moved more passively.

We also focused on the spatial distribution of phosphorylation of MRLC, since phosphorylation of MRLC is involved with regulation of stress fiber contraction and cell movement. Immunofluorescent observations stained with phosphorylated MRLC revealed that MRLC in a leader cell and the neighboring cells were highly phosphorylated, whereas MRLC in the follower cells were entirely dephosphorylated.[5] These results suggest that mesenchymal-amoeboid transition occur in an epithelial colony on the collagen gels.[6]

This role assignment may bring a harmony into the cell society, and as a result, it may lead to the collective movement, although we do not know how each cell gets assigned a role to migrate collectively and why the collagen gel causes the transition between amoeboid and mesenchymal types of movement.

2. Cellular Wave

We found another type of collective movement on a collagen gel.[7] After ending of cellular proliferation and collective movement, some strange waves are observed. We name this mode of movement "cellular wave". Each cell involved in the cellular wave elongates and shortens its body and moves forward a little bit. This changing of cell shape and slight movement evoke new movement in adjacent cells. And finally, these events propagate in an entire epithelial sheet; we identify this propagation as a cellular wave. This schematics may be easily understood if we imagine the traffic jam, where we move forward a little bit and intermittently.

Immediately after the microscopic observation, immunofluorescent staining of actin filaments was performed. We observed that the shapes of waving cells were deformed extremely, compared with the typical columnar morphology of epithelial cells. The waving cells extended the pseudopodia underneath the neighboring cells. These results indicate that both cell-cell interaction and morphological changing are dominant factors for the appearance of the cellular wave, although how epithelial cells detect the morphological changing of the neighboring cells is not known.

3. Lumen Formation of Epithelial Cells

It is widely known that epithelial cells form lumen structures such as cysts and tubules in 3D environment.[8] Recently, we found that collective cell movement occurred during lumen formation when an epithelial sheet on a collagen gel was overlaid with another collagen gel. To elucidate how MDCK cells form lumen in a 3D collagen gel, time-lapse images were captured by phase contrast microscopy. Most strikingly, turnup of the periphery of the epithelial sheet appeared within several hours after the gel overlay, and then collective cell movement continued until the complete formation of the lumen. For the further investigation, cellular fixation was performed during the lumen formation. Immunofluorescent images demonstrated that the entire epithelial sheet curved slightly immediately after the gel overlay, and then extrusion of marginal cells occurred along the overlaid gel surface,

resulting in the turnup of the epithelial sheet. These results suggest that epithelial sheets embedded in a collagen gel form a cyst structure by the collective cell movement.

Acknowledgments

We are grateful to Ms. K. Hayashi and Ms. Y. Ohmori for their examination and Ms. C. Irahara for her help with the statistical analyses. This work was supported in part by Grant-in-Aid for the 21st Century COE program on "Topological Science and Technology" and the Creative Scientific Research from the Ministry of Education, Culture, Sports, Science and Technology of Japan.

References

1. L. E. O'Brien, M. M. Zegers and K. E. Mostov, *Nat. Rev. Mol. Cell Biol.* **3**, 531 (2002).
2. M. M. Zegers, L. E. O'Brien, W. Yu, A. Datta and K. E. Mostov, *Trends Cell Biol.* **13**, 169 (2003).
3. H. Haga, C. Irahara, R. Kobayashi, T. Nakagaki and K. Kawabata, *Biophys. J.* **88**, 2250 (2005).
4. J. P. Rieu, A. Upadhyaya, J. A. Glazier, N. B. Ouchi and Y. Sawada, *Biophys. J.* **79**, 1903 (2000).
5. H. Haga, K. Hayashi and K. Kawabata, *Mol. Biol. Cell* **15** *supple.*, 179A (2004).
6. P. Friedl, S. Borgmann and Eva-B. Brocker, *J. Leukoc. Biol.* **70**, 491 (2001).
7. Y. Ohmori, H. Haga and K. Kawabata, *Cell Struct. Funct.* **30** *supple.*, 60 (2004).
8. B. Lubarsky and M. A. Krasnow, *Cell* **112**, 19 (2003).

INDECISIVE BEHAVIOR OF AMOEBA CROSSING AN ENVIRONMENTAL BARRIER *

S. TAKAGI*, Y. NISHIURA, T. NAKAGAKI, T. UEDA

Research Institute for Electronic Science, Hokkaido University, Sapporo 060-0812, Japan
** E-mail: takagi@es.hokudai.ac.jp*

K.-I. UEDA

Research Institute for Mathematical Sciences, Kyoto University, Sakyo-ku, Kyoto, 606-8502, Japan
E-mail: ueda@kurims.kyoto-u.ac.jp

We report here a new kind of behavior that seems to be 'indecisive' in an amoeboid organism, the *Physarum* plasmodium of true slime mold. The plasmodium migrating in a narrow lane stops moving for a period of time (several hours but the duration differs for each plasmodium) when it encounters the presence of a chemical repellent, quinine. After stopping period, the organism suddenly begins to move again in one of three different ways as the concentration of repellent increases: going through the repulsive place (penetration), splitting into two fronts of going throught it and turning (splitting) and turning back (rebound). In relation to the physiological mechanism for tip migration in the plasmodium, we found that the frontal tip is capable of moving further although the tip is divided from a main body of organism. This means that a motive force of front locomotion is produced by a local process at the tip. Based on this finding, a mathematical model for front locomotion is considered in order to understand the dynamics for both the long period of stopping and three kinds of behavior. A model based on reaction-diffusion equations succeeds to reproduce the experimental observation. The origin of long-time stopping and three different outputs may be reduced to the hidden instabilities of internal dynamics of the pulse, which may be a skeleton structure extracted from much more complex dynamics imbedded in the *Physarum* plasmodium.

*This work is supported by Grant-in-aid for Scientific Research No. 18500229 of the Japan Society for the Promotion of Science.

1. Introduction

So far behaviors of unicellular organism was expected to be simple and trivial. This is because there is no brain and nervous system in unicellular organism. In a higher animal, behaviors are determined as an output from information processing in a brain. However, an amoeba shows rich behaviors. In fact, a biologist, H. S. Jennings, already reported a hundred years ago that it is possible for us to feel the similar sort of feeling to a *Paramecium* as that to a dog if it would be as large as a dog.[1]

The plasmodium of *Physarum polycephalum*, true slime mold, is a large aggregate of protoplasm and crawls by amoeboid movement. This organism shows smart behaviors and its dynamical aspect is partially studied: tactic movement to stimulation[2,3] and maze solving.[4–7] Information processing is performed by the protoplasm in the plasmodium because of no brain. So cell dynamics is closely related to how smart behaviors emerge. In this sense, the plasmodium is a useful model organism to study information processing at cell level. Here we report a new kind of amoeboid behavior that seems to be *indecisive behavior* in the plasmodium. Here we define *indecisive behavior* as: when an organism encounters a different situation or a problem, it is unable to make a clear decision on a course of action for a period of time, and only being to act once a decision is made. A mathematical model for the behavior is proposed and discussion is made on how indecisive-like behavior appears in terms of nonlinear dynamics.

In the next section, we show the experiments and the results on the behaviors of plasmodium and on the locomotion activity of the frontal tip. Then we describe a mathematical model of pulse dynamics described in one-dimensional reaction diffusion system. The numerical results give that pulse dynamics shows almost the same behaviors as those of plasmodium.

2. Experiment

2.1. *Materials and methods*

The plasmodium of *Physarum polycephalum* (strain HU195 × HU200) was fed with oatmeal on a 1 % agar gel at 25 °C in the dark. Fixed amount, 100 mg, of the extending front of the cultured plasmodium was cut off and placed at an edge of an agar gel (1.5 %) lane of 1 cm in width and 30 cm in length. The prepared plasmodia exhibited almost one-dimensional locomotion and protoplasm distribution (see Fig. 1(a)). For the repellent region, an agar gel block containing quinine was embedded at the middle of a lane. The length of the repellent region was fixed at 10 mm and the concentra-

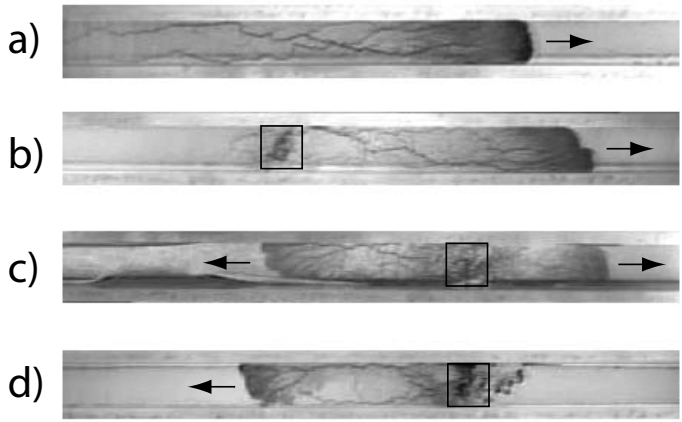

Fig. 1. Repellent in the middle of a lane causes a variety of cell behavior as its concentration varies. The arrows indicate the locomotion directions, and rectangles represent the regions containing a repellent. In each case, the plasmodia migrated from the left side in the figure. (a) A plasmodium migrating in a one-dimensional lane without repellent (control). (b) Penetration ([quinine]=4 mM), (c) splitting ([quinine] = 6 mM), (d) rebound ([quinine] = 8 mM). The width of the lane is 1 cm and the length of the repellent region is 1 cm.

tion of the repellent (quinine) was varied as 4, 6 and 8 mM. The experiment was done at 25 °C in dark condition. The movement of the plasmodia was monitored by the following method. The plasmodia were illuminated from below with an infrared ray ($\lambda \sim 950$ nm), the wavelength of which is harmless for the plasmodium,[8] and the transmitted light image was observed by time laps video camera, and analyzed on a personal computer. The place of the frontal tip of a migrating plasmodium was detected by subtracting the background image.

2.2. *Experimental result*

We found that the plasmodia exhibits 3 types of cell behavior depending on the concentration of quinine. The snapshots of the plasmodia exhibiting each response and the time traces of the places of the frontal tips are shown in Figs. 1 and 2, respectively. In each case, the plasmodium stopped at the repellent region for several hours after coming up there, *i.e.*, they were indecisive for a period of time, and finally exhibited various behaviors. When the quinine concentration was low (4 mM), the plasmodium went through the repellent region after about 6 hours indecision (Fig. 2(a)). When the

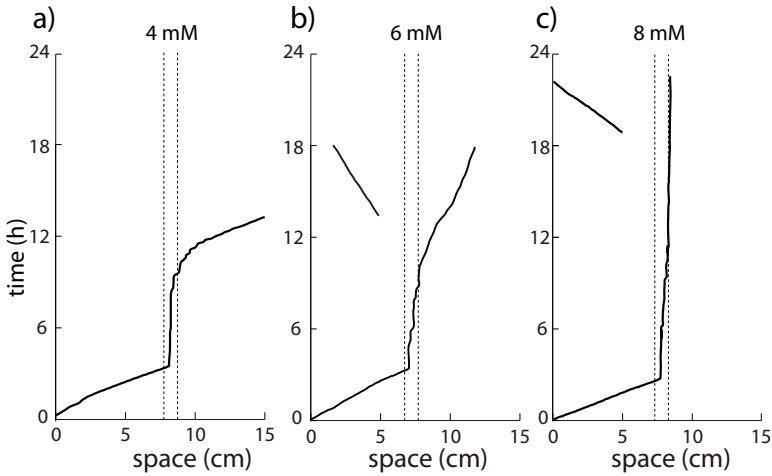

Fig. 2. Tip trajectories for each reaction (a) penetration, (b) splitting and (c) rebound. Experimental conditions are the same as Fig. 1.

quinine concentration was high (8 mM), the plasmodium turned back from the repellent region after about 15 hours indecision (Fig. 2(c)). At the intermediate quinine concentration (6 mM), the plasmodium exhibited both responses, that is, one part of the plasmodium went through the repellent region and the other part returned back; thus the locomotion front split into two fronts (Fig. 2(b)). When the plasmodium returns back, since the frontal tip is created around the end of the tail of the plasmodium, the returning tip trajectory starts at a point apart from the repellent region. In the case of splitting, decrease in the locomotion velocity after splitting is due to halving of the protoplasm, since locomotion velocity decreases as the total mass of the protoplasm decreases.[9] Here we note the following facts: around the condition in which the plasmodium shows splitting behavior, the behavior is not uniquely determined, that is, other behavior, penetration or rebound, is also observed under the same conditions; duration of indecision differs for each plasmodium even under the same condition.

2.3. *Experiment on the frontal tip activity of locomotion*

Here we describe only the essentials of the method and the result of the experiment to examine the locomotion activity of the frontal tip. A plasmodium was allowed to migrate in a narrow lane, similarly to the experiment above, and the frontal tip was divided from main body by cutting with a

surgical knife, that is, amputation of the frontal tip. The place of the amputation from the tip, d, was varied from 0.8 to 5 mm in the plasmodium with the length of ~ 90 mm, and the mean extension speed of the tip was measured before the amputation, v_0, and after the amputation, v_a.

Figure 3(a) shows the space-time plot of the thickness profile of a plasmodium. After the amputation, the tip extends at the almost the same velocity as before the amputation, while the rhythmic contraction disappears. The extension velocity is roughly constant from 5 to 1 mm amputation (Fig. 3(b)). It should be noted that the decrease of the extension velocity at small d can be caused by the damage due to the amputation. This result suggests that the rhythmic contraction is not a motive force of locomotion and extension of the frontal tip, and the frontal locomotion will be driven by a process localized at the tip.

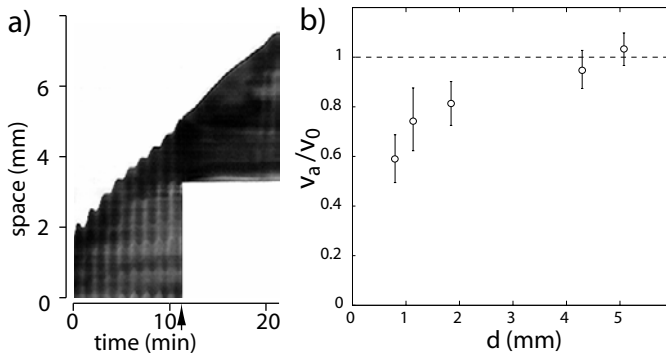

Fig. 3. Amputation of the tip to examine the locomotion activity of the frontal tip. (a) Space-time plot of thickness profile of a plasmodium directionally migrating in a narrow lane. The thickness is represented by grayscale; darker color corresponds to thicker protoplasm. The plasmodium migrates from bottom to top. At the timing indicated by the arrow, the frontal tip was divided from the main body that was removed after the amputation. Origins of the axes are determined arbitrarily. (b) Ratio of the locomotion velocities before, v_0, and after, v_a, the amputation, v_a/v_0.

3. Mathematical Model

We obtained clear evidence that the locomotion process is localized at the frontal tip. In other word, a tip having the locomotion activity is able to be the locomotion front. Besides, it was reported that polarized intracellular chemical pattern corresponds to the polarity of a plasmodium, *e.g.*, ATP

concentration is higher at the locomotion front and becomes lower toward the tail.[10,11] According to these facts, we consider the dynamics of polarized chemical pulse based on one-dimensional reaction diffusion system called Gray-Scott model,[12] in which we assume that the chemical pattern with pulse-like form corresponds to the activity of the locomotion front.

$$\begin{aligned} \frac{\partial u}{\partial t} &= D_u \frac{\partial^2 u}{\partial x^2} - uv^2 + f(1-u), \\ \frac{\partial v}{\partial t} &= D_v \frac{\partial^2 v}{\partial x^2} + uv^2 - (f + k(x))v, \end{aligned} \qquad x \in [0, L] \tag{1}$$

where $u = u(t, x)$ and $v = v(t, x)$ depend on time t and position x, $f > 0$ and $k > 0$ are kinetic parameters, and diffusion coefficients $D_u > 0$, $D_v > 0$ are constants. In this model, u and v represent substrate and product concentrations, respectively. Therefore, in relation to the *Physarum* plasmodium, we can consider that u and v correspond to nutrients and intracellular ATP concentrations, respectively. $k(x)$ is a perturbed parameter with heterogeneous distribution of bump type:

$$k(x) = \begin{cases} k_0, & x \in [0, x_0) \cup (x_1, L], \\ k_0 + \epsilon, & x \in [x_0, x_1], \end{cases} \tag{2}$$

where $k_0, \epsilon \in \mathbb{R}$. Note that ϵ denotes the height of the bump. For the case of single jump-discontinuity, a detailed analysis has been done by Dynamics of traveling pulses in heterogeneous media of jump type.[13] We integrate Eqs. (1) using the Crank-Nicholson method with $D_u/D_v = 2$, $L = 4.0$, $x_1 - x_0 = 0.2$ and time interval $\Delta t = 0.05$ with Neumann boundary conditions. In this study we fix the parameter $f = 0.024$. Figure 4 shows that the pulse exhibits three different responses when the pulse encounters a bump in the middle after stopping on it for a period of time, namely, the pulse shows the indecisive behavior. For low bump, the pulse can penetrate the bump after stopping period. For high bump, the pulse cannot penetrate the bump and turns back after stopping period. For intermediate bump, the pulse splits into two pulses, and one of them penetrates and the other returns back. Therefore, the pulse exhibits qualitatively the same behaviors as the plasmodium. The phase diagram of the pulse dynamics is shown in Fig. 5. The pulse shows penetration when ϵ is small, and it shows rebound when ϵ is large. When k_0 is small, there is a splitting region between the penetration and the rebound regions. Consequently, there are three behaviors for the pulse dynamics in the heterogeneous media of bump type, and the pulse changes its behavior depending on the parameter values of k_0 and ϵ. Here we can give a correspondence between model parameters (k_0 and ϵ) and

experimental conditions: k_0 represents the environmental conditions, *i.e.*, temperature, humidity, agar concentration and so on, and ϵ represents the repellent concentration at the middle of a lane, *e.g.*, quinine concentration; higher k_0 and ϵ values correspond to worse condition. We have obtained good correspondence between ϵ and quinine concentration for the pulse and the plasmodium behavior.

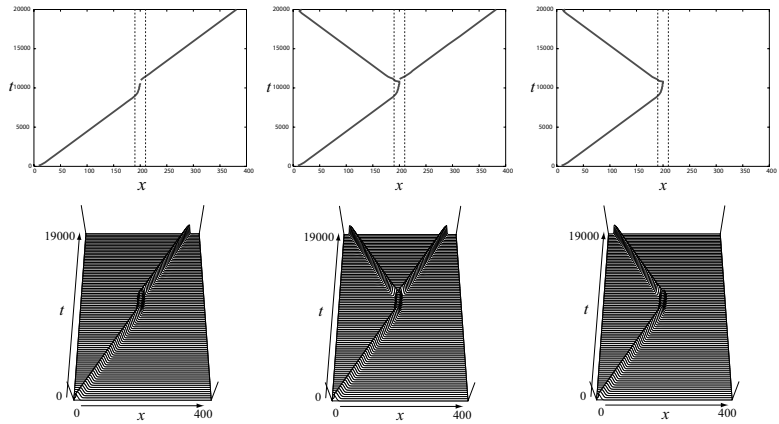

Fig. 4. Pulse dynamics of Gray-Scott model (Eqs. (1)) in heterogeneous media with different bump heights. Upper panel shows time traces of the wave fronts, and lower panel shows space-time plots of pulse dynamics. Left: Penetration ($\epsilon = 0.000216614$). Middle: splitting ($\epsilon = 0.000216618$). Right: rebound ($\epsilon = 0.000216619$). In each case $k_0 = 0.05543$. The bump ($[x_0, x_1], x_0 = 1.9, x_1 = 2.1$) is indicated by dotted lines.

4. Discussion

Even in an amoeba, indecisive-like behaviors are observed. Although the indecisive behavior is thought to be a higher function in the brain, it is possible at cell level. Capacity of information processing in a cell is much higher than expected. So further evaluation is needed.

Here we discuss a possible mechanism of indecisive-like behavior in terms of nonlinear dynamics. A key idea in the mathematical model proposed here is characterized by a recently suggested new concept of *scattor* (see, for instance, Nishiura *et al.*, *Chaos* (2003)[14]): a saddle-like structure which attracts a wide-open trajectories and sorts them out to several basins of different attractors. Loosely speaking, scattor corresponds to indecisive state and each different attractor corresponds to a different pulse behavior. As

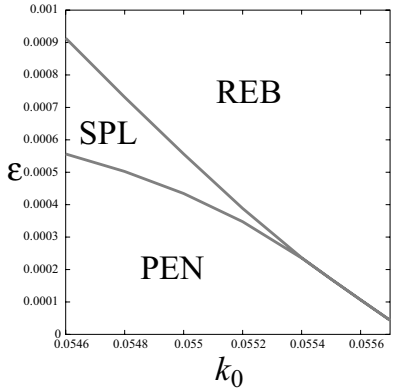

Fig. 5. Phase diagram of pulse dynamics for heterogeneous media. PEN: penetration, SPL: splitting, REB: rebound. Triple junction is $(k_0, \epsilon) \approx (0.0555, 0.0001705)$. The place of the bump is the same as in Fig. 4

parameters vary, closer to the scattor, longer the time for a trajectory to stay as the indecisive state. But the duration of time in real experiments is rather unpredictable under a small fluctuation, nevertheless the scattor dynamics as above could be regarded as a minimal dynamical model which can reproduce the observed behaviors in the real plasmodium. In this sense, this model may grasp a mathematical essence for the development of indecisive-like behaviors in true slime mold at higher abstraction level.

References

1. H. S. Jennings, *Amer. J. Psycol.* **10**, No.4 (1899).
2. K. Matsumoto, T. Ueda and Y. Kobatake *J. Theor. Biol.* **122**, 339 (1986).
3. K. Matsumoto, T. Ueda and Y. Kobatake *J. Theor. Biol.* **131**, 175 (1988).
4. T. Nakagaki, H. Yamada and Á. Tóth, *Nature* **407**, 470 (2000).
5. T. Nakagaki, H. Yamada and Á. Tóth, *Biophys. Chem.* **92**, 47 (2001).
6. A. Tero, R. Kobayashi, T. Nakagaki, *Physica* **A363**, 115 (2006).
7. A. Tero, R. Kobayashi, T. Nakagaki, *J. Theor. Biol.* accepted.
8. T. Ueda, Y. Mori, T. Nakagaki, Y. Kobatake, *Photochem. Photobiol.* **48**, 705 (1988).
9. T. Ueda in *Networks of Interacting Machines*, chap. 9, eds. D. Armbruster, K. Kaneko, A. S. Mikhailov (World Scientific, 2005).
10. Y. Mori, K. Matsumoto, T. Ueda, Y. Kobatake, *Protoplasma* **135**, 31 (1986).
11. T. Ueda, Y. Mori, Y. Kobatake, *Exp. Cell Res.* **169**, 191 (1987).
12. P. Gray, S. K. Scott, *J. Phys. Chem* **89**, 22 (1985).
13. Y. Nishiura, Y. Oyama, K. -I. Ueda, to appear in *Hokkaido Math. J.*
14. Y. Nishiura, T. Teramoto, K. -I. Ueda, *Chaos* **13**, 962 (2003)

EFFECTS OF AMOUNT OF FOOD ON PATH SELECTION IN THE TRANSPORT NETWORK OF AN AMOEBOID ORGANISM*

T. NAKAGAKI* and T. SAIGUSA

Creative Research Initiative Sousei, Hokkaido University
Sapporo 001-0021, Japan
**E-mail: nakagaki@es.hokudai.ac.jp*

A. TERO

School of Engineering, Hokkaido University,
Sapporo 060-8628, Japan
E-mail: tero@topology.coe.hokudai.ac.jp

R. KOBAYASHI

Department of Mathematical and Life Sciences,
Hiroshima University,
Higashi Hiroshima 739-8626, Japan
E-mail: ryo@math.sci.hiroshima-u.ac.jp

We studied the effect of the size of food sources (FSs) presented to the true slime mould *Physarum polycephalum* on the tubular networks formed by the organism to absorb nutrient. The amount of plasmodium gathering at an FS was shown to be proportional to both the concentration of nutrient and the surface area of the FS. We presented two FSs to test which connection the organism selected in response to varying amounts of food and derived a simple rule for connection persistence: the longer connection collapses earlier. A mathematical model for tube selection in response to amount of food was derived and predicted our experimental findings regarding the choice of connection. When three FSs were presented to the organism, the longer tubes were also the first to collapse, explained by the relative probability of disconnection. The size of the FS is thus a key parameter determining network formation.

*This work is supported by Grant-in-aid for Scientific Research No. 16654017, No. 15300098, No. 18650054 and No. 18650422 of the Japan Society for the Promotion of Science.

1. Introduction

Amoebae of the true slime mold *Physarum polycephalum* can solve a maze but little is known about the basis of this intelligent behavior at the cellular level. Here we describe the intelligent behavior of the true slime mold in a complex situation, and outline a mathematical model to describe it. The plasmodium of *Physarum* is an amoeba-like organism containing a network of tubular elements through which nutrients and signals are spread throughout the organism. When multiple small food sources (FSs) were presented to a starved plasmodium that was spread over an entire culture dish, it concentrated its substance over the site of each FS. Almost the entire substance of the plasmodium accumulated at the FSs, covering each of them in order to absorb nutrient, with only a few thick tubes connecting the quasi-separated components of the plasmodium.[1–4] By forming such a pattern the organism absorbs the maximum amount of nutrient in the minimum time. This strategy is implies that the plasmodium can solve a complex problem.[5] In order to investigate how this is achieved, we have studied the shapes and properties of the tube networks formed between two FSs of equal size as a function of their size. We propose a mathematical model, based on one proposed previously,[6] that takes into account the effect of variations in the amount of food presented to the plasmodium.

2. Accumulation of mass of organism to FS in relation to the amount of nutrient at the FS

We began by observing how the plasmodium responded to variation of the amount of nutrient at the FS. Various types of FS were given to a large plasmodium (10×60 cm^2) as shown in Fig. 1a and the plasmodial substance gathered on the FS was torn off and its wet weight measured. An agar block containing powdered oat flakes served as FS, and the concentration of the flakes and size of agar block were changed.

The amount of substance of the organism gathering at an FS proved to be proportional to the logarithm of the concentration of nutrient (1 to 100 mg/ml) at a fixed FS size ($1 \times 1 \times 1$ cm^3) and proportional to the surface area of the FS (3 to 30 cm^2) at a fixed concentration of nutrient (3 and 30 mg/ml), as shown in Figs. 1b and c.

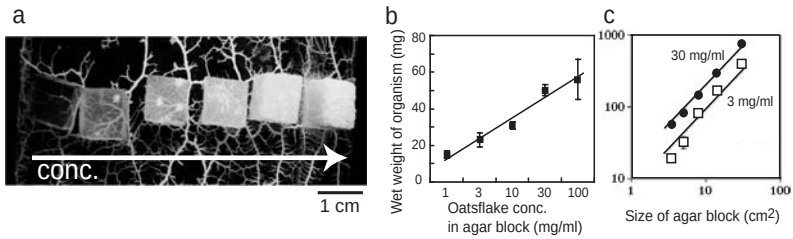

Fig. 1. Dependence of the mass of organism gathering at an FS on the amount of food present a) Photograph of a typical plasmodium gathering at cubic FSs of the same size ($1 \times 1 \times 1$ cm^3) but of different concentrations (0, 1, 3, 10, 30, and 100 mg/ml from left to right). b, c) Relationship between wet weight of the substance of the organism gathered at the FS and amount of food at the FS: b) dependence on concentration of FS and c) dependence on size of FS.

3. Fate of the connections between two FSs in relation to the amount of food present

Next we tested which connection the organism selected from the two possibilities shown in Fig. 2a, in response to variation of the size of the FS at a fixed concentration of oats. The volume of organism initially used was fixed but the amount of food at the FS was varied.

Figure 2b shows typical lengths of time for which connections were maintained. The broken bars indicate the existence of a connection: spaces not shaded gray indicate that the connection was broken. When the FS had a surface area of 0.4 cm^2, both connections persisted (left panel), whereas with an FS of surface area 0.7 cm^2 the longer connection disappeared (middle panel). At a surface area of 1.7 cm^2, the short connection also collapsed some time after the longer one had disappeared (right panel).

Figure 2c shows the time course of the mean number of tubes remaining with different amounts of applied food (FSs with surface areas of 0.2, 0.4, 0.7, 1.7 and 2.5 cm^2). The number of tubes decreased with time and also as the amount of food increased. In most cases the longer connection collapsed earlier than the shorter one, implying that there is a simple rule for connection persistence: the longer connection collapses earlier.

4. Order of tube collapse among five connections of different lengths between two FSs

To test the above selection rule we considered the situation of five connections, shown in Fig. 3a1. Figure 3b shows typical time courses of connection survival. The final number of surviving connections fell as food

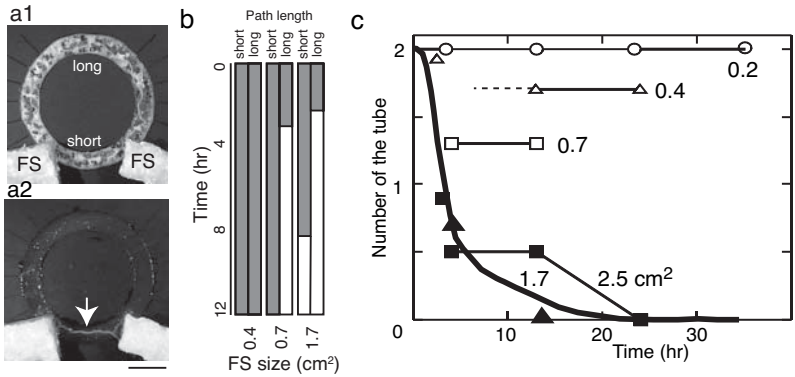

Fig. 2. Choice between two possible tubes as a function of the amount of food presented a) Photographs of typical results 0 a1 and 12 h a2 after FS presentation. The shorter connection remained (marked by the white arrow) while the longer one had collapsed. Scale bar: 1 cm. b) Typical durations of connections in relation to amount of food at FSs. Each gray bar indicates the persistence of a connection. c) Time course of the mean number of remaining tubes for different amounts of applied food. See main text for details.

size increased, with two, one, and zero connection(s) maintained for FSs of surface area 7, 10, and 13 cm^2, respectively. The order of collapse was essentially constant: the longer connection was lost earlier, with some exceptions such as the one indicated by the arrow in the middle panel. Nonetheless statistical analysis clearly showed that the longer tube tended to disappear earlier (Fig. 3c), and we may therefore conclude that our simple selection rule works for different amounts of food. Notice that the amount of food also determines when the selection process stops.

5. Mathematical modeling of tube selection between two FSs

Here we outline a mathematical model for tube selection in response to amount of food, based on previously proposed models.[6,7] Each path of a plasmodial tube is represented by a pipe M_i that has constant length L_i and variable conductance D_i, as shown in Fig. 4a. D_i is related to pipe thickness. Each FS acts as a source or a sink of sol flow. By assuming approximate Poiseuille flow, and the conservation laws for flux and incompressible fluids, the flux is given by: $Q_i = \frac{D_i}{L_i}(p_1 - p_2)$, where $p_{1,2}$ are the pressures at the two FSs, and the dynamics of conductance obey $\frac{dD_i}{dt} = \tau(\frac{|Q|_i^3}{|Q|_i^3+1} - D_i)$.

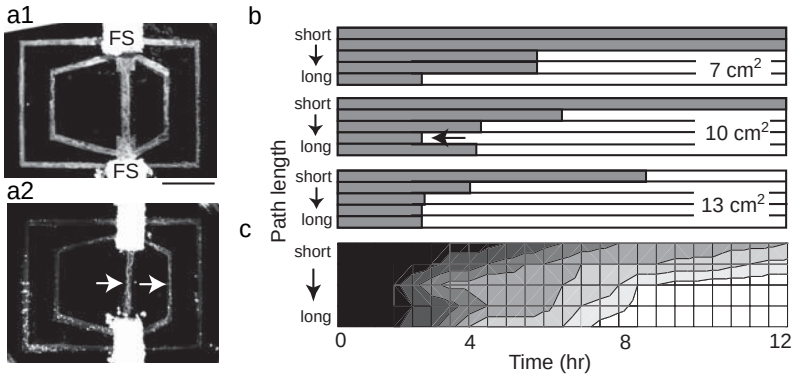

Fig. 3. Path selection from five possibilities a1) Photograph of initial shape of organism. The five connections between two equally sized FSs had lengths of 2, 4, 6, 8, and 10 cm. Scale bar: 1 cm. a2) A typical result for tube persistence. Only the shortest and the second shortest connections remain intact (marked by white arrows); the others have been discontinued. b) Typical time course of survival of connections. c) Statistical presentation of the variation in duration of connections. Data are from 12 experiments with FS surface areas of 10 cm^2. Darker gray shading indicates higher probability of persistence of connection.

These ideas have been described in detail previously.[6]

Here we introduce the variation in amount of food at $FS_{1,2}$. We assume that the total volume of protoplasm (V) is divided into two components: one for nutrient absorption (V_a), the other for tube formation and force generation (V_t). The next assumption is that V_a increases as the amount of food increases, so that the amount of food provided is expressed by V_a in the model. Therefore, only V_t affects the ensuing dynamics. The two FSs generate pressures of $p_1 = \beta(w_1 - s_1)$ and $p_2 = \beta(w_2 - s_2)$ where w is the volume of protoplasmic sol at FS and s the basal volume of protoplasmic sol (the physiological meaning of these equations was discussed in a previous paper[7]). The constant β refers to the stiffness of the protoplasmic gel. These volume variables are then given by: $s_1 = \frac{V_t}{2}(1 + sin2\pi\omega t)$, $s_2 = \frac{V_t}{2}(1 - sin2\pi\omega t)$, $\frac{dw_1}{dt} = -\sum_i Q_i$, $\frac{dw_2}{dt} = \sum_i Q_i$, where ω is the frequency of the rhythmic contractions of the organism.

Figure 4 shows the calculated evolution of connections at different FS sizes (three different V_a values). The longer connections can be clearly seen to collapse earlier while the number of remaining connections declines as the amount of food increases, with two, one, and zero connections at food source sizes (V_a) of surface area 5, 10 and 14 cm^2.

The mathematical model thus reproduces the simple experimentally ob-

served rules for choice of connection between two equal FSs: the longer connection is disrupted sooner than the shorter one, and the amount of food determines when the selection process ends. It also suggests a possible underlying mechanism: namely, that a large source of food reduces the volume of sol flow and this in turn leads to tube collapse.

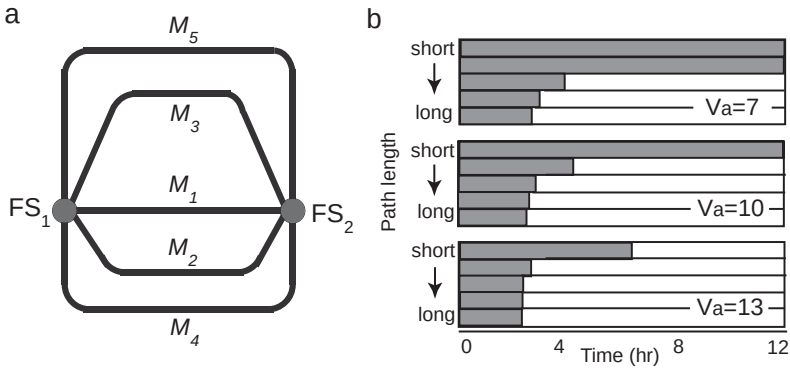

Fig. 4. Simulation of path selection in the plasmodial tube network a) Graphical representation of the initial shape of the organism: five connections, M_i,(i =1 to 5), with lengths of 2, 4, 6, 8, and 10 cm, between two equal FSs, FS_1 and FS_2. b) Time course of connection survival with food sizes (V_a) of 5, 10 and 14 cm^2. Parameter values: $V_a(V_t) = 7(10), 10(7), 13(4)$(for each simulation), $L_1 = 2.0, L_2 = 4.0, L_3 = 6.0, L_4 = 8.0, L_5 = 10.0$, $\beta = 1.5, \tau = 2.0, \omega = 36.0$ ($\Rightarrow$ Oscillation Period=100s). Initial Conditions: $D_1(0) = D_2(0) = D_3(0) = D_4(0) = D_5(0) = 1.0$, $w_1(0) = w_2(0) = V_t/2$. We determined that a tube collapsed when $D < 0.01$.

6. Possible physiological significance of tube selection involving three FSs

Figure 5a shows a typical example of the evolution of a tubular network connecting three FSs. The connecting tubes collapsed progressively when three FSs were placed at the vertices of an equilateral triangle below a circular organism, and the final network resembled the shortest connection of a Steiner minimum spanning tree.

In order to evaluate the transient shapes of the tube network we introduce the criteria:[4] fault tolerance (FT) and total length (TL) of the network. FT_n is the probability that the organism will not be fragmented if n accidental disconnections occur at random points along the tubes. Since the probability of disconnection of a tube is proportional to its length, a longer tube has a higher risk of disconnection.

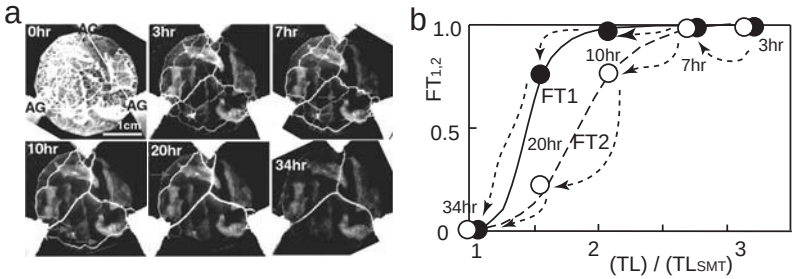

Fig. 5. Tube network with 3 FSs a) Photographs of a network 0, 3, 7, 10, 20, and 34 h after presentation of the FSs (AG), at the three vertices of an equilateral triangle. Scale bar: 1 cm. b) The FT-TL relationship of the tube network. The solid line and the broken line give the optimal FT values for any given value of TL. See main text for details.

TL and FT decrease as tubes collapse progressively, as shown in Fig. 5b. The data points are traced by the solid line (for FT_1) and the broken line (for FT_2). These lines are the master curves of the FT-TL relationship derived previously;[4] they indicate the optimal values of FT under the constraints of a specific TL for all TL values. This means that the organism reduces TL while optimizing FT. This is the rule underlying tube selection in the complex dynamics of a functional network.

The mathematical model proposed in this paper cannot explain the results obtained with three FSs, and we hope to extend the model to cover this situation in the near future. We believe that the mechanism of tube selection in *Physarum* plasmodium is a promising model for studying the adaptive dynamics of natural self-organizing networks.

References

1. T. Nakagaki, H. Yamada and Á. Tóth, *Nature* **407**, 470 (2000).
2. T. Nakagaki, H. Yamada and Á. Tóth, *Biophys. Chem.* **92**, 47 (2001).
3. T. Nakagaki, H. Yamada and M. Hara *Biophys. Chem.* **107** , 1 (2004).
4. T. Nakagaki, R. Kobayashi, T. Ueda and Y. Nishiura *Proc. R. Soc. Lond.* **271**, 2305 (2004).
5. T. Nakagaki, *Res. Microbiol.* **152**, 767 (2001).
6. A. Tero, R. Kobayashi, T. Nakagaki, *Physica* **A363**, 115 (2006).
7. A. Tero, R. Kobayashi, T. Nakagaki, *J. Math. Biol.* in press (2006).

LIGHT SCATTERING STUDY IN DOUBLE NETWORK GELS

M. FUKUNAGA*, M. TAKESADA and A. ONODERA

Division of Physics, Graduate School of Science, Hokkaido University, Kita 10 Nishi 8, 060-0810 Sapporo, Japan,
** E-mail :fukunaga@es.hokudai.ac.jp*

R. KUWADARA, J. P. GONG and Y. OSADA

Division of Biological Science, Graduate School of Science, Hokkaido University, Kita 10 Nishi 8, 060-0810 Sapporo, Japan

T. YAGI

Research Institute for Electric Science, Hokkaido University, Kita 12 Nishi 6, 060-0812 Sapporo, Japan

The dynamical property of thermal fluctuation in the double network gels was studied by frequency resolved light scattering method and time resolved impulsive stimulated light scattering method. Both methods give complimentarily wide range dynamical property over than twelve decades between 10 - 10^{13} Hz. The dynamic property in the double network gels shows a hierarchy over five levels.

1. Introduction

Polymer hydrogels have been considered to be one of the most promised "soft and wet" materials included a lot of functionality for applications in mechanobiology, biotechnology and so on. However, the origin of abundant functionalities is still ambiguous in polymer hydrogels. It is important to elucidate the basic mechanism of functionalities for applications.

Recently, the double network (DN) gels was discovered by Gong *et al.*[1] Ordinary, polymer hydrogels are very tender, because polymer hydrogels contains a significant amount of the water. So it is difficult to use new technology all but a few of device. DN gels achieved mechanical toughness higher than general polymer gels with a high percentage of water content.[1–4] Therefore, DN gels are paid attention as high mechanical toughness appli-

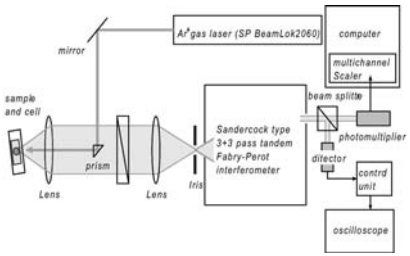

Fig. 1. The optical setup of light scattering.

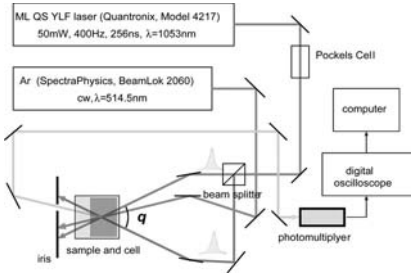

Fig. 2. The setup for impulsive stimulated light scattering.

cation for artificial muscle *etc.*

In the present work, we report polymer network dynamics in DN gels using frequency resolved light scattering (LS) and time resolved impulsive stimulated light scattering (ISLS).[5,6]

2. Experiment

The samples is PAMPS/PAAm DN gels, and the cross-liking ratio of first network (PAMPS) and second network (PAAm) is each 4 mol% and 0 mol%. The samples were placed in the optical cell filled with water in order to reduce the strong elastic scattering of the incident light.

The light scattering (LS) experiment system is shown in Fig. 1. The light source is the single-mode Ar^+ laser (SpecrtaPhysics, BeamLock 2060 with Z- and J- Lok). It was operated at the wavelength of $\lambda = 514.5$ nm with the output power of 300 mW. Sandercock type 3 + 3 pass tandem Fabry-Perot interferometer (JRS) has been used as spectrometer. The scattering angle is 180 degree. The intensity of the light is detected by photomultiplier (Hamamatsu R585).

The impulsive stimulated light scattering (ISLS) experiment system is shown in Fig. 2. The excitation laser is the mode-locked Q-switch YLF laser (Quantronix, Model 4217) operated at output power of 50 mW. The wavelength $\lambda = 1{,}053$ nm and the repetition rate is 400 Hz. The temporal width of the pulse was about 250 ps. The temporal and spatial overlap of the two coherent pulses cause temporally periodical interference in sample. In present case, the wave vector of excited phonon is $\mathbf{q} = 2.3\text{x}10^3$ cm^{-1}. The time dependence is probed by irradiation of a CW laser light from Ar^+ laser (SpectraPhysics, BeamLock 2060). The intensity of the light diffracted from the excited fluctuation is detected by a photomultiplier (Hamamatsu, R1635) and stored into a digital oscilloscope (Tektronix, TDS744A).

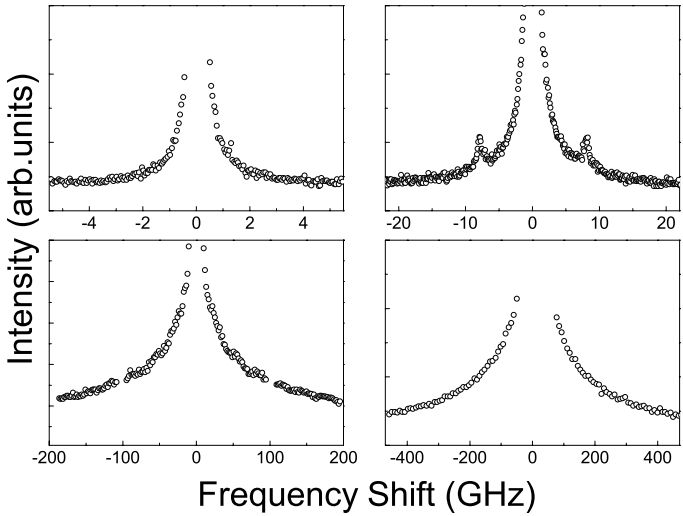

Fig. 3. The central peak spectra of DN gels.

3. Result

In frequency domain, central components of Fig. 1 were observed in spectra of DN gels over wide range by LS at room temperature. The profile of the central peak is not well fitted by single Lorentz function. The central component involves non-propagative Brownian motion of the polymer chains in the water. The central peak spectrum is originated in the feature of the polymer networks. In addition, we observed sharp peak at about 8 GHz. The pair of peaks shows the acoustic phonon mode in DN gels.

In time domain, the ISLS signal of the DN gels was shown as in Fig. 5 at room temperature. The signal is a good agreement for a single exponential function. The detail is described next section.

4. Discussion

The observed spectra are discussed using a simple model expressed by a single exponential function.[7] Hereafter this model is called as the superposition of single exponential model (SSE model). The SSE model gives the frequency dependence of the observed spectra $I(\nu, \mathbf{q})$ written as

$$I(\nu, \mathbf{q}) = \frac{A\gamma {\nu_a}^2}{({\nu_a}^2 - \nu^2)^2} + \sum_i \frac{B_i \Gamma_i}{\nu^2 + {\Gamma_i}^2} + I_{BG}, \tag{1}$$

Where the first term describes acoustic mode spectrum, the second term is the superposition of central peak spectra and the third term is background. ν_a and γ are the frequency of acoustic mode and the half width at half maximum (HWHM) of the acoustic mode spectrum, respectively. Γ_i is the HWHM of the i-th central peak spectrum. The suffix i means the order of central peak corresponding to the order of the dynamic hierarchy given by the SSE model. The coefficients A and B_i are the constants. Similarly, the model gives the time dependence of the observed signal as follows,

$$I(t, \mathbf{q}) = \left| \sum_i A_i \exp\left(-\frac{t}{\tau_i}\right) \right|^2 + I_{BG}, \tag{2}$$

where A_i and I_{BG} are the amplitude of the i-th relaxation processes and the background, respectively. The function expresses the contribution of the whole relaxation process to the thermal equilibrium state of the system.[7] It gives hierarchical levels denoted by the suffix i in the different relaxation time τ_i.

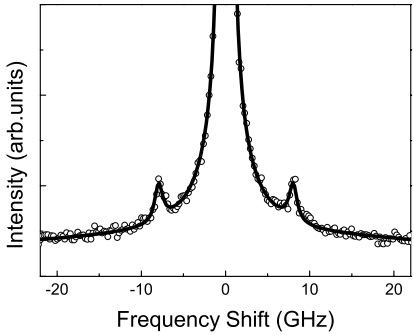

Fig. 4. The result of fit of central peak spectrum of DN gels by SSE model in frequency domain. The open circle shows data point and the solid line expresses fitting result of DN gels.

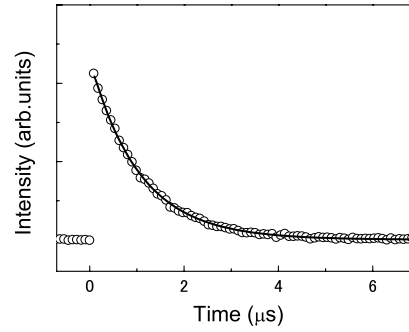

Fig. 5. The result of fit of relaxation processes of DN gels by SSE model in time domain. The open circle shows data point and the solid line expresses fitting result of DN gels.

The typical results of the least squares fit are shown in frequency domain of Fig. 4 and time domain of Fig. 5, respectively. The central peak spectrum is well fitted by four Γ_i and one τ_i. The relaxation times in DN gels are shown in Table 1. In this result, it was elucidated that the dynamical property of DN gels was expressed with the five level relaxation processes.

Table 1. The relaxation times for the hierarchical dynamics of the DN gels (PAMPS/PAAm).

	Double Network (PAMPS/PAAm) gel
1st level	1 x 10^{-12} s (LS)
2nd level	5 x 10^{-11} s (LS)
3rd level	5 x 10^{-10} s (LS)
4th level	6 x 10^{-9} s (LS)
5th level	2 x 10^{-6} s (ISLS)

5. Conclusion

The dynamic property of DN gels was studied in a wide dynamic range from 10 to 10^{13} Hz by two type light scattering methods. The result revealed existence of the hierarchical distribution of relaxation times over five levels. Our previous result in the single network (PAMPS) gels, the hierarchical dynamics was observed at six levels in same region.[7] The relation between the hierarchical dynamics and the functionality of polymer hydrogels is still unknown. But the present result should be important to elucidate the relation between the functionality and the dynamical hierarchy in polymer gels with the complicated-inhomogeneous system.

Acknowledgments

This work was supported by Grant-in-Aid for Creative Scientific Research (2) from MEXT No. 14GS0301 and Grant-in-Aid for the 21st Century COE program "Topological Science and Technology".

References

1. J. P. Gong, Y. Katsuyama, T. Kurokawa and Y. Osada, *Adv. Mater.* **15**, 1155 (2003).
2. Y.-H. Na, Y. Katsuyama, R. Kuwabara, T. Kurokawa, Y. Osada, M. Shibayama and J. P. Gong *Surf. Sci. Nanotech.*. **3**, 8 (2005).
3. Y. Tanaka, J. P. Gong and Y. Osada *Prog. Polym. Sci.* **30**, 1 (2005).
4. Y. Tanaka, R. Kuwabara, Y.-H. Na, T. Kurokawa, J. P. Gong and Y. Osada *J. Chem.Phys.B* **109**, 11559 (2005).
5. Y.-X. Yan and K. A. Nelson *J. Chem. Phys.* **87**, 6240 (1987).
6. Y.-X. Yan and K. A. Nelson *J. Chem. Phys.* **87**, 6257 (1987).
7. T. Yagi *et al.* Submitted.

BLOOD FLOW VELOCITY IN THE CHOROID IN PUNCTATE INNER CHOROIDOPATHY AND VOGT-KOYANAGI-HARADA DISEASE; AND MULTIFRACTAL ANALYSIS OF CHOROIDAL BLOOD FLOW IN AGE-RELATED MACULAR DEGENERATION

K. YOSHIDA* AND W. SAITO

Department of Ophthalmology and Visual Sciences, Hokkaido University Graduate School of Medicine, Sapporo 060-8638,Japan
**E-mail: kyoshida@med.hokudai.ac.jp*

H. FUJII

Department of Computer Science and Electronics, Kyushu Institute of Technology, Fukuoka 820-8502, Japan
E-mail: fujii@cse.kyutech.ac.jp

K. YAKUBO

Department of Applied Physics, Hokkaido University, Sapporo 060-8628, Japan
E-mail: yakubo@eng.hokudai.ac.jp

Recently, the important role of the choroidal circulation has been recognized in various fundus diseases, such as punctate inner choroidopathy (PIC), Vogt-Koyanagi-Harada (VKH) disease, and age-related macular degeneration (AMD). An apparatus based on the laser speckle phenomenon, which we call *laser speckle flowgraphy* (LSFG) has been used to measure the blood flow velocity in the retina and choroid with the diode laser. PIC presents in myopic women who complain of decreased visual acuity. VKH disease is a bilateral, granulomatous chorioretinitis. The composite map of the LSFG represent that blood flow velocity in the choroid was decreased in PIC and VKH. After the treatment, blood flow velocity in this area was increased in both disease and visual acuity recovered. LSFG appears to be a safe and sensitive means to evaluate these disease progression and response to therapy. A multifractal analysis has been performed for blood flow data in the composite map of the LSFG. In consequence, multifractality becomes clearly worse for the AMD patient compared to normal choroidal blood flows. The multifractal analysis of LSFG data represents an additional useful method to detect the early stage of AMD.

1. OCULAR BLOOD FLOW

The retina is the innermost layer of the eyeball. It is the site of transformation of light energy into a neural signal. The retinal artery provides nutrients to the inner retinal layers. The artery enters the retina through the optic nerve and branches in the retina. When photos are taken by camera, we can see optic nerve head and retinal artery and vein. The choroid is located out side of the retina and provides nutrients to the outer retina. The choroid consists primarily of blood vessels. The blood flow in the choroid is much more than retina. Retinal vascular diseases have been studied by fluorescein angiography (FA) and recently by indocyanine green angiography (ICG). FA demonstrates the blood flow in the retina. For example, we can see fluorescein leakages in the diabetic patients. ICG demonstrates the vessels in the choroid as well as in the retina. In the FA and ICG, the dynamic blood flow is observed only during the early phase of the angiography. In addition, fatal anaphylactic shock may occur following FA[1] and ICG.[2] Recently, distribution in ocular blood flow has been able to be investigated using two methods: scanning laser Doppler flowmetry and laser speckle flowgraphy (LSFG).[3,4]

2. LASER SPECKLE FLOWGRAPHY

Laser speckle flowgraphy (LSFG), can measure the blood flow velocity in the retina and choroids.[4–6] LSFG targets moving red blood cells in the eye (Fig. 1). A diode laser illuminates the ocular fundus. The reflected lights from the ocular tissue produce the speckle pattern at the plane, where the area sensor is focused. Reflected lights from moving erythrocytes induce blurring in the speckle pattern. The relative velocity of the erythrocytes is calculated from variations in the blurring, which we call the normalized blur value.[6,7] The area sensor with 100 × 100 pixels detects the NB value in a 1.5-mm-square area of the fundus. The NB value is calculated 16 times in 1 second and displayed as an NB map in either a false color-scale image or a gray-scale image. Recently, we enlarged the area of observation to 1.5 mm square and increased the contrast of the LSFG images. When applied to the ocular fundus, LSFG shows the retinal and choroidal components.[8] Figure 2 is a normalized blur map shown in false color scale. The scale bars indicate the normalized blur value. Recently, the important role of the choroidal circulation has been recognized in various diseases. In this study, the involvement of the choroidal circulation was investigated in the punctate inner choroidopathy (PIC), Vogt-Koyanagi-Harada disease (VKH)

and age-related macular degeneration (AMD).

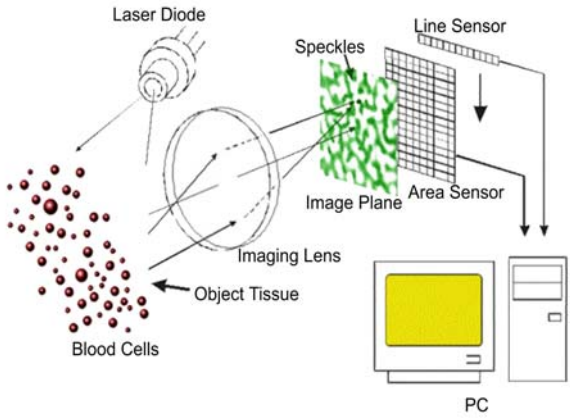

Fig. 1. Schematic diagram of laser speckle flowgraphy. The diode laser is in front of the objective lens and illuminates the fundus. The area sensor is installed in the fundus camera.

3. PUNCTATE INNER CHOROIDOPATHY

PIC presents in myopic women who complain of decreased visual acuity.[9,10] In the posterior pole, there are typical small creamy yellow lesions of the inner choroids and pigment epithelium (Fig. 2(a)). The LSFG represent that blood flow velocity in this area was decreased in PIC (Fig. 2(b)). After the treatment, blood flow velocity in this area was recovered (Fig. 2(c)). These results suggested that a decrease in the blood flow velocity in the choroid was involved in the clinical feature of the PIC, and also suggested that LSFG appears to be a safe and sensitive means to evaluate progression and response to therapy of PIC.

4. VOGT-KOYANAGI-HARADA DISEASE

VKH is considered as autoimmune disease acting against melanin protein. Therefore, every organ that contain melanin rich tissue is affected in VKH. It involves intraocular inflammations, meningitis, hearing impairment and integumentary impairment such as alopecia, vitiligo and poliosis. The choroid is melanin rich tissue. Therefore, the choroid is also target of

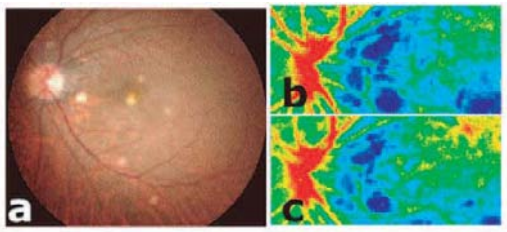

Fig. 2. Creamy yellow lesions in the punctate inner choroidopathy (a). The normalized blur map in the punctate inner choroidopathy before (b) and after (c) the treatment.

autoimmune reaction in VKH. At the onset of VKH, serous retinal detachment is presented in the patient and it cause visual loss (Fig. 3). Serous retinal detachment is considered as the result of impairment of retinal pigment epithelium followed by circulatory failure of choroidal vessels. It is considered that inflammatory reactions at the interstitial tissue in the choroid are the pathogenesis of circulatory failure of the choroid.[11–16] Indeed, multiple dark spots are seen in the early phase (choroidal phase) of FA. The dark spots are considered to reflect the focal impairment of choriocapillaris perfusion.

The LSFG represents that blood flow velocity in the choroid was decreased in Vogt-Koyanagi-Harada disease. After the treatment, blood flow velocity was increased (Fig. 3). These results suggested that LSFG also appears to be a sensitive means to evaluate progression and response to therapy for the Vogt-Koyanagi-Harada disease.

5. MULTIFRACTAL ANALYSIS OF CHOROIDAL BLOOD FLOW

AMD is the leading cause of severe visual loss in people over the age of 50 years in the western world and accounts for approximately 50 % of all cases of registered blindness.[17] In the AMD, there is an abnormal scar and blood beneath the macula: the center of the retina. Macula is important for the central area of vision. Vision loss is most likely to occur in the neovascular form of AMD, which is characterized by choroidal neovascularization (CNV), a proliferation of abnormal new blood vessels[18] that penetrate into the overlying subretinal pigment epithelial space. AMD is caused by choroidal neovascularization, which is a proliferation of abnormal new blood vessels under the retina.[19] A 33 % efficacy of CNV preventive treatment would reduce the rate of legal blindness caused by CNV by more than

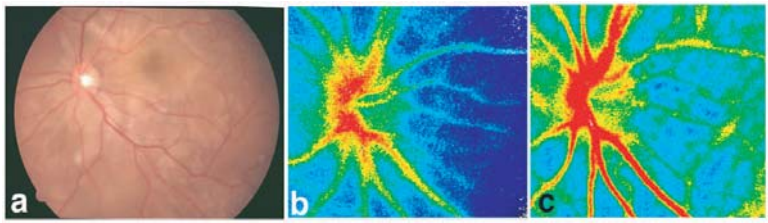

Fig. 3. White spots are seen in the fundus of the Vogt-Koyanagi-Harada disease (a). The normalized blur map in the Vogt-Koyanagi-Harada disease before (b) and after (c) the treatment.

50 %.[19] Therefore, there is potential benefit in discovering the early stage of AMD. To determine the relationship between the choroidal blood flow and AMD, a multifractal analysis has been performed for blood flow data in the LSFG map.

Here we consider the multifractal spectrum $f(\alpha)$ of blood flows in choroids. The magnitude of blood flow at a spatial point i can be regarded as the measure μ_i. We assume that the distribution of blood flow in normal choroids is multifractal. This speculation is based on the fact that most of natural distributions exhibiting their functions effectively show some kinds of criticality and do not bring any length scales. This suggests that multifractality of blood flow distributions in choroids can characterize the health condition of eyes. In order to quantify the degree of multifractality, we introduce the referential multifractal spectrum $f_0(\alpha)$. We adopt here $f_0(\alpha)$ as the multifractal spectrum for the voltage drop distribution in the hierarchical register network model (Fig. 4). The reasons of employing this model are that (i) the analytical form of $f_0(\alpha)$ can be obtained and (ii) the multifractality index based on this model spectrum $f_0(\alpha)$ is sensitive to anomalous blood flows. It should be noted that this method does not imply the spectrum $f_0(\alpha)$ represents the ideal blood flow. The analytical form of $f_0(\alpha)$ for the hierarchical resister network is given by

$$f_0(\alpha) = \frac{1}{2^{(\alpha_{\max}-\alpha_{\min})/2}} \left[(\alpha_{\max}-\alpha_{\min})\log(\alpha_{\max}-\alpha_{\min}) - (\alpha_{\max}-\alpha)\log(\alpha_{\max}-\alpha) - (\alpha-\alpha_{\min})\log(\alpha-\alpha_{\min})\right] , \tag{1}$$

where $\alpha_{\max}$ and $\alpha_{\min}$ are the maximum and minimum values of α. By measuring the deviation of $f(\alpha)$ for the observed blood flow from $f_0(\alpha)$ with observed values of $\alpha_{\max}$ and $\alpha_{\min}$, we evaluate the degree of multifractality of the blood flow. To this end, the domain of the function $f(\alpha)$ is rescaled by $\alpha \to \alpha' = (\alpha - \alpha_{\min})/(\alpha_{\max} - \alpha_{\min})$.

Therefore, the domain of the new function $\tilde{f}(\alpha')$ becomes $[0, 1]$. We

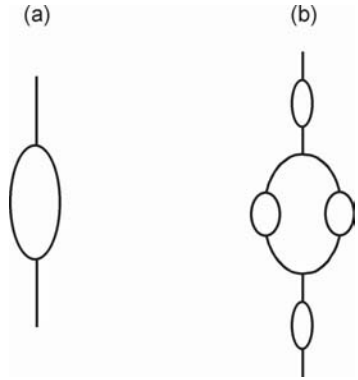

Fig. 4. Hierarchical resister network model. We start with a unit cell (a) constructed from four bonds of unit resistance. Next, the four bonds are replaced by unit cells (b). The hierarchical resister network can be obtained by repeating this procedure infinitely.

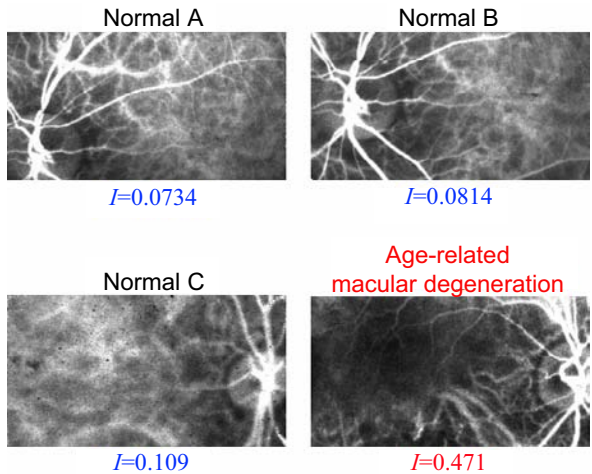

Fig. 5. The normalized blur map in the normal control and the age-related macular degeneration.

define the index I_0 quantifying the degree of multifractality by

$$I_0 = \int_0^1 \left[\tilde{f}(\alpha') - \tilde{f}_0(\alpha')\right]^2 d\alpha'. \tag{2}$$

It becomes possible to evaluate the deviation from $f_0(\alpha)$ independently of the domain of $f(\alpha)$. Furthermore, the quantity I_0 is rescaled by $I_{\max}$ which is the value of I_0 for the completely asymmetric spectrum $\tilde{f}(\alpha') = 2\alpha'$

($\alpha_0 = \alpha_{\min}$ or $\alpha_0 = \alpha_{\max}$ in this case) so that the maximum value of the index becomes unity. Thus, the final expression of the index I we employed is given by

$$I = \frac{9(\log 2)^2 \int_0^1 \left[\tilde{f}(\alpha') - \tilde{f}_0(\alpha')\right]^2 d\alpha'}{2\left[15 - 9\log 2 + 6(\log 2)^2 - \pi^2\right]}. \tag{3}$$

This quantity becomes small for a multifractal distribution and large for non-multifractal one.

The 240×240 pixel area including macula was analyzed with the composite map of LSFG, in which 3 pulsations were averaged into 1 pulsation. In normal eyes, index I is almost lower than 0.1. In contrast, multifractality becomes clearly worse for the AMD patient compared to normal eyes (Fig. 5). Index I was almost the same quantity for the each composite map when the several area was selected. The multifractal analysis of LSFG data may be an additional useful method to detect the AMD.

References

1. M. Hitosugi, T. Yokoyama, H. Kawato, Y. Motozawa, T. Nagai and S. Tokudome, *Med. Sci. Law* **44**(3), 264-5 (2004).
2. T. W. Olsen, J. I. Lim, A. Capone Jr, R. A. Myles and J. P. Gilman, *Arch. Ophthalmol.* **114**(a), 97 (1996).
3. G. Michelson, B. Schmauss, M. J. Langhans, J. Harazny and M. J. Groh, *J. Glaucoma* **5**(s), 99-105 (1996).
4. Y. Tamaki, M. Araie, K. Tomita, M. Nagahara, A. Tomidokoro and H. Fujii *Jpn. J. Ophthalmol.* **41**(1), 49-54 (1997).
5. H. Fujii, *Med. Biol. Eng. Comput.* **32**(3), 302-4 (1994).
6. Y. Tamaki, M. Araie, E. Kawamoto, S. Eguchi and H. Fujii, *Invest. Ophthalmol. Vis. Sci.* **35**(11), 3825-34 (1994).
7. Y. Tamaki, M. Araie, E. Kawamoto, S. Eguchi and H. Fujii, *Exp. Eye Res.* **60**(4), 373-83 (1995).
8. T. Nagaoka, N. Kitaya, R. Sugawara, H. Yokota, F. Mori, T. Hikichi, N. Fujio and A. Yoshida, *Br. J. Ophthalmol.* **88**(8), 1060-3 (2004).
9. A. Akman, S. Kadayifcilar and P. Aydin, *Eur. J. Ophthalmol.* **8**(3), 191-4 (1998).
10. P. A. Tiffin, R. Maini, S. T. Roxburgh and A. Ellingford, *Br. J. Ophthalmol.* **80**(1), 90-1 (1996).
11. N. Bouchenaki and C. P. Herbort, *Ophthalmology* **108**(1), 54-64 (2001).
12. T. Kohno, T. Miki, K. Shiraki, K. Kano, M. Matsushita, K. Hayashi and J. J. Laey *Br. J. Ophthalmol.* **83**(7), 822-33 (1999).
13. A. A. Okada, T. Mizusawa, J. Sakai and M. Usui, *Br. J. Ophthalmol.* **82**(10), 1175-81 (1998).

14. A. Pece, G. Bolognesi, U. Introini and R. Brancato, *Arch. Ophthalmol.* **115**(6), 804-6 (1997).
15. T. Harada, Y. Kanbara, T. Takeuchi, T. Niwa and T. Majima, *Eur. J. Ophthalmol.* **7**(2), 163-70 (1997).
16. Y. Oshima, S. Harino, Y. Hara and Y. Tano, *Am. J. Ophthalmol.* **122**(1), 58-66 (1996).
17. J. S. Slakter and M. Stur *Surv. Ophthalmol.* **50**(3), 263-73 (2005).
18. A. W. Walsh, L. E. Magargal, F. Wright and L. A. Donoso, *Ann. Ophthalmol.* **21**(9), 348-50 (1989).
19. D. M. Lanchoney, M. G. Maguire and S. L. Fine, *Arch. Ophthalmol.* **116**(8), 1045-52 (1998).

TOPOLOGICAL ANALYSIS OF PLACENTAL ARTERIES: CORRELATION WITH NEONATAL GROWTH *

H. YAMADA

Department of Obstetrics and Gynecology, Hokkaido University Graduate School of Medicine, Sapporo, Japan

K. YAKUBO

Department of Applied Physics, Graduate School of Engineering, Hokkaido University, Sapporo 060-8628, Japan

The aim of study was to assess whether any network index of placental surface arteries was associated with neonatal birth weight. Twenty-six placentas were randomly selected between 34 and 41 weeks of gestational ages. Placental weights ranged 385 to 770 g; and neonatal weights ranged 1960 to 3680 g. After visualization of placental surface arteries by a milk injection method, network indices including the number of nodes, network density, network diameter, average distance of nodes, and the degree centralization were determined. These network indices and placental weights were compared with neonatal birth weights. The Number of nodes, network density, network diameter, average distance of nodes, and the degree centralization were found to be as follows (Mean $\pm$ SD); 84.7 ± 29.3, 0.0262 ± 0.0088, 15.8 ± 2.77, 7.83 ± 1.13, 0.0263 ± 0.0091, respectively. We found that neonatal birth weights correlate with the number of nodes of placental surface arteries (correlation coefficient R=0.40) and placental weights (R=0.52) both. However, the number of nodes of placental surface arteries was not associated with the placental weights or the gestational age. We for the first time found that a topological factor, *i.e.*, the number of nodes of placental surface arteries correlated with neonatal growth. There was no correlation between numbers of nodes and placental weights. This suggests that the number of nodes affects fetal growth independent of placental weights. A topological factor of placental vasculization might significantly affect fetal growth in utero and determine risks of vascular diseases in their future lives.

*This work was supported in part by a Grant-in-Aid for the 21st Century COE program on Topological Science and Technology from the Ministry of Education, Culture, Sports, Science and Technology of Japan and by a Grant-in-Aid from the Ministry of Health, Labor and Welfare of Japan.

1. Introduction

The placenta functionally plays a key role in fetal development and growth. The placenta supply all materials required for fetal growth and energy production while removing products of fetal catabolism. Fetal deoxygenated, or "venous-like," blood flows to the placenta through the two umbilical arteries. At the junction of the umbilical cord with the placenta, the umbilical vessels branch repeatedly beneath the amnion and again within the dividing villi, finally forming capillary networks in the terminal division. Blood, with significantly higher oxygen content, returns from the placenta to the fetus through a single umbilical vein.

The branches of the umbilical vessels that transverse along the fetal surface of the placenta are referred to as the placental surface or chorionic vessels. These vessels are responsive to vasoactive substances. The placental surface arteries always cross over the placental surface veins. Immediately, before or just after entering the chorionic plate, the two umbilical arteries are joined by a transverse connection. The two placental surface arteries separate at chorionic plate to supply branches to the cotyledons. The arteries are end arteries, supplying one cotyledon, as the branch turns downward to piece the chorionic plate.

Previous studies have demonstrated that the umbilical cord length positively correlate with placental size and the neonatal birth weights.[1] It is well acknowledged that there is correlation between placental weights and neonatal birth weights. A recent study has found that digital measures of lateral chorionic plate growth correlated with the birth weights.[2] However, there has been no study concerning association between topological factors of placental vascularization and fetal/neonatal growth in humans so far.

The aim of study was to assess whether network indices, *i.e.*, topological determinants, of the placental surface arteries was associated with neonatal birth weights. To the best of our knowledge, this is the first report demonstrating correlation between topological factors of the placental surface arteries and the neonatal birth weights.

2. Materials and methods

2.1. *Patients characteristics*

Twenty-six placentas were randomly obtained with informed consent from 26 Japanese women whose pregnancies ended in the third trimester deliveries at 34 - 41 weeks of gestation (38.4 ± 1.6 weeks, mean ± SD). The placental weights ranged from 385 to 770 g (561 ± 115 g); and neonatal

birth weights ranged from 1960 to 3680 g (2794 ± 400 g).

After visualization of placental surface arteries by a milk injection method, branches of placental surface arteries were traced out on a paper. An equivalent network of representative placental arteries including nodes is shown in Fig. 1. Network indices including the number of nodes, network density, network diameter, average distance of nodes, and the degree centralization were determined. Then, correlations between neonatal birth weights, these network indices and placental weights were analyzed. Additionally, correlations between neonatal birth weights, the number of nodes and the gestational age were analyzed.

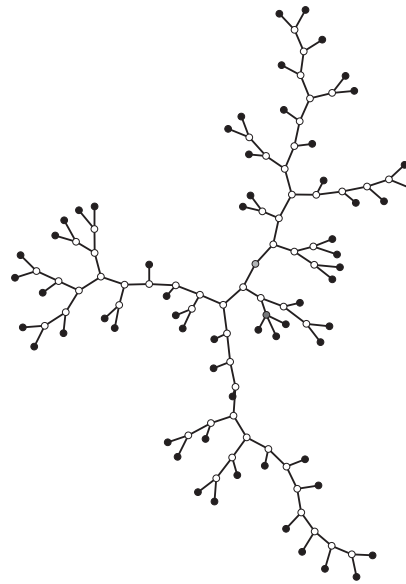

Fig. 1. An equivalent network of representative placental surface arteries. Types of nodes indicate the number of links (degree). Solid circle, solid square, open and gray circles represent nodes with one, two, three, and four links, respectively.

2.2. *Network indices as topological determinants*

Several indices characterizing topology of equivalent networks of placental arteries, which were evaluated in this work, are briefly explained.[3] Networks consist of links and nodes which correspond to arterial canals and their branch points, respectively. The number of nodes (N) represents the scale of a network and provides the most fundamental and important topological

constant. The ratio of the total number of links to the possible maximum number of links in a network with the same nodes is called the network density (ρ). Denoting the total number of links by k, the network density ρ is given by

$$\rho = 2k/N(N-1)$$

If there is no loops in the network (namely, the tree graph) as in the case of the placental arterial network, $k = N$-1. Therefore, in this case,

$$\rho = 2/N$$

The network diameter (L) is defined as the maximum number of links of the shortest-paths between any two nodes in the network. The average distance of nodes (l) is the average value of the numbers of links of the shortest-paths between any two nodes in the network. This quantity is roughly proportional to the network diameter (L). We also evaluated the degree centralization (C) which is the average of ratios of degrees of nodes to their maximum degree (the number of links connected to a node) over all nodes. Namely, denoting the degree of the ith node by k_i, the degree centralization C is given by

$$C = \frac{1}{N}\sum_{i}^{N}\frac{k_i}{N-1}$$

Although one of the most important index characterizing network structures is the cluster coefficient, this quantity is always zero for networks without loops as shown in Fig. 1 and we do not evaluate it in this work.

3. Results

Five network indices including the number of nodes, network density, network diameter, average distance of nodes, and the degree centralization in twenty-six placentas are shown in Table 1. We found that neonatal birth weights correlate with the number of nodes of placental surface arteries with the correlation coefficient R being 0.40 (Fig. 2(a)) and with placental weights (R=0.52) (Fig. 3) both. These values of the correlation coefficient for 26 samples implied that the probabilities p of the estimated correlation coefficient r of the population being negative were 0.041 and 0.006, respectively. In other words, the maximum/minimum values of r within the 95% confidence interval were 0.68/ 0.02 for data in Fig. 2(a) and 0.76/ 0.17 for data in Fig. 3. The correlation between neonatal birth weights and

Table1. Network indices of placental arteries (n=26)

Network indices	Mean	SD	Range
Number of nodes	84.7	29.3	44 - 156
Network density	0.0262	0.0088	0.0127 - 0.0444
Network diameter	15.8	2.77	13 - 26
Average distance of nodes	7.83	1.13	6.59 - 10.9
Degree centralization	0.0263	0.0091	0.0132 - 0.0498

the network density ρ was equivalent to that of Fig. 2(a), because the network density is inversely proportional to the number of nodes N for tree graphs such as arterial networks as shown previously. The average distance of nodes of arterial networks of placental surfaces probably correlated with neonatal birth weights (R=0.37, p=0.06) (Fig. 4). Since the network diameter L is roughly proportional to the average distance l, L also weakly correlated with neonatal birth weights (R=0.32, p=0.11). However, the pla-

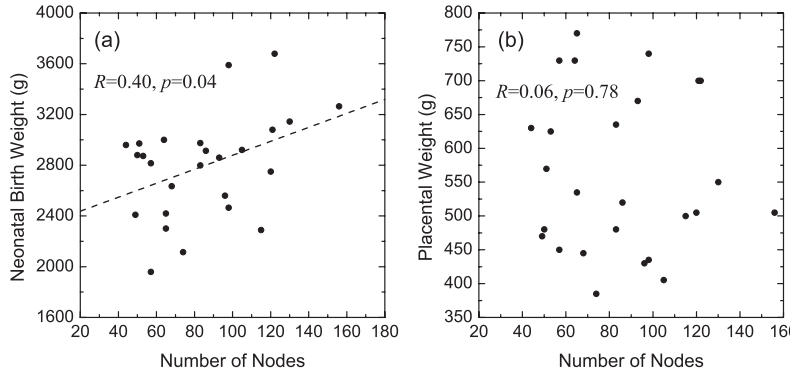

Fig. 2. Number of nodes of placental surface arteries in relation to neonatal birth weights (a) and placental weights (b).

cental weight was not related to the number of nodes of placental surface arteries (R=-0.06, p=0.78) (Fig. 2(b)). The maximum and minimum values (r_{max} and r_{min}) of the estimated correlation coefficient r of the population within the 95% confidence interval were 0.34 and -0.44, respectively, which crossed the value of zero.

The degree centralization C had no correlation with the neonatal birth weights (R=-0.29, p=0.15, r_{max}= 0.11, r_{min}= -0.61). We evaluated correlations of neonatal birth weights with other topological indices such as

the first and second Zagreb group indices,[4] the Randic connectivity index,[5] and the Platt index,[6] which are used to characterize network structures and chemical connectivity of polymer compounds. We did not find any correlation between these indices and neonatal birth weights.

We found that the gestational age significantly affected neonatal birth weights (R=0.55, p=0.004), but not number of nodes of placental surface arteries (R=0.07, p=0.73), (Fig. 5).

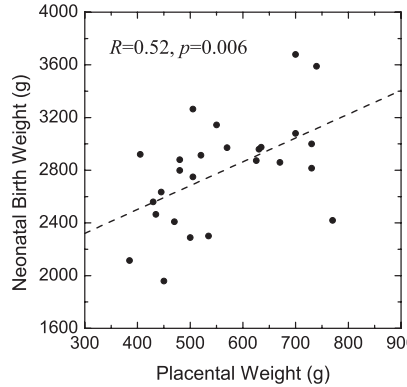

Fig. 3. Correlation between neonatal birth weights and placental weights.

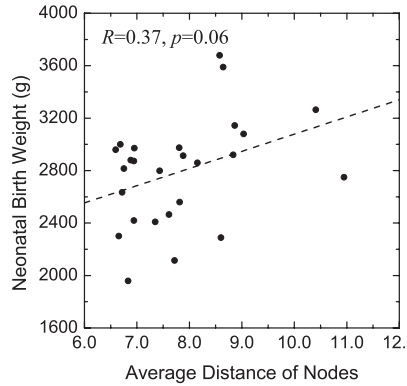

Fig. 4. Correlation between neonatal birth weights and average distance of nodes of placental surface arteries.

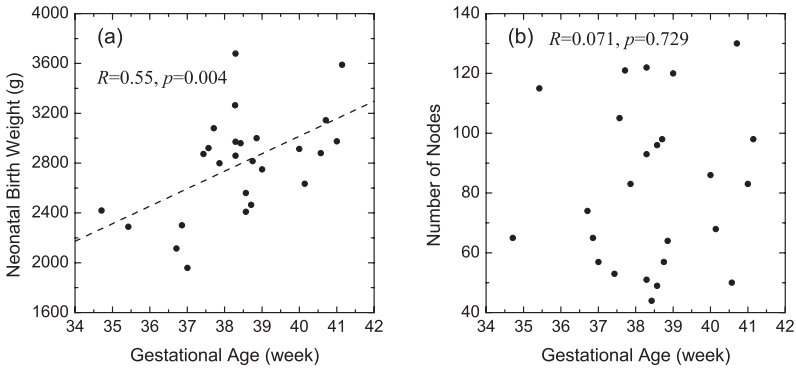

Fig. 5. Neonatal birth weights (a) and number of nodes of placental surface arteries (b) in relation to the gestational age.

4. Discussion

In this study, we for the first time found that a topological factor, *i.e.*, the number of nodes of the placental surface arteries correlated with neonatal birth weights. Weak correlations between the average distance of nodes, the network diameter of placental surface arteries, and neonatal birth weights were also found. The average distance of nodes is deeply related to the scale of a network and seems to correlate with the number of nodes where there is no loop structure. The number of nodes substantially depends on the number of branches of the placental surface arteries. This suggests that the topological structure in the development of the placental surface arteries, which directly connect the cotyledon in the placenta and umbilical arteries from a fetus, plays critical roles in the fetal growth and development. It is likely that the more branches of the placental surface arteries develop, the more effectively nutrition can be supplied to a fetus. It is well acknowledged that there is high correlation between placental weights and neonatal birth weights.[2] This was the case in the present study as well, suggesting that there was no or the least bias in placenta sampling in the present study. However, we found no correlation between the number of nodes and placental weights. This suggests that the number of nodes affects fetal growth independent of placental weights. We found that a novel factor, *i.e.*, a topological network of placental vascularization, significantly affect fetal growth in utero.

Intrauterine fetal growth restriction is a primary cause of low birth weight and accounts for notable perinatal morbidity. When fetal growth is slowed sufficiently to result clinically in intrauterine fetal growth restric-

tion, there is a significantly increased risk of cerebral palsy, short stature and sub-normal intellectual and psychological performance during later childhood.[7–9] Even within the normal range, smaller size at birth is associated with an increased incidence of cardiovascular and metabolic diseases in later life.[10] Therefore, the topological network of the placental surface arteries might be related to vascularization in fetuses; and the underdeveloped topological network might enhance risks of cardiovascular and metabolic diseases in their future lives. In the present study, we found no association between the number of nodes and the gestational age. Therefore, a topological network of placental vascularization, which affects fetal growth in utero, might be determined during early and/or mid trimesters of gestation. The topological determinants of placental surface arteries might predict fetal growth and risks of diseases in their later lives. Recent studies have demonstrated that many genetic factors significantly influence the fetal weight.[11] The topological network of the placental surface arteries might be further associated with these genetic factors.

In the present study, we for the first time demonstrated that a novel, topological analysis was one of the many useful methodologies to investigate features of vascularization in humans. Further studies are needed to understand whether any association exists between the number of nodes and abnormal pregnancies such as fetal growth restriction and preterm delivery enrolling a large number of subjects. We expect that the topological assessment will be more popular in future studies on human diseases.

References

1. A. Agboola. *Int. J. Gynaecol. Obstet.* **16**, 238 (1978).
2. C. M. Salafia, E. Maas, J. M. horp, B. Eucker, J. C. Pezzullo and D. A. Savitz. *Am. J. Epidemiol.* **162**, 991 (2005).
3. S. N. Dorogovtsev and J. F. F. Mendes, (Oxford University Press, Oxford, 2003), pp. 1-271.
4. I. Gutman, B. Ruscic, N. C. F. Trinajstic and C. F. Wilcox Jr. *J. Chem. Phys.* **62**, 3399 (1975).
5. M. Randic. *J. Am. Chem. Soc.* **97**, 6609 (1975).
6. J. R. Platt. *J. Phys. Chem.* **56**, 328 (1952).
7. R. S. Strauss. *JAMA* **283**, 625 (2000).
8. P. H. Gray, P. Jones and M. J. O'Callaghan. *Dev. Med. Child.* Neural. **43**, 580 (2001).
9. E. M. Lundgren, S. Cnattingius, B. Jonsson and T. Tuvemo. *Pediatr. Res.* **50**, 91 (2001).
10. D. J. P. Baker. *Fetal programming and public health. In: Fetal Programming: Influences on Development and Disease in Later Life.*, eds. O'Brien PMS,

Wheeler T, Barker DJP, (RCOG Press, London, 1999) pp. 3-11.
11. H. Yamada, F. Sata, Y. Saijo, R. Kishi and H. Minakami. *Semin. Thromb. Hemost.* **31**, 334 (2005).

IV

Criticality in Pure and Applied Physics

This page intentionally left blank

DROPLETS IN DISORDERED METALLIC QUANTUM CRITICAL SYSTEMS

A. H. CASTRO NETO

Department of Physics, Boston University, Boston, MA 02134, USA

B. A. JONES

IBM Almaden Research Center, San Jose, CA 95120, USA

We present a field theory for a structurally disordered magnetic system coupled to a metallic environment near a quantum critical point. We show that close to the magnetic quantum critical point droplets are formed due to the disorder and undergo dissipative quantum dynamics. We argue that the problem has a characteristic energy scale, the droplet Kondo temperature, that determines the crossover energy scale from weak to strong coupling. Our results have direct significance for the Griffiths-McCoy singularities of itinerant magnets.

Keywords: Quantum criticality; Disordered systems; Griffiths singularities.

1. Introduction

The behavior of itinerant magnets close to quantum critical points (QCP) has been a subject of intense research in the last few years. It has been found experimentally that a broad class of systems show anomalous metallic behavior in the paramagnetic phase.[1,2] Since a large number of such systems are structurally disordered due to chemical substitution, the question arises of the importance of disorder for the understanding of the anomalies observed in the experiments. We have proposed that the anomalous behavior observed in some of these systems can be understood in terms of Griffiths-McCoy singularities close to a QCP.[3,4] These singularities occur in the context of percolation theory on a discrete lattice when clusters of spins tunnel quantum mechanically. In the presence of a metallic environment we have shown that electrons scatter against clusters leading to a *cluster Kondo temperature* associated with their dissipative quantum dynamics.[4] We found that while dissipation freezes the clusters when the system is close enough to the QCP, there is still possibility of quantum behavior in a large

region in the parameter space around the QCP. In this case small Kondo temperatures can be obtained even for relatively small clusters dropping the requirement of cluster "rarity" as a condition for anomalous magnetic behavior.[4] These results put our approach in proximity to the single ion Kondo disorder theories.[5]

Millis, Morr and Schmalian (MMS)[6] proposed that a single isolated local perturbation close to a QCP of an itinerant Ising magnet produces large droplets with internal structure that are blocked from tunneling due to dissipative effects.[7] While that theory has similar features to the Griffiths-McCoy scenario proposed by us, their theory is intended to be valid for clean critical systems with a vanishing small amount of local defects. Experimentally this scenario can be realized by introducing a very small amount of impurities into clean stoichiometric compounds like $CeRu_2Ge_2$[8] or $CePd_2Si_2$[9] and driving the system close to a QCP by application of hydrostatic pressure. These calculations were extended to a finite concentration of impurities[10] leading to results that are in agreement with our early predictions.[4] In fact, we have recently shown the mathematical equivalence of the two theories.[11–13] Different authors have reached similar conclusions[14–16] and the experimental data in many materials give support to this scenario.[2,17]

In this work we show, using the replica method, that a finite density of impurities leads to Griffiths-McCoy singularities in a region close to a QCP. We demonstrate that in the presence of disorder the droplet is structureless and its typical size is set by the magnetic correlation length, ξ. More importantly, we demonstrate that the droplets have a typical droplet Kondo temperature, T_K, that varies continuously with the distance from the QCP and vanishes when the system is sufficiently close to it. These results apply to a broad class of models for strongly correlated electrons (such as the Hubbard model)[18] and are in agreement with our previous *microscopic* analysis of the disordered Kondo lattice model.[4]

2. The model

The starting point of our analysis of droplet formation close to a QCP is the Hertz action for a critical itinerant magnetic system in d spatial dimensions[18] (we use units such that $\hbar = k_B = 1$):

$$S = \frac{1}{2\beta} \sum_{n,\mathbf{q}} \left(\omega_n^2 + \gamma \Gamma_q |\omega_n| + q^2 + r \right) |\varphi(\omega_n, \mathbf{q})|^2$$

where ω_n and $\mathbf{q}$ are the Matsubara frequency and momentum, respectively, γ is the coupling between the order parameter $\varphi(\mathbf{x}, \tau)$ and the particle-hole

continuum, Γ_q gives the momentum dependence of the dissipative coupling ($\Gamma_q = q^{-\zeta}$ with $\zeta = 0$ for antiferromagnets, $\zeta = 1$ for clean ferromagnets and $\zeta = 2$ for disordered ferromagnets). The distance from the QCP is controlled by r. In the ordered phase $r < 0$ indicating an instability towards long range order and at the QCP we have $r = 0$. In this work we focus entirely on the paramagnetic phase where $r > 0$ so that we can parametrize $r = \xi^{-2}$. Disorder is introduced into the problem as a random variation of r in real space:

$$S_{dis} = -\frac{1}{2}\int d\mathbf{x}\int_0^\beta d\tau\, \delta r(\mathbf{x})\ \varphi^2(\mathbf{x},\tau)$$

which is assumed to be Gaussian distributed with width u, that is, the probability distribution is given by:

$$P(\delta r) \propto \exp\left\{-\frac{1}{4u}\int d\mathbf{x}\ (\delta r(\mathbf{x}))^2\right\} \tag{1}$$

so that $\overline{\delta r(\mathbf{x})} = 0$ and

$$\overline{\delta r(\mathbf{x})\delta r(\mathbf{y})} = u\ \delta^d(\mathbf{x}-\mathbf{y})$$

where the average is calculated with (1). The reason for the appearence of droplets in the problem is that the Gaussian distribution (1) allows for local values of $\delta r(\mathbf{x})$ (the tails of the distribution) such that $r - \delta r(\mathbf{x}) < 0$, that is, it allows for local order even in the absence of long range order. These locally ordered regions in a surrounding paramagnetic media are called droplets.

Since we are not interested in one particular realization of the disorder we study the average free energy using replicas.[19] We introduce n replicas of the order parameter φ_a with $a = 1, ..., n$ and calculate the average free energy, $\overline{F} = (\overline{Z^n} - 1)/n$, taking the limit of $n \to 0$ at the end of the calculation. It can be easily shown that a new term is generated in the quantum action:

$$\mathcal{S}_{dis} = -\frac{u}{4}\sum_{a,b}\int d\mathbf{x}\int_0^\beta d\tau\int_0^\beta d\tau'\varphi_a^2(\mathbf{x},\tau)\varphi_b^2(\mathbf{x},\tau')\,.$$

Notice that the disorder not only generates interactions between fields in different replicas but also couples the fields in the imaginary time direction. Our calculations can also be carried out with a non-linear term of the form $g\varphi^4(\mathbf{x},\tau)$ with no fundamental change in the results, and so for simplicity we omit it (this term is important for the stability of the replica solution and should be kept in studying the gaussian fluctuations[20]).

3. Replica symmetry breaking

We first study the problem of droplet formation by investigating the static, classical, part of the action. In this case $\varphi_a(\mathbf{x},\tau) = \psi_a(\mathbf{x})$ where ψ_a is obtained from the variational solution of the static part of the action:

$$-\nabla^2\psi_a(\mathbf{x}) + r\psi_a(\mathbf{x}) - u\beta\psi_a(\mathbf{x})\sum_b \psi_b^2(\mathbf{x}) = 0\,. \tag{2}$$

This equation is quite revealing. If the problem were to be replica symmetric, that is, $\psi_a(\mathbf{x}) = \psi_0(\mathbf{x})$ for all values of a, the last term in (2) would scale like $n\psi_0^2(\mathbf{x})$ and would vanish in the limit of $n \to 0$. This would imply that the only solution in the paramagnetic phase ($r > 0$) is the trivial solution $\psi_0 = 0$. Thus, in order for droplets to form in the paramagnetic phase one needs the replica symmetry to be broken. We follow Dotsenko[20] who studied the classical problem in detail and assume a non-trivial replica solution such that for $a = 1, ..., k$ we have $\psi_a(\mathbf{x}) = \psi_k(\mathbf{x})$ while $\psi_a(\mathbf{x}) = 0$ for $a = k+1, ..., n$. Here $k > 1$ is an integer that determines the degree of the symmetry breaking process. Using this particular solution we see that (2) can be rewritten as:

$$-\nabla^2\psi_k(\mathbf{x}) + r\psi_k(\mathbf{x}) - u\beta k\psi_k^3(\mathbf{x}) = 0\,. \tag{3}$$

This equation is non-linear Schrödinger equation and can be thought as the equation for a classical particle moving in a non-linear potential.

A naive conclusion from this discussion would be that the "energy" would be minimized for $\psi = \pm\infty$, a solution that is clearly unphysical. It should be kept in mind that the replicated action is **not** the actual free energy of the problem; the latter is only obtained after we take the limit of $n \to 0$ at the end of the calculation (this fact is a standard consequence of the application of the replica method[19]). Dotsenko has shown that the stable static solutions of this problem are the maxima of the potential. Mathematically this can be proved by showing that all the eigenvalues of the fluctuation matrix (the Hessian) are real and positive.[20] The maxima are associated with the two possible configurations of the droplet (spin configurations pointing up and down). Equation (3) can be rescaled if we define

$$\psi_k(x) = \sqrt{\frac{r}{u\beta k}}\phi(\sqrt{r}x) \tag{4}$$

so that $\phi(z)$ obeys a scale independent equation:

$$-\nabla_z^2\phi(z) + \phi - \phi^3 = 0 \tag{5}$$

where $z = \sqrt{r}x$. The proper boundary conditions are $\phi(0) =$ constant and $\phi(z \to \pm\infty) = 0$. Equation (5) has exponentially decaying solutions for $x \gg 1/\sqrt{r}$ and is smooth for $x < 1/\sqrt{r}$. This can be contrasted with the solution found by MMS for a local defect in which the droplet is such that for $x < 1/\sqrt{r}$ the droplet profile decays like $1/x$ (here such a behavior does not occur in $d < 4$). Moreover, it is clear that the typical size of the droplet is the magnetic correlation length:

$$R \approx \frac{1}{\sqrt{r}} = \xi \,.$$

Thus droplets become arbitrarily large close to the QCP.

The action for the static droplet can be calculated by substitution of (4) into the original action, and the free energy, after summing over the replicas, reads:[20]

$$\frac{F_D^0}{V} \approx -ur^{d/2} \exp\left\{-\frac{r^{2-d/2}E_2}{4u}\right\}$$

where $E_N = \int d^d z \phi^{2N}(z)$ and V is the volume of the system. As pointed out by Dotsenko the non-analytic, non-perturbative, dependence of the free energy on the disorder strength u for $d < 4$ shows that the static field theory reproduces the classical Griffiths result in a percolating lattice.[21] Obviously in order to study quantum or Griffiths-McCoy singularities[22–26] we have to allow the droplet to tunnel between the two maxima of the potential.

4. Droplet tunneling

In order to study the tunneling of the droplet we assume a *rigid* droplet approximation:

$$\varphi(\mathbf{x}, \tau) = \psi_k(\mathbf{x}) X(\tau) \tag{6}$$

where all the dynamics is encapsulated in $X(\tau)$. This choice assumes that the droplet tunnels as a whole. Direct substitution of (6) into the action leads to:

$$Z[X] \approx \int DX(\tau) \; \exp\left\{-\frac{r^{2-d/2}E_2}{u}\mathcal{F}[X]\right\}$$

where

$$\mathcal{F}[X] = \frac{1}{\beta}\int_0^\beta d\tau \Bigg\{ \frac{M}{2}\left(\frac{dX}{d\tau}\right)^2 + \frac{X^2(\tau)}{2} - \frac{1}{4\beta}X^2(\tau)\int_0^\beta d\tau' X^2(\tau') + \frac{\eta}{4\pi}\int_{-\infty}^{+\infty} d\tau' \frac{(X(\tau)-X(\tau'))^2}{(\tau-\tau')^2} \Bigg\} \tag{7}$$

is the replica free energy for $X(\tau)$. The coefficients in (7) are:

$$M = \frac{E_1}{E_2}\, r^{-1}$$
$$\eta = \frac{\gamma G_\zeta}{E_2}\, r^{-(1+\zeta/2)} \tag{8}$$

that can be associated with the "particle" mass and dissipation coefficient, respectively. Here $G_\zeta = \int d^d q\, q^{-\zeta}|\phi_q|^2$, ϕ_q is the Fourier transform of $\phi(z)$ and periodic boundary conditions are assumed: $X(\tau+\beta) = X(\tau)$. Observe that $\mathcal{F}$ describes a Caldeira-Leggett action[27] for the motion of a dissipative particle in a non-local, non-linear, potential which, for slowly varying configurations of $X(\tau)$ reduces to the potential discussed by Dotsenko.[20] At low temperatures the problem described in (8) can be reduced to the so-called dissipative two level system problem[28] where only the maxima of the potential, that is $X(\tau) = \pm 1$, and the paths linking these points, contribute to the free energy. The amount of damping in the tunneling of the droplet can be estimated by comparing the parameters in (8). We have weak damping when $\eta \ll \omega_0 M$ while for strong damping one has $\eta \gg \omega_0 M$ ($\omega_0 = 2$ is the undamped frequency of motion in our dimensionless units). Notice that the crossover from weak to strong dissipation occurs at $r = r_c$ where (using (8))

$$r_c \approx \left(\frac{\gamma G_\zeta}{2E_1}\right)^{2/\zeta}$$

which indicates that close to the QCP ($r < r_c$) the droplet motion is highly damped. The tunneling splitting between the two configurations $X = \pm 1$ is given by:[28]

$$\Delta = \omega_{cl} e^{-8M\omega_{cl}}$$

where ω_{cl} is the classical frequency of oscillation. On the one hand in the weakly dissipative regime ($r > r_c$) one has $\omega_{cl} \approx \omega_0$ and therefore the

tunneling splitting is:

$$\Delta_{r>r_c}(r) \approx 2e^{-a/r} \tag{9}$$

where $a = 16E_1/E_2$ is a universal constant. On the other hand in the strongly dissipative regime ($r < r_c$) we have $\omega_{cl} \approx M\omega_0^2/\eta$ and therefore

$$\Delta_{r<r_c}(r) \approx \frac{4r^{\zeta/2}}{\gamma} e^{-br^{\zeta}} \tag{10}$$

where $b = 32E_1/(\gamma G_\zeta)$ is a non-universal constant. For antiferromagnets ($\zeta = 0$) the tunneling splitting is constant close to the QCP while it vanishes in the case of ferromagnets ($\zeta = 1, 2$). Another important parameter is the Caldeira-Leggett dissipative coupling given by:

$$\alpha(r) = \frac{2\eta}{\pi} = \left(\frac{r_0}{r}\right)^{1+\zeta/2} \tag{11}$$

where we used (8) and defined

$$r_0 = \left(\frac{2\gamma G_\zeta}{\pi E_2}\right)^{1/(1+\zeta/2)} . \tag{12}$$

Observe that the dissipative coupling diverges at the QCP. As is well-known this problem has a characteristic crossover energy scale that can be associated with the Kondo temperature, T_K, of an anisotropic Kondo impurity model.[28] This energy scale separates the region of strong and weak coupling and for $\alpha < 1$ is given by:

$$T_K(r) \approx W \left(\frac{\Delta(r)}{W}\right)^{\frac{1}{1-\alpha(r)}} \tag{13}$$

where W is a cut-off energy scale. For $\alpha > 1$ we have $T_K = 0$ and the droplet is frozen. Notice that according to (11) the freezing of the droplet occurs for $r < r_0$. This indicates that close to the QCP droplets are frozen. Observe that r_0 given in (12) is a non-universal quantity which depends on parameters that cannot be obtained in a continuum field theory. Depending on the microscopic parameters the freezing of the droplets can occur in the region of weak damping if $r_0 > r_c$ or strong damping if $r_0 < r_c$, affecting the value of the tunneling splitting given in (9) and (10). Thus $T_K(r)$ is finite and a continuous function of the distance from the QCP in agreement with our previous analysis.[4] In fact for $r \gg r_0$ the droplets become free to tunnel. Although we have discussed the physics of a single droplet it is clear that if we take into account a distribution of tunneling splittings Δ it will lead to the Griffiths-McCoy singularities discussed in[3] producing non-universal power law behavior in the magnetic susceptibility, $\chi(T)$, and specific heat

coefficient $\gamma(T) = C(T)/T$, such that $\chi(T) \propto \gamma(T) \propto T^{-1+\lambda(r)}$ where $\lambda < 1$ varies with the distance to the critical point.[26] The phase diagram is shown in Fig. 1.

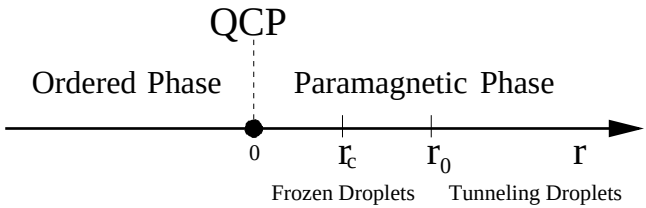

Fig. 1. Phase diagram as a function of the parameter r: the system is ordered for $r < 0$; droplets are frozen in the paramagnetic phase for $0 < r < r_0$ and can quantum tunnel for $r > r_0$.

Direct comparison of (13) with our previous results in Ref. 4 indicates that the two problems map into each other if $N \propto \xi^2$ where N is the number of spins in the cluster. Another interesting consequence of our calculation is the sharp contrast between the case of ferromagnetic and antiferromagnetic droplets. For antiferromagnetic droplets ($\zeta = 0$) the dissipation coefficient in (11) scales with ξ^2 while in the case of a clean ferromagnet ($\zeta = 1$) we find $\alpha \propto \xi^3$ indicating stronger damping. For a ferromagnetic system with diffusive electrons ($\zeta = 2$) damping becomes even stronger with $\alpha \propto \xi^4$. This indicates, in agreement with our previous analysis,[4] that dissipation is more important in the case of ferromagnetic droplets than in the case of antiferromagnetic ones. Since the great majority of systems studied experimentally are of the antiferromagnetic type[1] our results indicate that dissipation does not freeze the droplets in a region of the parameter space around the QCP.

A clear way to interpolate between our results and those in the opposite, single impurity, regime would be to perform our calculation for a Poisson distribution of Dirac delta potentials.[29] In this case the problem is characterized by two physical parameters: the density of impurities ρ and the strength of the potential V. A universal Gaussian distribution like the one discussed in this paper is obtained by taking the limit of $\rho \to \infty$ and $V \to 0$ so that $u = \rho V^2$ is constant. On the other hand the single impurity limit studied in Ref. 6 is obtained by letting $\rho \to 0$.

5. Conclusion

In summary, we have studied the problem of droplet formation and dynamics close to a QCP of a disordered itinerant Ising magnet. We find that the droplets have a typical Kondo temperature (associated with their dissipative quantum dynamics) that varies continuously with the distance from the QCP. We show that the characteristic Kondo temperature of the droplet is finite except in a non-universal region (dependent on microscopic details) close to the QCP. These results are in agreement with our previous analysis of quantum Griffiths-McCoy singularities in the disordered Kondo lattice model and extends the validity of our results to other strongly correlated systems.

Acknowledgments

We acknowledge invaluable discussions with H. Castillo, V. Dotsenko, A. J. Millis, D. Morr and J. Schmalian. A.H.C.N. was supported through NSF grant DMR-0343790.

References

1. A. H. Castro Neto, *Some Modern Aspects of the Physics of Strongly Correlated Systems* (UAM Ediciones, Madrid, 2001).
2. G. R. Stewart, *Rev. Mod. Phys.* **73**, p. 797 (2001).
3. A. H. Castro Neto and B. A. Jones, *Phys. Rev. Lett.* **81**, p. 3531 (1998).
4. A. H. Castro Neto and B. A. Jones, *Phys. Rev. B* **62**, p. 14975 (2000).
5. V. Dobrosavljevic and E. Miranda, *Phys. Rev. Lett.* **69**, p. 1113 (1992).
6. A. Millis, D. Morr and J. Schmalian, *Phys. Rev. Lett.* **87**, p. 167202 (2001).
7. O. P. Sushkov, *Phys. Rev. B* **62**, p. 12135 (2000).
8. H. Wihelm, K. Alami-Yadri and D. Jaccard, *Phys. Rev. B* **59**, p. 3651 (1999).
9. N. D. Mathur, F. M. Grosche, S. R. Julian, I. R. Walker, D. M. Freye, R. K. W. Haselwimmer and G. G. Lonzarich, *Nature* **394**, p. 39 (1998).
10. A. Millis, D. Morr and J. Schmalian, *Phys. Rev. B* **66**, p. 174433 (2002).
11. A. H. Castro Neto and B. A. Jones, *Europhys. Lett.* **71**, p. 790 (2005).
12. A. Millis, D. Morr and J. Schmalian, *Europhys. Lett.* **72**, p. 1052 (2005).
13. A. H. Castro Neto and B. A. Jones, *Europhys. Lett.* **72**, p. 1054 (2005).
14. N. Shah and A. J. Millis, *Phys. Rev. Lett.* **91**, p. 147204 (2003).
15. T. Vojta and J. Schmalian, *Phys. Rev. Lett.* **95**, p. 237206 (2005).
16. J. A. Hoyos and T. Vojta, *cond-mat/0605036, volume =, year = .*
17. M. C. de Andrade, R. Chau, R. P. Dickey, N. R. Dilley, E. J. Freeman, A. Gajewski, M. B. Maple, R. Movshovich, A. H. Castro Neto, G. E. Castilla and B. A. Jones, *Phys. Rev. Lett.* **81**, p. 5620 (1998).
18. J. A. Hertz, *Phys. Rev. B* **14**, p. 1165 (1976).
19. M. Mezard, G. Parisi and M. A. Virasoro, *Spin Glass Theory and Beyond* (World Scientific, New Jersey, 1987).

20. V. S. Dotsenko, *Jou. Phys. A* **32**, p. 2949 (1999).
21. R. B. Griffiths, *Phys. Rev. Lett.* **23**, p. 17 (1969).
22. B. M. McCoy and T. T. Wu, *Phys. Rev.* **176**, p. 631 (1968).
23. D. S. Fisher, *Phys. Rev. Lett.* **69**, p. 534 (1992).
24. M. Y. Guo, R. N. Bhatt and D. A. Huse, *Phys. Rev. Lett.* **72**, p. 4137 (1994).
25. H. Rieger and A. P. Young, *Phys. Rev. Lett.* **72**, p. 4141 (1994).
26. M. J. Thill and D. A. Huse, *Physica A* **214**, p. 321 (1995).
27. A. O. Caldeira and A. J. Leggett, *Ann. Phys.* **149**, p. 347 (1983).
28. A. J. Leggett, S. Chakravarty, A. T. Dorsey, M. P. A. Fisher, A. Garg and W. Zwerger, *Rev. Mod. Phys.* **59**, p. 347 (1983).
29. C. Chamon and C. Mudry, *Phys. Rev. B* **63**, p. 100503 (2001).

IMPORTANCE OF STATIC DISORDER AND INHOMOGENEOUS COOPERATIVE DYNAMICS IN HEAVY-FERMION METALS

O. O. BERNAL

Department of Physics and Astronomy
California State University
5151 State University Drive
Los Angeles, 90032 CA, USA
E-mail: obernal@calstatela.edu

Nuclear Magnetic Resonance (NMR) and Muon Spin Rotation (μSR) experiments are effective for the detection of inhomogeneous statics and/or dynamics in the spin systems housed by non-Fermi liquid (NFL) materials. This paper describes the properties that can be probed using these techniques and the techniques' sensitivity to magnetic disorder. The paper also reviews NMR and μSR work in some heavy fermion, NFL, materials that lie near a quantum critical point. NFL behavior is found at low temperature in a number of materials that can be tuned towards quantum criticality by the suppression of antiferromagnetism. The NFL regime is signaled by unusual behavior of thermodynamic and transport properties. The study of NMR and μSR parameters in some of these systems reveals strongly inhomogeneous magnetic susceptibilities due to structural disorder, which in turn is found to be an important factor in determining their NFL character. At the lowest temperatures, the spin dynamics in such systems are due to cooperative fluctuations of inhomogeneous type, similar to the spin dynamics of spin glasses, but with zero spin-freezing temperature. The spectroscopic data permit the comparison between electronic disorder and slow spin fluctuations, which turn out to be correlated in NFL systems.

1. Correlated, Heavy, Non-Fermi-Liquid Electron Systems

Intermetallic compounds containing transition metal and lanthanide, or actinide ions, present a variety of magnetic and charge properties with novel and complicated ground state structures. The low temperature (T) properties of these systems indicate the existence of interactions—correlations—between localized and conduction electrons.[1] The correlations lead to new states of renormalized *quasiparticles* whose inertia surpasses that of free electrons by one, two, or even three orders of magnitude. These *heavy*

electron (fermion) materials display a plethora of low-T phase transitions, where new ordered states of matter are realized. Among these states, dipolar, quadrupolar, and octupolar order have been observed, but the most ubiquitous of all orders is the antiferromagnetic order. This is in part due to the localized nature of unpaired f and d electrons in magnetic ions (such as those obtained from U, Ce, Ni, Cu, and similar metals), which often is preserved in the intermetallic compounds that contain them. Localized electrons tend to participate in collective modes of low entropy—ordered states—by means of interactions that are mediated by overlap with conduction electrons.

One of the areas of active research in recent years has been the study of systems in which the antiferromagnetic phase can be suppressed by pressure, magnetic field, or composition.[2] In most cases, successful suppression of antiferromagnetism in a controlled manner results in a new kind of material for which a search for an ordered ground state appears to be frustrated in the sense that the system does not have a lower entropy state to settle into. Figure 1 illustrates these statements with the use of a generic phase

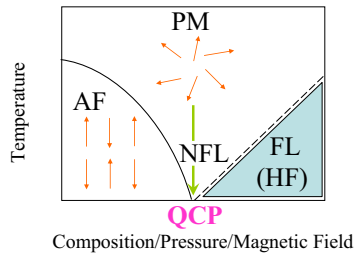

Fig. 1. Generic phase diagram of a correlated-electron system. The abscissa can be any of the control parameters indicated. The phases are PM: paramagnetic, AF: antiferromagnetic, FL (HF): Fermi liquid (Heavy Fermion). QCP: quantum critical point induced at $T = 0$ by the variation of the control parameter. Arrows: magnetic order or disorder as suggested by the pattern. The NFL behavior is obtained when the system is cooled towards the QCP.

diagram. At high temperatures the system is paramagnetic PM. But on lowering T at low (high) values of the control parameter, the system orders antiferromagnetically AF (crosses over to the Fermi liquid (FL) or heavy fermion (HF) regime). On the other hand, if the system is cooled at the critical value of the control parameter, its thermodynamic and transport

properties present singular behavior due to the presence of a quantum critical point (QCP) at $T = 0$.

This unusual response is termed non-Fermi-Liquid (NFL) behavior, because the frustration experienced by the material in reaching an ordered ground state cannot be understood within the FL theory—a paradigm established by Lev Landau in 1957.[3] In the FL theory, a fluid of interacting Fermi particles can be renormalized and the quasiparticle excitations of the renormalized fluid mapped one to one with those of a free electron gas. One of the most quoted examples of a Fermi liquid is the single impurity Kondo system in which a lone magnetic ion is embedded in a noble (free-electron gas) metal host. The presence of the impurity in the metal creates correlations between the hitherto-free conduction electrons, inducing a crossover to a low-T state that is characterized by a heavier electronic mass, but otherwise with properties similar to those of a normal metal. In the FL regime the specific heat $C(T) \propto T$, the magnetic susceptibility $\chi(T) =$ constant, and the electrical resistivity $\Delta\rho(T) = \rho(T) - \rho(0) \propto T^2$. NFL behavior is, on the other hand, signaled by a logarithmic divergence in the Sommerfeld coefficient $\gamma = C(T)/T$, a power-law or logarithmic divergence of $\chi(T)$, and a sub quadratic power-law dependence of $\Delta\rho(T)$; therefore, it can be taken as quantum critical behavior associated with a $T_c = 0$ phase transition.

NFL behavior was first found in heavy-fermion-derived solid solutions.[4,5] These systems have a large concentration of magnetic (Kondo) impurities. In fact, $UCu_{5-x}Pd_x$ and $CeCu_{6-x}Au_x$,[6] for instance, have a whole lattice of these "impurities." Stoichiometric HF compounds, typically described as having no degree of crystallographic or substitutional disorder, such as $CeNi_2Ge_2$, and $YbRh_2Si_2$, have also been found to exhibit NFL behavior.[7] Thermodynamic and transport measurements in these kinds of materials indicate that the Fermi-liquid description appropriate to conventional Kondo systems does not apply.[6,8] Qualitatively, the ground state of a concentrated Kondo system depends on the relative strength of Ruderman-Kittel-Kasuya-Yosida (RKKY) interactions between magnetic impurities (favoring magnetic order) and of local conduction-electron/magnetic-impurity interactions, *i.e.*, the Kondo effect (favoring Pauli paramagnetism).[9] In terms of the exchange integral J, the strength of the RKKY interaction grows as J^2; the Kondo temperature T_K varies exponentially with J^{-1} (*i.e.*, $T_K \sim \exp[-(\rho J)^{-1}]$, where ρ is the density of states at the Fermi energy). For $T = 0$, there must be a transition from a magnetic (long-range order) to a non-magnetic phase at some value of $J = J_c$. A system with $J \sim J_c$ is therefore near a magnetic instability. This is consistent

with the expectations that on diluting the magnetic interactions between impurities by ionic substitution, one is suppressing the antiferromagnetic transition and driving the system towards quantum criticality.[2]

2. Spectroscopic Techniques: NMR and μSR

Static and dynamic properties of local and internal magnetic fields can be measured by NMR/μSR and provide information about the structure of solids at the microscopic level.[10]

The paramagnetic shift K measures the local spin susceptibility χ at the nuclear/muon sites. Figure 2 presents a schematic drawing of the ba-

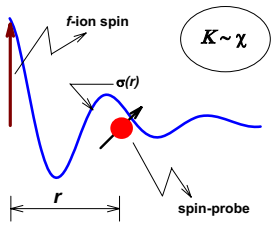

Fig. 2. Schematic drawing for the RKKY interaction of a localized f electron in the material and a spin probe a distance r away. The spin probe for NMR (μSR) is a nucleus belonging to the compound (an implanted muon). The RKKY interaction is mediated by the conduction electrons which are spin polarized [$\sigma(r)$] by the f moment. The oval indicates that the paramagnetic shift K is a measure of the f-spin susceptibility χ.

sic RKKY interaction between a spin probe (muon or nucleus) and the f moment of localized electrons in a correlated electron system. Static inhomogeneity is probed by the (NMR/μSR) spectral linewidth Γ, which indicates the extent to which the static magnetic fields are distributed in the material. Furthermore, the ratio Γ/K has been found to provide important insight into the role played by structural disorder and its correlation with NFL behavior.[11] For instance, a T dependence of Γ/K immediately indicates magnetic disorder (distributed $\chi(T)$), the strength of which can be inferred to be weak ($\Gamma/K \sim 0$)[12] or strong ($\Gamma/K \gtrsim 1$).[13] Similarly, a T-independent Γ/K ratio reveals a homogeneous $\chi(T)$, even if its value is relatively large. In the latter case Γ/K indicates strong disorder in the spin-probe coupling (hyperfine field) to the local environment.[14]

Temporal fluctuations in the local fields caused by quasiparticle spin excitations can be detected by nuclear/muon spin relaxation rate experiments. Relaxation data complements and augments the information about

disordered environments by providing a means to evaluate whether the relaxation time is spatially inhomogeneous and provides clues of whether the relaxation is induced by single-particle, as opposed to collective, fluctuations.[11]

3. NMR/μSR and $UCu_{5-x}Pd_x$

One of the most studied systems to date is the substitutional alloy $UCu_{5-x}Pd_x$.[5] It displays NFL regimes for at least two compositions ($x = 1.0, 1.5$). The material is isostructural to parent UCu_5 (fcc $AuBe_5$ structure; space group $F\overline{4}3m$, with two crystallographically inequivalent copper sites in the ratio 4 : 1 at the 16*e* and 4*c* positions, Wyckoff notation). As a consequence of this, the $x = 1$ compound could be completely ordered, whereas in $x = 1.5$, substitutional disorder must exist; see Fig. 3.

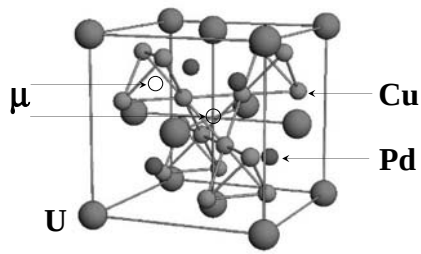

Fig. 3. Expected ordered structure of UCu_4Pd and location of spin probes (μ and Cu nucleus) with respect to the magnetic (U) and non-magnetic (Cu and Pd) ions.

Indication that disorder was important to understand the behavior of $UCu_{5-x}Pd_x$ came first from NMR/μSR experiments.[13,15] These experiments revealed a strong intrinsic magnetic inhomogeneity in χ. The original analysis of the NMR and μSR data on this system was developed along the lines of a phenomenological model, introduced to account for the experimental facts. The single-impurity "Kondo disorder" (KD) model introduced in Ref. 13 successfully accounts for the susceptibility, NMR/μSR, and specific heat data of this material for temperatures above 2 K. In the KD model, moderate disorder in the Kondo couplings g ($g \equiv \rho J$) leads to a broad distribution $P(T_K)$ of Kondo temperatures. Weak divergences of the thermodynamic parameters as $T \to 0$ follow as long as $T \gg T_K$ for some fraction of the Kondo impurities.

The KD model was later stated in more formal theoretical grounds and has been successful, particularly for $UCu_{5-x}Pd_x$.[16] There is also a broader approach to understanding inhomogeneous NFL behavior, *i.e.*, the theory of Griffiths-McCoy phases (GP).[17,18] In the GP theory, there is quantum coexistence of a metallic-paramagnetic Fermi-liquid (Kondo effect) and a granular-magnetic phase (RKKY interactions) which leads to singular behavior in the thermodynamics at low T.[19] A detailed description of the GP theory is presented elsewhere in these proceedings. However, μSR experiments have shown that neither a KD nor a GP scenario, as originally introduced, is sufficient to account for the unusual inhomogeneous dynamics of $UCu_{5-x}Pd_x$.[11] As was inferred by MacLaughlin *et al.* after analyzing the stretched-exponential behavior of the muon relaxation function $\{\exp[-(\Lambda t)^K]$, where K is not to be confused with the paramagnetic shift$\}$ and its time/field scaling (t/H^γ), the measured relaxation is spatially inhomogeneous and induced by collective modes of correlated spins. This behavior resembles more that of a spin glass just above the spin-glass transition temperature, except that in the case of $UCu_{5-x}Pd_x$, there is no indication of a finite-temperature spin-glass transition.[20] The system is more closely related to a *quantum* spin glass.[21] Thus, more work needs to be done to assess the validity of disorder-driven NFL theories and understand how they connect with quantum spin-glass physics. Such work shall answer some of the outstanding questions regarding NFL behavior in $UCu_{5-x}Pd_x$.

4. NMR/μSR in Other NFL Systems

Work by MacLaughlin and collaborators[11,12,14,15] has also shown that the effects of disorder are not always strong enough to account for all of the NFL behavior. This increases the validity of using theoretical models developed for clean systems to understand the NFL physics.[8,22] Nevertheless, the muon spin relaxation function has been determined and compared in several NFL systems, including both "clean" (ordered) and "dirty" (disordered) ones. In cleaner systems (such as $CeNi_2Ge_2$ and $YbRh_2Si_2$), the relaxation function is closer to being single-exponential, *i.e.*, $K \sim 1$, indicating a more homogeneous relaxation time.[11] With increased disorder, *e.g.*, for systems such as $CeCu_{5.9}Au_{0.1}$ and CePtSi, the value of K drops from 1: stretched exponential behavior. Clean systems show slow relaxation and time-independent spin-spin autocorrelation function; disordered systems are glassy, displaying fast relaxation and a Power Law spin-spin autocorrelation function.[21] For most systems, however, the spin relaxation time-field scaling indicates that the relaxation is due to collective modes of

spin fluctuations: relaxation by independent relaxing centers is ruled out.

Finally, a correlation exists between electronic disorder and slow spin fluctuations in all NFL materials studied as evidenced by Fig. 4(a) (from MacLaughlin *et al.* Ref. 11). The relaxation rate and the stretched exponential character of the relaxation function decrease with residual resistivity. Thus, it is observed that disorder induces a slow-down of spin fluctuations. On the other hand, Fig. 4(b) indicates that no correlation is found if one examines the relaxation time against a measure of the fluctuation energy scales associated with the Sommerfeld coefficient of different systems. Thus, the relaxation is not influenced by the thermodynamic energy scales.

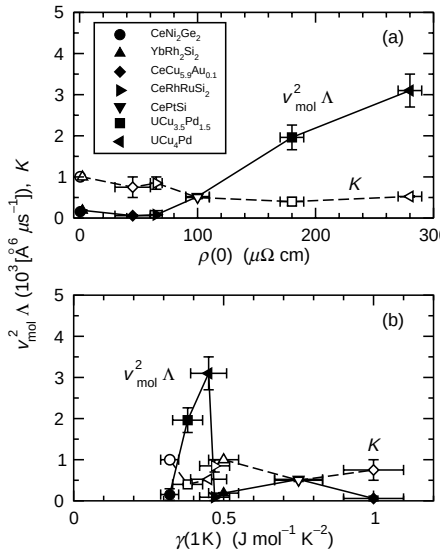

Fig. 4. Normalized muon stretched-exponential relaxation rate Λ (filled symbols) and exponent K (open symbols) vs (a) residual resistivity $\rho(0)$ and (b) Sommerfeld coefficient $\gamma(T = 1\ \mathrm{K})$. Increasing stretched exponential behavior yields $K < 1$. From Ref. 11.

Acknowledgments

The author wishes to thank D. E. MacLaughlin, R. H. Heffner, and all the μSR group collaborators he has had the opportunity to work with since 1997. Work at CSULA is supported by the NSF/DMR-0203524&0604015.

References

1. For a recent review of theoretical progress, see: E. Miranda and V. Dobrosavljević *Rep. Prog. Phys.* **88**, 2337 (2005).
2. See, *e.g.*, G.R. Stewart, *Rev. Mod. Phys.* **73**, 797 (2001); P. Coleman, M.B. Maple, and A. Millis (eds) *Proceedings of the Conference on Non-Fermi Liquid Behavior in Metals (Santa Barbara, CA); J. Phys.: Condens. Matter* **8**, 9675 (1996); and references therein.
3. L. D. Landau, *Soviet Physics JETP* **3**, 920 (1957).
4. C.L. Seaman *et al.*, *Phys. Rev. Lett.* **67**, 2882 (1991); B. Andraka and A. M. Tsvelik, *Phys. Rev. Lett.* **67**, 2886 (1991).
5. B. Andraka and G. R. Stewart, *Phys. Rev. B* **47**, 3208 (1993).
6. H. v. Löhneysen *et al.*, *Phys. Rev. Lett.* **72**, 3262 (1994).
7. K. Heuser, E.-W. Scheidt, T. Schreiner, and G. R. Stewart, *Phys. Rev. B* **57**, R4198 (1998); J. D. Thompson, R. D. Parks, and H. A. Borges, *J. Mag. Mag. Mat.* **54–57**, 377 (1986); P. Gegenwart et al, *Phys. Rev. Lett.* **82**, 1293 (1999); F. Steglich et al, *Physica B* **280**, 349 (2000).
8. See, *e.g.*, A. Schröder et al, *Phys. Rev. Lett.* **80**, 5623 (1998); P. Coleman, *Physica B* **259-261**, 353 (1998).
9. R. Jullien, J. Fields, and S. Doniach, *Phys. Rev. Lett.* **38**, 1500 (1977).
10. *Principles of Nuclear Magnetism*, A. Abragam, Oxford University Press, Oxford (1961); *Muon Spin Rotation Spectroscopy: Principles and Applications in Solid State Physics*, A. Schenck, A. Hilger, Bristol and Boston (1985).
11. D. E. MacLaughlin *et al.*, *J. Phys: Condens. Matter* **99**, S4479 (2004).
12. K. Ishida *et al.*, *Phys. Rev. B* **68**, 184401 (2003).
13. O. O. Bernal, D.E. MacLaughlin, H. G. Lukefahr, and B. Andraka, *Phys. Rev. Lett.* **75**, 2023 (1995).
14. D. E. MacLaughlin *et al.*, *Phys. Rev. B* **65**, 184401 (2002).
15. O. O. Bernal *et al.*, *Phys. Rev. B* **54**, 13000 (1996); D.E. MacLaughlin, O.O. Bernal, and H.G. Lukefahr, *J. Phys.: Cond. Matter* **8**, 9855 (1996); D. E. MacLaughlin et al, *Physica B* **230–232**, 606 (1997); D. E. MacLaughlin *et al.*, *Phys. Rev. B* **58**, R11849 (1998); O. O. Bernal, *Physica Status Solidi (b)* **220**, 335 (2000).
16. E. Miranda and V. Dobrosavljević, *Physica* **B259–261**, 359–61 (1999); E. Miranda, V. Dobrosavljević and G. Kotliar, *Phys. Rev. Lett.* **78**, 290 (1997).
17. R. B. Griffiths, *Phys. Rev. Lett.* **23**, 17 (1969).
18. A. H. Castro Neto, G. Castilla, and B. A. Jones, *Phys. Rev. Lett.* **81**, 3531 (1998).
19. M. C. de Andrade *Phys. Rev. Lett.* **81**, 5620 (1998).
20. D. E. MacLaughlin *et al.*, *Phys. Rev. Lett.* **87**, 066402 (2001).
21. A. Keren, P. Mendels, I. A. Campbell and J. Lord, *J. Phys. Rev. Lett.* **77**, 1386 (1996).
22. D. L. Cox, *Phys. Rev. Lett.* **59**, 1240 (1987); M. A. Continentino, *Z. fur Physik B* **101**, 197 (1996); A. J. Millis, *Phys. Rev. B* **48**, 7183 (1993); A. M. Tsvelik and M. Reizer, *Phys. Rev. B* **48**, 9887 (1993); S. Kambe *et al.*, *J. Phys. Soc. Japan* **65**, 3294 (1996).

COMPETITION BETWEEN SPIN GLASS AND ANTIFERROMAGNETIC PHASES IN HEAVY FERMION MATERIALS*

S. SÜLLOW

Institute for Physics of Condensed Matter,
Technical University of Braunschweig,
Mendelssohnstr. 3,
38106 Braunschweig, Germany
E-mail: s.suellow@tu-bs.de

For heavy fermion materials, moderate crystallographic disorder can induce new magnetic ground states such as spin glass phases. Here, I will review the experimental situation for one specific case, URh_2Ge_2. I will demonstrate that there is a competition between the spin glass phase and antiferromagnetism and discuss implications of this observation.

1. Introduction

In recent years, for heavy fermion compounds, an archetypical class of correlated electron systems, it has been demonstrated that already moderate levels (*viz.*, broken translational invariance for $\sim$ 10 % of all unit cells) of crystallographic disorder play a very dominant role regarding material properties. In general, there is consensus that for heavy fermions, which as result of competing energy scales are situated close to magnetic instabilities, electronic correlations and disorder effects are very much enhanced.[1,2] The view is that this is a consequence of the competing energy scales showing a very strong functional dependence on the local hybridization strength J. For instance, in the Doniach model these energy scales are associated to the Kondo effect, $k_B T_K \propto (N(E_F) \exp(-1/JN(E_F)))^{-1}$, and the RKKY exchange, $k_B T_{RKKY} \propto J^2 N(E_F)$ ($N(E_F)$: density of states at the Fermi level). Disorder leads to spatial variations of the hybridization strength, which locally translates into very large variations of the competing energy

*This work is supported by the Deutsche Forschungsgemeinschaft under grant no. SU229/1-3.

scales. Beyond such basic ideas, however, a detailed theoretical understanding of this sensitivity to disorder is lacking.

Phenomenologically, the dependence of the ground state properties of heavy fermion materials on crystallographic disorder can be captured in a phase diagram which incorporates both the dependence of the physical properties on the hybrdization strength and the level of disorder.[3] This phase diagram reflects two main concepts. On the one hand, within the Doniach model the magnetic phase diagram of crystallographically ordered heavy fermions is thought to be accessible by tuning the hybridization J between localized f and conduction electrons,[4] and which experimentally can be achieved by means of applied pressure.[5] On the other hand, the disorder can be modelled as a distribution of local hybridization values within a range ΔJ around the average value J, *i.e.*, the local hybridization lies in the interval $J \pm \Delta J$. This can lead to a situation in which spin glass phases compete with the other ground states of the Doniach model.

A schematic phase diagram visualizing this situation, and which summarizes the experimental situation as it is now, is sketched in Fig. 1. So far, about 40 different heavy fermion systems have been identified, for which disorder is known to affect the physical properties and for which the phase diagram in Fig. 1 bears relevance (for a review see Ref. 3). In the context discussed here, most importantly these experiments have revealed the existence of a distinct spin glass phase for moderate disorder levels. In contrast, while there is some theory indicating that under certain conditions spin glass phases may appear in disordered heavy fermion systems,[6,7] in these models *a priori* it is assumed that the disorder is sufficient to produce a spin glass state. It is far from clear if this is a reasonable assumption, given the actual disorder levels in heavy fermion spin glasses. Moreover, these models are inherently incapable to describe the relationship of spin glass and antiferromagnetic ground states, even though there are various fundamental questions regarding this topic, first of all if there is a gradual transition from spin glass to antiferromagnet or not.

Experimental investigations into this topic are hampered by sample quality and lack of control over actual disorder levels. Most materials reported on so far are polycrystalline, and metallurgical/structural investigations have usually not been carried out to fullest extent. However, there is one material, URh_2Ge_2, for which experiments do shed some light on the nature of the relationship of spin glass and antiferromagnet.[2,8,9]

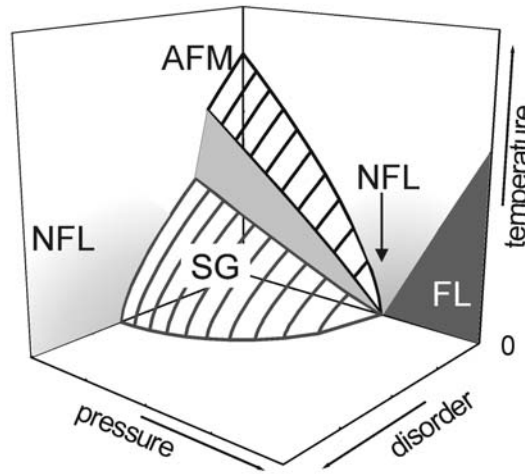

Fig. 1. Schematic phase diagrams of heavy fermions in the presence of competing interactions as function of the independent control parameters pressure = hybridization J and disorder = ΔJ, with the antiferromagnetically ordered (AFM), spin glass (SG) phases and Non-Fermi-Liquid (NFL) and Fermi Liquid (FL) regimes; for details see text.

2. Experimental review

URh_2Ge_2 is the first heavy fermion material, for which a spin glass ground state has been identified unambiguously. Evidence for the existence of a spin glass phase in as-grown single crystalline material stems from techniques such as dc-susceptibility (depicted in Fig. 2 for field cooled (FC) and zero field cooled (ZFC) measurement in a field of 50 G applied along a and c axes). Here, at a freezing temperature T_f of about 9 K a cusp in the susceptibility is observable, with prounounced magnetothermal hysteresis from the spin glass freezing below T_f. Additional evidence for a spin glass ground state comes from ac-susceptiblity, μSR studies, neutron scattering and specific heat.[5,10]

Single crystal x-ray diffraction experiments[11] indicate that URh_2Ge_2 crystallizes in the tetragonal $CaBe_2Ge_2$ structure (space group $P4/nmm$, Fig. 3), with room temperature lattice parameters of $a = 4.165$ Å and

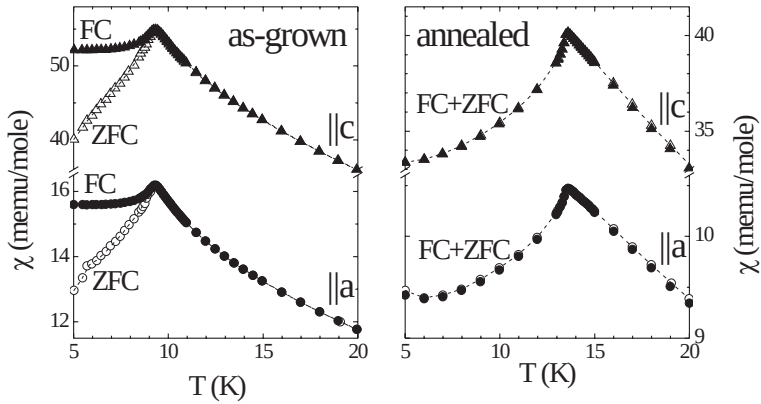

Fig. 2. Field cooled (FC) and zero field cooled (ZFC) dc susceptibility measurements in 50 G of as-grown and annealed URh_2Ge_2; for details see text.

$c = 9.792$ Å. As long as topological frustration does not play a role, for a spin glass to occur there must be crystallographic disorder in the structure. For URh_2Ge_2, combining XAFS data with the result of the single crystal diffraction study,[11–13] the disorder is identified as arising from about 10 % Rh/Ge site exchange. The U ions are translationally invariantly arranged, with layers of U atoms on a square lattice stacked along the c axis.

If single crystalline URh_2Ge_2 is annealed in order to reduce the level of disorder (in our case two subsequent heat treatments: 1 week at 900 °C + 2nd week at 1000 °C), we find that the spin glass ground state has been replaced by an antiferromagnetic one, which now occurs at a distinctly higher temperature $T_N = 13.4$ K (from the maximum in $d(\chi T)/dT$). This is illustrated in Fig. 2, where the dc-susceptibilty of annealed URh_2Ge_2 measured in 50 G is plotted. Similarily, if polycrystalline material is investigated, the magnetic ground state is either found to be a spin glass below $T_f \sim 9$ K or an antiferromagnet with $T_N \sim 13$ K.[14,15] Intermediate states like cluster glass phases with a finite correlation length and blocking temperatures between T_f and T_N are never observed.

Conversely, both in single crystal x-ray diffraction and XAFS a structural difference between as-grown and annealed material URh_2Ge_2, and

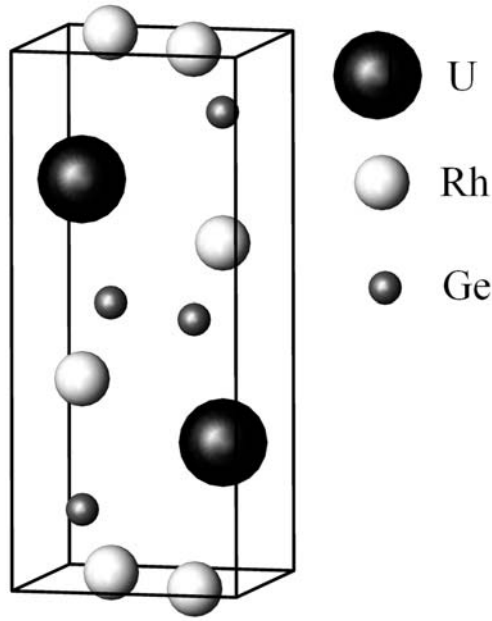

Fig. 3. The tetragonal crystal structure, space group *P4/nmm*, of URh_2Ge_2.

similarily in x-ray powder diffraction on polycrystalline samples URh_2Ge_2 with different magnetic ground states, cannot be resolved.[11,13–15] In these techniques spin glass and antiferromagnet material appear to be identical within experimental resolution (±5 % Rh/Ge site exchange).

3. Discussion

Our basic finding of a non-detectable structural difference for materials with distinctly different ground states suggest that the transition from spin glass to antiferromagnet is discontinous. Hence, we have a situation as sketched in Fig. 1, with a distinct phase boundary between spin glass and antiferromagnetism. Obviously, the question is why as function of disorder such a phase boundary should have to be crossed, or if an additional mechanism is required to drive the system from the one into the other state.

For an antiferromagnetic heavy fermion material, if only the disorder level is continuously increased, the expectation would be that the transition temperature will be continuously suppressed in a way as typically discussed

in Griffiths phase related scenarios.[16,17] As this is clearly not the case for URh_2Ge_2, instead we might hypothesize that the occurrence of spin glass phases for heavy fermion materials follows similar principles as for reentrant spin glass systems like $EuSr_{1-x}S_x$.[18,19] The argument would be that for the U ions on the square lattice in the tetragonal $a-b$ plane there are competing interactions between nearest (NN) and next nearest neighbors (NNN) (for instance a ferromagnetic NN interaction J_1 vs. an antiferromagnetic NNN coupling J_2). The level of Rh/Ge site exchange would balance the ratio J_1/J_2, this way controlling the behavior of the U ions on the square lattice. The magnetic state of the bulk material is either a spin glass (if frustration and disorder leads to a frozen-in state within the tetragonal plane) or an antiferromagnetic one (because of the antiferromagnetic coupling along the tetragonal c axis of ferromagnetically coupled planes).

Unfortunately, there are problems with this hypothesis. The model still would predict states with transition and freezing temperatures intermediate to the ones experimentally observed. In fact, we even should find a multicritical point. Experimentally, coexistence of spin glass and antiferromagnet has been observed for some samples URh_2Ge_2,[14] but only of a spin glass phase below $T_f \sim 9$ K and an antiferromagnetic one below $T_N \sim 13$ K. This seems to indicate rather a coexistence of spin glass and antiferromagnetic phase in spatially separated areas.

Moreover, our hypothesis brings with it a topological aspect to the occurence of a spin glass phase in heavy fermion materials. The theory of reentrant spin glasses considers materials with dominant short range magnetic interactions. The occurence of spin glass phases is the result of special topologies, where magnetic exchange along different paths results in competing magnetic interactions. Considering the — compared to ordinary magnetic metals — large number of heavy fermion spin glasses, it appears unreasonable to assume that only for the heavy fermion systems such fairly restrictive conditions are met.

In consequence, it appears that for heavy fermion systems additional mechanisms need to be taken into consideration for an explanation of the spin glass behavior. One line of argumentation might be as follows. If the disorder causes sufficiently large variations of the competing energy scales, it might result in a situation where in some areas of the material the energy scale tending to suppress magnetic moments (the Kondo effect) wins, in other areas the one promoting magnetic order (RKKY exchange).

With this in mind, if we take a heavy fermion antiferromagnet like URh_2Ge_2 and introduce some disorder, initially we will just suppress the

transition temperature somewhat. But if we increase the disorder to a degree that locally there are regions in the material where the f magnetic moments are fully suppressed (*viz.*, if holes are generated on the magnetic lattice), a qualitatively new situation appears, as this corresponds to a dilution of the system. Hence, in a system like URh_2Ge_2, if we start with a perfectly ordered material and introduce some Rh/Ge site exchange, initially we deal with a random bond problem, with the U ions placed on a regular lattice. As soon as with the disorder locally magnetic moments are fully screened, the problem starts to become a random site problem. We might speculate that the transition from a random bond to a random site problem possibly is related to the transition from an antiferromagnet to a spin glass. Ultimately, this transition would be a consequence of the correlated state of heavy fermions, or in other words the effect of disorder on the competing energy scales. In a more general context, it would imply that these correlated electron materials would represent model substances for the transition from the random bond to the random site disorder problem.

Acknowledgments

I would like to acknowledge the various contributions made to the experimental work presented here by C. H. Booth, W. J. L. Buyers, R. Feyerherm, S. W. Han, I. Maksimov, T. E. Mason, A. A. Menovsky, S. A. M. Mentink, J. A. Mydosh, G. J. Nieuwenhuys, A. Otop, and D. Tomuta. Further, fruitful discussions with W. Brenig, A. H. Castro Neto and E. Miranda are gratefully acknowledged.

References

1. K. I. Wysokinski, *Phys. Rev. B* **60**, 16376 (1999).
2. S. Süllow, M. B. Maple, R. Chau, D. Tomuta, G. J. Nieuwenhuys, A. A. Menovsky, and J. A. Mydosh, *J. Magn. Magn. Mat.* **226-230**, 35 (2001).
3. A. Otop, S. Süllow, M. B. Maple, A. Weber, E. -W. Scheidt, T. J. Gortenmulder, and J. A. Mydosh, *Phys. Rev. B* **72**, 024457 (2005).
4. S. Doniach, in *Valence Instabilities and Related Narrow Band Phenomena*, edited by R. D. Parks (Plenum, New York, 1977), p. 169; *Physica B* **91**, 231 (1977).
5. S. Süllow, M. C. Aronson, B. D. Rainford, and P. Haen, *Phys. Rev. Lett.* **82**, 2963 (1999).
6. A. Theumann, B. Coqblin, S. G. Magalhaes, and A. A. Schmidt, *Phys. Rev. B* **63**, 054409 (2001).
7. M. Kiselev, K. Kikoin, and R. Oppermann, *Phys. Rev. B* **65**, 184410 (2002).
8. S. Süllow, G. J. Nieuwenhuys, A. A. Menovsky, J. A. Mydosh,

S. A. M. Mentink, T. E. Mason, and W. J. L. Buyers, *Phys. Rev. Lett.* **78**, 354 (1997).
9. S. Süllow, S. A. M. Mentink, T. E. Mason, R. Feyerherm, G. J. Nieuwenhuys, A. A. Menovsky, and J. A. Mydosh, *Phys. Rev. B* **61**, 8878 (2000).
10. G. J. Nieuwenhuys, S. Süllow, A. A. Menovsky, J. A. Mydosh, R. H. Heffner, L. P. Le, D. E. MacLaughlin, O. O. Bernal, and A. Schenck, *J. Magn. Magn. Mat.* **177-181**, 803 (1998).
11. R. Feyerherm, private communication (2003).
12. C. H. Booth, S. W. Han, S. Süllow, and J. A. Mydosh, *J. Magn. Magn. Mat.* **272-276**, 941 (2004).
13. C. H. Booth, private communication (2004).
14. S. Süllow, I. Maksimov, F. J. Litterst, and J. A. Mydosh, *Acta. Phys. Pol. B* **34**, 1153 (2003).
15. A. Otop, I. Maksimov, F. J. Litterst, J. A. Mydosh, and S. Süllow, *J. Magn. Magn. Mat.* **272-276**, E1019 (2004).
16. R. B. Griffiths, *Phys. Rev. Lett.* **23**, 17 (1969).
17. A. H. Castro Neto, G. Castilla, and B. A. Jones, *Phys. Rev. Lett.* **81**, 3531 (1998).
18. K. Binder, W. Kinzel, and D. Stauffer, *Z. Physik B* **36**, 161 (1979).
19. K. Binder and A. P. Young, *Rev. Mod. Phys.* **58**, 801 (1986).

EMERGENT PHASES VIA FERMI SURFACE RECONSTRUCTION NEAR THE METAMAGNETIC QUANTUM CRITICAL POINT IN $U(Ru_{1-x}Rh_x)_2Si_2$

K. H. KIM and Y. S. OH*

CSCMR & FPRD, School of Physics and Astronomy, Seoul National University, Seoul 151-747, S. Korea
E-mail: khkim@phya.snu.ac.kr

N. HARRISON, P. A. SHARMA, and M. JAIME

NHMFL, Los Alamos National Laboratory, MS E536, Los Alamos, NM 87545, USA

H. AMITSUKA

Graduate School of Science, Hokkaido University, N10W8 Sapporo 060-0810,Japan

J. A. MYDOSH

Institute of Physics II, University of Cologne, 50937 Cologne, Germany

The intricate relationship between quantum criticality and phase formation in correlated materials is one of challenging issues to be understood in current condensed matter physics. Herein, we summarize our recent findings in the heavy fermion compounds $U(Ru_{1-x}Rh_x)_2Si_2$ (x=0, 2, 2.5, 3, and 4 %) that can enlighten our understanding on the open issue. Careful electrical transport and thermodynamic measurements in the high magnetic field B region up to 45 tesla uncover the formation of multiple phases via avoiding the quasiparticle divergence near their putative metamagnetic quantum critical points (QCPs) at low temperature (T) region. From the established B vs. T phase diagram in the series of samples, we find a clear link between the B-dependence of the phases and that of the putative QCP. This observation constitutes an archetypal case that the field-tuned metamagnetic quantum criticality is intimately related to the formation of the thermodynamic phases. In addition, using the Hall effect studies in the x=0 and 4 % samples, we find discontinuous changes of the Hall coefficient at the phase boundaries between the field-induced phases

*Work partially supported by KOSEF through CSCMR and Seoul R&BD.

and neighboring Fermi liquid states, indicating the Fermi surface is sharply reconstructed in the phase formation process near the putative QCP.

1. Introduction

A quantum critical point (QCP) and related quantum fluctuations induced by pressure or dopant concentration have been proposed as the origin of quasiparticle pairing to form unconventional superconductivity in correlated electron systems.[1] In addition, quasiparticle instabilities such as effective mass divergence or equivalently a vanishing Fermi energy, often observed in close proximity to the QCP, can cause the metallic ground state to become unstable against the formation of novel low temperature orders. However, clear experimental data supporting the latter case are still lacking, and proof of phase formation via avoiding a quasiparticle instability itself remains a formidable experimental challenge.

Of the many strongly correlated intermetallic compounds, URu_2Si_2 has been a subject of continuing interest for more than twenty years.[2] The so-called "hidden order" (HO) transition at 17.5 K and the coexisting unconventional superconductivity below 1.5 K are unresolved in their nature. It was recently found that when the HO is suppressed under very high B of ∼35 T, complex multiple phases are formed with the concomitant signatures of quantum criticality at B_{QCP} ∼38 T.[3–5] This observation, in turn, suggests that URu_2Si_2 can be a new model system in which the QCP is involved in the creation of some (or all) of the field-induced multiple phases. However, the complexity of the phase diagram near the suppression field of the HO and B_{QCP} makes all attempts to understand correlations between the QCP and the phase formation quite difficult. In contrast, the dilute substitution of Rh in place of Ru, so as to yield $U(Ru_{1-x}Rh_x)_2Si_2$, is known to provide another effective way of suppressing the HO via tuning of the c/a ratio.[6] Thus, the diluted system can provide a unique opportunity to study quantum criticality at high magnetic fields in the absence of the HO.[6,7]

In this report, we summarize our systematic magnetoresistance, thermodynamic, and Hall effect measurements to establish the phase diagram in $U(Ru_{1-x}Rh_x)_2Si_2$ ($x = 0$, 2, 2.5, 3 and 4 %), and to provide compelling evidence of a nexus between multiple phases and metamagnetic quantum criticality, thereby avoiding quasiparticle instabilities. Furthermore, Hall effect measurements reveal discontinuous changes of the Hall coefficient at the phase boundaries, supporting the existence of drastic Fermi surface reconstruction in the phase formation process near the putative quantum

critical point.

2. Experimentals

Single crystals of $U(Ru_{1-x}Rh_x)_2Si_2$ of composition $x = 0$, 2, 2.5, 3 and 4 %, were grown using the Czochralski method .[6] Magnetization measurements were performed using a mid-pulse magnet,[4] while resistivity measurements were carried on in the 45 T hybrid magnet at Tallahassee as well as in the mid-pulse magnet at Los Alamos.[5,7] The specific heat measurements were also performed in the hybrid magnet using a Si-based plastic calorimeter and a standard relaxation method.[8] For the Hall experiments, samples were cut into a standard Hall geometry with 6-wire contacts in the tetragonal *ab* plane.[9] Two phase sensitive ac lock-in amplifiers were used to simultaneously measure the longitudinal and transverse voltage signals under a pulsed magnetic field B with $\sim$ 100 ms duration. Transverse voltages taken at a positive B were subtracted from those at a negative B at the same temperature to get the Hall resistivity. The consistency between phase boundaries determined both in the mid-pulse magnet and in the hybrid magnet,[7] prove that isothermal conditions are achieved in the pulse magnet experiment. In all the measurements, B was applied along the c-axis, the magnetic easy axis of samples.

3. Results and discussion

3.1. *Construction of phase diagram*

Figure 1 (left panel) reveals the high field phase diagram and evidences of quantum criticality in $U(Ru_{1-x}Rh_x)_2Si_2$ (from $x = 0$ to 4 %) as determined from extremities in $\partial\rho/\partial B$ ($\partial\rho/\partial T$) as well as magnetization steps. The specific heat studies also confirmed the phase boundaries for both $x = 0$[3] and 4 %.[3,8] For $x = 0$ %, while the dominant HO phase is destroyed around 35.2 T, a new phase III has been found.[4] In addition, phase II and phase V were identified as rather weak features.[5] With increasing x, the region occupied by phase II expanded while the HO phase as well as phase III & V are suppressed. Once $x = 4$ %, all signatures of the HO phase have vanished at low magnetic fields, leaving the system in a heavy-Fermi-liquid (HFL) ground state. Then, at high magnetic fields, only 'phase II' is stabilized between $\sim$ 26 and 38 T. The magnetic field that optimizes/maximizes the transition temperature of phase II, defined as $B_{\rm II}$, can be used to characterize the relevant field scale for the phase formation. In addition, the metamagnetic transition field $B_{\rm M}$ can be estimated by extrapolating the local maxima of

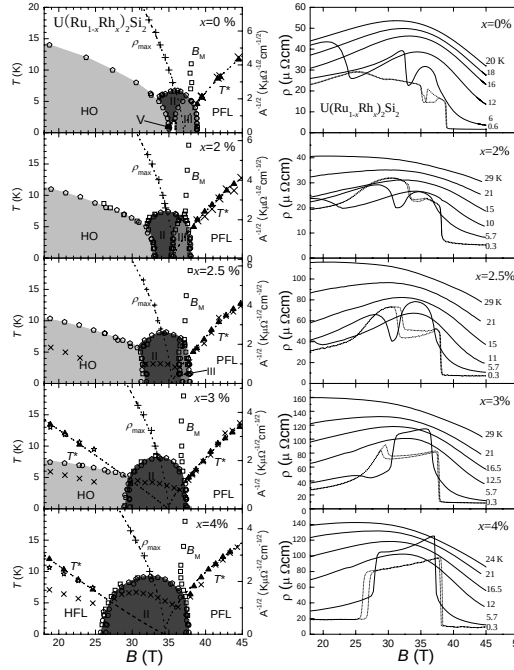

Fig. 1. (Left panel) B vs. T phase diagram of $U(Ru_{1-x}Ru_x)_2Si_2$ for compositions $x = 0$, 2, 2.5, 3 and 4 %, in which the ordered phases are shaded for clarity. Open squares correspond to maxima in χ, open circles (pentagons) correspond to sharp extremities in $\partial\rho/\partial B$ ($\partial\rho/\partial T$). '+' symbols delineate the T and B coordinate of the maxima $\rho_{\max}$ in the magnetoresistivity, while solid triangles delineate the crossover temperature T^* from low temperature T^2 resistivity behaviour to high temperature sub-linear behaviour. Dotted lines correspond to fits to the function $T(B) \propto |B - B_{\rm QCP}|^{\alpha}$, as described in the text. '×' symbols represent $A^{-1/2}$ plotted using the right-hand axes, while '⋆' symbols represent the same data re-scaled for $B < B_{\rm QCP}$ as described in the text. 'PFL' and 'HFL' refer to a polarized-Fermi-liquid and a heavy-Fermi-liquid-state, respectively. (Right panel) ρ vs. B data close to the QCP at selected temperatures. All the compounds exhibit magnetoresistivity maxima $\rho_{\max}$, which extrapolates to the putative $B_{\rm QCP}$ in the left panel. ρ vs. B data at the lowest temperatures (dotted lines) are drawn for both increasing and decreasing B, while data for decreasing B are shown at the other temperatures. Extremities in $\partial\rho/\partial B$ were used to determine phase boundaries in the left panel.

χ at high temperatures .[4]

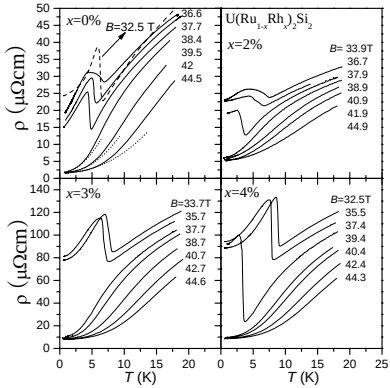

Fig. 2. ρ vs. T data of $U(Ru_{1-x}Rh_x)_2Si_2$ at selected magnetic fields for warming. For x=0 %, ρ vs. T data at 32.5 T (dotted line) show the increase of resistivity at low temperature, due to stabilization of hidden order (HO), while for $x = 3$ and 4 %, the increase in ρ is due to the stabilization of phase II. All the compounds exhibit a normal Fermi liquid behavior at high field regions above $B_{\rm QCP}$. This is illustrated in the high field data of x=0 %, in which the T^2 fitting (dotted lines) is performed at low temperatures.

3.2. *Evidences of quantum criticality*

Quantum criticality for all the compounds is evidenced as (1) the emergence of a broad maximum $\rho_{\rm max}$ in the magnetoresistivity, as shown in Fig. 1 (right panel) [5,10] and (2) the collapse of the effective Fermi energy $\varepsilon_{\rm F}$, which can be inferred from both the exponent n and the prefactor A of ρ on fitting its temperature dependence to $\rho(T) = \rho_0 + AT^n$. As shown in Fig. 2, all the compounds exhibit normal Fermi liquid behaviour above $B_{\rm QCP}$ in which $\rho = \rho_0 + AT^n$ with $n \approx 2$. As T is increased, n crosses over from a value of $n \gtrapprox 2$ to $n \leq 1$ at a characteristic temperature T^* (solid triangles), which can be extracted from the maximum position of $\partial\rho/\partial T$.

This crossover is observed at fields both above and below $B_{\rm QCP}$ for $x \geq 3$ and 4 % owing to the weakening of the HO phase. Fitting the $[T_{\rho\ \rm max}, B]$ and [T^*,B] loci to functions of the form $T_{\rho\ \rm max}$ or $T^* \propto |B - B_{\rm QCP}|^\alpha$, have provided different exponents α but a common value of $B_{\rm QCP}$. This is suggestive of a single QCP hidden beneath phases II and/or III at all concentrations $0 \leq x \leq 4$ %.

It was previously found that all the compounds show the saturation of magnetization of about $\approx 1.5\mu_B$/U above $B_{\rm QCP}$,[4,7] being characterized as a spin-polarized-Fermi-liquid (PFL) state. Therefore, the putative QCP uncovered in $U(Ru_{1-x}Rh_x)_2Si_2$ (from $x = 0$ to 4 %) is expected to separate

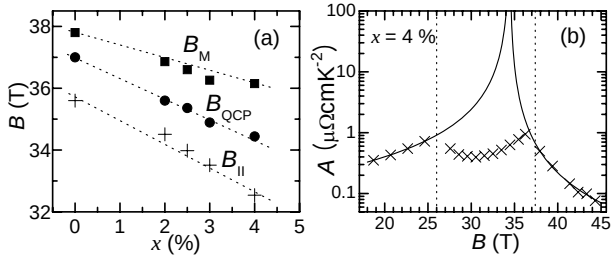

Fig. 3. (a) Plot of A versus B for $x = 4$ %, with fits to the function $A \propto |B - B_{\rm QCP}|^{\alpha}$ in the regions outside phase II, which is enclosed between dotted lines. (b) Comparison of the trends in $B_{\rm II}$, $B_{\rm QCP}$ and $B_{\rm M}$ as x is varied.

a region between a HFL at low B and a PFL state at high B region. A general scaling proportionality, $T^* \propto A^{-1/2} \propto \varepsilon_{\rm F}$, is shown to apply for both HFL and PFL regions as shown in Fig. 1.

3.3. *Nexus between phase formation and quantum critical point via avoiding quasiparticle instability*

In Fig. 3(a), we show that $B_{\rm QCP}$, $B_{\rm M}$ and $B_{\rm II}$ move together as x is varied, with the difference in field of a few percent between them being approximately independent of x. Because $B_{\rm II}$ represents a center of the region where phases are stabilized, the present correlation among $B_{\rm QCP}$, $B_{\rm M}$ and $B_{\rm II}$ directly proves the link between a metamagnetic QCP and phase boundaries.

As shown in Fig. 3(b), the A parameter, estimated outside phase II, systematically increases and becomes divergent on approaching $B_{\rm QCP}$ for x=4 %. This is equivalent to a singularity of the electronic density of states $g(\varepsilon_{\rm F}) \approx 2/3\varepsilon_{\rm F}$ per electron at the Fermi energy. ($A^{-1/2} \propto \varepsilon_{\rm F}$ for a Fermi liquid) Thus, $\varepsilon_{\rm F}$ is extrapolated to become zero at $B_{\rm QCP}$ in Fig. 1. We note that a singularity in $g(\varepsilon_{\rm F})$ is avoided inside phase II for x=3 and 4 % because the divergence of A at $B_{\rm QCP}$ is quenched inside phase II. This observation suggests a scenario in which the formation of phases lowers the total energy of the system by avoiding the QCP and the resultant quasiparticle instability by opening a partial gap at $\varepsilon_{\rm F}$.[10] This scenario in turn provides a natural mechanism for the link in the locations of the phases and the QCP.

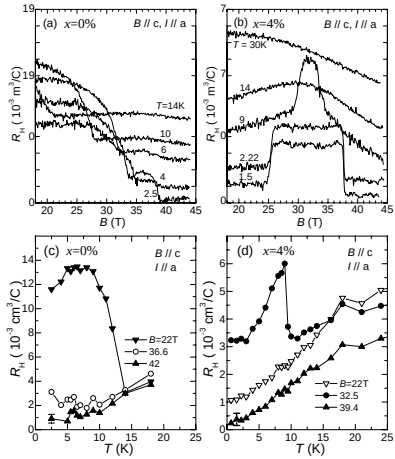

Fig. 4. B-dependent $R_{\rm H}$ of Rh (a) x=0 % and (b) 4 % doped sample. T-dependent $R_{\rm H}$ of Rh (c) x=0 % and (d) 4 % doped samples at selected B in each phase region.

3.4. *Discontinuous Hall coefficient changes*

B and T-dependent Hall coefficients, $R_{\rm H} = \rho_{xy}/B$ are displayed in Fig. 4 for Rh x=0 % and 4 % samples. Almost constant but clearly different values of $R_{\rm H}$ are observed in each region of Fermi-liquid states in both samples. Due to the inertness of $R_{\rm H}$ with B, this observation immediately suggests that $R_{\rm H}$ at low temperatures mainly includes the orbital contribution, and thus directly reflects the existence of different Fermi surface volume in each phase region of both compounds. When a spherical one band Fermi surface is assumed, for the undoped sample, the effective carrier density $n_{\rm Hall} \equiv -1/R_{\rm H}e{=}\sim 0.03$/U inside the HO state has sharply changed into $n_{\rm Hall}$ of ~ 0.15/U inside phase II, and an abrupt increase up to $n_{\rm Hall}$ of $\sim 1 \pm 0.5$/U in the PFL region. Even for the x=4 % sample, $n_{\rm Hall}$ of ~ 0.15/U inside phase II shows a sharp increase up to $n_{\rm Hall}$ of $\sim 1 \pm 0.5$/U in the PFL region. It is quite noteworthy that for both compounds, the jump in $n_{\rm Hall}$ is comparable to ~ 1 electron/U in the PFL state. Thus, this observation strongly supports that a significant reconstruction of the Fermi surface has occurred to result in a jump in the carrier density while the system abandoning the HO and phase II or III to reach the PFL region ($B > B_{\rm QCP}$). Furthermore, the abrupt change of $R_{\rm H}$ suggests that the transitions into or out of phase II and III are discontinuous as consistent with the first order nature of transitions at the phase boundary.

4. Summary

The present results show that the field-tuned quantum criticality in $U(Ru_{1-x}Rh_x)_2Si_2$ plays an important role in the creation of novel field-induced phases. Furthermore, the Hall coefficient behaviors provide a convincing evidence of Fermi surface reconstruction to result in the Fermi surface volume changes in the phase formation process near the metamagnetic quantum critical point.

This work is performed under the auspices of the National Research Laboratory program by the Korean Ministry of Science and Technology, the KRF (KRF-2005-070-C00044), the US National Science Foundation, the US Department of Energy, Florida State, and the Dutch Foundation FOM.

References

1. R. B. Laughlin *et al.*, *Adv. Phys.* **50**, 361 (2001). ; S. Sachdev, *Science* **288**, 475 (2000); H. Löhneysen, J. Magn. Magn. Mat. **200**, 532 (1999).
2. T. T. M. Palstra *et al.*, *Phys. Rev. Lett.* **55**, 2727 (1985).
3. M. Jaime *et al.*, *Phys. Rev. Lett.* **89**, 287201 (2002).
4. N. Harrison, M. Jaime and J. A. Mydosh, *Phys. Rev. Lett.* **90**, 096402 (2003).
5. K. H. Kim *et al.*. *Phys. Rev. Lett.* **91**, 256401 (2003).
6. M. Yokoyama *et al.*, *J. Phys. Soc. Jpn.* **73**, 545 (2004).
7. K. H. Kim *et al.*, *Phys. Rev. Lett.* **93**, 206402 (2004).
8. A. V. Silhanek *et al.*, *Phys. Rev. Lett.* **95**, 026403 (2006).
9. Y. S. Oh *et al.*, *Physica B* (in press); *ibid*, to be published.
10. S. A. Grigera *et al.*, *Science* **294**, 329 (2001).

CONTINUOUS EVOLUTION OF THE FERMI SURFACE OF $CeRu_2Si_2$ ACROSS THE METAMAGNETIC TRANSITION

R. DAOU*

Department de Physique, Université de Sherbrooke, Sherbrooke, Quebec J1K 2R1, Canada
** E-mail: rdaou@physique.usherb.ca*

C. BERGEMANN

Shoenberg Laboratory for Quantum Matter, Cavendish Laboratory, Dept. Physics, University of Cambridge, JJ Thomson Avenue, Cambridge CB3 0HE, UK

S. R. JULIAN

Department of Physics, University of Toronto, 60 St George St, Toronto M5S 1A7, Canada

New magnetotransport measurements of the heavy fermion compound $CeRu_2Si_2$ suggest that the metamagnetic transition (MMT) that occurs in an applied magnetic field of 7.8 T is continuous down to <10 mK. We propose a new model of the MMT that does not involve localization of the f-electron and the discontinuities in transport properties that such localization would imply.

Keywords: $CeRu_2Si_2$; metamagnetism; heavy fermions; electronic topological transition

1. Introduction

The heavy fermion compound $CeRu_2Si_2$ displays a metamagnetic transition (MMT) when a field of $7.8/\cos\theta$ T is applied, where θ is the angle between the applied field and the c-axis.[1] The magnetisation increases roughly linearly until close to the MMT field, where it is rapidly enhanced before flattening out somewhat.[2] The electronic specific heat[3] is enhanced from its zero field value of 350 $\mathrm{mJ \cdot mol^{-1} \cdot K^{-2}}$ to 500 $\mathrm{mJ \cdot mol^{-1} \cdot K^{-2}}$ at the MMT field, after which it falls to about 100 $\mathrm{mJ \cdot mol^{-1} \cdot K^{-2}}$ at 16 T. There is also a large magnetostriction effect where the volume of the sam-

ple changes by about 0.1 % when crossing the MMT. The structure remains the same, however.

The proximity of this material to the quantum critical point between antiferromagnetic and Fermi liquid states (as observed in the isoelectronic compound $CeRu_2Ge_2$[4]) has led to the suggestion that the MMT is a transition from a state where the Ce *f*-electron is itinerant at low field to a state where it is localized at high field.

The volume of the reciprocal lattice enclosed by the *f*-localized and *f*-itinerant Fermi surfaces must differ by an amount equivalent to one electron. The topologies of the calculated Fermi surfaces are also considerably different, depending on whether the *f*-electron is included or not.[5,6]

This scenario presents a number of problems, including that of the 'missing mass'. Only 20 % of the specific heat in the high field state can be accounted for using the localized *f*-electron bandstructure calculations and de Haas-van Alphen measurements of the quasiparticle masses.[7] The question arises of how *f*-localization can take place. All transport and thermodynamic properties of $CeRu_2Si_2$ measured as a function of magnetic field at low temperature suggest that the MMT is a continuous, crossover transition. Localization of an *f*-electron would imply, however, a sudden change in the volume and topology of the Fermi surface, which should be manifest as discontinuities in the transport properties.

2. Experiment

We set out to extend the range of the magnetic field and temperature dependent data on electrical transport, in order to see if any discontinuities had escaped previous observation.[8] The sample used was grown by F. S. Tautz in Cambridge and had a residual resistivity of 0.4 $\mu \cdot \Omega \cdot$ cm. The magnetoresistance and Hall effect were measured at $<$10 m·K, in magnetic fields of up to 16 T. From a simplistic point of view, the Hall effect measures the number of electrical carriers. A sudden change in the number of carriers (as implied by a change in the volume of the FS) should lead to a discontinuity in the Hall effect. The results of this experiment are shown in Fig. 1a.

3. Interpretation

The lack of any discontinuities in the magneto-transport suggested that some kind of continuous mechanism was responsible for the MMT in $CeRu_2Si_2$. Some features in the magnetoresistance and Hall effect remained that required explanation. One simple model that we proposed[9]

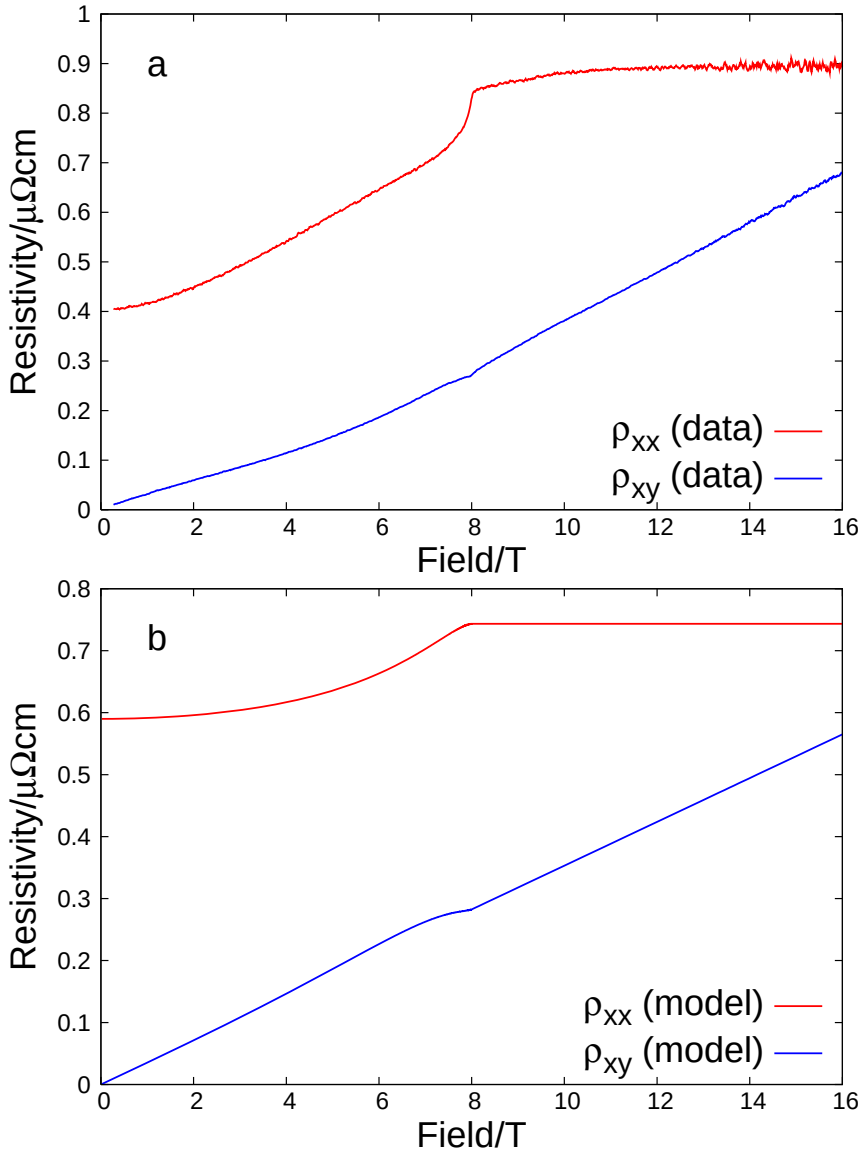

Fig. 1. a) Magnetoresistance and Hall effect in $CeRu_2Si_2$ at <10 mK. $j \parallel ab$, $B \parallel c$. b) Calculated orbital resistivity at $T = 0$ from splitting of spherical FS model.

was the large, non-linear spin-splitting of the heavy quasiparticle sheet of the Fermi surface. In the low field state this sheet carries quasiparticles with a large proportion of *f*-character, and their mass is strongly renormalised to $>100\,m_e$. This sheet is relatively large and the size and angular dependence of orbits observed by de Haas-van Alphen agree with the calculated size and shape of the sheet.

Our new model proposes that this sheet is split into two spin-subbands by the applied magnetic field, and that the splitting is complete by the MMT field of 7.8 T, as is shown schematically in Fig. 2. At this field the minority spin-subband shrinks to a point and vanishes. The total volume of the Fermi surface is conserved, however, since the volume of the majority subband increases to compensate. At higher fields, there is no further change in the volume of the sheet. Figure 1b shows the results of a simple calculation using a single-band, spherical Fermi surface that is spin-split continuously in this way. The only free parameter in this model is the mean free path—the size of the sphere used is the same as that of the observed heavy sheet, the dispersion relation is assumed to be free-electron-like and the splitting is taken to be proportional to the applied field.

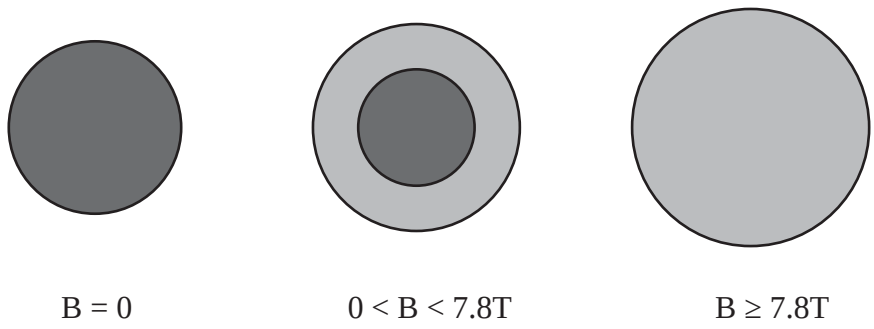

Fig. 2. Model of MMT in $CeRu_2Si_2$. One spin-surface of one sheet of the Fermi surface expands while the other contracts. The total volume is conserved. Full spin-splitting is acheived by the MMT field of 7.8 T, thereafter no further change occurs.

The agreement with the data is remarkable, given the simplicity of the model used. The 'kinks' at the MMT field have the correct sense and the saturation of the magnetoresistance and the linearity of the Hall resistivity above the MMT are reproduced qualitatively.

4. Consequences of the model

The first consequence of the model is that the Fermi surface cannot change much in high fields. The Fermi level must lie in the hybridisation gap of the heavy fermion band. If it passes through, we would expect a new sheet of the Fermi surface to form and this would affect the transport in a way that cannot be reconciled with the data.

The specific heat requires more interpretation than the transport if it is to fit in this scenario. The specific heat is in general proportional to the density of electronic states at the Fermi surface; the density of states approaching a band edge in three dimensions follows $N(\varepsilon) \sim (\varepsilon_F - \varepsilon_c)^{1/2}$. Since the density of states of this simple model falls continuously, it cannot straightforwardly account for the peak observed in the specific heat. The theory of electronic topological transitions (ETT), of which the case of a Fermi surface sheet shrinking to a point is an example, indicates that close to the transition thermodynamic fluctuations make a significant contribution to the specific heat.[10] These fluctuations take the form $\sim T/(\varepsilon_F - \varepsilon_c)^{1/2}$, which is similar to the behaviour of the obvserved low temperature specific heat. The implied divergence at the ETT itself ($\varepsilon_F = \varepsilon_c$) is only achieved in the limit of zero temperature and in the absence of impurities. Otherwise a finite value of the fluctuation contribution at the ETT is predicted.

The magnetisation is less problematic. The simple model predicts a linear rise in the magnetisation before saturation after 8 T. What is observed is a narrower rise that occurs in over about a 1 T range near 8 T, with a tendency towards saturation. This can be accounted for by the effect of magnetostriction, which is unaccounted for in the model. The difference between constant volume and constant pressure susceptibilities has been investigated[2] and shows that the constant pressure curve is narrower by a factor of ten. The model assumes a constant volume for the material, while the experiments are performed at constant pressure. The large magnetostriction that accompanies the MMT therefore could have the effect of narrowing the transition considerably. The incomplete saturation above 8 T is likely then a consequence of the multi-band nature of the real material. Further polarisation can take place on the other sheets of the Fermi surface in higher fields.

The new model also requires a slight reinterpretation of de Haas-van Alphen (dHvA) data. DHvA measures the extremal cross-sectional area perpendicular to an applied magnetic field and the quasiparticle masses of the various sheets of the Fermi surface. Previously, the observation of a large orbit in the high field state suggested that the localized *f*-electron

bandstructure calculation was more appropriate.[11,12] A similar sized orbit also exists in the itinerant *f*-electron calculation, however, although it is only observed in the low field state when applied hydrostatic pressure moves the MMT up to higher fields which are more favourable to dHvA observations.[6] Thus if the itinerant *f*-electron picture is appropriate both above and below the transition, then every observed dHvA orbit can be accounted for equally well.

This has the further consequence of providing an explanation for the 'missing mass' problem. The measured specific heat coefficient should match that calculated from the product of the calculated density of states and the quasiparticle masses observed by dHvA. If the localized *f*-electron Fermi surface is used as the model, then no more than 20 % of the measured specific heat coefficient can be accounted for, and there are no unobserved Fermi surface sheets which might account for the rest. If on the other hand the itinerant *f*-electron calculation is used, up to 60 % of the specific heat can be accounted for using observed sheets, while the large fully spin-polarised surface remains unobserved. This provides a possible location where the remaining 'missing mass' may be found, but it may prove difficult to observe this sheet directly since it is both large and the quasiparticles on it are expected to be strongly renormalised, which makes observation by dHvA difficult.

5. The electronic topological transition

The ETT is not a phase transition in the usual sense. It was categorised by Lifshitz as an order 2.5 phase transition at $T = 0$, meaning that the second derivatives of the free energy have small discontinuities, while the third derivatives tend to infinity.[10] The fluctuations associated with the ETT are only divergent at zero temperature. It has the character of a crossover for $T > 0$. These characteristics are reminiscent of the behaviour of a system near a quantum critical point.

This behaviour can be compared to the case of $Sr_3Ru_2O_7$, which also exhibits a metamagnetic transition in similar applied fields. In this case a finite temperature critical point can be tuned to zero temperature by rotation of the sample with respect to the field, but the difference between the low- and high-field states has not been established unequivocally.[13] A new phase bounded by first order transitions is found in the vicinity of the quantum critical point.

6. Summary

We have proposed that the metamagnetic transition in $CeRu_2Si_2$ is an electronic topological transition, in which a spin-subband of the Fermi surface vanishes continuously. This provides an explanation for the continuous nature of the MMT and can be reconciled with previous data. The relationship to other metamagnets such as $Sr_3Ru_2O_7$ remains unclear.

References

1. J. Flouquet *et al. Physica (Amsterdam)* **319B**, 251 (2002).
2. See *e.g.* J. Flouquet *et al. Physica B* **215**, 77 (1995) and references therein.
3. H. P. van der Meulen *et al. Phys. Rev. B* **44**, 814 (1991).
4. S. Sullow *et al. Phys. Rev. Lett.* **82**, 2963 (1999).
5. H. Yamagami and A. Hasegawa *J. Phys. Soc. Jpn* **62**, 592 (1993).
6. H. Aoki *et al. J. Phys. Soc. Jpn* **70**, 774 (2001).
7. F. S. Tautz, Ph.D. thesis, University of Cambridge (UK, 1994).
8. S. Kambe *et al. Solid State Comm.* **95**, 449 and **96**, 175 (1995).
9. R. Daou, C. Bergemann and S. R. Julian *Phys. Rev. Lett.* **96**, 026401 (2001).
10. Ya. M. Blanter *et al. Phys. Rep.* **245**, 159 (1994).
11. H. Aoki *et al. J. Phys. Soc. Jpn* **62**, 3157 (1993).
12. M. Takashita *et al. J. Phys. Soc. Jpn* **65**, 515 (1996).
13. S. A. Grigera *et al. Science* **306**, 5699 (2004).

PHASE TRANSITION BETWEEN THE ITINERANT AND THE LOCALIZED f-ELECTRON STATES IN HEAVY FERMION ANTIFERROMAGNET $Ce(Ru_{0.9}Rh_{0.1})_2(Si_{1-y}Ge_y)_2$

Y. TABATA*, C. KANADANI, R. YAMAKI, T. TANIGUCHI and S. KAWARAZAKI

Graduate School of Science, Osaka University,
Toyonaka, Osaka 560-0043, Japan
**E-mail: yang@ltfridge.ess.sci.osaka-u.ac.jp*

We have presented recent results of neutron scattering experiments for the pseudo-binary alloy system $Ce(Ru_{0.9}Rh_{0.1})_2(Si_{1-y}Ge_y)_2$. The base material $Ce(Ru_{0.9}Rh_{0.1})_2Si_2$ is an itinerant antiferromagnetic(AFM) heavy fermion. By substituting Ge for Si, we effectively apply negative pressure to the itinerant AFM phase through lattice expansion and the magnetic order is shifted to a localized AFM order. A drastic change of the magnetic wave vector has been observed around $y \sim 0.26$, which may corresponds to a 1st order phase transition between the itinerant- and the localized-AFM phases.

A focus of recent experimental and theoretical studies on heavy fermion systems close to antiferromagnetic (AFM) quantum critical points (QCP) is directed toward revealing the nature of the fixed point, *i.e.*, whether it is an itinerant antiferromagnet (spin density wave, SDW) type[1,2] or a locally-critical fixed point.[3] Several recent experimental studies suggest a possibility of the locally QCP.[4,5] In this case, a reconstruction of Fermi surfaces, between large Fermi surfaces of heavy quasi-particles and small ones of bare conduction electrons, occurs at the QCP. Recent theoretical works[6,7] predicted that the locally QCP is relevant for systems with two dimensional spin fluctuations, in agreement with the experimental results of $CeCu_{5.9}Au_{0.1}$.[8]

On the other hand, relevance of the SDW-type QCP was proposed for the AFM QCP of $Ce(Ru_{1-x}Rh_x)_2Si_2$ by an accurate measurement of the dynamical susceptibility.[9] $CeRu_2Si_2$ has three short-range AFM correlations with wave vectors $\boldsymbol{q}_1 = (0.3\,0\,0)$, $\boldsymbol{q}_2 = (0.3\,0.3\,0)$ and $\boldsymbol{q}_3 = (0\,0\,0.35)$,[10,11] and the AFM correlation with $\boldsymbol{q}_3$ develops a long-range AFM order by small amount of Rh-doping $x \geq x_c \simeq 0.04$,[12–14] as shown in

Fig. 1. In the case of the SDW-type QCP, the instability of Fermi surfaces is separated from the AFM QCP and a phase transition between the itinerant- and the localized-AFM orders will be found. In the course of searching for such a phase transition, we have studied magnetic properties of a pseudo-binary alloy system $Ce(Ru_{0.9}Rh_{0.1})_2(Si_{1-y}Ge_y)_2$. The base material $Ce(Ru_{0.9}Rh_{0.1})_2Si_2$ belongs to the itinerant AFM heavy fermion.[15] By substituting Ge for Si, we can effectively apply negative pressure to the itinerant-AFM phase through lattice expansion and the magnetic order can be shifted to the localized-AFM order.[16] In this article, recent results of neutron scattering experiments for $Ce(Ru_{0.9}Rh_{0.1})_2(Si_{1-y}Ge_y)_2$ and the possibility of a 1st order phase transition between the itinerant- and localized-AFM orders are reported.

Single crystalline samples of $Ce(Ru_{0.9}Rh_{0.1})_2(Si_{1-y}Ge_y)_2$ for $y = 0.00$, 0.20, 0.26 and 0.30 were grown by the Czochralski pulling method with a use of a tetra-arc furnace. The samples were annealed at 1000 °C in a vacuumed quartz tube. The neutron scattering experiments were performed on the triple-axis spectrometer GPTAS at the JRR-3M reactor of the Japan Atomic Energy Research Institute(JAERI).

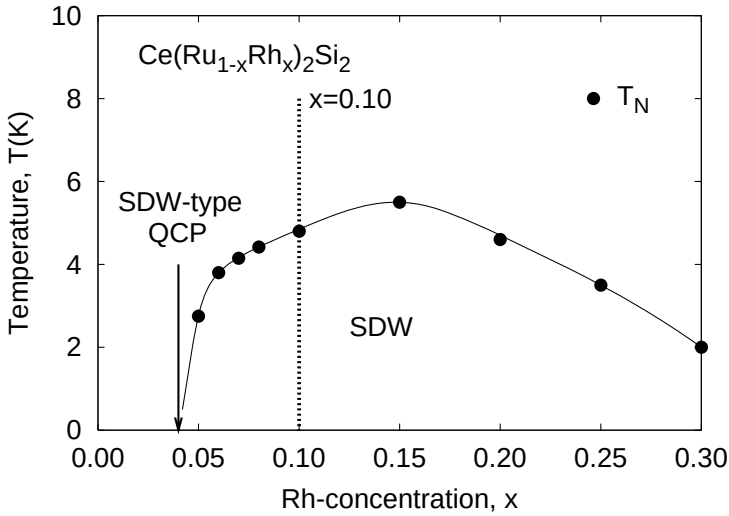

Fig. 1. The Phase diagram of $Ce(Ru_{1-x}Rh_x)_2Si_2$ for $0.0 \leq x \leq 0.3$, reproduced from Ref. 12-15.

We show temperature dependences of the integrated intensity of the

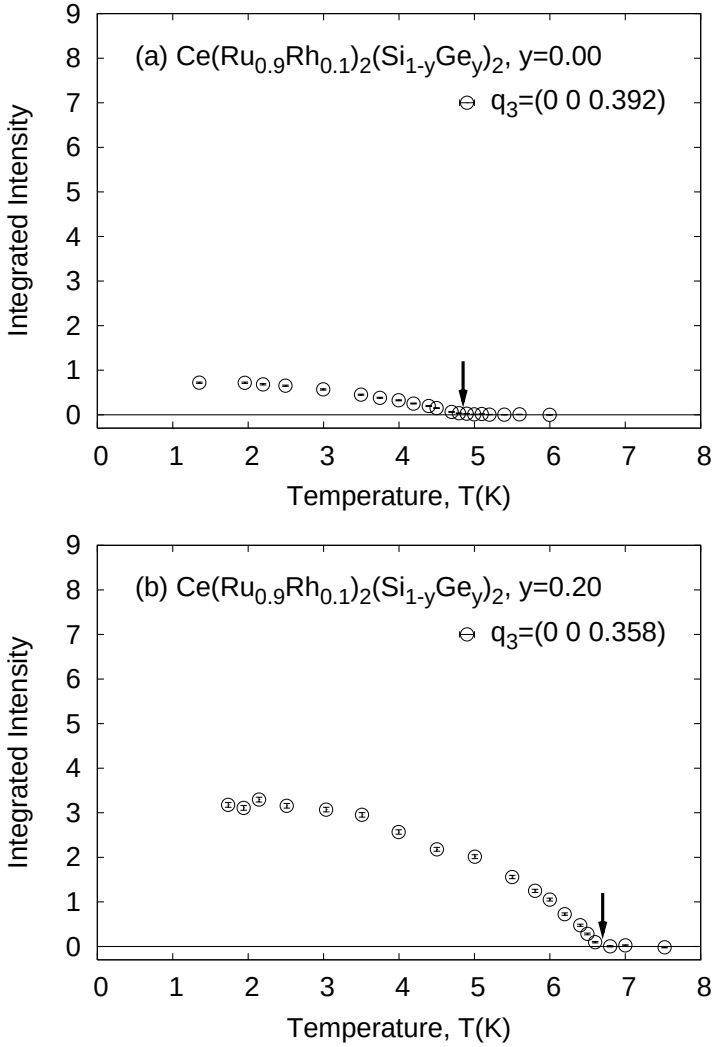

Fig. 2. Temperature dependences of the integrated intensity of the magnetic scattering with $\boldsymbol{q}_3 = (0\,0\,k)$ for (a) y=0.00 and (b) y=0.20. $k = 0.392$ and 0.358 for $y = 0.00$ and 0.20 respectively

magnetic scattering for $y = 0.00$, 0.20, 0.26 and 0.30 in Figs. 2(a), (b) and Figs. 3(a), (b), respectively . For $y \leq 0.20$, the magnetic wave vector of the AFM order is $\boldsymbol{q}_3 = (0\ 0\ k)$ ($\boldsymbol{q}_3$-phase), and the value of k depends on y.[16] On the other hand, the magnetic wave vector of the $y = 0.30$ compound

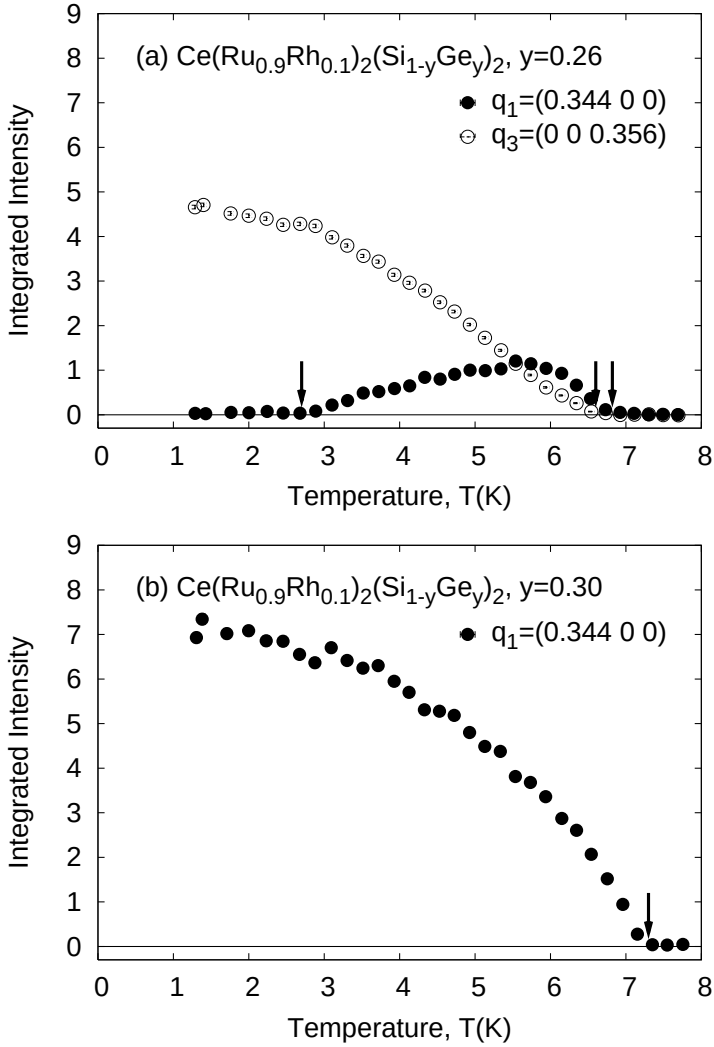

Fig. 3. Temperature dependences of the integrated intensity with the magnetic scatterings with $\boldsymbol{q}_1 = (0.344\,0\,0)$ and $\boldsymbol{q}_3 = (0\,0\,0.35)$ for (a) y=0.26 and (b) y=0.30. For $y = 0.30$, only the magnetic scattering with $\boldsymbol{q}_1$ was observed.

is $\boldsymbol{q}_1 = (0.344\,0\,0)$ ($\boldsymbol{q}_1$-phase). In the intermediate Ge concentration, for $y = 0.26$, we have found two magnetic scatterings with $\boldsymbol{q}_1$ and $\boldsymbol{q}_3$ (= (0 0 0.35)). First, the magnetic order with $\boldsymbol{q}_1$ appears at $T_{\rm N} = 6.9$ K, and the order with $\boldsymbol{q}_3$ develops below 6.6 K. Two magnetic orders coexist between

2.8 K and 6.6 K. Below 2.8 K, only the $\boldsymbol{q}_3$-phase survives.

We have also observed 3rd harmonics of the magnetic scatterings with $\boldsymbol{q}_1$ and $\boldsymbol{q}_3$ to examine the nature of the respective magnetic orders. The ratio of the amplitudes of the 3rd harmonic component to the fundamental one, $r = A_{3\boldsymbol{q}}/A_{1\boldsymbol{q}}$, in the $\boldsymbol{q}_3$-phase at the lowest temperature for $y = 0.00$, 0.20 and 0.26 are 0.035, 0.059 and 0.088 respectively, where the amplitude of the magnetic modulation A is proportional to the square root of the integrated intensity of the magnetic scattering. These values are much less than 1/3 which is expected for a completely squared-up modulation, and hence, the modulation of the $\boldsymbol{q}_3$-phase is nearly sinusoidal even in the Ge-concentration of $y = 0.26$. On the other hand, the value of r in the $\boldsymbol{q}_1$-phase for $y = 0.30$ is 0.20, which is close to 1/3. It indicates that the $\boldsymbol{q}_1$-phase has the squared-up type modulation.

The type of magnetic modulation indicates that the $\boldsymbol{q}_1$- and the $\boldsymbol{q}_3$-phases have localized and itinerant natures respectively. Consequently, the drastic change of the magnetic wave vector should correspond to the change between the itinerant- and the localized-AFM orders, namely the change of the Fermi surfaces between the large and the small ones. And the co-existence of two magnetic orders in the intermediate Ge-concentration, for $y = 0.26$, strongly suggests that the alternation of the itinerant- and the localized-AFM orders in $Ce(Ru_{0.9}Rh_{0.1})_2(Si_{1-y}Ge_y)_2$ system is a 1st order phase transition.

In summary, we have studied the negative chemical pressure effect to the itinerant-AFM phase in $Ce(Ru_{0.9}Rh_{0.1})_2Si_2$ by Ge-doping, and have discovered the change of the magnetic wave vector corresponding to the 1st order phase transition between the itinerant- and the localized-AFM phases.

References

1. T. Moriya and T. Takimoto, *J. Phys. Soc. Jpn.* **64**, 960 (1995).
2. J. A. Hertz, *Phys. Rev. B* **14**, 1165 (1976); A. J. Milis, *ibid.* **48**, 7183 (1993).
3. P. Coleman, C. Pépin, Q. Si and R. Ramazashvili, *J. Phys. Condens. Matter* **13**, R723 (2001).
4. A. Schröder, G. Appeli, R. Coldea, M. Adams, O. Stockert, H. v. Löhneysen, E. Bucher, R. Ramazashvili and P. Coleman, *Nature*, **407**, 351 (2000).
5. S. Paschen, T. Lühmann, S. Wirth, P. Gegenwart, O. Trovarelli, C. Geibel, F. Steglich, P. Coleman and Q. Si, *Nature*, **432** 881 (2004).
6. Q. Si, S. Rabello, K. Ingersent and J. L. Smith, *Nature* **413**, 804 (2001).
7. Q. Si, *cond-mat/0601001.*
8. O. Stockert, H. v. Löhneysen, A. Rosch, N. Pyka and M. Loewenhaupt, *Phys. Rev. Lett.* **80**, 5627 (1998).

9. H. Kadowaki, Y. Tabata, M. Sato, N. Aso, S. Raymond and S. Kawarazaki, *Phys. Rev. Lett.* **96**, 016401 (2006).
10. H. Kadowaki, M. Sato and S. Kawarazaki, *Phys. Rev. Lett.* **92**, 097204 (2004).
11. L. P. Regnault, W. A. C. Erkelens, J. Rossat-Mignot, P. Lejay and J. Flouquet, *Phys. Rev. B* **38**, 4481 (1988).
12. S. Kawarazaki, M. Sato, H. Kadowaki, Y. Yamamoto and Y. Miyako, *J. Phys. Soc. Jpn.* **66**, 2473 (1997).
13. C. Sekine, T. Sakakibara, H. Amitsuka, Y. Miyako and T. Goto, *J. Phys. Soc. Jpn.* **61**, 4536 (1992).
14. Y. Tabata, T. Taniguchi, M. Sato, S. Kawarazaki and Y. Miyako, *J. Phys. Soc. Jpn.* **67**, 2484 (1998).
15. S. Kawarazaki, K. Watanabe, M. Miyamura and Y. Uwatoko, *J. Phys. Soc. Jpn.* **69** Suppl. A, 53 (2000).
16. K. Watanabe, Y. Uwatoko, Y. Tabata, H. Kadowaki, C. Kanadani, T. Taniguchi and S. Kawarazaki, *J. Phys. Soc. Jpn.* **72**, 1751 (2003).

RELATION BETWEEN MAGNETISM AND METAL-INSULATOR TRANSITION IN Mn-DOPED $SrRuO_3$*

M. Yokoyama*, C. Satoh, K. Fujita and Y. Nishihara

Faculty of Science, Ibaraki University, Mito 310-8512, Japan
**E-mail: makotti@mx.ibaraki.ac.jp*

H. Kawanaka and H. Bando

National Institute of Advanced Industrial Science and Technology, Tsukuba 305-8568, Japan

Neutron powder diffraction experiments were carried out on the insulating phase of the mixed compounds $SrRu_{1-x}Mn_xO_3$ for $0.4 \leq x \leq 0.6$. We have found that the ferromagnetic phase observed at $x \sim 0$ changes into the C-type antiferromagnetic phase above $x \geq 0.4$. In addition, this transition accompanies the structural variation from orthorhombic phase ($x \sim 0$) to tetragonal phase ($x \geq 0.4$). With increasing x, the AF moment is strongly enhanced from 1.1 μ_B ($x = 0.4$) to 2.6 μ_B ($x = 0.6$), which is tightly coupled with the elongation of the tetragonal c/a ratio. We suggest from the experimental results that the evolution of the AF order in the insulating phase is generated by the superexchange interaction originating in the strong electronic correlation between the d electrons on Ru and Mn ions.

The relationship between magnetism and metal-insulator transition in the transition-metal oxides is a fascinating subject in the condensed-matter physics. The distorted perovskite compound $SrRuO_3$ (the $GdFeO_3$ type orthorhombic structure: space group of $Pnma$) is the itinerant ferromagnet with the Curie temperature of $\sim$ 160 K and the ordered moment of $\sim$ 1.1 μ_B.[1] Recently, it is found in the Mn-doped compounds $SrRu_{1-x}Mn_xO_3$ that the itinerant ferromagnetic phase is suppressed by increasing x, and then replaced by a new insulating phase above $x_c \sim 0.3 - 0.4$.[2,3] Above x_c, the magnetic susceptibility shows a cusp-like anomaly, suggesting that the antiferromagnetic (AF) order develops in the insulating phase. Such a

*This work is supported by a Grant-in-Aid for Scientific Research from the Ministry of Education, Culture, Sports, Science and Technology of Japan.

variation in the magnetic states is expected to be strongly correlated with nature of the metal-insulator transition, and it is therefore interesting to investigate the magnetic properties in the insulating phase microscopically. In the present study, we have performed neutron powder diffraction experiments for $SrRu_{1-x}Mn_xO_3$ with the intermediate Mn concentration range.

The polycrystalline samples of $SrRu_{1-x}Mn_xO_3$ with $x = 0.4$, 0.5 and 0.6 were prepared by the conventional solid-state method, whose details are described elsewhere.[3] The neutron diffraction measurements for the powdered samples were performed in the temperature range between 20 and 290 K, using the HERMES spectrometer installed at the research reactor JRR-3M of Japan Atomic Energy Agency. The wavelength of the incident neutron beam 1.82035 Å is selected by the (331) reflection of a Ge monochromator.

Figure 1(a) shows the neutron powder diffraction profile for $x = 0.4$ at 290 K. Interestingly, the diffraction pattern indicates that the system forms the tetragonal crystal structure, in contrast to the orthorhombic one for $x \sim 0$. We have found that the Bragg-peak intensities can be fairly well explained by assuming the tetragonal $I4/mcm$ symmetry (Fig. 1(b)). The same structure is also observed for $x = 0.5$ and 0.6. Our preliminary experiments on the whole x range revealed that the transition from the orthorhombic structure to the tetragonal structure occurs at $x \sim 0.3$, and it

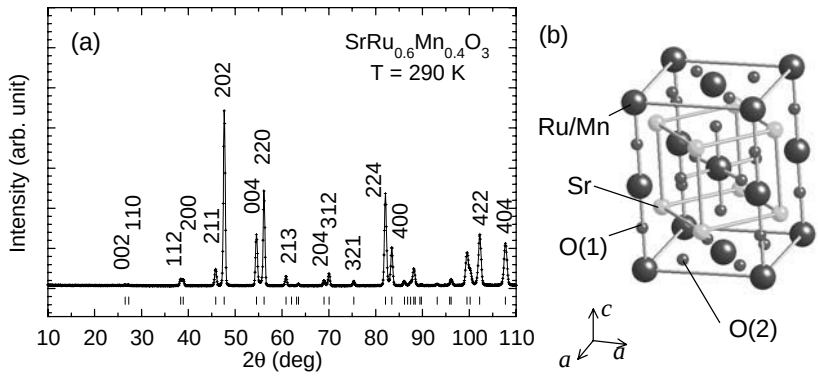

Fig. 1. (a) Neutron powder diffraction profile for $SrRu_{0.6}Mn_{0.4}O_3$ at $T = 290$ K. The calculated Bragg-peak positions based on the tetragonal $I4/mcm$ symmetry are also plotted with the vertical markers. (b) The unit cell of $SrRu_{1-x}Mn_xO_3$ with the tetragonal $I4/mcm$ symmetry, where ionic position are assigned to Sr $(0, 1/2, 1/4)$, Ru/Mn (0,0,0), O(1) $(0, 0, 1/4)$, and O(2) $(1/4 + u, 3/4 + u, 0)$.

corresponds to the boundary between the metallic and insulating phases.[4] The tetragonal crystal structure observed in our samples basically coincides with the first report,[5] but differs from the recent ones,[2,6] where the orthorhombic structure is kept up to $x = 0.6$. Although the reason for the discrepancy is not clear in the present stage, it is probably caused by the unexpected differences in the synthesized conditions of the samples.

Temperature variations of the neutron powder diffraction profiles for $x = 0.6$ are shown in Fig. 2(a). At 20 K, we have observed new Bragg peaks corresponding to (hkl) reflections with $h + k = odd$ and $l = even$. Their intensities show a tendency to decrease with increasing the scattering angle, indicating that they originate in the magnetic order. In addition, we have observed no other additional reflection due to AF or ferromagnetic order. These results indicate that the system has an AF order with a modulation of $q = (1, 0, 0)$, called the C-type structure in the perovskite compounds (Fig. 2(b)). The magnetic Bragg-peak intensities are reduced with increasing temperature, and then vanished at ~ 230 K. This temperature is consistent with the Néel temperature estimated from the cusp-like

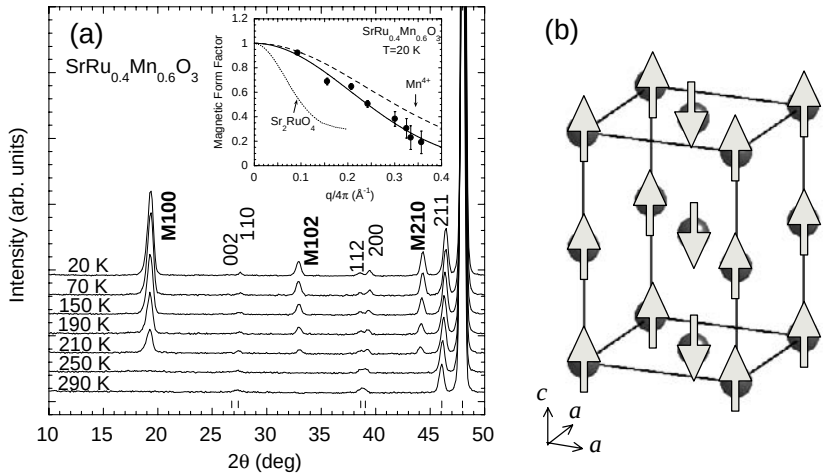

Fig. 2. (a) Low-angle part of the neutron powder diffraction profiles for $SrRu_{0.4}Mn_{0.6}O_3$, obtained under several temperatures. The calculated nuclear Bragg-peak positions are also plotted with the vertical markers. The inset shows the magnetic form factor at 20 K for $x = 0.6$. For the comparison, the experimental data for Sr_2RuO_4 [Ref. 7] and the calculated data for Mn^{4+} [Ref. 8] are also shown. (b) The spin arrangement on the Ru/Mn ions in the C-type AF structure, depicted in the unit cell of the tetragonal $I4/mcm$ symmetry.

anomaly in the magnetic susceptibility. We have further estimated the q dependence of the magnetic form factor $f(q)$ multiplied the magnitude of the staggered moment μ_0 from the integrated intensities of these magnetic Bragg peaks, in order to clarify the polarization of the AF moment. By assuming the AF moment to be polarized along the tetragonal c axis, we obtained a monotonic $f(q)$ curve without an improperly large oscillation (inset of Fig. 2(a)). The angle between the staggered moment and the c direction is considered to be less than 5° even if the moment is canted. The same magnetic properties are also observed for $x = 0.4$ and 0.5.

Displayed in Fig. 3(a) are x variations of μ_0 at 20 K. μ_0 at 20 K for $x = 0.4$ is estimated to be 1.1(2) μ_B, which is quite close to the magnitude of the ferromagmetic moment at $x = 0$. On the other hand, μ_0 strongly develops with further doping Mn, and reaches 2.6(1) μ_B at $x = 0.6$. The strong enhancement of the μ_0 value within the small x range may be caused by a decrease in conductivity of the d electrons in Ru/Mn ions with doping Mn. Such a feature is also seen in the $f(q)$ curve for $x = 0.6$, which shows a slower relaxation than $f(q)$ for the itinerant 4d electrons in the Ru^{4+} state of Sr_2RuO_4 [Ref. 7] (inset of Fig. 2(a)).

We expect that the strong enhancement of the AF state accompanies the variations of the lattice system through the hybridization between the d electrons in the Ru/Mn ions and their ligands. In Fig. 3(b), we show the x variations of the unit-cell volume V and the $c/a(\equiv \eta)$ ratio obtained in the AF phase ($T = 20$ K) and the paramagnetic phase ($T = 290$ K). We

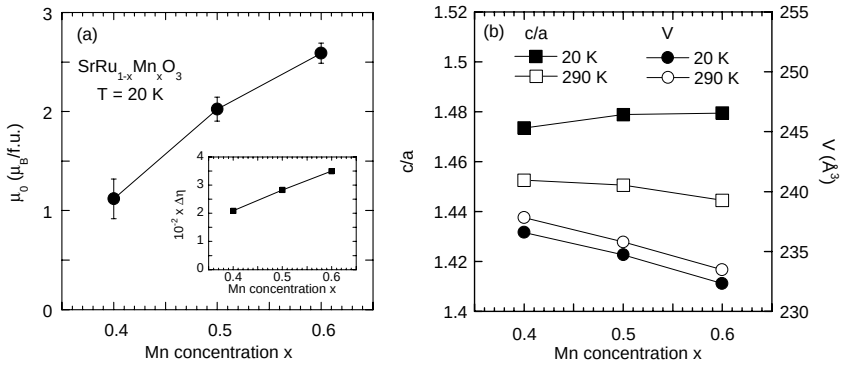

Fig. 3. x variations of (a) the staggered moment at 20 K, and (b) the unit-cell volume and the c/a ratio ($\equiv \eta$) at 20 K and 290 K for $SrRu_{1-x}Mn_xO_3$ ($0.4 \leq x \leq 0.6$). The inset of (a) shows the difference of η between 20 K and 290 K: $\Delta\eta = \eta(20\text{ K}) - \eta(290\text{ K})$.

have observed that V shrinks with increasing x at both 20 K and 290 K. At both the temperatures, the decreasing rates $\partial \ln V/\partial x$ are estimated to be the same value ($\sim -9.0 \times 10^{-2}$), indicating that the evolution of the AF phase is not correlated with the shrink of V. In contrast, η becomes large with increasing x at 20 K, while it decreases at 290 K. The difference of the η values between 20 K and 290 K linearly increases with increasing x (inset of Fig. 3(a)), which is roughly consistent with the development of μ_0. We suggest from these features that the c/a ratio is strongly coupled with the AF order.

The AF phase observed in the intermediate x range is found to have the C-type structure, which is completely different from the order parameters in both the Mn- and Ru-rich regions, *i.e.* the G-type AF order in pure $SrMnO_3$[9] and the ferromagnetic order in pure $SrRuO_3$.[1] In addition, the magnitude of the ordered moment in this AF phase is much larger than that for the ferromagnetic phase. Since the ferromagnetic to AF transition accompanies the metal-insulator transition, this enhancement is considered to be attributed to the itinerant to localized d electron transition due to the strong electronic correlation effect, that is, the system is in the crossover region from $W/U > 1$ to $W/U \ll 1$, where W and U are the d-band width and the on-site Coulomb potential. In this context, we expect that the present systems with intermediate x range belong to the latter condition, and the C-type AF order observed in them originates in the superexchange interaction induced between the d electrons on the Ru/Mn ions, as is argued in the Mott-type insulators. In the mechanism of the superexchange interaction, the positions of the Ru/Mn ions and the O ions play a key role in the stability of the AF order. We have observed that the tetragonal c/a ratio strongly develops in the AF phase, which should involve a shrinkage of the Ru/Mn-O(2) bond length (see Fig. 1(b)). This may enhance the superexchange interaction between the nearest neighbor Ru/Mn ions in the c plane, generating the C-type AF order.

We also wish to stress that this AF state is connected with the variations of the spin and valence states in Ru and Mn ions. The spin states in pure $SrRuO_3$ and $SrMnO_3$ are realized to be the low-spin Ru^{4+} ($S = 1$) and high-spin Mn^{4+} ($S = 3/2$) configurations, respectively. It is clear that a simple combination of these states cannot compose the homogeneous C-type AF order. We thus expect that the other valence states are mixed in the intermediate x range, which might reduce the dissimilarity of the spin states between Ru and Mn ions. In fact, recent x-ray photoemission studies on $SrRu_{1-x}Mn_xO_3$ revealed that the Ru^{5+}/Mn^{3+} state develops

with increasing x.[10]

In summary, we found the evolution of the C-type AF order in the insulating phase of $SrRu_{1-x}Mn_xO_3$ with $x = 0.4$, 0.5 and 0.6. The magnitude of the AF moment is strongly enhanced with increasing x, suggesting that the nearly localized d electrons in Ru and Mn ions are responsible for the AF order, in contrast to the itinerant features of the 4d electrons in pure $SrRuO_3$. The development of the AF moment is found to be accompanied by the enhancement of the tetragonal c/a ratio. We suggest from these experimental results that the evolution of the AF order is ascribed to the appearance of the superexchange interaction in the c plane, which is enhanced by the reduction of the Ru/Mn-O(2) bond length.

References

1. A. Callaghan *et al.*, *Inorg. Chem.* **6**, 1572 (1966).
2. G. Cao *et al.*, *Phys. Rev. B* **71**, 035104 (2005).
3. M. Yokoyama *et al.*, *J. Phys. Soc. Jpn.* **74**, 1706 (2005).
4. H. Kawanaka *et al.*, to be published.
5. Y. Xu, X. Chen and Y. Chen: unpublished (JCPDS 52-428).
6. R. K. Sahu *et al.*, *Phys. Rev. B* **66**, 144415 (2002).
7. T. Nagata *et al.*, *Phys. Rev. B* **69**, 174501 (2004).
8. T. Hahn, *International Tables for Crystallography* (D. Riedel Publishing Co., Boston MA, 1995) Vol. A, p 391.
9. T. Takeda and S. Ohara, *J. Phys. Soc. Jpn.* **37**, 275 (1974).
10. Y. Aiura, private communications.

MAGNETIZATION STUDY OF PAIRING AND VORTEX STATES IN Sr_2RuO_4

K. TENYA*, R. YAMAHANA, A. ISHII and H. AMITSUKA

Department of Physics, Hokkaido University, Sapporo 060-0810, Japan
**E-mail: tenya@phys.sci.hokudai.ac.jp*

M. YOKOYAMA

College of Science, Ibaraki University, Mito 310-8512, Japan

K. DEGUCHI

Department of Physics, Nagoya University, Nagoya 161-8602, Japan

Y. MAENO

Department of Physics, Kyoto University, Kyoto 606-8502, Japan
International Innovation Center, Kyoto University, Kyoto 606-8501, Japan

Static magnetization measurements of Sr_2RuO_4 have been performed down to 0.1 K. For $H \parallel [100]$ an anomalous increase of magnetization is observed at H_2 which is located just below H_{c2}. Besides the above anomaly, a small kink is found in the magnetization curves at 8.9 kOe, suggesting an additional superconducting transition due to the lifting of the degenerate order parameter. For $H \parallel [001]$ anomalous successive flux-jumps are observed around zero field in the magnetization curves. Possible origins of such anomalous magnetization are discussed from the viewpoints of the pairing symmetry and the topological change in the vortex lattice configuration.

Keywords: unconventional superconductivity; Sr_2RuO_4; static magnetization.

1. Introduction

Superconductivity in strongly correlated electron systems has been attracting much interest because the appearance of unconventional superconductivity together with the non-Fermi liquid behaviors is observed in many compounds.[1] Among them, the layered compound Sr_2RuO_4 is a unique superconductor for which two-dimensional Fermi liquid properties as well as its Fermi-surface topology have been experimentally characterized

in detail.[2] In addition, the possibility of spin-triplet pairing with a two-component "chiral" order parameter $\boldsymbol{d}(\boldsymbol{k}) \propto \boldsymbol{z}(k_x \pm i\,k_y)$ is inferred from several experimental observations such as (i) the appearance of a spontaneous internal field with broken time-reversal symmetry,[3] (ii) the invariance of the spin-susceptibility in the superconducting state,[4] (iii) the unconventional field distribution in the square vortex-lattice[5] and (iv) the novel phase-sensitive behaviors in the π-junction SQUID.[6]

In this pairing symmetry, the domain formation of the two states $\boldsymbol{z}(k_x + i\,k_y)$ and $\boldsymbol{z}(k_x - i\,k_y)$ is expected.[7] Under the magnetic field parallel to the [001] axis, the vortices in the $\boldsymbol{z}(k_x + i\,k_y)$ domain should show different structures from those in the $\boldsymbol{z}(k_x - i\,k_y)$ domain because of the difference in the winding number of the phase in the vortices. It is natural to anticipate that the domain formation with unconventional vortex structures affects the macroscopic superconducting properties.

On the other hand, recent specific heat and thermal conductivity measurements[8,9] have revealed that an additional superconducting transition occurs just below the upper critical field H_{c2} only for the field perpendicular to the [001] axis. In addition, the upper critical field H_{c2} seems to be paramagnetically suppressed for $H \perp [001]$ at low temperatures,[8] inconsistent with the above pairing scenario.

It is worthwhile to inspect the magnetization in the superconducting state which reflects the paramagnetic suppression of the superconductivity as well as the vortex configurations. We have performed static magnetization measurements of Sr_2RuO_4 down to 0.1 K.

2. Experimental Procedure

A single crystal of Sr_2RuO_4 was prepared by a floating-zone method in an infrared image furnace.[10] The superconducting transition temperature T_c was 1.42 K. Magnetization measurements up to 20 kOe were performed at temperatures ranging from 0.1 K to above T_c and in the field directions parallel to the [100] and [001] axes, using a capacitive Faraday force magnetometer installed in a ^{3}He-^{4}He dilution refrigerator.[11] Each magnetization measurement was started from the state in which a weak reverse field up to 5 kOe was applied in order to make the sample into the mixed state.

3. Results and Discussions

Figure 1 shows an example of the magnetization curves $M(H)$ of Sr_2RuO_4 at 0.14 K in the field parallel to the [100] direction. Here the normal state

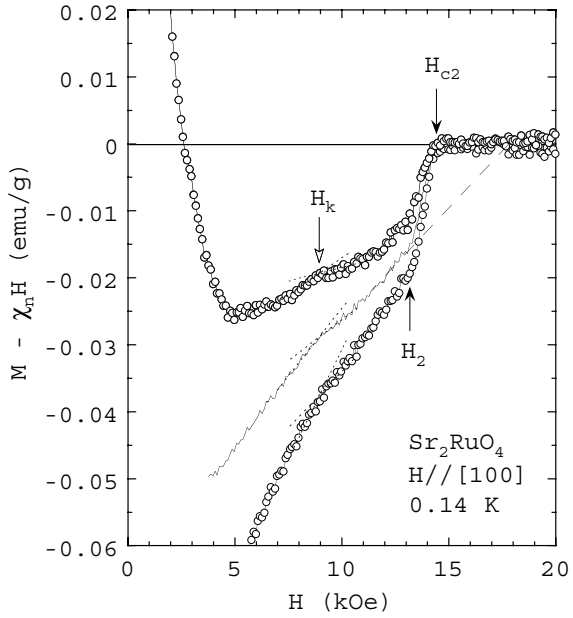

Fig. 1. Magnetization curves of the single crystal Sr_2RuO_4 at 0.14 K for $H \parallel [100]$, where the normal state contribution $\chi_n H$ has been subtracted. The thin solid line is the equilibrium magnetization obtained by averaging the hysteresis.

contribution $\chi_n H$ has been subtracted. A thin solid line in the figure is the equilibrium magnetization $M_{eq}(H)$ which is obtained by averaging the increasing- and decreasing-field data in the mixed state.[12] The lower critical field H_{c1} is not well resolved in this experiment. The strong irreversibility appearing at low fields is due to the ordinary flux pinning effect. The hysteresis, that strongly depends on the amount of impurities or defects, rapidly decreases with increasing field, leading to the high-quality of the sample. H_{c2} is defined as the field above which the irreversibility vanishes within experimental accuracy.

The magnetization curves show a clear anomaly at 13.1 kOe just below H_{c2}: The magnetization shows a rapid increase at the field. This onset field corresponds to the second superconducting transition field H_2 obtained by the specific heat and ac susceptibility measurements.[8,13] The position of H_2 is found to be independent of the field-scan directions as well as that of H_{c2}, indicating that the both transitions at H_2 and at H_{c2} are considered to be of second order. The H_2-anomaly disappears when the field is inclined from

the basal plane by a few degrees, consistent with the previous results.[8] The onset field H_2 gradually decreases with increasing temperature and seems to merge with H_{c2} around 1 K.

In conventional superconductors the equilibrium magnetization linearly increases up to H_{c2} with increasing field, in strong contrast with the present results. Without H_2-anomaly the superconductivity in Sr_2RuO_4 could survive up to about 18 kOe as shown by the broken line in the figure, suggesting that the superconductivity is strongly suppressed above H_2.

A small kink of the magnetization curves is observed at H_k (= 8.9 kOe), as shown by an open arrow. This kink-anomaly also disappears when the field is inclined from the basal plane by a few degrees. The kink position slightly shifts to lower fields as the temperature increases. The kink is, however, smeared with temperature and cannot be traced up above 0.6 K. It should be noted that this magnetization behavior at H_k is quite similar to that at the superconducting B-C transition field H_{BC} in UPt_3 where the degeneracy of the two-component order-parameter is lifted.[12] The kink at

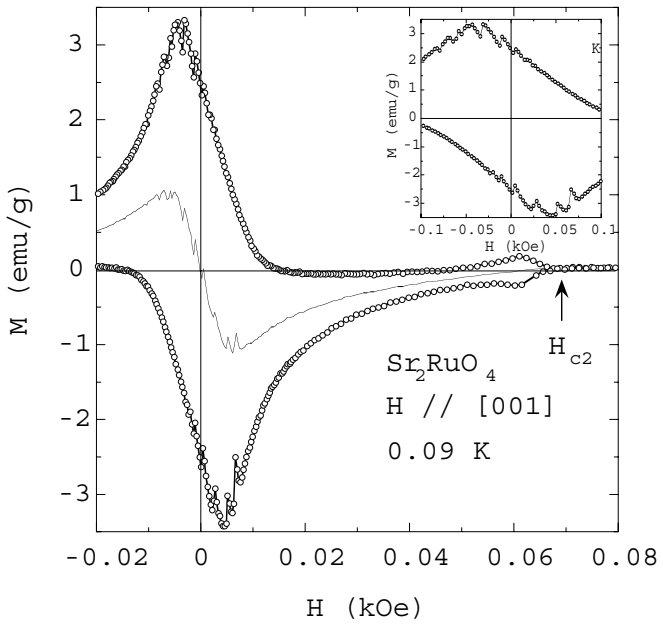

Fig. 2. Magnetization curves of Sr_2RuO_4 at 0.09 K for $H \parallel [001]$. The thin solid line is the equilibrium magnetization. The inset shows successive flux-jumps of the magnetization around zero field.

$H_{\rm k}$ may originate from an additional superconducting transition which is caused by the lifting of the order parameters $\boldsymbol{z}(k_x \pm i\,k_y)$.

Figure 2 shows the isothermal magnetization curves of Sr_2RuO_4 in the field parallel to the [001] direction. The irreversibility in $M(H)$, which rapidly decreases with field in the low fields, increases again in a narrow region just below $H_{\rm c2}$. This is so-called "peak effect", occasionally observed in type-II superconductors. A thin solid line in the figure is the equilibrium magnetization $M_{\rm eq}(H)$: $M_{\rm eq}(H)$ smoothly increases up to $H_{\rm c2}$ with increasing field. This indicates that an additional phase does not exist in the superconducting mixed state for $H \parallel [001]$, in strong contrast with the results for $H \parallel [100]$.

It should be noted that anomalous successive flux-jumps of the hysteretic magnetization are observed around zero field: The flux-jumps are observed at temperatures below about 0.3 K. Anomalous dip structure in the local magnetization was observed around zero-field in a micro-Hall probe measurements as well,[14] and the origin of these results are considered to be the same. The origin of the anomalies are not clear at present stage, but a possible origin is the vortex pinning at the $\boldsymbol{z}(k_x \pm i\,k_y)$ chiral domain boundaries which leads to the avalanche-like penetration of the vortices at very weak fields.[15]

4. Summary

We performed the static magnetization measurements of Sr_2RuO_4 in the field parallel and perpendicular to the [100] direction. For $H \parallel [001]$ successive flux-jumps appear around zero field. For $H \parallel [100]$ anomalous magnetization behaviors are observed around 9 kOe and 13 kOe besides the superconducting-normal transition. Above the latter field the superconductivity is found to be strongly suppressed. The anomaly at the former field is considered to originate from an additional superconducting transition which is caused by the lifting of the order parameters $\boldsymbol{z}(k_x \pm i\,k_y)$.

Acknowledgments

This work has been partially supported through the 21COE Program on "Topological Science and Technology" by the Ministry of Education, Culture, Sport, Science and Technology.

References

1. For example, N. Oeschler, F. Kromer, T. Tayama, K. Tenya, P. Gegenwart, G. Sparn and F. Steglich, *Acta Physica Polonica B* **34**, 255 (2003).
2. A. P. Mackenzie and Y. Maeno, *Rev. Mod. Phys.* **75**, 657 (2003).
3. K. Ishida, H. Mukuda, Y. Kitaoka, K. Asayama, Z. Q. Mao, Y. Mori and Y. Maeno, *Nature (London)* **396**, 658 (1998).
4. G. M. Luke, Y. Fudamoto, K. M. Kojima, M. I. Larkin, J. Merrin, B. Nachumi, Y. J. Uemura, Y. Maeno, Z. Q. Mao, Y. Mori, H. Nakamura and M. Sigrist, *Nature (London)* **394**, 558 (1998).
5. P. G. Kealey, T. M. Riseman, E. M. Forgan, L. M. Galvin, A. P. Mackenzie, S. L. Lee, D. Mck. Paul, R. Cubitt, D. F. Agterberg, R. Heeb, Z. Q. Mao and Y. Maeno, *Phys. Rev. Lett.* **84**, 6094 (2000).
6. K. D. Nelson, Z. Q. Mao, Y. Maeno and Y. Liu, *Science* **306**, 1151 (2004).
7. M. Ichioka and K. Machida, *Phys. Rev. B* **65**, 224517 (2002).
8. K. Deguchi, M. A. Tanatar, Z. Q. Mao, T. Ishiguro and Y. Maeno, *J. Phys. Soc. Jpn.* **71**, 2839 (2002).
9. M. A. Tanatar, S. Nagai, Z. Q. Mao, Y. Maeno and T. Ishiguro, *Phys. Rev. B* **63**, 064505 (2001).
10. Z. Q. Mao, H. Fukazawa and Y. Maeno, *Mat. Res. Bull.* **35**, 1813 (2000).
11. T. Sakakibara, H. Mitamura, T. Tayama and H. Amitsuka, *Jpn. J. Appl. Phys.* **33**, 5067 (1994).
12. K. Tenya, M. Ikeda, T. Tayama, T. Sakakibara, E. Yamamoto, K. Maezawa, N. Kimura, R. Settai and Y. Onuki, *Phys. Rev. Lett.* **77**, 3193 (1996).
13. H. Yaguchi, T. Akima, Z. Q. Mao, Y. Maeno and T. Ishiguro, *Phys. Rev. B* **66**, 214514 (2002).
14. T. Tamegai, K. Yamazaki, M. Tokunaga, Z. Q. Mao and Y. Maeno, *Physica C* **388-389**, 499 (2003).
15. M. Sigrist and D. F. Agterberg, *Prog. Theor. Phys.* **102**, 965 (1999).

SINGLE-SITE EFFECTS OF Pr IONS DOPED IN $ThRu_2Si_2$

A. MORISHITA*, Y. SAITO, K. MATSUDA, T. WAKABAYASHI,
I. KAWASAKI, K. TENYA and H. AMITSUKA

Division of Physics, Graduate School of Science, Hokkaido University, Sapporo, Japan
**E-mail: amori@phys.sci.hokudai.ac.jp*

We investigated thermal, magnetic and transport properties for the dilute system $Th_{1-x}Pr_xRu_2Si_2$ ($x = 0.05$ and 0.1). The $4f$ electronic specific heat C_{4f}/T shows a Schottky anomaly at $\sim$ 10 K, and the $4f$ contribution to magnetic susceptibility χ_{4f} shows a saturation tendency below this temperature. Both C_{4f}/T and χ_{4f} are well scaled by the doped Pr concentration, and fitted by crystalline-electric-field (CEF) calculations based on the singlet ground state. The electrical resistivity ρ shows normal metallic behavior. The Kondo screening seems not to occur in this dilute system.

1. Introduction

So far, single-site effects of U ions doped in RRu_2Si_2 (R = Th, Y and La) have been intensively studied to clarify the single-site $5f$-electronic state in URu_2Si_2.[1] These dilute systems show a remarkably strong uniaxial magnetic anisotropy along the tetragonal c-axis. On the other hand, the temperature dependence of physical quantities observed at low temperature is different depending on the host metals. For example, the dilute system $Th_{1-x}U_xRu_2Si_2$ shows the non-Fermi-liquid (NFL) behavior,[2] whereas $La_{1-x}U_xRu_2Si_2$ does not, and shows the formation of the local Fermi-liquid (LFL) state.[3,4] The theoretical study of the f^2-impurity Anderson model (f^2-IAM), which is an extension of the two-channel Kondo model,[5] explains the NFL-LFL variation as the result of the competition between the c-f hybridization strength and the energy gap between the Γ_5 crystalline-electric-field (CEF) doublet ground state and an excited singlet,[6,7] and suggests that the LFL becomes stable if the hybridization strength is larger than the energy gap. However, this theory predicts the residual entropy at $T = 0$ K, which is inconsistent with experimental results of specific heat in magnetic field.[4] On the other hand, the numerical renormalization group

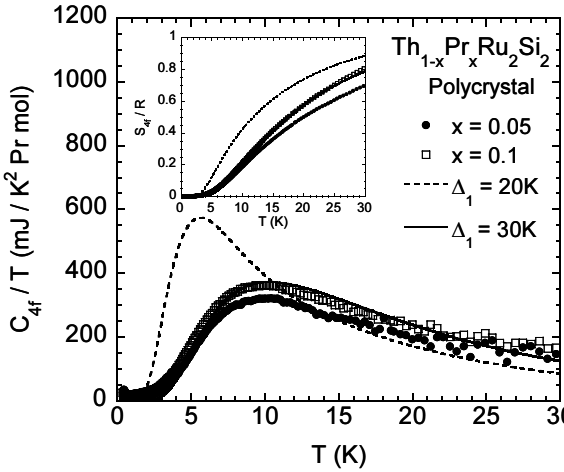

Fig. 1. The $4f$ electronic specific-heat coefficient C_{4f}/T for $Th_{1-x}Pr_xRu_2Si_2$ ($x = 0.05$ and 0.1). The solid and dotted lines are the results of CEF calculations (Δ_1 is defined in the text). The inset shows the $4f$ electronic entropy estimated from C_{4f}/T.

study for the f^2-IAM based on the CEF singlet ground state can also explain the crossover between the NFL and LFL states.[8] This theory predicts the absence of the residual entropy at $T = 0$ K, but has a difficulty of the explanation for the strong magnetic anisotropy. To understand the low-temperature properties of the dilute U systems, it is very important to clarify the CEF level scheme on U ions doped in these different host metals.

The tetravalent U ion (U^{4+}) and trivalent Pr ion (Pr^{3+}) involve the same ground J multiplet ($J = 4$). The $4f$ electrons in $PrRu_2Si_2$ are well localized at the Pr ions.[9,10] Therefore, dilute Pr systems $R_{1-x}Pr_xRu_2Si_2$ (R = Th, Y and La) may serve as a good reference to investigate the fundamental CEF level scheme for the corresponding dilute U systems. So far, the La dilution system $La_{1-x}Pr_xRu_2Si_2$ has been studied,[11] where the $4f$ electronic state of the single Pr ion is simply explained by the singlet-singlet CEF model, and the Kondo screening seems not to occur.

In this paper, we present single-site effects of Pr ions doped in $ThRu_2Si_2$, which are investigated by means of the specific heat, magnetic susceptibility and electrical resistivity measurements for polycrystalline samples of $Th_{1-x}Pr_xRu_2Si_2$ ($x = 0.05$ and 0.1). We discuss the CEF and Kondo effects of the Pr ions, and compare them with the anomalous behavior observed in the dilute U system $Th_{1-x}U_xRu_2Si_2$.

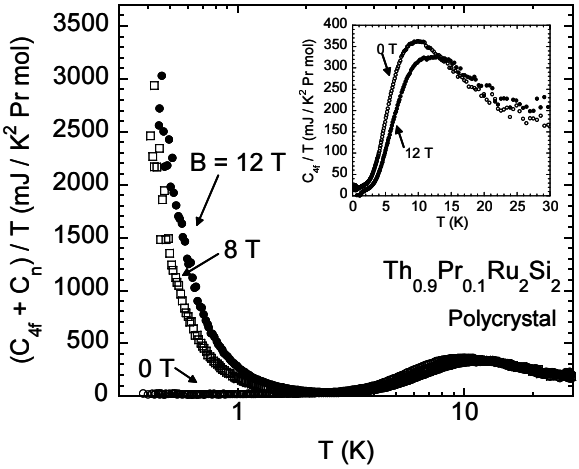

Fig. 2. Temperature variations of the specific heat divided by temperature $(C_{4f}+C_n)/T$ for $Th_{0.9}Pr_{0.1}Ru_2Si_2$ in magnetic fields. C_{4f} and C_n indicate the contributions of the $4f$ electrons and the Pr nuclear spins, respectively. The inset shows the C_{4f}/T data at $B = 0$ T and 12 T.

2. Experimental

Polycrystalline samples $Th_{1-x}Pr_xRu_2Si_2$ ($x = 0$, 0.05 and 0.1) were prepared by arc melting. Specific heat was measured with thermal relaxation method in the temperature range from 0.4 K to 60 K and in the field range 0 T $\leq B \leq$ 12 T using ^{3}He refrigerator (Heliox; Oxford Instruments). DC magnetization was measured for powdered sample using a SQUID magnetometer (MPMS; Quantum Design) from 2 K to 300 K. Electrical resistivity was measured with a standard four-wire DC method from 1.3 K to room temperature using ^{4}He refrigerator.

3. Results and Discussions

Temperature variations of the $4f$ electronic specific heat C_{4f}/T for $Th_{1-x}Pr_xRu_2Si_2$ ($x = 0.05$ and 0.1) are shown in Fig. 1. The non $4f$ contribution were subtracted using the specific-heat data for $ThRu_2Si_2$. The inset of Fig. 1 shows the $4f$ electronic entropy defined by $S_{4f} = \int_{0.4\mathrm{K}}^{T} dT\, C_{4f}/T$. The peak structures seen at ~ 10 K are Schottky anomaly due to CEF effect. The experimental data are well scaled by the doped Pr concentration, and described by the CEF calculation based on the singlet-singlet $(\Gamma_{t1}^{(1)} - \Gamma_{t2})$ level scheme[10] with the energy splitting of $\Delta_1 \equiv \Delta_{\Gamma_{t1}^{(1)}-\Gamma_{t2}} = 30$

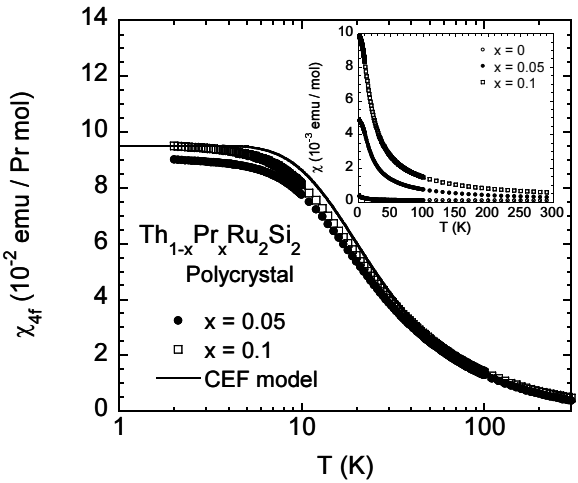

Fig. 3. The $4f$ contribution to magnetic susceptibility χ_{4f} for $Th_{1-x}Pr_xRu_2Si_2$ (x = 0.05 and 0.1). The inset shows temperature variations of magnetic susceptibility χ.

K. This Δ_1 value is somewhat larger than that reported for the La system ($\Delta_1 \sim 20$ K),[11] suggesting that the entropy release is shifted to higher temperature by changing the host ions from La to Th. The finite C_{4f}/T value of ~ 20 mJ/K^2 Pr mol remains at the lowest temperature. The $4f$ electrons may be thus incompletely localized in the Th dilution system.

In Fig. 2, we show the magnetic-field variations of the specific heat $C_{4f} + C_n$ for $Th_{0.9}Pr_{0.1}Ru_2Si_2$, where C_n ($\propto 1/T^3$) indicates the Schottky component of the Pr nuclear spins. In the inset of Fig. 2, we plot the C_{4f}/T data obtained by subtracting the nuclear Schottky contributions using the specific-heat data at $B = 12$ T. The C_{4f}/T data at high-field region do not exhibit the evolution of additional Schottky anomaly due to the Zeeman splitting of the CEF levels. Furthermore, the entropy is balanced at ~ 40 K between $B = 0$ T and 12 T. These results support the singlet-singlet CEF model.

The inset of Fig. 3 shows the temperature variation of the magnetic susceptibility χ for the $Th_{1-x}Pr_xRu_2Si_2$ (x = 0, 0.05 and 0.1). The saturation tendency of χ below ~ 10 K also suggests the singlet CEF ground state: the Van-Vleck susceptibility is dominant below this temperature. In Fig. 3, we plot the $4f$ contribution to magnetic susceptibility χ_{4f} for $Th_{1-x}Pr_xRu_2Si_2$ ($x = 0.05$ and 0.1) , which is obtained by subtracting the magnetic susceptibility for $ThRu_2Si_2$. The χ_{4f} data are well scaled by the

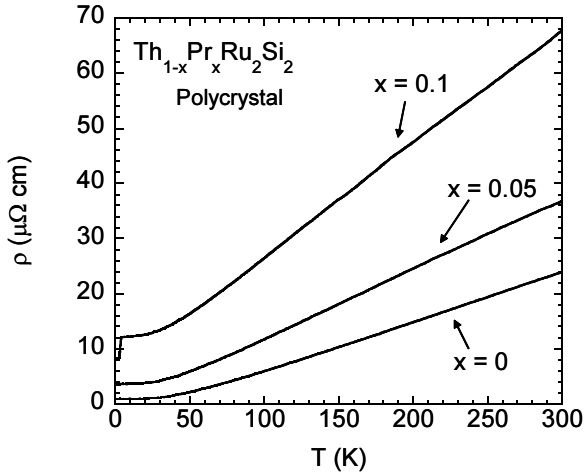

Fig. 4. The electrical resistivity for $Th_{1-x}Pr_xRu_2Si_2$ (x = 0, 0.05, 0.1).

doped Pr concentration, and are well fitted by the CEF calculation based on the singlet ground state, where we took an average of a- and c-axis magnetic susceptibilities with the ratio $\chi_a : \chi_c = 2 : 1$.

In Fig. 4, we plot temperature variations of the electrical resistivity $\rho(T)$ for $Th_{1-x}Pr_xRu_2Si_2$ (x = 0, 0,05 and 0.1). The contributions of the Pr ions to $\rho(T)$ cannot be exactly estimated for the difficulty caused by using the polycrystalline samples. $\rho(T)$ for all samples show normal metallic behavior from room temperature to ~ 1.3 K. The anomaly due to the Kondo effect is not observed. $\rho(T)$ for $x = 0.1$ suddenly decreases at ~ 4 K. We suppose that this is due to the mixing of some impurities that show superconductivity, such as Pb. They may be produced in the process of the radioactive decay of Th. The evolution of the superconductivity is actually observed in the magnetization at the low magnetic field of 10 mT. However, this is not a bulk property because the specific-heat data show no anomaly at this temperature.

The C_{4f}/T, χ_{4f} and ρ data for $Th_{1-x}Pr_xRu_2Si_2$ obtained in the present experiments indicate the absence of the strong many-body effect on the $4f$ electrons such as the Kondo screening, and can be well explained by assuming the two CEF singlets to be low-lying. The $4f$ electrons at the Pr ions doped in $ThRu_2Si_2$ is thus considered to be well localized due to very weak c-f hybridization. This feature is very different from the dilute system $Th_{1-x}U_xRu_2Si_2$, which shows the NFL behavior due to anoma-

lous many-body effects. These properties are considered to be strongly connected with the characteristics of the low-energy CEF states. The strong magnetic anisotropy observed in $R_{1-x}U_xRu_2Si_2$ (R = Th, Y and La) suggests that the energy splitting between the Γ_5 doublet and singlet states is very large.[2] In addition, the present experiments revealed that the $4f$ electrons in $Th_{1-x}Pr_xRu_2Si_2$ have the CEF singlet ground state. To clarify the origin of the NFL behavior in $Th_{1-x}U_xRu_2Si_2$ by exactly understanding the CEF effect of these dilute systems, we are planning to investigate the low-temperature properties of $R_{1-x}Pr_xRu_2Si_2$ (R = Th, Y and La) using single-crystalline samples.

4. Summary

In summary, we investigated thermal, magnetic and transport properties for the dilute system $Th_{1-x}Pr_xRu_2Si_2$ (x = 0.05 and 0.1). Both C_{4f}/T and χ_{4f} are well scaled by the doped Pr concentration, and fitted by CEF calculations based on the singlet ground state. The electrical resistivity ρ shows normal metallic behavior. The anomaly due to the Kondo effect is not observed in the $\rho(T)$ data. From these results, we suggest that the $4f$ electrons are localized in this dilute system.

Acknowledgments

This work is supported by "The 21st Century COE Program Topological Science and Technology, Hokkaido University".

References

1. H. Amitsuka *et al.*, *Physica* **B281**&**282**, 326 (2000).
2. H. Amitsuka and T. Sakakibara, *J. Phys. Soc. Jpn.* **63**, 736 (1994).
3. K. Marumoto, T. Takeuchi and Y. Miyako, *Phys. Rev.* **B54**, 12194 (1996).
4. M. Yokoyama *et al.*, *J. Phys. Soc. Jpn.* **71**, 3037 (2002).
5. D. L. Cox, *Phys. Rev. Lett.* **59**, 1240 (1987).
6. M. Koga and H. Shiba, *J. Phys. Soc. Jpn.* **65**, 3007 (1996).
7. Y. Shimizu, A. Hewson and O. Sakai, *J. Phys. Soc. Jpn.* **68**, 2994 (1999).
8. S. Yotsuhashi, K. Miyake and H. Kusunose, *J. Phys. Soc. Jpn.* **71**, 389 (2002).
9. A. M. Mulders *et al.*, *Phys. Rev.* **B56**, 8752 (1997).
10. R. Michalski, Z. Ropka and R. J. Radwanski, *J. Phys.* **C12**, 7609 (2000).
11. K. Marumoto, F. Takayama and Y. Miyako, *J. Magn. Magn. Mater.* **177-181**, 353 (1998).

^{51}V-NMR STUDIES OF HEISENBERG TRIANGULAR SYSTEM V15 CLUSTER

Y. FURUKAWA*, Y. NISHISAKA, K. KUMAGAI

Department of Physics, Faculty of Science, Hokkaido University, Sapporo, 060-0810, Japan
**E-mail: furu@phys.sci.hokudai.ac.jp*

P. KÖGERLER

Department of Physics and Astronomy, Ames Laboratory, Iowa State University, Iowa 50011, USA

^{51}V nuclear magnetic resonance (NMR) measurements below 100 mK using a ^{3}He-^{4}He dilution refrigerator have been carried out to investigate the magnetic states of V ions in the V15 cluster. It is revealed experimentally that the V^{4+} (s=1/2) spins on the outer hexagons are in a singlet state and V ions on the inner triangle has s=1/2 spin moments at low temperature.

1. Introduction

The nanoscale molecular magnet $K_6[V_{15}As_6O_{42}(H_2O)]_8H_2O$ (in short, V15) has attracted much interest as the cluster is considered to be a typical s=1/2 Heisenberg triangular system.[1] The V15 cluster is comprised of fifteen V^{4+} ions with s=1/2,[1,2] which are arranged in a quasi-spherical layered structure with a triangle sandwiched between two hexagons. Figure 1 shows the configuration of V^{4+} (s=1/2) ions and exchange coupling scheme in V15 cluster where all exchange interactions between V^{4+} spins are antiferromagnetic (AF).[1,2] Each hexagon of the cluster consists of three pairs of strongly coupled spins with J_1∼-800 K. Each spin of the V^{4+} ions in the central triangle is coupled with the spins in both hexagons with J_2=-150 K and J_3=-300 K,[2] resulting in a very weak exchange interaction between the spins within the triangle with J_0=-2.44 K.[3] At low temperatures, the magnetic properties of the V15 cluster are considered to be determined only by the three V^{4+} spins on the triangle (a frustrated s=1/2 triangle system) because the V^{4+} spins on the hexagons are reasonably assumed to result in a spin singlet state due to the strong AF interaction of J_1∼-800

K. In fact, magnetic properties such as the magnetization curve[4] and the T dependence of the magnetic susceptibility at low temperature[3] were well explained by an s=1/2 triangular Heisenberg model. There is, however, no direct experimental confirmation for the singlet state of the V^{4+} spins on the hexagons and s=1/2 spin state of V ions on the triangle. In this paper, we report the ^{51}V nuclear magnetic resonance (NMR) results for the cluster, which provide a direct proof for the singlet state of the V^{4+} spins on the hexagons and s=1/2 spin of V ions on the triangle in the V15 clutser.

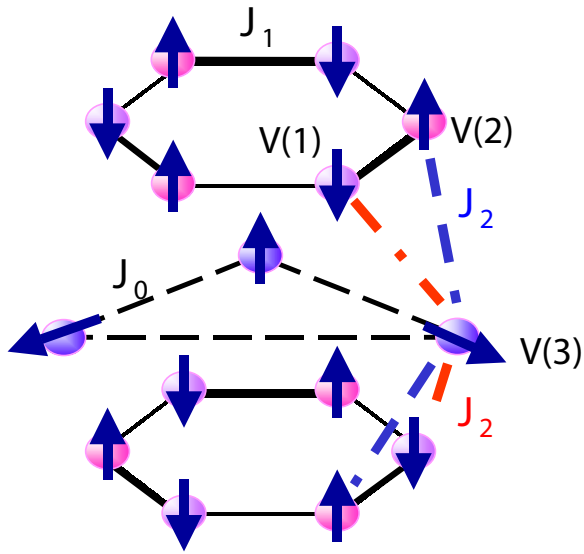

Fig. 1. Configuration of V^{4+} (s=1/2) ions (solid circles) and exchange coupling scheme in V15 cluster. The three equivalent V ions on the triangle are labeled as V3. The two non-equivalent V ions on the hexagons are labeled as V1 and V2, respectively.

2. Experimental

Polycrystalline samples of $K_6[V_{15}As_6O_{42}(H_2O)]_8H_2O$ were prepared as described elsewhere.[5] NMR measurements were carried out using a phase-coherent spin echo pulse spectrometer below 1 K using ^{3}He-^{4}He dilution refrigerator. The ^{51}V-NMR spectra were obtained by sweeping the external magnetic field at constant frequencies.

3. Results and discussion

Figure 2(b) shows the ^{51}V-NMR spectrum measured at T=50 mK and f=50.78 MHz. Two peaks labeled as P2 and P3 in the figure are observed with almost equal intensity around H∼4 T where the ground state of the cluster is S=3/2. Another ^{51}V-NMR signal labeled as P1 shown in Fig. 2(a) is also observed at different resonance frequency in the S=3/2 ground state.

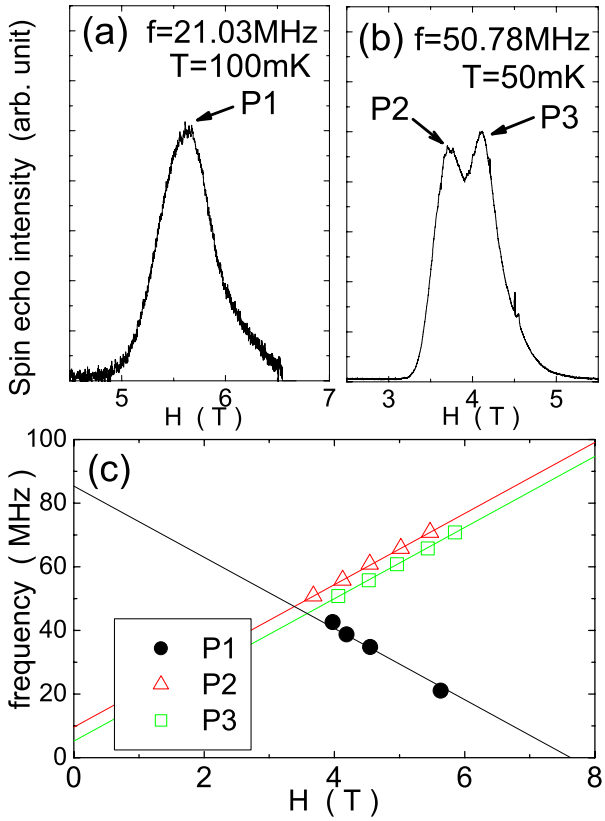

Fig. 2. (a) ^{51}V-NMR spectrum measured at T=100 mK and f=21.03 MHz. (b) ^{51}V-NMR spectrum measured at T=50 mK and f=50.78 MHz. (c) External magnetic field dependence of resonance frequency for each ^{51}V-NMR peak measured below ∼100 mK.

Figure 2(c) shows the external field dependence of the resonance frequencies for the three ^{51}V-NMR signals. With increasing the magnetic field, the P2 and P3 shift to a higher frequency, while P1 shift to a lower frequency. The slope of the magnetic field dependence of the resonance

frequency is ∼|11.3| MHz/T for each peak, which coincides with the gyromagnetic ratio γ_N(=11.293 MHz/T) of the ^{51}V nucleus. As the resonance frequency is proportional to the vector sum of the internal field (H_{int}) and external field (H_{ext}) as $f=\gamma_N(H_{int}+H_{ext})$, internal field is estimated to be -76.5 kOe for P1, 8 kOe for P2 and 4 kOe for P3. The internal magnetic field of V^{4+} ions with s=1/2 is considered to be dominated by inner-core polarization mechanism which induces a large negative internal field of the order of -100 kOe/μ_B at the nuclear site. Since the value of -76.5 kOe for P1 is close to a reported value of -85 kOe/μ_B for the inner-core polarization mechanism of V^{4+} ions in VO_2,[6] ^{51}V-NMR signal labeled as P1 is assigned to V^{4+} ions with s=1/2. Unfortunately, since we can observe ^{51}V-NMR signal (P1) only at low temperatures, we can not estimate an exact value of the hyperfine coupling constant from the so-called K-χ plot. Therefore we tentatively use the value of -85 kOe/μ_B for the hyperfine coupling constant for the inner-core polarization of the V^{4+} ions in the V15 cluster. This would be a reasonable because the coupling constant for the inner-core polarization mechanism is known to be unchanged so much for the same ions. Using a relation H_{int}=A<S> with A=-85 kOe/μ_B, the spin moment for the V site is estimated to be 0.89 μ_B whose direction is parallel to the external field.

On the other hand, P2 and P3 with small and positive internal fields can not be explained in terms of inner-core polarization mechanism, indicative of no spin moments on the V^{4+} ions. There are two possibilities for the origin of the hyperfine field at the V sites with no spin moments, that is, dipolar fields and transferred hyperfine fields (THF) from the V^{4+} spins with net spin moments. In the case of a powder sample, the dipolar fields yield a broadening of the peak but no net shift, while the net shift of the peak can be produced by THF. Thus the observed net shift for both peaks suggests that the internal field at the V sites is mainly due to THF from the spins on other V ions. We have checked this conclusion by measuring the ^{51}V-NMR spectrum in a single crystal for which the observed spectrum is identical to that of the polycrystalline sample. This means that the dipolar contributions to the internal field are negligible and THF is isotropic. The isotropic THF should depend on the distance between the two V ions because it originates from the strength of V-O-V covalent bond. The distance between the V3 and V2 ions is 3.73 Å which is longer than the 3.02 Å distance between the V3 and V1 sites.[1] The shortest distance is 2.87 Å between the V1 and V2 sites. With taking the almost equal signal intensity for P2 and P3 into consideration, the two V ions observed in the spectrum

shown in Fig. 2(b) can be considered as the two V ions in the hexagon, while P1 can be assigned to the V3 site in the triangle. The peaks P2 and P3 can then be assigned to the V1 and V2 sites, respectively, because the distance between the V3 and V1 ions is shorter than the distance between the V3 and V2 ions.

Thus we conclude that both V ions on the hexagon have no net spin moments at low temperature. These results are direct evidences for the magnetic state for each V ions, where V^{4+} ions in the triangle have almost full moments of s=1/2 and the V^{4+} spins on the hexagon are in singlet state. This is a direct confirmation of the spin structure of the V15 cluster in its S=3/2 ground state from microscopic point of view.

Acknowledgments

The present work was in part supported by 21 Century COE Programs "Topological Science and Technology" at Hokkaido University from the Ministry of Education, Culture, Sports, Science and Technology of Japan. One of the authors (Y. F.) also thanks the Sumitomo Foundation for financial supports.

References

1. A. L. Barra, D. Gatteschi, L. Pardi, A. Müller, and J. Döring, *J. Am. Chem. Soc.* **114**, 8509 (1992).
2. D. Gatteschi, L. Pardi, A. L. Barra and A. Müller, *Mol. Eng.* **3**, 157 (1993).
3. G. Chaboussant1, R. Basler, A. Sieber, S. T. Ochsenbein, A. Desmedt, R. E. Lechner, M. T. F. Tell-ing, P. Kögerler, A. Müller and H.-U. Güdel, *Europhys. Lett.* **59**, 291 (2002).
4. I. Chiorescu, W. Wernsdorfer, B. Barbara, A. Müller and H. Bögge, *J. Magn. Magn. Mater.* **221**, 103 (2000).
5. J. Choi, L. A. W. Sanderson, J. L. Musfeldt, A. Ellern and P. Kögerler, *Phys. Rev. B* **68** 064412 (2003).
6. K. Takanashi, H. Yasuoka, Y. Ueda and K. Kosuge, *J. Phys. Soc. Jpn.* **52** 3953 (1983).

MENGER SPONGE-LIKE FRACTAL BODY CREATED WITH A DESIGNED TEMPLATE METHOD

H. MAYAMA[1*] and K. TSUJII[1,2]

[1] *Nanotechnology Research Center, Research Institute for Electronic Science, Hokkaido University, Sapporo 001-0021, Japan*
and [2] *CREST, JST, Japan*
[*] *E-mail: mayama@es.hokudai.ac.jp*

Fractal body, a porous silica with cross-sectional fractal dimension $D_{cs} = 1.87$ was created by a sol-gel reaction of tetramethyl orthosilicate (TMOS) using unique template particles. D_{cs} was maintained over *ca.* three decades in pore size from 0.05 - 30 μm and its density $\rho = 0.35$ g·cm^{-3}. Based on the obtained D_{cs}, pore size distribution and ρ, it was concluded that its fractal geometry was closer to Menger sponge (fractal dimension $D = 2.73$) at the 7th generation, a mathematical model of fractal body. Our experimental strategy would allow us to design fractality of porous materials in real space.

1. Introduction

Dimension is an essential control parameter as shown in charge density wave (CDW)[1] and quantum Hall effect.[2] Recently, it has been clarified that some systems with non-integer dimension (fractal) express new phenomena of the localization of electromagnetic wave[3] and super liquid-repellency,[4–6] *etc.*[7] Therefore, various new phenomena must be still lying behind fractal dimension. To investigate the uniqueness of fractal in real space, it is very important to establish an experimental strategy to create various materials with different fractality under designed experiment. Some materials such as aerogel, silicagel and DLA colloids have fractal dimension at $\sim$ 10 nm,[8] but, it is very difficult to control their dimension because they are prepared by accident.

Here we show the first experimental strategy on the creation of a fractal body resembling Menger sponge[9] with a novel template method. We designed the experimental procedure on the basis of the knowledge of experimental study on super water-repellent surface.[4] Our strategy is the first step to design fractality of porous materials in real space.

2. Experiment

2.1. *Experimental strategy*

The essence was to prepare "fractal particles" (Figs. 1(a) and 1(b)), *i.e.*, particles with "fractal surface structure" using alkylketene dimer (AKD) corresponding to pores in Menger sponge, where AKD spontaneously forms fractal surface structure.[4] If we would fill remained space between the densely packed fractal particles with a suitable monomer solution (Fig. 1(c)), solidify it (Fig. 1(d)) and remove the particles by any method (Fig. 1(e)), then a fractal body would be created (Fig. 1(f)). This strategy allows us to create fractal dimension between two characteristics scales (cutoffs) of the fractal particle, *i.e.*, scales of surface structure and particle diameter as shown in experimental study on the super water-repellent surface.[4]

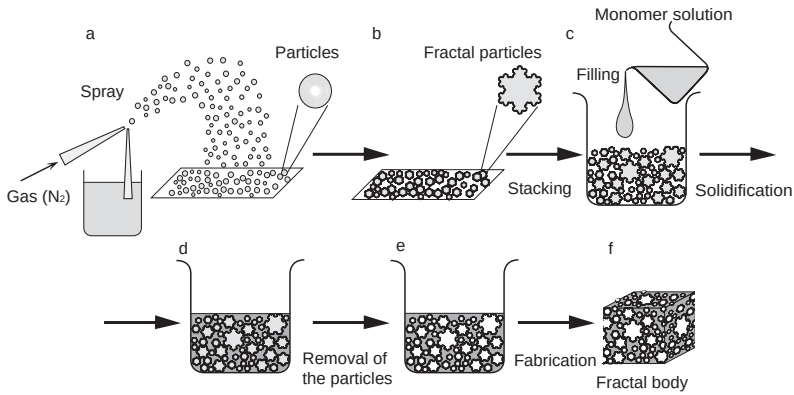

Fig. 1. Experimental scenario to create a fractal body. (a) Preparation of fractal particles as templates of pores in fractal body by a spray technique. (b) Spontaneous formation of surface structure. (c) - (d) Molding. (e) Removal of templates. (f) A fabricated fractal body as a cube.

2.2. *Experimental procedures*

Along this line, we created a fractal body. AKD was supplied by Arakawa Chemical Industries, Ltd. Chemical structure is shown elsewhere,[4] but two alkyl chains of AKD used in this work were $C_{14}H_{29}$ and $C_{16}H_{33}$ in the mixing ratio of C_{14} : C_{16} = 3 : 7 - 4 : 6. To prepare fractal AKD particles, the $n-$Hexane (Wako Pure Chemical Industries, Ltd.) solution which

contains *ca.* 5 wt % AKD was sprayed by nitrogen gas and then the particles were stood at room temperature for the spontaneous formation of fractal surface structure. The spontaneous formation was observed by SEM (Hitachi, S-5200). Then, fractal AKD particles were packed. A tetramethyl orthosilicate (TMOS, Shin-Etsu Chemical Co., Ltd.) solution was adopted as the monomer solution, and it was added gently into the remained space between the particles, where the solution contains the ratio of TMOS, H_2O and methanol (Wako Pure Chemical Industries, Ltd.) at 1 : 4 : 5 in molar ratio at pH = 6.86. It was stood at room temperature for 3 days for sol-gel reaction. Then, it was calcined at 500 °C for 2 h in air. To determine cross-sectional fractal dimension D_{cs}, the sample (porous silica) was fabricated using a focused ion beam (FIB, Hitachi FB-2100) and then cross sections were observed by SEM. D_{cs} was determined by the box-counting method for their pictorial images obtained by image processing. Fractal dimension as a body was estimated from mathematical model from D_{cs}.

3. Results and discussion

Figure. 2(a) shows typical SEM images of AKD particles (diameter $d \geq 5$ μm) at different time and their corresponding representations. The surface of the particles was smooth after the preparation, but it fully bloomed after 4 weeks. In the spray technique, various particles of different size ($d = 0.5$ - 100 μm) and different shapes were prepared. We also found that smaller particles ($d < 5$ μm) spontaneously formed a piece of flake as shown in Fig. 2(b), which corresponds to the smallest template and the thickness of petal was 50-100 nm.

After calcination of the sol-gel product, porous silica was obtained. Its density was 0.35 g·cm^{-3}, whereas the density of silica prepared by same process without AKD particles was 2.4 g·cm^{-3}. Therefore, the porosity of the porous silica was 85% (15 vol % for silica, volume fraction $f = 0.15$). The f will be discussed later in terms of D_{cs}.

Next, we observed cross sections of the prepared porous silica to determine D_{cs}. Figures 3(a) and 3(b) show typical SEM images of cross sections at different magnification and their corresponding pictorial images. Wide distribution of shape and size of pores was observed. Each pore corresponds to a fractal AKD particle. Figure 3(c) shows a fabricated fractal body, which looks like a Menger sponge. D_{cs} was determined by a box-counting method from the above pictorial images. In the box-counting method, the following

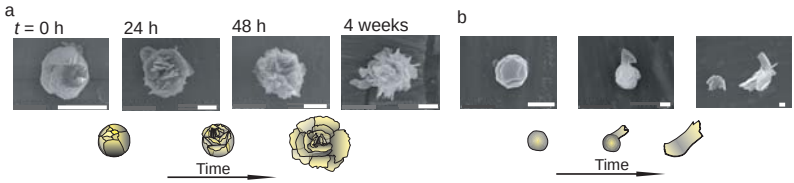

Fig. 2. Typical SEM images of spontaneous formation of fractal AKD particles with time course (bars: 5 μm) and its schematic representation. (a) Diameter $d \geq 5\mu$m and (b) $d < 5\mu$m.

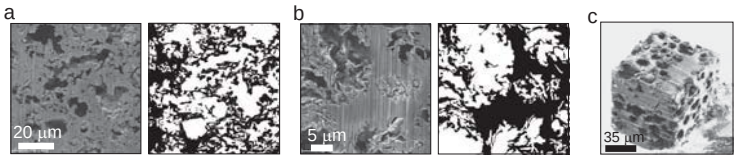

Fig. 3. Observation of the created fractal body. (a) - (b) SEM images of cross section of porous silica (left) and their pictorial images (right) at different magnification. (c) SEM image of a fabricated fractal body.

relation is satisfied.

$$N(r) \propto r^{-D} \tag{1}$$

where $N(r)$ is the number of boxes occupied by a fractal pattern, r is the box size and D is the fractal dimension. Figure 4(a) indicates the result of the box-counting method obtained from more than 30 cross sections. The $N(r)$ seems to be monotonically decreased with increasing r, however, there are two inflection points in the fitting line at *ca.* 50 nm and 30 μm, where the former and the latter are corresponding to the thickness of a flake and the maximum size of the particles, respectively. D_{cs} between two cutoffs is determined to be 1.87 ± 0.03, whereas it is determined to be 2.0 below 50 nm and above 30 μm within experimental error. This indicates that the characteristic scales of template particles determine the cutoffs. We thus accomplished the creation of a fractal body with the designed experiment.

To investigate the importance of surface structure of the template particle, same experiment was carried out for porous silica using AKD particles with smooth surface before the spontaneous formation of surface structure. D_{cs} was determined to be 2.0 over whole range although we skip the detail. The effect arising from particle size distribution is negligible. Thus, it was shown that surface structure of template particle is essential in fractal body.

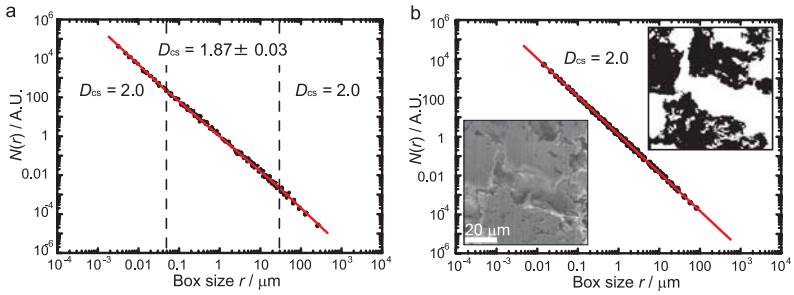

Fig. 4. $\log N(r)$ *vs.* $\log r$ plots in the cross-sectional area for fractal body and non-fractal body. (a) Created fractal body. The D_{cs} between *ca.* 50 nm and *ca.* 30 μm is determined to be 1.87 ± 0.03, whereas the D_{cs} in other regions are 2.0 within experimental error. (b) Created non-fractal body. D_{cs} is determined to be 2.0 over whole range within experimental error. The insets show a typical SEM image (left) and its pictorial one (right), respectively.

Let's discuss briefly about the geometry of the created fractal body. Menger sponge and a fractal skewed web,[9] which are constructed from identical cubes and triangular pyramids, respectively, are helpful to consider the above. In the former, D_{cs} is 1.89 (= log8/log3) from Eq. (1) because 8 identical units are generated in cross section by size ratio $r_{size} = 1/3$,[10] while the latter $D_{cs} = 1.58$ (= log3/log2) because 3 identical units are generated by $r_{size} = 1/2$. Therefore, the created fractal body is considered to be closer to Menger sponge in terms of D_{cs}.

Volume fraction is also helpful for discussion because it reflects fractal geometry. In both Menger sponge and the skewed web, their volume fractions f_n at n-th generation are represented as $(20/27)^n$ and $(1/2)^n$,[11,12] respectively, where $n = 1, 2, \cdots$. If the n can be estimated from the cut-offs in which the fractal structure is maintained, one can also discuss the fractal geometry of the created fractal body in comparison with the mathematical models on the basis of f and f_n. In this work, the width of pore size distribution in which $D_{cs} = 1.87$ was *ca.* three decades, which corresponds to the ratio between maximum and minimum pore sizes in the models. $n \sim 7$ in Menger sponge because the pore size at $n = 1$ becomes *ca.* 10^{-3} times smaller by 6 times size reductions ($r_{min}/r_{max} \sim 10^{-3} \sim (1/3)^6$, $n = 1 + 6 = 7$), where r_{min} and r_{max} are minimum and maximum pore sizes, respectively. On the other hand, $n \sim 11$ in the skewed web because $r_{min}/r_{max} \sim 10^3 \sim (1/2)^{10}$ which means ten times size reductions from $n = 1$. Based on their n, volume fraction is obtained as f_{Menger} at $n = 7 \sim 0.12$ and f_{web} at $n = 11 \sim 5 \times 10^{-4}$. The experimental $f = 0.15$

is close to f_{Menger} at $n = 7$. We thus obtained a consistent result that the created body was quite similar to the Menger sponge at the 7th generation in fractal geometry.

In conclusion, we described here the experimental strategy to realize a fractal body. Our strategy would be universal and also helpful to design the geometries of porous materials such as catalysis, adsorption and cell adhesion materials.

Acknowledgements

This work was supported by a Grant-in-Aid for Scientific Research (B) (No. 16310077) from Ministry of Education, Culture, Sports, Science, and Technology (K.T), and a Grant-in-Aid for Young Researcher (No. 123) from Northern Advancement Center of Science and Technology (NOASTEC), Japan (H.M.).

References

1. P. Monçeau, N. P. Ong and A. M. Portis, *Phys. Rev. Lett.* **37**, 602 (1976).
2. K. v. Klitzing, G. Dorda and M. Pepper, *Phys. Rev. Lett.* **45**, 494 (1980).
3. M. W. Takeda, S. Kirihara, Y. Miyamoto, K. Sakoda and K. Honda, *Phys. Rev. Lett.* **92**, 093902 (2004).
4. S. Shibuichi, T. Onda, N. Satoh and K. Tsujii, *J. Phys. Chem.* **100**, 19512 (1996).
5. K. Tsujii, T. Yamamoto, T. Onda and S. Shibuichi, *Angew. Chem. Int. Ed.* **36**, 1011 (1997).
6. H. Yan, K. Kurogi, H. Mayama and K. Tsujii, *Angew. Chem. Int. Ed.* **44**, 3453 (2005).
7. G. K. S. Wong, P. A. Crowell, H. A. Cho and J. D. Reppy, *Phys. Rev. Lett.* **65**, 2410 (1990); G. Lawes, S. C. J. Kingsley, N. Mulders and J. M. Parpia, *Phys. Rev. Lett.* **84**, 4148 (2000).
8. O. Malcai, D. A. Lidar, O. Biham and D. Avnir, *Phys. Rev. E* **56**, 2817 (1997).
9. Benoit B. Mandelbrot, *The Fractal Geometry of Nature*, W. H. Freeman and Company, New York, 1977.
10. In Eq. (1), r can be substituted by r_{size} because the relation between r and r_{size} is represented by $r \propto Ar_{\mathrm{size}}$ (A: an arbitrary constant).
11. The Menger sponge at $n = 1$ is constituted from 20 identical cubes, then its volume fraction $f_{n=1} = 20/27$. The sponge at $n = 2$ is constructed from of 20 units of the volume-reduced sponge at $n = 1$ (volume ratio $v = 1/27$), then $f_{n=2} = f_{n=1} \times (1/27) \times 20 = (20/27)^2$. Therefore, $f_n = (20/27)^n$ for the n-th generation.
12. The web at $n = 1$ is constituted from 4 identical triangular pyramids, then its volume fraction $f_{n=1} = 4/8 = 1/2$. The web at $n = 2$ is constructed

from 4 units of the volume-reduced web at $n = 1$ ($v = 1/8$), then $f_{n=2} = f_{n=1} \times (1/8) \times 4 = (1/2)^2$. Therefore, $f_n = (1/2)^n$ for the n-th generation.

NONLINEAR LATTICE RELAXATION MECHANISM FOR PHOTOEXCITED DIMETAL-HALLIDE CHAIN COMPOUNDS

J. OHARA* and S. YAMAMOTO

Division of Physics, Hokkaido University, Sapporo 060-0810, Japan
**E-mail: ohara@phys.sci.hokudai.ac.jp*

In order to reveal the lattice relaxation processes of photoexcited states in dimetal hlaid chains, we employ a one-dimensional extended Peierls-Hubbard Hamiltonian and simulate the time evolution of photoexcited system within time-dependent Hartree-Fock approximation. We demonstrate that charged solitons, neutral solitons, and polarons are simultaneously photogenerated. This situation strikingly differs from one in conventional monometal-halid chains.

1. Introduction

The nonlinear excitations such as solitons[1] and polarons[2] have been attracting much attention as the carriers of charge and spin transport in low-dimensional electron-phonon coupled systems. From the viewpoint of both fundamental science and the application to electronic devices, many researchers have been vigorously studying the dynamic properties of those excitations. Their photogeneration mechanisms[3,4] and responses to an applied electric field[5,6] are widely known, especially in polyacethylene.

In recent years, quasi-one-dimensional dimetal(MM)-halide(X) chain compounds, abbreviated as MMX chains, have been extensively investigated among theorists and experimentalists, owing to their unique properties originating from competing electron-electron and electron-lattice interactions.[7–9] MMX chains are classified into two families according to their constituent ligands pop[10,11] (pop = $P_2O_5H_2^{2-}$) and dta[12,13] (dta = $CH_3CS_2^-$). These ground states are topologically degenerate.[14,16] An analogy between these materials and polyacethylene leads to the expectation that the local excitations are photoinduced in MMX chains. The static properties of those excitations such as effective mass and formation energy

have been reported.[15] However, there are few studies of their dynamics. Some of *MMX* chains exhibit metallic behavior at room temperature.[16] Then we take more and more interest in solitons and polarons as charge and/or spin carriers. In the present work, we develop our previous study of adiabatic potential energy surfaces.[17] To obtain further insight into the dynamic features of the photoproducts, we simulate the time evolution of photoexcited states.

2. Calculational Procedure

We consider one-dimensional $\frac{3}{4}$-filled single-band extended Peierls-Hubbard Hamiltonian

$$\begin{aligned} H = & -\sum_{n,s}\left[t_{MXM} - \alpha(l_{n:+} + l_{n+1:-})\right]\left(a^{\dagger}_{n+1,s}b_{n,s} + b^{\dagger}_{n,s}a_{n+1,s}\right) \\ & -\sum_{n,s} t_{MM}\left(b^{\dagger}_{n,s}a_{n,s} + a^{\dagger}_{n,s}b_{n,s}\right) - \beta\sum_{n,s}\left[l_{n:-}a^{\dagger}_{n,s}a_{n,s} + l_{n:+}b^{\dagger}_{n,s}b_{n,s}\right] \\ & + U_M\sum_{n}\left(n_{n,+}n_{n,-} + m_{n,+}m_{n,-}\right) \\ & + \sum_{n,s,s'}\left(V_{MM}n_{n,s}m_{n,s'} + V_{MXM}m_{n,s}n_{n+1,s'}\right) \\ & + \frac{K_{MX}}{2}\sum_{n}\left[l^2_{n:-} + l^2_{n:+}\right] + \frac{M_M}{2}\sum_{n}\dot{v}^2_n + \frac{M_X}{2}\sum_{n}\dot{u}^2_n, \end{aligned} \tag{1}$$

where $n_{n,s} = a^{\dagger}_{n,s}a_{n,s}$ and $m_{n,s} = b^{\dagger}_{n,s}b_{n,s}$ with $a^{\dagger}_{n,s}$ and $b^{\dagger}_{n,s}$ being the creation operators of an electron on the Md_{z^2} with spin s=±(up and down) in the nth *MMX* unit. Figure 1 shows the schematic representation of *MMX* chains. t_{MM} and t_{MXM} describe the intra- and interdimmer transfer integrals, respectively, U_M, V_{MM}, and V_{MXM} are the on-site, intradimmer, and interdimmer Coulomb repulsions. α and β are the site-off- and site-diagonal electron-lattice couplings, $l_{n:-} = v_n - u_{n-1}$ and $l_{n:+} = u_n - v_n$ with u_n and v_n being, respectively, the chain-direction displacements of the halogen and metal dimmer in the nth *MMX* unit, K_{MX} is the metal-halogen spring constant. Every M-M moiety is not deformed because it is locked

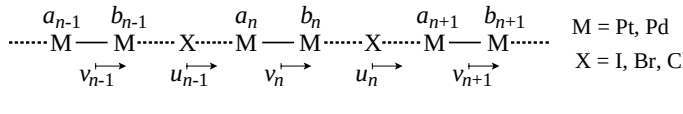

Fig. 1. Schematic representation of *MMX* chains.

by surrounding ligands. We set t_{MXM} and K_{MX} equal unity and $t_{MM} = 2t_{MXM}$. The other parameters are taken as $U_M = 0.5, V_{MM} = 0.25, V_{MXM} = 0.15, \alpha = 0.0$, and $\beta = 1.2$, which are relevant to typical pop compounds. M_M and M_X are the mass of metal dimmer and halogen,respectively. We set optical phonon energy as $\hbar\omega = 0.017$, where $\omega = \sqrt{2K_{MX}/M_{\rm eff}}$ and $\frac{1}{M_{\rm eff}} = \frac{1}{M_M} + \frac{1}{M_X}$.

To simulate the relaxation of photoexcited state, we have to find a ground state in this system. The Coulomb terms in Eq. (1) are treated within the Hartree-Fock approximation and the lattice displacements are adiabatically determined by minimizing the ground state energy. Then we obtain perfectly halogen-sublattice dimmerization state as the self-consistent solution of the Hartree-Fock Hamiltonian($H_{\rm HF}$). This is so called charge-density-wave(CDW) state, which is actually observed in pop compounds.[14]

Within the time-dependent Hartree-Fock approximation,[18] the Schrödinger equation is expressed

$$i\hbar\frac{\partial}{\partial t}|\nu, t\rangle = H_{\rm HF}|\nu, t\rangle, \tag{2}$$

where $|\nu, t\rangle$ is the one-particle state which is the νth eigenstate of $H_{\rm HF}$ at only $t = 0$. The classical motion of equations for the lattice displacements are expressed

$$M_M\ddot{v}_n(t) = -\frac{\partial}{\partial v_n(t)}\langle H_{\rm HF}\rangle|_t, \quad M_X\ddot{u}_n(t) = -\frac{\partial}{\partial u_n(t)}\langle H_{\rm HF}\rangle|_t, \tag{3}$$

where $\langle H_{\rm HF}\rangle|_t$ means the quantum average at time t. The evolution of the electronic wave functions and the lattice displacements is obtained by solving Eq. (2) and Eq. (3). In order to express an initial photoexcited state at $t = 0$, we create artificially an electron-hole pair by changing the electron occupation in the ground state. In our numerical calculation, time is discretized. The time slice Δt is set equal to $0.001\omega^{-1}$. To solve Eq. (2) numerically, we use the fractal decomposition of exponential operators[19] within $O(\Delta t^3)$. In this paper, we set the number of unit cells equal to 108.

3. Photogeneration of Solitons and Polarons

Before simulate the time evolution, we define bond order on the nth MMX unit at time t as,

$$y(t, n) = \frac{1}{4}(-1)^n\big(u_{n-1}(t) - 2u_n(t) + u_{n+1}(t)\big). \tag{4}$$

In CDW state, its value dose not depend on the positions(n) because the displacements of halogen-sublattice are described as $u_n = (-1)^n u$. Since soliton(polaron) is formed with an inversion(no inversion) of the sign of bond order, we focus on the evolution of $y(t, n)$.

Figures 2(a) and (b) visualize the formation processes of charged soliton pair $\mathrm{S}^{+} - \bar{\mathrm{S}}^{-}$ and neutral soliton pair $\mathrm{S}^{0\downarrow} - \bar{\mathrm{S}}^{0\uparrow}$, respectively, where the system is in the first excited state at t=0 by photoexciting. Charged and neutral solitons convey net charge and spin, respectively. The relaxation processes connected to soliton pairs are composed of two stages. First, excitons of the Franck-Condon type are trapped by self-induced local lattice distortions($t\omega \simeq 20$). Second, the thus self-trapped exciton(STE)s are dissociated into soliton pairs. This picture consists with the result in our previous work.[17] In Fig. 2, initial conditions are different between charged and neutral soliton channels. In charged soliton channel, we initially add small randomness to the lattice displacements in the perfectly dimmerization state. This means that the relaxation into $\mathrm{S}^{+} - \bar{\mathrm{S}}^{-}$ pair from STE requires the assistance of phonons. This fact is more detailed in conventional monometal(M)-halide(X) chain compounds, abbreviated as MX chains.[20]

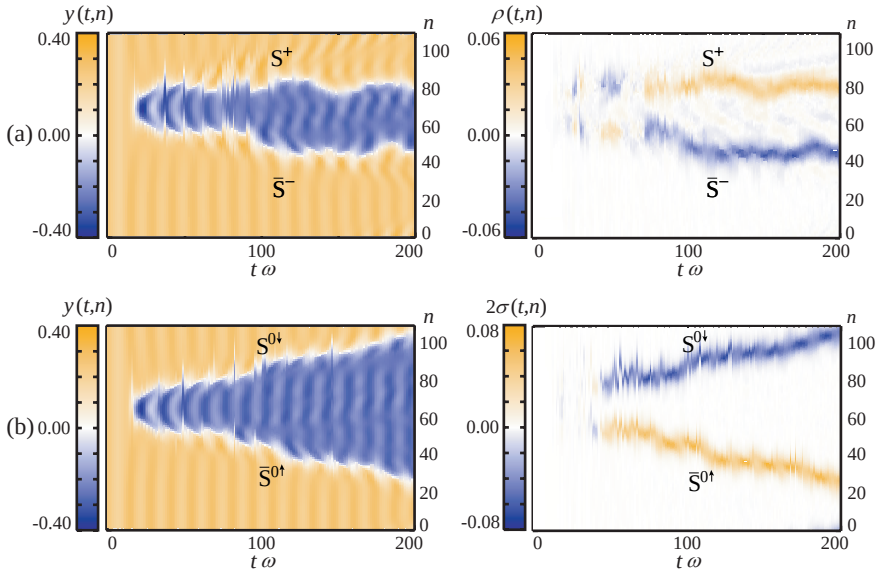

Fig. 2. Nonlinear lattice relaxation channels connected to the charged(a) and neutral(b) soliton pairs, while $y(t, n)$, $\sigma(t, n)$, and $\rho(t, n)$ are respectively, bond order, net spin density, and net charge density on the nth MMX unit at time t.

Figure 3 describes the photogeneration process of polaron pair $P^{-\downarrow} - P^{+\uparrow}$, where the system is in the forth excited state at t=0 by photoexciting. Polarons convey both net charge and spin. The formation mechanism of $P^{-\downarrow} - P^{+\uparrow}$ pair is different from one of $S - \bar{S}$ pair. Exciton of the Franck-Condon type directly relaxes into well separated $P^{-\downarrow} - P^{+\uparrow}$ pair. According to the variational calculations of adiabatic potential energy surfaces,[17] an energy barrier exists between STE and $P^{-\downarrow} - P^{+\uparrow}$ pair. Then STE has no chance to relax into polarons in this system.

In conventional MX chains, it has never been observed that charged solitons and neutral solitons are simultaneously photogenerated, probably because either $S^{+} - \bar{S}^{-}$ or $S^{0\downarrow} - \bar{S}^{0\uparrow}$ pair are necessarily higher in energy than STE.[20] In MMX chains, however, no energy barrier between STE and both soliton pairs should result in the open of both relaxation channels.[17] Our simulation results justify the above prediction. The difference about the soliton channels between MX and MMX chains originates from the difference of the strength of the Coulomb interactions. MMX chains exhibit intermediate e-e interactions($V_{MM} \ll U_M \leq t_{MXM}$)[21,22] and metal binucleation should reduce the on-site repulsion. In this regime, the dynamic features of photoexcited MMX chains are noted above. However, when U_M is comparable with one in MX chains, which is not relevant to realistic compounds, the low-lying adiabatic energy surfaces are very similar to ones in MX chains.[17]

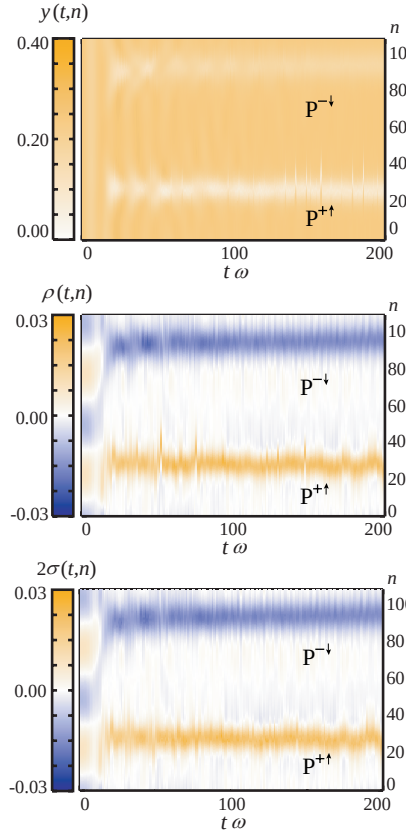

Fig. 3. Nonlinear lattice relaxation channels connected to the polaron pairs, while $y(t,n)$, $\sigma(t,n)$, and $\rho(t,n)$ are respectively, bond order, net spin density, and net charge density on the nth MMX unit at time t.

4. Summary

We have simulated the time evolution of photoexcited states in MMX chains within the time-dependent Hartree-Fock approximation and revealed the photogeneration mechanisms of solitons and polarons. The relaxation channels connected to charged solitons, neutral solitons, and polarons coexist in MMX chains, which is never the case with conventional MX chains. These results may give new insight into the availability of MMX chains as electronic devices.

Acknowledgments

The authors thank K. Iwano and H. Okamoto for fruitful discussions. This work was supported by the 21 COE program on Topological Science and Technology from the Ministry of Education, Culture, Sport, Science and Technology of Japan and the Japan Society for the Promotion of Science.

References

1. W. P. Su, J. R. Schrieffer and A. J. Heeger, *Phys. Rev. Lett.* **42**, 1698 (1979).
2. D. K. Campbell, A. R. Bishop and K. Fesser, *Phys. Rev. B* **26**, 6862 (1982).
3. W. P. Su and J. R. Schrieffer, *Proc. Natl. Acad. Sci. USA* **77**, 5626 (1980).
4. J. Orenstein and G. L. Baker, *Phys. Rev. Lett.* **49**, 1043 (1982).
5. Y. Ono and A. Terai, *J. Phys. Soc. Jpn.* **59**, 2893 (1990).
6. S. V. Rakhmanova and E. M. Conwell, *Appl. Phys. Lett.* **75**, 1518 (1999).
7. M. Kuwabara and K. Yonemitsu, *J. Mater. Chem.* **11**, 2163 (2001).
8. S. Yamamoto, *Phys. Rev. B* **64**, 120102-1(2001)
9. H. Matsuzaki, *et al.*, *Phys. Rev. Lett.* **90**, 1043 (2003).
10. C. -M. Che, *et al.*, *J. Am. Chem. Soc.* **105**, 4604(1983)
11. R. J. H. Clark, *et al.*, *Inog. Chem.* **25**, 409(1986)
12. C. Bellitto, *et al.*, *Inog. Chem.* **22**, 444(1983)
13. S. Ikeuchi, *et al.*, *Phys. Rev. B* **66**, 115110-1(2002)
14. N. Kimura, *et al.*, *Chem. Phys. Lett.* **220**, 40 (1994).
15. S. Yamamoto, *Phys. Rev. B* **66**, 165113-1(2002)
16. H. Kitagawa, *et al.*, *J. Am. Chem. Soc.* **121**, 10068(1999)
17. J. Ohara and S. Yamamoto, *Phys. Rev. B* **73**, O451222-1(2006)
18. A. Terai and Y. Ono, *Prog. Theor Phys. Suppl.* **No. 113**, 177 (1993).
19. M. Suzuki, *Phys. Lett. A* **62**, 319 (1990).
20. K. Iwano, *J. Phys. Soc. Jpn.* **66**, 1088 (1996).
21. S. M. Weber-Mlibrodt, *et al.*, *Phys. Rev. B* **45**, 6435(1992).
22. A. Mishima and K. Nasu, *Phys. Rev. B* **39**, 5758(1989).

REAL SPACE RENORMALIZATION GROUP ANALYSIS WITH THE REPLICA METHOD FOR THE TWO-DIMENSIONAL ISING SPIN GLASS

T. HASEGAWA* and K. NEMOTO

Division of Physics, Graduate School of Science, Hokkaido University, Kitaku, Kita 10-jo Nishi 8-chome, Sapporo 060-0810, Japan
**E-mail: hase@statphys.sci.hokudai.ac.jp*

We propose a new analytical approach to discuss the existence of the spin glass (SG) phase. We apply the real space renormalization group (RG) to the replica Hamiltonian of the two dimensional Ising Edwards-Anderson model. Our RG equations under the replica symmetric (RS) ansatz show the flow diagram that indicates the existence of the SG phase. The critical exponent for the SG transition has a plausible value while that of the multicritical point (MCP) is a complex number. We consider that the latter is due to not taking the RS breaking into account. Indeed we find that the RS breaking parameter is relevant both at the SG critical point and the MCP, indicating the nontriviality of the SG phase of this model.

1. Introduction

In the random bond Ising spin system, where ferromagnetic and antiferromagnetic interactions between spins are randomly distributed, the spin orientation cannot be uniform in space, even at low temperature. This sort of the systems is called the spin glass (SG). In the SGs, it sometimes happens that spins become randomly frozen at low temperature. This phase is called the SG phase. At the ferromagnetic (FM) phase, spins have tendency to orient uniformly, and spin configuration is stable against thermal fluctuation. At the paramagnetic (PM) phase, spins orient randomly, and thermal fluctuation changes spin configuration totally. At the SG phase, spins orient randomly, but spin configuration is stable against thermal fluctuation. It has been established that the mean field model of Ising SG has the SG phase at low temperature.[1,2] The present interest is the phase transition picture for realistic finite dimensional SGs. In this paper, we propose a new analytical approach to discuss the existence of the SG phase of the

two dimensional (2D) Ising SG model: the combination of the real space renormalization group (RG) and the replica method.

2. Model

The system under consideration is the Ising spin system with nearest-neighbor interactions J_{ij} on the triangular lattice:

$$H = -\sum_{<ij>} J_{ij} S_i S_j, \tag{1}$$

$$P(\{J_{ij}\}) = \frac{1}{\sqrt{2\pi J^2}} \exp\Big[\frac{-(J_{ij}-J_0)^2}{2J^2}\Big], \tag{2}$$

where $\{S_i\}$ are the Ising spin variables. The interactions $\{J_{ij}\}$ are random variables obeying the Gaussian distribution with mean J_0 and variance J^2. This model is called the Edwards-Anderson (EA) model.[3] To use RG scheme, which are powerful tools to investigate critical phenomena, we need to deal with the randomness of interactions. The replica method is a way around this difficulty. The replica method makes use of the identity

$$[\log Z_J]_{\rm av} = \lim_{n\to 0} \frac{[{Z_J}^n]_{\rm av} - 1}{n}, \tag{3}$$

where $[\cdots]_{\rm av}$ means the average over the distribution of interactions (configurational average). One prepares n copies of the original systems, and evaluates the configurational average of the product of their partition functions Z^n, instead of evaluating the configurational average of the free energy,

$$\begin{aligned}[{Z_J}^n]_{\rm av} &= [({\rm Tr}_s e^{-\beta H})^n]_{\rm av} \\ &= [{\rm Tr}_{s^1}{\rm Tr}_{s^2}\ldots{\rm Tr}_{s^n} e^{-\beta\sum_a^n H^a}]_{\rm av} \equiv {\rm Tr} e^{-\beta H_{\rm n}}.\end{aligned} \tag{4}$$

The transformed systems by the replica method are spacially regular. Note that finally one must take the limit $n \to 0$. Thus we obtain the effective Hamiltonian;

$$-\beta H_n = K_0 \sum_{<ij>}\sum_{a=1}^{n} S_i^a S_j^a + K^2 \sum_{<ij>}\sum_{<ab>} S_i^a S_j^a S_i^b S_j^b + \frac{nNzK^2}{4}, \tag{5}$$

where $K_0 = \beta J_0$, $K = \beta J$, and $\beta = 1/k_{\rm B}T$. N is the number of spins, z being the coordination number. Here a and b are replica indices running from 1 to the number of replica n. The sum over $\langle ab\rangle$ runs over all replica pairs.

3. Method

Our approach to attack the SG problem is the application of the real space RG proposed by Niemeijer and van Leeuwen (NvL)[4] to the effective Hamiltonian (Fig. 1). We obtain the RG equations at any replica number n about

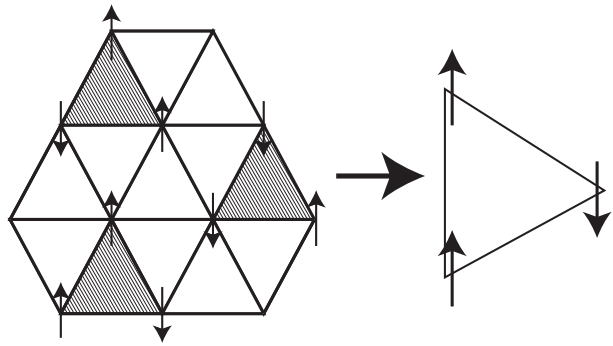

Fig. 1. NvL RG is done by rescaling transformation from the site spin system to the cell spin system on the triangular lattice. The cells are shown as shaded. The direction of a cell spin is determined by the majority rule among the spins in its cell.

two parameters K_0, K, characterizing the effective Hamiltonian. The RG equations are obtained under replica symmetry (RS) ansatz. The RG equations of this model are as follows:[5]

$$K_0' = 2[1 - 2f_1(K_0, K)]^2 K_0, \tag{6}$$

$$K' = \sqrt{2}[1 - 4f_1(K_0, K) + 4f_2(K_0, K)]K, \tag{7}$$

$$f_k(K_0, K) = [X^n]_z^{-1}[\exp(2kKz_1)X^{n-k}]_z, \tag{8}$$

$$X = \exp(4K_0 + 2Kz_0) + \sum_{\mu=1}^{3} \exp(2Kz_\mu), \tag{9}$$

where

$$[\cdots]_z = \int_{-\infty}^{\infty} \prod_{j=0}^{3} \frac{\mathrm{d}z_j}{\sqrt{2\pi}} \exp(-\frac{1}{2}z_j^2) \cdots . \tag{10}$$

4. Results

From the RG equations, we can investigate the RG flow of the 2D SG system. The flow diagram of the EA model is indicated as Fig. 2 and Table 1. The present result indicates

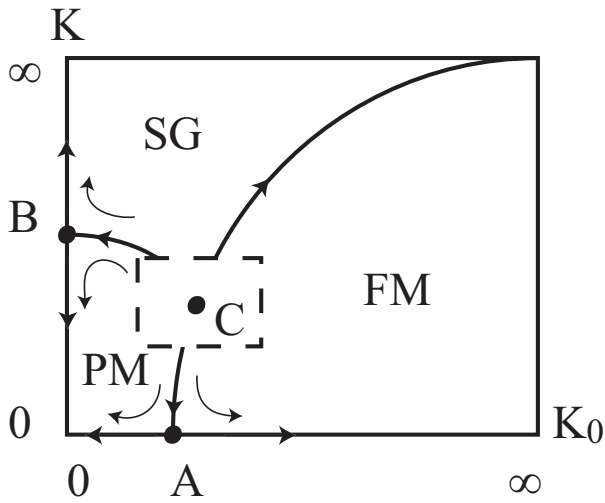

Fig. 2. The schematic flow diagram of the 2D EA model plotted in K_0-K plane. The unstable fixed points are labeled **A**, **B** and **C**. The point **B** indicates the existence of the SG phase at a finite temperature. The point **C** is the multicritical point (MCP), at which our RG equations show that critical exponent ν is a complex number.

Table 1. The positions and the critical exponents $1/\nu$ of unstable fixed points **A**, **B** and **C** shown in Fig. 2 for the 2D EA model.

fixed point	position (K_0,K)	critical exponent $1/\nu$
A	(0.336, 0)	0.88
B	(0, 1.623)	0.55
C	(0.632, 1.037)	0.59 ± 0.25i

- the fixed point **B** means the existence of the SG phase in the 2D EA model.
- the point **C** corrresponds to the multicritical point (MCP) where PM, FM, and SG phases merge, and the critical exponent thereby

is a complex number.

The latter means that the RG flows are not correctly described there. Indeed numerical result shows that RG flow forms a vortex around the MCP. We consider that this failure at the MCP is due to not taking the RS breaking (RSB) into account. It is known that in the mean field theory of SG, the RS solution becomes unstable and the RSB occurs at the low temperature.[6,7] To investigate the stability of the RS solution, we introduce the 1RSB-like parameter L:

$$\{K_{ab}^2\} = K^2 \begin{pmatrix} U & \dots & U \\ U & \dots & U \\ \vdots & \ddots & \vdots \\ U & \dots & U \end{pmatrix} + L^2 \begin{pmatrix} U & & & 0 \\ & U & & \\ & & \ddots & \\ 0 & & & U \end{pmatrix}, \tag{11}$$

where U is an $m \times m$ matrix whose elements are all 1, and there are n/m blocks in the whole matrix. The first term of r.h.s., corresponds to the parameter in the case of the RS ansatz while the second term represents a perturbation to the RS solution. Now, the RG equations are extended into functions of three variables, K_0, K, and L. The RS solution is unstable (stable) against the perturbation if the perturbation parameter L is relevant (irrelevant) around $L = 0$. The derivation of the extended RG equations is straightforward.[5] Indeed, from the obtained RG equations, $K_0' = K_0'(K_0, K, L)$, $K' = K'(K_0, K, L)$, and $L' = L'(K_0, K, L)$, we can find that $\frac{\partial L'}{\partial L}|_{L=0} > 1$ and thus the replica symmetry breaks at MCP.

5. Summary

We have tried to apply the real space RG to the replica Hamiltonian of the 2D Ising EA model. Our result indicates the existence of the SG phase for the 2D EA model. Unfortunately the critical exponent at the MCP is a complex number, which means that the RG flow forms a vortex around the MCP. Here we have shown that the RS solution is unstable against 1RSB like perturbation and therefore we expect that this fact indicates non-triviality of the SG phase.

Acknowledgment

This work is supported by the 21st Century Center of Excellence (COE) program entitled "Topological Science and Technology", Hokkaido University.

References

1. M. Mézard, G. Parisi and M. A. Viraroso: *Spin Glass Theory and Beyond* (World Scientific, Singapore, 1987).
2. H. Nishimori: *Statistical Physics of Spin Glasses and Information Proceeding: An Introduction* (Oxford University Press, Oxford, 2001).
3. S. F. Edwards and P. W. Anderson: *J. Phys. F* **5**, 965 (1975).
4. Th. Niemeijer and J. M. J. van Leeuwen: *Phase Transitions and Crtical Phenomena* , eds. C. Domb and M. S. Green (Academic Press, London, 1976) Vol.6, p.425.
5. T. Hasegawa and K. Nemoto: to appear in *J. Phys. Soc. Jpn.* Vol.75 No.7 .
6. G. Parisi: *J. Phys. A* **13**, 1101 (1980).
7. G. Parisi: *J. Phys. A* **13**, L115 (1980).

QUANTUM NETWORK MODELS AND THEIR SYMMETRY PROPERTIES

T. OHTSUKI

Department of Physics, Sophia University,
7-1 Kioicho, Chiyodaku, Tokyo 102-8554, Japan
E-mail: ohtsuki@sophia.ac.jp

K. M. SLEVIN

Department of Physics, Osaka University,
1-1 Machikaneyama, Toyonaka, Osaka 560-0043, Japan
E-mail: slevin@margaux.phys.sci.osaka-u.ac.jp

Network models are both simple and general. In solid states physics, quantum network models that take into account the wave nature of the electron have been the subject of intense research. One example is the Chalker–Coddington model that describes the quantum Hall effect (J. T. Chalker, P. D. Coddington, J. Phys., C **21** 2665 (1988)). In this paper we focus on the transfer matrices that describe these models. We emphasize the symmetry properties of these matrices and the consequences for eigenvalue and transport properties.

Keywords: Chalker–Coddington model, quantum network model, quantum Hall effect, Anderson localization

1. Introduction

Since its discovery in 1980,[1] the quantum Hall effect has been the subject of intense study, both theoretical and experimental. The effect occurs in two dimensional electron systems that are subjected to high perpendicular magnetic fields, so high that all the conduction electrons are contained in only the lowest few Landau levels. Anderson localization, a quantum interference phenomenon that occurs when electrons are subject to a random potential, is the reason that the plateau of the Hall conductivity is observable.[2] Electrons in a disordered two dimensional system subject to a high perpendicular magnetic fields are described by the Hamiltonian,[3]

$$H = \frac{1}{2m}(\vec{p} + e\vec{A})^2 + V(\vec{r}). \tag{1}$$

Here $e(>0)$ is the elementary charge, $\vec{A}$ is the vector potential giving rise to the magnetic field $\vec{B} = (0, 0, B)$, and V is the random potential.

The matrix representation of the above Hamiltonian in the Landau state basis is very complicated because many off-diagonal elements appear. While in the tight-binding basis we have to contend with Landau band mixing, which is irrelevant as regards the quantum Hall transition. The Chalker–Coddington model[4] is free from these difficulties. The model is based on the following observations:

(1) In very high magnetic fields, the magnetic length $\ell_B = \sqrt{\hbar/eB}$ becomes shorter than the potential correlation length ℓ_c. The electrons then exhibit a classical cyclotron motion with the center drifting along the contours of the random potential.[5]
(2) Quantum mechanical tunneling of electrons between equipotential lines occurs at the saddle points of the random potential.

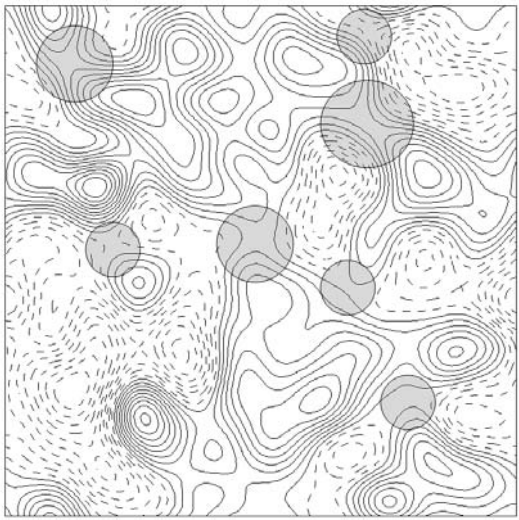

Fig. 1. Potential landscape. The shaded circles indicate saddle points.

We display a schematic of a random potential in Fig. 1. The saddle points are indicated by shaded circles. Regarding the saddle points as nodes and the equipotential lines as links that carry particle fluxes, we describe the quantum mechanical tunneling at the nodes by a 2×2 S matrix. In this

way the quantum Hall problem is mapped to a quantum network model called the Chalker–Coddington model. Details of the derivation are given in the review by Kramer, Ohtsuki and Kettemann.[3] While the structure of the Chalker–Coddington network model is regular, the phase factor along a link is random, reflecting the random length of the equipotential line from one saddle point to another. Since the particle fluxes propagating along the links interfere with each other quantum mechanically, this network model is essentially different from classical network models. In this paper, we concentrate on the transfer matrices that relate the particle fluxes in different layers of the system. We emphasize the symmetry properties of these matrices and the consequences of those symmetries for eigenvalue and transport properties.[6]

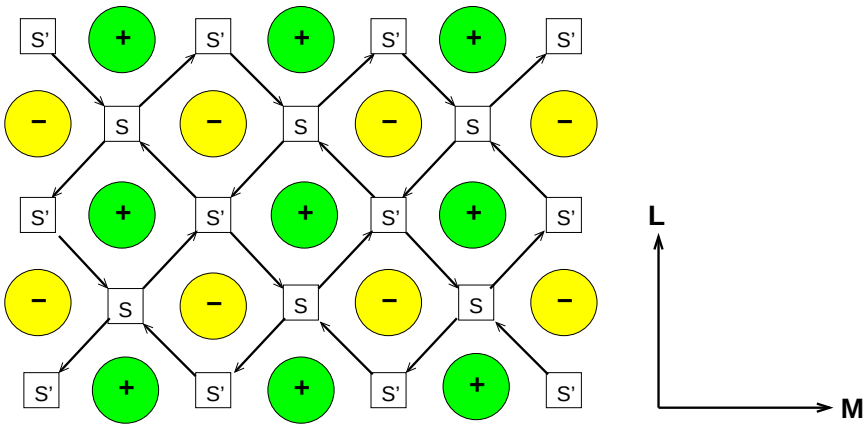

Fig. 2. The Chalker–Coddington network model. Nodes S and its $\pi/2$ rotation S' are described by 2×2 S matrices. M is the number of nodes in the direction of current flow and L the number of nodes transverse to it. The $+$ and $-$ symbols indicate potential hills and valleys, respectively.

2. Symmetry Properties

We consider a two terminal geometry where reservoirs are attached to the left and right hand sides of the sample. We assume L nodes in the L direction in Fig. 2. This means that we have L incoming and L outgoing particle fluxes at the left and right sides.

2.1. *S matrix*

The S matrix relates incoming flux amplitudes to outgoing amplitudes. In the present situation,

$$\begin{bmatrix} o^{\mathrm{L}} \\ o^{\mathrm{R}} \end{bmatrix} = S \begin{bmatrix} i^{\mathrm{L}} \\ i^{\mathrm{R}} \end{bmatrix}, \tag{2}$$

where i^{L} (i^{R}) denotes the vector of flux amplitudes coming from the left (right) side, and o^{L} (o^{R}) the vector of flux amplitudes outgoing to the left (right). These vectors are all L dimensional vectors and S is a $2L$ dimensional square matrix. S consists of submatrices,

$$S = \begin{bmatrix} r & t' \\ t & r' \end{bmatrix} \tag{3}$$

where r (r') is an L dimensional square matrix describing the reflection of flux coming from the left (right) of the sample, and t (t') describing the transmission of flux from left (right) to right (left). Since particle flux is conserved

$$|i^{\mathrm{L}}|^2 + |i^{\mathrm{R}}|^2 = |o^{\mathrm{L}}|^2 + |o^{\mathrm{R}}|^2. \tag{4}$$

This leads to a unitarity condition,

$$SS^{\dagger} = S^{\dagger}S = 1_{2L}. \tag{5}$$

Here 1_n is the n dimensional identity matrix.

The Chalker–Coddington model does not have time reversal symmetry (TRS) because the particle fluxes on the links are directed. It is possible to recover TRS by adding counter-directing links. If we arrange that each outgoing flux is the time reversed state of some incoming flux, the TRS condition imposed on S is,

$$S = S^{\mathrm{T}}. \tag{6}$$

Here S^{T} means transpose of the matrix S.

So far we have not considered the spin degree of freedom. We have two ways to include spin-flip process. One is through spin-scattering where both TRS and spin rotation symmetry (SRS) are broken. Another is through the spin-orbit scattering where SRS is broken but TRS is preserved. In the latter case, the condition on S reads

$$S = -S^{\mathrm{T}}. \tag{7}$$

This has an important physical consequence; the transmission eigenvalues (eigenvalues of $t^{\dagger}t$) are always doubly degenerate.

2.2. *Transfer matrix*

The transfer matrix T relates the particle flux amplitudes at the left side to the particle flux amplitudes at the right side. In the present situation,

$$\begin{bmatrix} o^{\mathrm{R}} \\ i^{\mathrm{R}} \end{bmatrix} = T \begin{bmatrix} i^{\mathrm{L}} \\ o^{\mathrm{L}} \end{bmatrix}. \tag{8}$$

Since particle flux is conserved,

$$|i^{\mathrm{L}}|^2 - |o^{\mathrm{L}}|^2 = |o^{\mathrm{R}}|^2 - |i^{\mathrm{R}}|^2. \tag{9}$$

This leads to a so-called pseudo-unitarity condition,

$$\Sigma_3 = T^\dagger \Sigma_3 T\,, \tag{10}$$

where

$$\Sigma_3 = \begin{bmatrix} 1_L & 0_L \\ 0_L & -1_L \end{bmatrix}. \tag{11}$$

Here 0_L is the L dimensional zero matrix. Pseudo-unitarity guarantees that the eigenvalues of $T^\dagger T$ occur in reciprocal pairs $\lambda, 1/\lambda$.

In the presence of TRS, the transfer matrix T satisfies

$$\Sigma_1 T \Sigma_1 = T^*\,, \tag{12}$$

where

$$\Sigma_1 = \begin{bmatrix} 0_L & 1_L \\ 1_L & 0_L \end{bmatrix}, \tag{13}$$

and T^* means complex conjugation of T. It follows that in this case the transfer matrix can always be transformed to a real matrix by a unitary transformation.

When we break SRS while preserving TRS, we have

$$\Sigma_2 T \Sigma_2 = -T^*\,, \tag{14}$$

where

$$\Sigma_2 = \begin{bmatrix} 0_L & -\mathrm{i}1_L \\ \mathrm{i}1_L & 0_L \end{bmatrix}. \tag{15}$$

This condition guarantees that the eigenvalues of $T^\dagger T$ are always doubly degenerate.

Detailed derivations, and an explanation of the differences between these particle flux transfer matrices and the wavefunction transfer matrices, can be found in a forthcoming monograph the authors.[6]

3. Summary

We have reviewed the Chalker–Coddington model that describes the quantum mechanical propagation of electrons in random media. We discussed the symmetry of the network model and the consequences for the S matrices and transfer matrices. From particle flux conservation, unitarity (5) and pseudo-unitarity (10) should always hold.

According to the classfication used in random matrix theory,[7] systems with both TRS and SRS have orthogonal symmetry, those with TRS but without SRS have symplectic symmetry and those without either symmetry are unitary. The S matrices and transfer matrices with orthogonal symmetry satisfy (6) and (12), respectively, while with symplectic symmetry (7) and (14) are satisfied.

If we impose additional discrete symmetries, 7 other symmetries appear.[8] For the total of 10 symmetries there are corresponding quantum network models.[3]

References

1. K. von Klitzing, G. Dorda, M. Pepper, *Phys. Rev. Lett.* **45**, 494 (1980).
2. H. Aoki, T. Ando, *Solid State Commun.* **38**, 1079 (1981).
3. B. Kramer, T. Ohtsuki, S. Kettemann, *Physics Reports* **417**, 211 (2005).
4. J. T. Chalker, P. D. Coddington, *J. Phys. C* **21**, 2665 (1988).
5. M. Tsukada, *J. Phys. Soc. Jpn.* **41**, 1466 (1976).
6. K. Slevin, T. Ohtsuki, *Anderson Localisation: The Numerical Approach* (unpublished).
7. M. L. Mehta, *Random Matrices, 3rd edition* (Elsevier, New York, 2004).
8. A. Altland, M. R. Zirnbauer, *Phys. Rev. B* **55**, 1142 (1997).

FRACTALITY OF CRITICAL PERCOLATION NETWORKS

M. MITOBE* and K. YAKUBO†

Department of Applied Physics, Graduate School of Engineering,
Hokkaido University,
Sapporo 060-8628, Japan
** E-mail: mitobe@eng.hokudai.ac.jp*
† E-mail: yakubo@eng.hokudai.ac.jp

The self-averaging nature of statistical quantities at criticality has been studied by examining infinite clusters in two-dimensional bond percolation systems at the percolation threshold p_c. We calculate fractal dimensions Δ_f for individual clusters and obtain the distribution function of Δ_f. It has been clarified that the system size dependence of the variance $\mathrm{var}(\Delta_f)$ can be explained by the scaling theory if eliminating non-fractal critical clusters (NFCC) from the original ensemble of infinite clusters. This implies the absence of the self-averaging nature at the critical point of percolation systems because of the existence of NFCC at p_c even in the thermodynamic limit.

Keywords: Percolation; Critical fluctuations; Fractal; Universality.

1. Introduction

Percolation theory describes a large number of physical and chemical phenomena such as gelation processes, transport in amorphous materials, hopping conduction in doped semiconductors, quantum Hall effect, and many other applications.[1–3] In addition, it forms the basis for studies of the flow of liquids or gases through porous media. The most striking feature of the percolation model lies in its criticality at the percolation threshold p_c.[4] Above the critical concentration p_c, there exists an infinite (percolating) cluster in the system. This cluster has its characteristic length $\xi \propto |p-p_c|^{-\nu}$, *i.e.*, the correlation length. No other length scale exists in the system if p is close to p_c. Since ξ diverges at $p = p_c$, the infinite cluster just at p_c takes a fractal structure. The exponent describing self-similarity of the spatial extent of the critical percolating cluster is the fractal dimension. These properties are quite similar to thermodynamic second-order phase transitions. In fact, the percolation system can be regarded as a kind of the Potts model which in-

cludes the Ising model exhibiting a ferromagnetic phase transition.[5] There exists, however, crucial difference between thermal and geometrical critical phenomena. In the case of thermal critical phenomena, observed physical quantities are always averaged in time even at the critical point. This is related to the fact that thermal fluctuations induce critical phenomena. We have powerful tools, such as the scaling theory and the renormalization group theory, to describe critical behaviours of such averaged quantities. On the contrary, fluctuations are stochastic and quenched in a percolation system. Statistical quantities of the percolation system not at the threshold p_c are averaged over subsystems of finite size ξ (self-average). Just at the percolation threshold, however, it is not obvious that the self-average is taken for these quantities, because the correlation length ξ diverges. In the case of the absence of the self-average, one cannot determine critical properties just at the critical point, such as the fractal dimension or the ac conductivity exponent, from a single critical sample. It is, therefore, quite important to clarify whether the self-average is taken for statistical quantities in an infinite critical system.

In this paper, we study the self-averaging nature at the critical point by examining fractality of individual critical percolation clusters. In order to elucidate this problem, we form a large number of critical percolating clusters on two-dimensional square lattices and examine statistical properties of their structures. Results show that there exist non-fractal critical clusters (NFCC) with a finite probability even in infinite systems though the most probable (typical) critical clusters are fractal critical clusters. This implies that statistical quantities are not self-averaged in a single critical percolation system.

2. Distribution of fractal dimensions

There exist several types of percolation models. In this paper, we concentrate the bond-percolation model formed on a regular lattice. The reason why we adopt this model is the advantage in the shortness of the lower cut-off of the length scale for which the critical system can be regarded as a fractal. A bond-percolation system is constructed by the following simple procedures. At first, adjacent lattice points are randomly connected by bonds with probability p. A clump of lattice points connected each other by bonds is regarded as a cluster. The average cluster size, namely, the average number of lattice points included in clusters, increases with the probability p, and the largest cluster size diverges when p exceeds a certain value p_c (percolation threshold). The continuous but drastic change at

this point provides the percolation transition. Many of previous numerical works confirm that critical percolating clusters take fractal structures. A simple scaling argument leads the relation $D_{\rm f} = d - \beta/\nu$, where $D_{\rm f}$ and d are the fractal and Euclidean dimensions, respectively. Especially, $\beta = 5/35$ and $\nu = 4/3$ for two-dimensional percolation systems give $D_{\rm f} = 91/48 \approx 1.8958$. This value of $D_{\rm f}$ is also believed to be universal.

If the structure of a cluster is fractal, the density of sites belonging to the cluster behaves as $\varrho(r) \propto r^{\Delta_{\rm f}-d}$, where $\varrho(r)$ is the site density within a region of radius r and $\Delta_{\rm f}$ is the fractal dimension defined for the specific cluster. It should be emphasized that we must distinguish $\Delta_{\rm f}$ for individual infinite clusters from $D_{\rm f}$ for typical clusters. The fractal nature of a cluster can be also characterized by the density-density correlation function $G(\boldsymbol{r}_n)$ between two points apart each other by $\boldsymbol{r}_n$, namely, $G(\boldsymbol{r}_n) = (1/N)\sum_m \rho(\boldsymbol{r}_m)\rho(\boldsymbol{r}_m + \boldsymbol{r}_n)$, where $\rho(\boldsymbol{r}_n)$ is the density at the position $\boldsymbol{r}_n$ and N is the total number of sites. It should be noted that any average procedures are not included in this expression. In a percolation cluster, $\rho(\boldsymbol{r}_n)$ takes unity if the site $\boldsymbol{r}_n$ belongs to the cluster and zero otherwise. If the system is isotropic in a statistical sense as percolation systems are so, the correlation function depends only on $|\boldsymbol{r}_n|$. In such a case, this correlation function can be written as $G(r) = \langle\rho(\boldsymbol{r})\rho(0)\rangle$, where $\langle\cdots\rangle$ denotes the average over the choices of the origin $\boldsymbol{r} = 0$ and directions of $\boldsymbol{r}$. The quantity $\langle\rho(\boldsymbol{r})\rho(0)\rangle$ is proportional to the probability that a site belonging to the cluster exists at a distance r from another site in the cluster. This probability is proportional to the site density $\varrho(r)$ within a sphere of radius r. Using the expression for $\varrho(r)$, the correlation function $G(r)$ for fractal clusters, then, behaves as

$$G(r) \propto r^{\Delta_{\rm f}-d} \ . \tag{1}$$

We determine the fractal dimensions $\Delta_{\rm f}$ of individual critical percolation clusters by the least-square fit with Eq. (1).

Just at the percolation threshold, some of the largest clusters are spanned over the whole systems, while others are not. Since our purpose is to clarify fractality of infinite clusters at $p = p_{\rm c}$ in the thermodynamic limit, only the spanning clusters are considered. In this context, the choice of boundary conditions determines the efficiency of numerical calculations. We adopt periodic boundary conditions in the present work. In addition that periodic boundary conditions minimize undesired boundary effects, the probability that the maximum critical cluster is spanned over the system is significantly high compared to the case of systems with open bound-

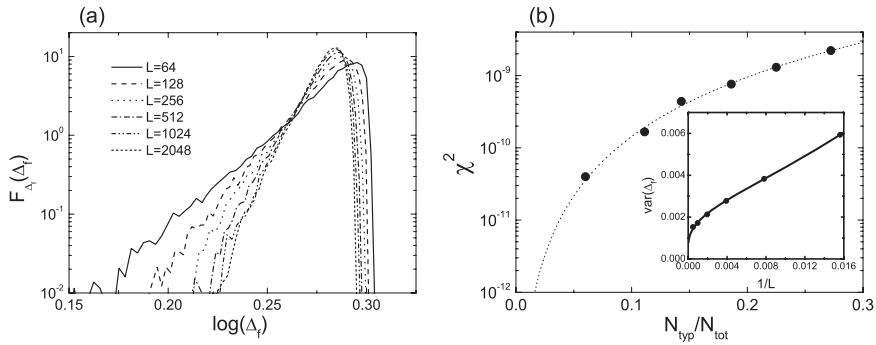

Fig. 1. (a) Distribution functions of fractal dimensions of individual critical clusters formed in several system sizes. (b) Values of χ^2 of the fitting of the L dependence of $\mathrm{var}(\Delta_\mathrm{f})$ as a function of $N_\mathrm{typ}/N_\mathrm{tot}$. The inset shows the L dependence of $\mathrm{var}(\Delta_\mathrm{f})$ for the whole critical cluster samples.

ary conditions. This implies that the statistical advantage in the number of spanning clusters provides accurate results in the case of periodic boundary conditions.

The distribution function of Δ_f for several system sizes are shown in Fig. 1(a). The fractal dimension Δ_f fluctuates over samples in finite systems whereas the width of the distribution function becomes narrower as the system size increases. For any system sizes, the distribution functions of Δ_f much lower than the typical (mode) values $\Delta_\mathrm{f}^\mathrm{typ}$ obey power laws, while they decrease rapidly for $\Delta_\mathrm{f} > \Delta_\mathrm{f}^\mathrm{typ}$. This means that there exist critical clusters characterized by very small fractal dimensions at least in finite systems. To see quantitatively the system size dependence of the variance of Δ_f, we plot $\mathrm{var}(\Delta_\mathrm{f})$ as a function of $1/L$ by filled circles in the inset of Fig. 1(b). The variance distinctly decreases as increasing L.

3. Non-fractal critical clusters

Let us analyze the L dependence of $\mathrm{var}(\Delta_\mathrm{f})$ by assuming that all of spanning critical clusters take fractal structures and the cluster size m is proportional to L^{Δ_f}, *i.e.*,

$$m = \gamma L^{\Delta_\mathrm{f}} \ , \tag{2}$$

where γ is a constant over samples. This implies that the fluctuation of m is due to the fluctuation of Δ_f. In this case, the distribution function of Δ_f is simply related to the distribution function of m by

$$F_m(m)dm = F_{\Delta_\mathrm{f}}(\Delta_\mathrm{f})d\Delta_\mathrm{f} \ . \tag{3}$$

Using Eqs. (2) and (3), the average $\langle \Delta_{\rm f} \rangle = \int \Delta_{\rm f} F_{\Delta_{\rm f}} d\Delta_{\rm f}$ is given by

$$\langle \Delta_{\rm f} \rangle = \frac{\langle \ln m \rangle}{\ln L} - \frac{\ln \gamma}{\ln L} \ . \tag{4}$$

Denoting the geometric mean of m by M, $\langle \ln m \rangle$ is equal to $\ln M$. Since the geometric mean M is proportional to the most probable (typical) value of the cluster size, we have

$$M = cL^{D_{\rm f}} \ , \tag{5}$$

where c is a constant coefficient and $D_{\rm f}$ is the fractal dimension of the typical percolation cluster. It should be noted that $D_{\rm f}$ is the fractal dimension argued in the scaling theory and predicted as $D_{\rm f} = 91/48 \approx 1.8958$. In fact, the L dependence of our numerical data $\langle \ln m \rangle$ gives $D_{\rm f} = 1.8955 \pm 0.0002$. Thus, we obtain

$$\langle \Delta_{\rm f} \rangle - D_{\rm f} = \frac{\ln(c/\gamma)}{\ln L} \ . \tag{6}$$

Furthermore, the variance $\mathrm{var}(\Delta_{\rm f}) = \int [\Delta_{\rm f} - \langle \Delta_{\rm f} \rangle]^2 F_{\Delta_{\rm f}}(\Delta_{\rm f}) d\Delta_{\rm f}$ can be calculated as

$$\mathrm{var}(\Delta_{\rm f}) = \frac{\mathrm{var}(\ln m)}{(\ln L)^2} \ , \tag{7}$$

where $\mathrm{var}(\ln m)$ is the variance of $\ln m$. The scaling argument shows that $\mathrm{var}(\ln m)$ does not depend on the system size L for very large L. Due to our finite system sizes, however, we should take into account the scaling correction for $\mathrm{var}(\ln m)$, where $\mathrm{var}(\ln m)$ can be written as $\mathrm{var}(\ln m) = v_\infty + aL^{-y}$, where v_∞ and a are constants and y is an irrelevant exponent. In this case, $\mathrm{var}(\Delta_{\rm f})$ is given by

$$\mathrm{var}(\Delta_{\rm f}) = \frac{v_\infty + aL^{-y}}{(\ln L)^2} \ . \tag{8}$$

Solid line in the inset of Fig. 1(b) represents the least square fit for the data of filled squares by Eq. (8) with three fitting parameters v_∞, a, and y. The curve seems to agrees well with our numerical data.

Here we should remark that the individual fractal dimension $\Delta_{\rm f}$ shown in Fig. 1(a) are forcedly calculated by the least-square fit even if Eq. (1) does not hold. Therefore, there is a possibility of a violation of the initial assumption to derive Eq. (8), namely, all critical clusters are fractal and satisfy Eq. (2). In order to check this possibility, we evaluate the variance $\Gamma = \mathrm{var}[\log G(r) - \log G^*(r)]$ where $G^*(r) = G_0 r^{\Delta_{\rm f} - d}$ with the coefficient G_0 and $\Delta_{\rm f}$ obtained by the least-square fit for $G(r)$.[6] The quantity Γ is

small (large) when a given cluster is close to (far from) fractal. Introducing a criterial value Γ^*, clusters with $\Gamma < \Gamma^*$ can be regarded as typical. Figure 1(b) shows the value of χ^2 (a measure of the goodness-of-fit) of the fitting of var($\Delta_{\rm f}$) with Eq. (8) only for typical clusters as a function of $N_{\rm typ}/N_{\rm tot}$, where $N_{\rm tot}$ is the number of total spanning samples averaged over different sizes ($N_{\rm tot} = 40,000$ in this study) and $N_{\rm typ}$ is the average number of typical clusters which varies with Γ^*. χ^2 decreases with decreasing $N_{\rm typ}/N_{\rm tot}$, which means, even in infinite systems, non-fractal critical clusters (NFCC) prevent us to analyze data along the relation Eq. (8) based on the assumption that all of spanning critical clusters take fractal structures. These analyses of fluctuations of fractal dimensions suggest the existence of NFCC in infinite critical systems and that statistical quantities are not self-averaged within a single crtical percolation cluster.

4. Conclusions

We study, from a viewpoint of fractality, the self-averaging nature of statistical quantities of infinite clusters in two-dimensional bond percolation systems at the critical point. We have calculated the distribution function of fractal dimensions $\Delta_{\rm f}$ defined for individual samples. If we eliminate non-fractal critical clusters (NFCC) with large Γ from the ensemble of spanning critical clusters, the L dependence of the variance var($\Delta_{\rm f}$) can be explained by the scaling theory taking into account its correction term. This implies the absence of the self-averaging nature at the critical point of percolation systems because there exist NFCC at the percolation transition point even in the thermodynamic limit. Our finding corresponds to the existence of anomalously localized states at the Anderson transition point[6] and requires us to take an ensemble average when determining critical properties just at the critical point.

References

1. D. Stauffer and A. Aharony, *Introduction to Percolation Theory*, (Taylor & Francis, London, 1994).
2. M. Sahimi, *Applications of Percolation Theory*, (Taylor & Francis, London, 1994).
3. M. B. Isichenko, *Rev. Mod. Phys.* **64**, 961 (1992).
4. D. Stauffer, *Phys. Rep.* **54**, 1 (1979).
5. F. Y. Wu, *Rev. Mod. Phys.* **54**, 235 (1982).
6. H. Obuse and K. Yakubo, *Phys. Rev. B* **69**, 125301 (2004).

ISING PHASE TRANSITION ON CURVED SURFACES

Y. SAKANIWA*, I. HASEGAWA and H. SHIMA

Department of Applied Physics, Graduate School of Engineering, Hokkaido University, Sapporo 060-8628, Japan
**E-mail: sakaniwa@eng.hokudai.ac.jp*

Critical behaviour of the two-dimensional Ising model defined on a pseudosphere is numerically studied. Employing the finite-size scaling analysis, we observe a quantitative deviation of static critical exponents from the case of the Ising lattice model on a flat plane. This finding indicates the occurrence of a novel universality class of the Ising model on negatively curved surfaces.

1. Introduction

The two-dimensional Ising model is the simplest system exhibiting a second-order phase transition.[1] This model has long served as fertile testing grounds for innumerable projects in statistical physics, mainly due to its broad applicability to real systems and the availability of analytic solutions for its physical quantities. Thorough investigations on this model have thus far evidenced that its critical behavior is universal to a large extent depending on a small number of parameters of the system.[2]

Conventionally the two-dimensional Ising model is assumed to be defined on a flat plane.[3] In the last decade, however, there has been a growing interest in the nature of the Ising model assigned on a curved surface.[4–12] This interest is partly motivated by its relevance to quantum gravity theory,[13–15] and partly by the substantial progress in nanotechnology that makes it possible to produce curved magnetic layers of desired shapes.[16] A main concern of this subject is whether the surface curvature of the underlying geometry is responsible for determining the universality class of the system. Introducing a finite curvature into the underlying geometry alters the essential symmetry of the Hamiltinian describing the system; therefore, it may affect the universal quantities of the system such as values of critical exponents.

Several investigations have suggested that, when the underlying geom-

etry of the Ising model is topologically equivalent to a sphere,[5–8,10] the critical exponents do not deviate from the known values on the planer Ising model. It is unconvincing, however, whether this conclusion can be applied to the cases of general curved geometry. This is firstly because, the closed form of sphere-like surfaces disable to take the thermodynamic limit with keeping a constant surface curvature. Secondly because, in most systems studied so far, the magnitude of curvature is spatially concentrated on a portion of the surface, even producing a conical singularity. These unfavorable features would hinder to extract purely the curvature effect on critical properties from other incidental contributions.

A possible means to cope with the above inexpediency is to exploit a surface that can spread out infinitely with keeping a nonzero curvature. A typical example is a surface of constant negative curvature, called a pseudosphere.[17,18] The pseudosphere is a simply connected and infinite surface, in which the Gaussian curvature at arbitrary points possesses a constant negative value. Hence, it serves as an exemplary geometry to consider the curvature effect on the critical properties of the system. It is noteworthy that the pseudosphere enters in various physical issues ranging from quantum physics,[19,20] the string theory[21] to cosmology,[22] wherein the geometric character underlying the system is of great significance.

In the present article, we consider the critical behavior of the two-dimensional Ising model assigned on the pseudosphere, aiming to clarify the effect of surface curvature on the universality class of the system. By means of Monte Carlo simulations and the finite-size scaling analysis, we have revealed that a series of critical exponents exhibit distinct values from those in a planer Ising model. These findings establish the advent of a novel universality class for the Ising model induced by a finite curvature of the underlying geometry.

2. Poincaré disk model

The pseudosphere is defined as one sheet of the double-sheeted hyperboloid:

$$x^2 + y^2 - z^2 = -1 \quad (z \geq 1), \tag{1}$$

that is constructed in the Minkowski space. It follows from the Minkowskian metric $ds^2 = dx^2 + dy^2 - dz^2$ that Eq. (1) specifies the locus of points whose square distance from the origin are equal to -1. Hence, it is called a *pseudo*-sphere having the radius $i = \sqrt{-1}$ by analogy with the sphere.

While the above definition is rigorous, it is clumsy for computations since three coordinates are used for only two degrees of freedom. We thus

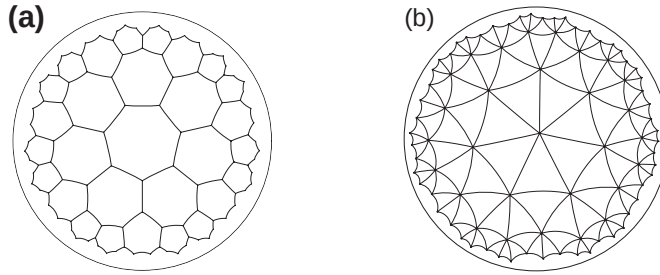

Fig. 1. A regular heptagonal (left) and triangular (right) lattice embedded on the Poincaré disk. All polygons depicted in the figures are equilateral and congruent in the sense of the metric given in Eq. (2).

use an alternative representation of the pseudosphere which is more convenient to deal with; it is the Poincaré disk model. Suppose that the upper hyperboloid sheet is projected onto the x-y plane through the following mapping: $(x, y, z) \rightarrow \left(\frac{x}{1+z}, \frac{y}{1+z}\right)$. This transforms the upper sheet to a unit circle endowed with the metric

$$ds^2 = f(dx^2 + dy^2), \quad f = \frac{4}{(1 - x^2 - y^2)^2}. \tag{2}$$

The unit circle possessing the metric (2) is referred to as a Poincaré disk, serving as a compact representation of the pseudosphere (The boundary of the disk corresponds to the points at infinity of the hyperboloid). In fact, the Gaussian curvature κ on the disk,[23] determined by $\kappa = -\frac{1}{f^2}\left(\frac{\partial^2}{\partial x^2} + \frac{\partial^2}{\partial y^2}\right)\log f$, taken $\kappa = -1$ at arbitrary points on the disk.

Notably, on the Poincaré disk, it is possible to build a wide variety of *equilateral* polygonal lattices that are impossible to be realized on a flat plane. Figures 1(a) and (b) each illustrates a heptagonal and triangular lattice embedded on the Poincaré disk. Although polygons depicted in the figures appear to be distorted, they all are surely equilateral and congruent in the sense of the metric of Eq. (2). In what follows, we proceed our argument in terms of the lattice depicted in Figs. 1(a) and (b).

3. Model and methods

We have considered the two-dimensional ferromagnetic Ising model with the Hamiltonian $H = -J\sum_{<i,j>} s_i s_j$, where the Ising spin variable s_i takes the values ± 1, and $< i, j >$ denotes a pair of nearest-neighbor sites on lattices with the fixed boundary condition. The coupling strength J between neigh-

boring spins is defined to be a constant, which is due to the fact that all the Ising spins assigned on the pseudosphere is equally-spaced. Throughout this work, units of J/k_{B} and J are used for temperatures and energies, respectively. The order parameter m per site for a given configuration of $\{s_i\}$ is given by $m = \sum_{i=1}^{N} s_i/N$, where N is total number of sites. The expectation value of the order parameter $\langle m \rangle$ as well as the k-th moments $\langle m^k \rangle$ at a temperature T are determined by employing Monte Carlo simulations. Sampling of the configurational space has been carried out by the cluster flip algorithm,[24] and the averaging were taken from 5×10^4 configurations.

Critical exponents characterizing the universality class of the system have been obtained by using the finite-size scaling technique. The scaling hypothesis says that, in the vicinity of the transition temperature T_c, the free energy $f(T, N)$ for a finite system size N obeys the scaling law:

$$f(T, N) = N^{-(2-\alpha)/\mu} \cdot F\left(\varepsilon N^{1/\mu}\right), \ \varepsilon = |T - T_c|/T_c \ . \tag{3}$$

Appropriate differentiation of the free energy yields the spontaneous magnetization $m(T, N) = \langle |m| \rangle$ and the magnetic susceptibility $\chi(T, N) = N\frac{\langle m^2 \rangle - \langle |m| \rangle^2}{k_{\mathrm{B}} T}$, whose scaling behaviors are expressed by

$$m(T, N) \propto N^{-\beta/\mu} \cdot m_0(x), \quad \text{and} \quad \chi(T, N) \propto N^{\gamma/\mu} \cdot \chi_0(x), \tag{4}$$

with the argument $x = \varepsilon N^{1/\mu}$. Here, the exponents β, γ and μ are referred to as the critical exponent for the magnetization m, susceptibility χ, and the correlation volume $\xi_V \propto \varepsilon^{-\mu}$, respectively. These expornents can be accurately evaluated by the χ^2-fitting procedure; in-depth explanations regarding this technique are given in Ref. 25.

4. Results

Figures 2(a) and (b) show the spontaneous magnetization $m(T, N)$ of the Ising model with (a) heptagonal and (b) trianglar lattice sturucture. Each figure shows typical behavior indicating the occurrence of the ferromagnetic transition; in the vicinity of a critical temprature, the slope of a tangent line of $m(T)$ become divergent with increasing system size N. We have also calculated the zero-field susceptibility $\chi(T, N)$ of the two lattices, and found a sharp peak[26] at $T \sim 1.2$ and $T \sim 3.0$, respectively, characterizing the Ising phase transition (figures are omitted). Table 1 surmmarises numerical results of critical exponents and critical temprature evaluated by the finit-size scaling analysis. The most striking fact is that, both for the heptagonal and trianglar lattices, all the exponents take values different from the exact

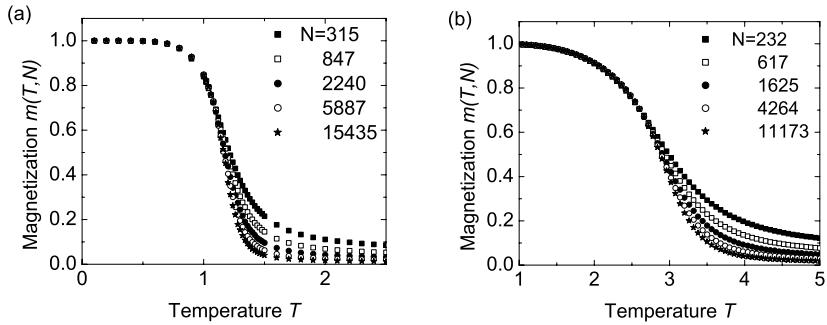

Fig. 2. Spontaneous magnetization $m(T, N)$ of the regular heptagonal (a) and triangle (b) Ising model defind on the pseudosphere.

solution of the planer Ising model (The value $\mu = 2$ is based on the relation $\mu = \nu d$ with $\nu = 1$ and $d = 2$.[27]). These quantitative deviations can not be attributed to some complexity of the model as is done for some decorated Ising models. Indeed, our models are quite simple as similar to the conventional planer Ising model: the exchange interaction J, which is the function of length, takes the single constant value $J = 1$, and only the nearest-neighbor couplings are taken into account. These naturally conclude that the deviation of the exponents from the planer case originates purely from the negative curvature of the underlying geometry. Slight differences of the values of β, γ, and μ between the two lattices (heptagonal and triangular) may result from the contribution of the boundary spins. Preliminary studies have revealed that, when reducing the boundary effects, each exponents goes to have a unique value independent of the lattice structure. In this context, we conclude that negative surface curvature gives rise to a novel universality class of the mounted Ising model.

Before closing the article, it deserves comment on another scenario that may account for the deviation of the critical exponents of our systems. In the present work, we have considered the two-dimensional Ising lattice models embedded on a specific geometry (*i.e.*, a pseudosphere) that allows establishing wide variety of equilateral polygonal lattices on it. Meanwhile, the Ising systems identical to those above can be constructed on *arbitrary* geometry (even in the three-dimensional space), provided that the coupling strength J assumes constant independently of the distance between neighboring spins. In the latter case, the concept of "geometry" is no longer

Table 1. Comparison between our numerical result of critical exponents with the exact solution of the planar case[Ref. 2].

	β	γ	μ	T_c
heptagonal	0.61(2)	2.21(4)	3.44(6)	1.26(1)
triangular	0.73(3)	2.25(2)	3.6(4)	3.34(4)
planar[Ref. 2]	1/8	7/4	2	

discarded; instead, the behavior of the system should be determined by the "connectivity" of the system. In fact, the relevance of the connectivity to the critical properties of the Ising system has attracted enormous interest over the last few years,[28–30] wherein the magnitude of J is defined independently of the separation of the neighboring spins. In the same way, our heptagonal and triangular Ising models displayed in Figs. 1(a) and (b) can be considered as distorted lattices (not equilateral) equipped a constant value of J; this implies that the connectivity should play a crucial role in determining critical exponents of the system. In the context, it is interesting to study the universal behavior of our systems from the viewpoint of connectivity. We still emphasize that, if the coupling strength J depends on the separation of spin (as is the case in most physical systems), novel scaling behavior observed in the present study can be realized not by an alteration in connectivity, but by a geometric alteration on embedding surface.

Acknowledgment

This work was supported in part by a Grant–in–Aid for Scientific Research from the Japan Ministry of Education, Science, Sports and Culture. One of the authors (H.S.) thanks the financial supports from the 21th Century COE "Topological Sciences and Technologies".

References

1. B. Kaufman *Phys. Rev.* **76** 1232 (1949)
2. M. E. Fisher *Rev. Mod. Phys.* **70** 653 (1998)
3. L. Onsager *Phys. Rev.* **65** 117 (1994)
4. R. Rietman, B. Nienhuis and J. Oitmaa *J. Phys. A: Math. Gen.* **25** 6577 (1992)
5. O. Diego, J. Gonzalez and J. Salas *J. Phys. A: Math. Gen.* **27** 2965 (1994)
6. Ch. Hoelbling and C. B. Lang *Phys. Rev. B* **54** 3434 (1996)
7. J. González *Phys. Rev. E* **61** 3384 (2000)
8. M. Weigel and W. Janke *Europhys. Lett.* **51** 578 (2000)

9. J. C. A. d'Auriac, R. Mélin, P. Chandra, and B. Douçot *J. Phys. A: Math. Gen.* **34** 675 (2001)
10. Y. Deng and H. W. J. Blöte *Phys. Rev. E* **67** 036107 (2003)
11. R. Costa-Santos *Phys. Rev. B* **68** 224423 (2003)
12. B. Doyon and P. Fonseca *J. Stat. Mech.* P07002 (2004)
13. V. A. Kazakov *Phys. Lett. A* **119** 140 (1986)
14. P. Di Francesco, P. Ginsparg and J. Zinn-Justin *Phys. Rep.* **254** 1 (1995)
15. C. Holm and W. Janke *Phys. Lett. B* **375** 69 (1996)
16. J. I. Martín *et al.*, *J. Magn. Magn. Mater.* **256** 449. (2003)
17. H. S. M. Coxeter *Introduction to Geometry* (Wiley, New York, 1969)
18. P. A. Firby and C. F. Gardiner, *Surface Topology* (Ellis Horwood, London, 1991)
19. N. L. Balazs and A. Voros *Phys. Rep.* **143** 109 (1986)
20. J. E. Avron, M. Klein, A. Pnueli and L. Sadun *Phys. Rev. Lett.* **69** 128 (1992)
21. E. D'Hoker and D. H. Phong *Rev. Mod. Phys.* **60** 917 (1988)
22. J. Levin *Phys. Rep.* **365** 251 (2002)
23. H. Shima and Y. Sakaniwa, *J. Stat. Mech.* 08017 (2006)
24. U. Wolff *Phys. Rev. Lett.* **62** 361 (1989)
25. D. P. Landau and K. Binder *A Guide to Monte Carlo Simulations in Statistical Physics* (Cambridge University Press, 2000)
26. H. Shima and Y. Sakaniwa, *J. Phys. A* **39** 4921 (2006)
27. R. Botet, R. Jullien and P. Pfeuty *Phys. Rev. Lett* **49** 478 (1982)
28. A. Barrat and M. Weigt *Eur. Phys. J. B* **13** 547-560 (2000)
29. A. Aleksiejuk, J. A. Holyst and D. Stauffer *Physica A* **310** 260-266 (2002)
30. S. N. Dorogovtsev, A. V. Goltsev and J. F. F. Mendes *Phys. Rev. E* **66** 016104 (2002)

QUANTUM CONFINEMENT IN DEFORMED CYLINDRICAL SURFACES

H. TAIRA* and H. SHIMA

Department of Applied Physics, Graduate School of Engineering, Hokkaido University, N-13, W-8, Kita-ku, Sapporo, 060-8628, Japan
** E-mail: taira@eng.hokudai.ac.jp*

We have investigated electron states confined in a cylindrical surface whose radius is smoothly varied within a limited region. The quantum confinement normal to the surface results in an effective potential energy that is a function of the local surface curvature. This curvature-induced potential strongly affects the electronic structures of the lowest-lying states, and further yields bounded states at the deformed region. These suggest the possibility to control electric conductivity of nanostructures by inducing a local deformation.

1. Introduction

Recent development of the fine processing technology enables us to produce nanoscale conducting materials with a novel geometry.[1–3] Of particular interst is a kind of nano structures consisting of curved layers; fullerenes, carbon nanotubes, and carbon nanohones are cases in points. In these systems, the energy scale of the quantum states in the confining direction is substantially larger than the kinetic energy parallel to the surface. Besides, the coherent length of conducting electrons may be comparable to the entire size of the system. Thereby, it is expected that intrinsic geometry of curved surfaces should be relevant to the quantum nature of electrons moving in curved layers. Despite of their great interest, theoretical understanding of the geometric effect on the determination of electric structures has largely remained intact.

The present study deals with a fundamental problem regarding the two dimensional electron systems confined in locally deformed cylindrical surfaces. Reformation of the Schrödinger equation in terms of the Riemannian geometry reveals that the quantum confinement to a curved surface gives rise to modification of the kinetic energy operator and a potential term.[4–6] Particular noteworthy is that the resulting potential energy is a

function of the local curvature of the surface, and thus strongly affects the electronic structures at the deformed region. In fact, we have numerically observed that a certain kind of local deformation of cylindrical surfaces engenders a local attractive potential, then yielding bounded states at the lowest eigenenergies. We hope that our findings open a way of novel quantum devices that are based on a local mechanical deformation.

2. Schrödinger's equation in curved surfaces

In what follows, we focus on a specific situation in which electrons are constrained to move along a curved surface. This is realized by introducing an infinite potential well that confines the electrons within a thin layer of constant thickness d. By taking the limit of $d \to 0$, we obtain the Schrödinger equation for the electrons confined to a curved surface. This limiting procedure was initially suggested by da Costa,[7] and has been successfully applied to quantum mechanical problem in novel geometries.[8–11]

Before proceeding the actual formulation, we briefly review the mathematical expression of vector differential operators in curved spaces.[12] The most important point is that, in a curvilinear coordinate system, the basis vectors $\boldsymbol{e}_i (i = 1, 2, 3)$ are functions of the position. Hence, the derivative of a vector $\boldsymbol{v} = v^j \boldsymbol{e}_j$ reads

$$\frac{\partial \boldsymbol{v}}{\partial x^i} = \frac{\partial v^j}{\partial x^i} \boldsymbol{e}_j + v^j \frac{\partial \boldsymbol{e}_j}{\partial x^i} = \frac{\partial v^j}{\partial x^i} \boldsymbol{e}_j + v^j \Gamma^k_{ji} \boldsymbol{e}_k, \tag{1}$$

where the coefficient Γ^k_{ji}, called a Christoffel symbol, is the kth component of the vector $\partial \boldsymbol{e}_j / \partial x^i$. By interchanging the dummy indices j and k in Eq. (1), we attain

$$\frac{\partial \boldsymbol{v}}{\partial x^i} = \left(\frac{\partial v^j}{\partial x^i} + v^k \Gamma^j_{ki} \right) \boldsymbol{e}_j \equiv v^j_{;i} \boldsymbol{e}_j. \tag{2}$$

Here, the quantity $v^j_{;i}$ is called the covariant derivative of v^j with respect to x^i. It reduces to the simple partial derivative $\partial v^j / \partial x^i$ in Cartesian coordinates, since all the Γ^j_{ki} vanish.

It follows from Eq. (2) that the divergence of a vector $\boldsymbol{v}$ in a curved space is given by

$$\nabla \cdot \boldsymbol{v} \equiv v^i_{;i} = \frac{\partial v^i}{\partial x^i} + v^k \Gamma^i_{ki} = \frac{1}{\sqrt{g}} \frac{\partial}{\partial x^i} \left(\sqrt{g} v^i \right), \tag{3}$$

where $g_{ij} = \boldsymbol{e}_i \cdot \boldsymbol{e}_j$, $g^{ij} = [g_{ij}]^{-1}$, $g = det[g_{ij}]$, and the identity* $\Gamma^i_{ki} = (1/\sqrt{g})(\partial\sqrt{g}/\partial x^k)$ was employed. If we replace $\boldsymbol{v}$ in Eq. (3) by $\nabla\phi$, we will obtain the Laplacian $\nabla^2\phi$. In fact, by rewriting the contravariant components v^i in Eq. (3) as $v^i = g^{ik}v_k = g^{ik}(\partial\phi/\partial x^k)$, we obtain

$$\nabla^2\phi = \frac{1}{\sqrt{g}}\frac{\partial}{\partial x^i}\left(\sqrt{g}g^{ik}\frac{\partial\phi}{\partial x^k}\right), \tag{4}$$

which serves as a kinetic energy operator in a curvilinear coordinate system.

Now we follow the limiting procedure suggested by da Costa[7] to yield the Schrödinger equation for the two-dimensional confined system. We first introduce a confining potential $V(x^1, x^2, x^3)$ in terms of a three-dimensional curvilinear coordinate; the curved surface in question is represented by $x^3 = 0$. The potential becomes, after a proper limiting procedure,[4] $V = 0$ if $x^3 = 0$ and $V = \infty$ otherwise. This allows to separate the x^3 dependence in the Hamiltonian of the confined system, and eventually provides the key equation:

$$-\frac{\hbar^2}{2m^*}\left[\frac{1}{\sqrt{g}}\frac{\partial}{\partial x_i}\left(\sqrt{g}g^{ij}\frac{\partial}{\partial x_j}\right) - \left(H^2 - D\right)\right]\sigma = E\sigma. \tag{5}$$

Here, σ is the wave function of confined particles, H and D are the mean curvature and Gaussian curvature of the surface, respectively. Due to the limiting procedure ($x^3 \to 0$), g^{ij} in Eq. (5) is a 2×2 matrix. The most striking is the occurrence of an effective potential term, $-(H^2 - D)$, in Eq. (5). This non-trivial term results from the quantization of the motion normal to the surface, and depends only on local geometry of the surface, neither on mass nor charge of the particle. In the following sections, we shall see that this effective potential plays a significant role in determining electronic structures of the confined system.

3. Model and methods

Amongst various geometries, we concern locally-deformed cylindrical surfaces depicted in Figs. 1(a) and (b). These surfaces are parametrised by

$$\boldsymbol{r} = [R(u)\cos\phi, R(u)\sin\phi, u], \tag{6}$$

where the u-dependence of the radius $R(u)$ is given by[9]

$$R(u) = R_0\left[1 + \beta\exp\left(\frac{-2u^2}{\alpha^2 R_0^2}\right)\right], \tag{7}$$

*This identity is derived from the expression of Γ^i_{kj} in terms of g_{ij}: $\Gamma^i_{kj} = \frac{g^{il}}{2}\left(\frac{\partial g_{jl}}{\partial x^k} + \frac{\partial g_{kl}}{\partial x^j} - \frac{\partial g_{kj}}{\partial x^l}\right)$

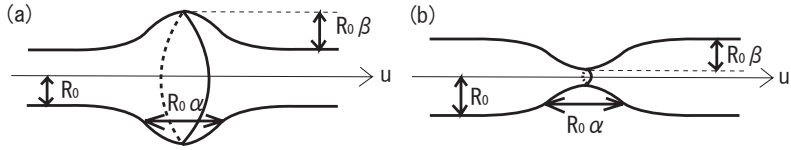

Fig. 1. Schematic illustration of deformed cylindrical surfaces. The definitions of the parameters R_0, α and β are given in text.

with $-\infty < u < \infty$. Our model thus involves the three parameters: R_0 (the radius of an undeformed part), α ($R_0\alpha$ determines the spatial extention of the deformed part along the u-axis), and β ($R_0\beta$ determines the extention of a bulge or constriction).

Due to the rotational symmetry of the surfaces, the Schrödinger equation (5) can be further simplified by substitution

$$\sigma(u,\phi) = \frac{t(u)}{\sqrt{R(u)f(u)}}\frac{e^{im\phi}}{\sqrt{2\pi}}, \tag{8}$$

where $f(u) = [1 + (dR/du)^2]^{-1/2}$ and m is the quantum number of angular momentum. Eventually, we have the Schrödinger equation for $t(u)$ as

$$-f^2\frac{d^2t}{du^2} - V_d t = \epsilon t, \quad V_d = f^2\left(\frac{d\Gamma}{du} - \Gamma^2\right) + H^2 - D - \frac{m^2}{R^2}, \tag{9}$$

where $\Gamma(u) = -(1/2Rf)[d(Rf)/du]$. Hereafter, we call V_d the deformation-induced potential. In actual calculation, the continuous variable u was discretized, and the eigenfunctions of Eq. (9) were evaluated by a direct diagonalization scheme. The radius R_0 is fixed at $R_0 = 50$ in unit of the lattice constant, and the length L of the cylinder is taken as $L = 1000$.

4. Results and discussions

Figure 2 shows the spatial profile of the deformation-induced potential $V_d(u)$ and that of the square amplitude of the ground-state eigenfunction, denoted by $|t(u)|^2$. The parameters $\alpha = 1.1$, $\beta = 1.2$, and $m = 0$ are considered. We see from the figure that V_d provides a sharp potential well at the deformed part ($u \sim 0$), wherein the ground-state wavefunction is tightly localized. The occurrence of the sharp potential well is attributed to the fact that, for the values of α and β denoted above, the term $f^2(d\Gamma/du - \Gamma^2)$ involved in V_d (see Eq. (9)) takes a considerably large positive value at u=0. It is also noteworthy that the spatial variation of $V_d(u)$ is rather intricate, whereas the deformation of the surface is quite smooth.

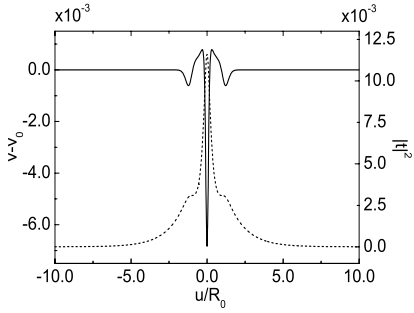

Fig. 2. Spatial profiles of the potential V_d (solid line) and that of the squared amplitude of the ground-state eigenfunction $|t|^2$ (dotted line) with $m = 0$. Parameters are taken as $\alpha = 1.1$ and $\beta = 1.2$.

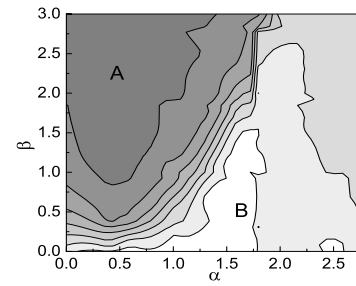

Fig. 3. Contour plot of the localization length ξ of the ground-state in the $\alpha - \beta$ plane.

As expected from Eq. (9), the degree of localization of the lowest- lying states is affected by values of the parameters α and β. This is illustrated in Fig. 3, the contour plot of the localization length ξ of the ground-state. The localization length ξ is defined by $\xi = 1/\left(\sum_{i=1}^{n} |t_i|^2\right)^2$, where n is the whole system size and t_i is the amplitude of the wavefunction at the ith site. Figure 3 shows that the ground-state eigenfunction may be strongly localized (the region A, *i.e.*, $\xi \ll n$), or may be extended over the whole system (the region B, *i.e.*, $\xi \sim n$) depending on the values of α and β. Particularly noteworthy is the α-dependence of ξ; for a given β, ξ does not increase monotonously with α, but exhibit a peak at $\alpha \sim 1.5$ followed by a decrease at $\alpha > 2.0$. The decrease in ξ at large α is somewhat unexpected, since an increase in α simply reduces the curvature radius of the cylindrical surface along the u- direction, thus yielding an almost flat cylindrical surface. In fact, the non-trivial behavior of ξ is accounted for by considering complicated α- and β-dependence of the potential V_d; quantitative discussions of this scheme will be given elsewhere.

Finally, we investigated eigenstates of the non-zero angular momentum $m \neq 0$. Due to the presence of the term R^2/m^2 in Eq. (9), the m is also relevant to the electronic structure of the low-lying states as well as to the spatial profile of V_d. As a matter of fact, once $m \geq 1$, only the term $m^2/R(u)^2$ in Eq. (9) becomes dominant to determine the u-dependence of $V_d(u)$ and that of $|t(u)|^2$. This is clearly shown in Figs. 4(a) and (b);

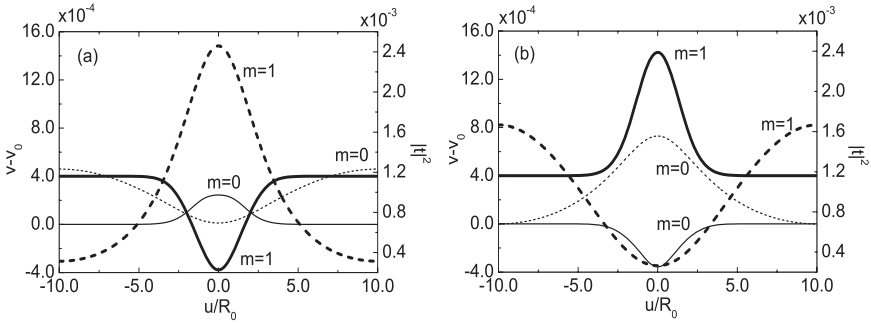

Fig. 4. Spatial profiles of V_d (solid line) and $|t|^2$ (dashed line) for the two lowest-lying states: $m = 0$ (thin) and $m = 1$ (thick). The parameters are $\beta = 0.1$ for (a), $\beta = -0.1$ for (b), and $\alpha = 2.8$ for both.

the profile of $V_d(u)$ for $m = 1$ can be well approximated by $m^2/R(u)^2$, and the sign of V_d at $u = 0$ for $m = 1$ is in opposite to that for $m = 0$. Consequently, the effect of local deformation on the electronic structures is crucially different between the case of $m = 0$ and $m \geq 1$. This implies the possibility to control selectively the electronic structure of low-lying states with $m = 0$.

References

1. S. Tanda *et al.*, *Nature (London)* **417**, 397 (2002).
2. K. T. Shimizu *et al.*, *Phys. Rev. Lett.* **89**, 117401 (2002).
3. X. Duan *et al.*, *Nature (London)* **425**, 274 (2003).
4. M. Encinosa and L. Mott, *Phys. Rev. A* **68**, 014102 (2003).
5. M. Ikegami, *et al.*, *Prog. Theor. Phys.* **88**, 229 (1992).
6. J. Gravesen, M. Willatzen, and L. C. Lew Yan Voon, *J. Math. Phys.* **46**, 012107 (2005).
7. R. C. T. da Costa, *Phys. Rev. A* **23**, 1982 (1981).
8. H. Aoki *et al.*, *Phys. Rev. B* **65**, 035102 (2002).
9. G. Cantele ,D. Ninno, and G. Iadonisi, *Phys. Rev. B* **61**, 13730 (2000).
10. A. Marchi, S. Reqqiani and M. Rudan, *Phys. Rev. B* **72**, 035403 (2005).
11. N. Fujita and O. Terasaki, *Phys. Rev. B* **72**, 085459 (2005).
12. K. F. Riley, M. P. Hobson and S. J. Bence, *Mathematical Methods for Physics and Engineering: A comprehensive Guide-US-, 2nd Edition*, (Cambridge Univ. Press, New York, 2002).

TOPOLOGICAL SPIN CURRENTS DUE TO NONADIABATIC QUANTUM PUMPING

K. YAKUBO† and M. MORIKAWA*

Department of Applied Physics, Graduate School of Engineering, Hokkaido University, Sapporo 060-8628, Japan

†*E-mail: yakubo@eng.hokudai.ac.jp*

Studying quantum pumping in a one-dimensional electron system with a time-varying double δ potential, it has been clarified that nonadiabatic pumping currents are qualitatively different from adiabatic ones. We also elucidate that a finite pure spin current can be expected in a nonadiabatically driven system under a magnetic field, in which no chaotic character is exhibited.

1. Introduction

Broken time-reversal symmetry quantum systems can induce quantum currents such as persistent currents in nanoscale rings. Some of time-varying potentials may break time-reversal symmetry and thus generate a quantum current in the system. This type of novel transport is known as quantum pumping.[1,2] In particular, quantum pumping under slowly varying potentials (adiabatic pumping) has been extensively studied since the pioneering work by Thouless.[3] Quantum currents due to the adiabatic pumping can be regarded as topological currents as a consequence of the Berry phase yielded by slowly varying parameters describing systems. In the presence of a magnetic field, quantum pumping may generate a pure spin current which carries no charges but spins. Pure spin currents without dissipation play an important role in the spintronics and have been confirmed experimentally.[4] It has been suggested that the pure spin current is realized in a quantum chaos system. On the contrary, we have little knowledge on currents by *nonadiabatic* quantum pumping, namely pumping currents by fast varying potentials. It is quite important to clarify quantum transport

*Present address: Software Technology Department, Software Unit, Fujitsu Limited, Numazu 410-0396, Shizuoka, Japan.

under nonadiabatic pumping, not only for fundamental understanding of pumping currents but also for applications to nanoscale devices.

In this paper, we study charge and spin currents pumped by nonadiabatically driven δ potentials in a one-dimensional system. Nonadiabatic pumping induces plural sidebands of electronic states. We have shown that nonadiabatic pumping currents are quite different from adiabatic ones, and complicated interferences between sideband states lead to pure spin currents even in a simple system without exhibiting chaotic properties.

2. Systems and Formalism

Let us consider a one-dimensional electron system with the potential:

$$V(x,t) = [V_{0\mathrm{L}} + V_{\mathrm{L}}\cos(\omega t)]\,\delta\left(x + \frac{a}{2}\right) + [V_{0\mathrm{R}} + V_{\mathrm{R}}\cos(\omega t - \phi)]\,\delta\left(x - \frac{a}{2}\right) , \tag{1}$$

where $V_{0\mathrm{L}}$, V_{L}, $V_{0\mathrm{R}}$, and V_{R} are constant. This system can be separated by three parts, namely the left-hand side of the left δ potential (region I), the region between two δ barriers (region II), and the right-hand side of the right δ potential (region III). Wavefunctions in these regions are written as $\Psi_{\mathrm{I}}(x,t) = e^{ik_0 x - iEt/\hbar} + \psi_{\mathrm{r}}(x,t)$, $\Psi_{\mathrm{II}}(x,t) = \psi_{\mathrm{a}}(x,t) + \psi_{\mathrm{b}}(x,t)$, and $\Psi_{\mathrm{III}}(x,t) = \psi_{\mathrm{t}}(x,t)$ for an electron incident from the left-hand side with energy E and momentum $\hbar k_0 = \sqrt{2m^*E}$. The oscillating δ potentials in Eq. (1) yield sideband states with energy $n\hbar\omega$ ($n = 0, \pm1, \pm2, \dots$). Thus, we can write $\psi_{\mathrm{t}}(x,t)$, for example, as

$$\psi_{\mathrm{t}}(x,t) = \sum_{n=-\infty}^{\infty} t_n e^{ik_n x} e^{-i(E+n\hbar\omega)t/\hbar} , \tag{2}$$

where $k_n = \sqrt{2m^*(E+n\hbar\omega)}/\hbar$. Other wavefunctions can be expressed in a similar way with expansion coefficients r_n, a_n, and b_n. The matching conditions of the wavefunctions Ψ_{I}, Ψ_{II}, and Ψ_{III} give the relations between the expansion coefficients. After some manipulations, we can write this relation as

$$\hat{A}_n \boldsymbol{x}_n + \hat{B}_n \boldsymbol{x}_{n+1} + \hat{C}_n \boldsymbol{x}_{n-1} + \delta_{n0}\hat{I}\boldsymbol{z}_n = 0 , \tag{3}$$

where $\boldsymbol{x}_n$ and $\boldsymbol{z}_n$ are the two-dimensional vectors with their elements $(t_n, r_n + \delta_{n0}e^{-ik_n a})$ and $(-2ik_n e^{-ik_n a/2}, 0)$, respectively, and $\hat{I}$ is the 2×2 unit matrix. Symbols $\hat{A}_n$, $\hat{B}_n$, and $\hat{C}_n$ are the 2×2 matrix depending on k_n, $V_{0(\mathrm{L,R})}$, $V_{(\mathrm{L,R})}$, and ϕ. The recurrence formula Eq. (3) can be solved by using the continued fraction technique. This enables us to calculate the transmission amplitude t_n for the sideband n.

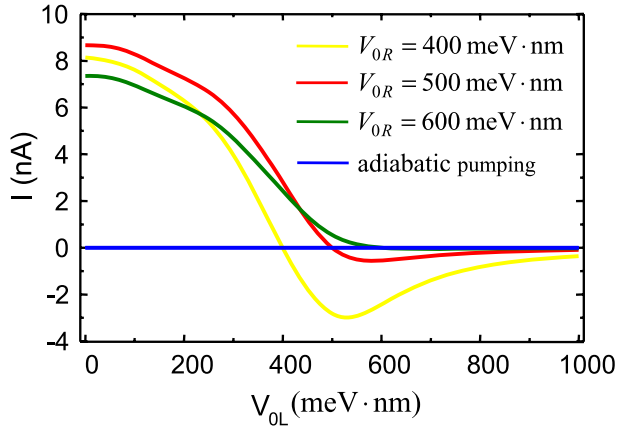

Fig. 1. Pumping currents in a one-dimensional electron system driven by the double δ potential oscillating nonadiabatically in phase. Colors represent values of right static δ potential.

The transmission probability $T_{\rm L}(E)$ for electrons incident from the left-hand side with energy E is then given by $T_{\rm L}(E) = \sum_n k_n |t_n|^2/k_0$. In one-dimensional problems, the current from the left-hand side to the right-hand side is $I_{\rm L} = -(e/h)\int_0^{E_{\rm f}} T_{\rm L}(E)dE$, where $E_{\rm f}$ is the Fermi energy. The net current is the difference between $I_{\rm L}$ and $I_{\rm R}$ which is the current from the right-hand side to the left-hand side and can be calculated similarly. Therefore, the total current I at zero temperature is given by

$$I = I_{\rm L} - I_{\rm R} = -\frac{e}{h}\int_0^{E_{\rm f}} \left[T_{\rm L}(E) - T_{\rm R}(E)\right] dE \ . \tag{4}$$

In the presence of the time-reversal symmetry, $T_{\rm L}(E)$ is the same as $T_{\rm R}(E)$ and I is always zero. When the time-reversal symmetry is broken by driven potentials, $T_{\rm L}(E) \neq T_{\rm R}(E)$ in general. Thus, we will have a finite pumping current in such cases.

3. Charge and Spin Pumping Currents

We demonstrate, at first, differences between adiabatic and nonadiabatic pumping by calculating charge pumping currents. The system is described by Eq. (1) with $a = 100\,$nm, $V_{\rm L} = V_{\rm R} = 500\,$meV·nm, and $\phi = 0$. In general, the pumping current strongly depends on the phase difference ϕ. In the case of the adiabatic pumping, it is known that no pumping current flows when $\phi = 0$. Figure 1 shows the $V_{0\rm L}$ dependence of the nonadiabatic pumping currents, taking into account the Floquet scattering for $V_{0\rm R} = 400\,$meV·nm,

500 meV·nm, and 600 meV·nm. In contrast to the adiabatic pumping, we see finite currents by the nonadiabatic pumping. It should be noted that the pumping current becomes zero if $V_{0\mathrm{L}} = V_{0\mathrm{R}}$. This is because the driven double δ potential does not break the time-reversal symmetry. We also confirmed that a finite pumping current is induced in a driven system with $V_{\mathrm{R}} = 0$ (only one δ potential oscillates) for which no adiabatic pumping current is expected. Hence, we conclude that nonadiabatic pumping currents are largely different from adiabatic ones.

Next, we consider the spin current pumped by the driven δ potentials. From a viewpoint of the spin degrees of freedom, the charge pumping current I_{c} is expressed as $I_{\mathrm{c}} = I_{\uparrow} + I_{\downarrow}$, where $I_{\uparrow}$ and $I_{\downarrow}$ are the pumping currents of up-spin and down-spin electrons, respectively. If we define $I_{\mathrm{s}} = I_{\uparrow} - I_{\downarrow}$, I_{s} means the spin current. In the absence of a magnetic field, up-spin states and down-states are degenerated, and $I_{\uparrow}$ is equal to $I_{\downarrow}$. Therefore, we have no spin current in this case. If we apply a magnetic field to the system, however, the energy of the up-spin state becomes different from that of the down-spin state by the Zeeman energy $\boldsymbol{\mu}_{\mathrm{s}} \cdot \boldsymbol{B}$. In this case, the transmission probability $T_{\mathrm{L,R}}(E = E_{\uparrow})$ is not the same as $T_{\mathrm{L,R}}(E = E_{\downarrow})$, which leads to $I_{\uparrow} \neq I_{\downarrow}$ from Eq. (4). As a consequence, we can expect a finite spin current in the quantum pumping system under a magnetic field. In particular, if $I_{\uparrow} = -I_{\downarrow}$, the finite spin current $I_{\mathrm{s}} = 2I_{\uparrow}$ flows without charge current. We call such a spin current the *pure spin current*. The pure spin current may play an important role in the field of spintronics, because the pure spin current does not accompany energy dissipation. In fact, the pure spin current has been experimentally observed in an adiabatic condition.[4] To have a large pure spin current, it is necessary that the transmission probability $T_{\mathrm{L,R}}(E)$ has a complicated energy dependence. This condition is, in the adiabatic pumping, supposed to be satisfied in a quantum chaos system such as electrons in a quantum dot.[4] We consider that the complexity of the energy dependence of the transmission probability can be also realized by complicated interferences between sideband states induced by nonadiabatic Floquet scattering. In order to examine the possibility of the pure spin current by the nonadiabatic quantum pumping without any quantum chaos, we calculate spin currents in a system described by Eq. (1).

Figure 2 shows the up-spin current $I_{\uparrow}$, down-spin current $I_{\downarrow}$, total charge current I_{c}, and the spin current I_{s} induced by the adiabatic pumping as a function of $V_{0\mathrm{L}}$. We used the same parameters as those for Fig. 1 except for $\phi = \pi/2$ and $V_{0\mathrm{R}} = 500\,\mathrm{meV{\cdot}nm}$. The magnetic field subject to the system is $B = 4.32\,\mathrm{T}$ for which the Zeeman splitting energy is 0.1 meV by

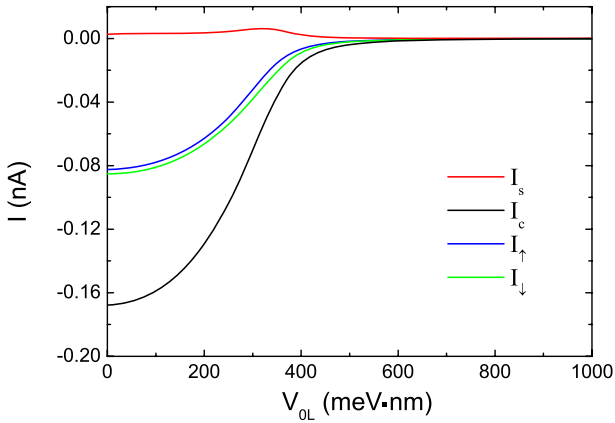

Fig. 2. Spin and charge currents in a one-dimensional electron system driven by the double δ potential oscillating *adiabatically* with $\phi = \pi/2$ as a function of the left static δ potential.

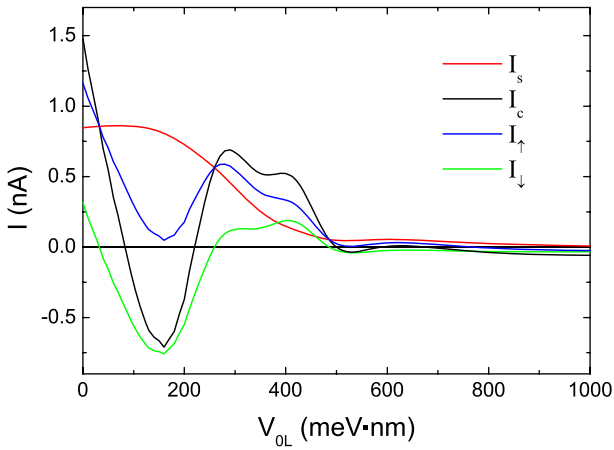

Fig. 3. Spin and charge currents in a one-dimensional electron system driven by the double δ potential oscillating *nonadiabatically* with $\phi = \pi/2$ as a function of the left static δ potential.

assuming the g factor to be 0.4 corresponding to GaAs. Here we have chosen as $E_{\mathrm{f}\uparrow} = 9.34\,\mathrm{meV}$ and $E_{\mathrm{f}\downarrow} = 9.44\,\mathrm{meV}$. Although $I_\uparrow$ is slightly different from $I_\downarrow$ due to the magnetic field and the spin current I_s becomes nonzero, we have no pure spin current (i.e., $I_\mathrm{s} \neq 0$ but $I_\mathrm{c} = 0$) in this case. This is because the transmission probabilities at two different energy by 0.1 meV are not very different due to non-chaotic character of the system.

Figure 3 represents $I_\uparrow$, $I_\downarrow$, I_c, and I_s by the nonadiabatic pumping with

$\hbar\omega = 0.5\,\mathrm{meV}$. Other parameters are the same as those for Fig. 2. In contrast to the adiabatic case, the pure spin current flows at some values of $V_{0\mathrm{L}}$ ($V_{0\mathrm{L}} \simeq 100\,\mathrm{meV{\cdot}nm}$ and $220\,\mathrm{meV{\cdot}nm}$, for example). The finite pure spin current originates from complicated interferences between sideband states induced by the nonadiabatic quantum pumping. In fact, we have confirmed that the pure spin current disappears by reducing the number of active sidebands by decreasing $V_{\mathrm{L(R)}}$. We can conclude from these results that the nonadiabatic pumping in addition to the chaotic nature of the system is crucial for a large pure spin current.

4. Conclusions

We study pumping currents in one-dimensional electron systems with time-varying double δ potential. It has been clarified that nonadiabatic pumping currents are quite different from adiabatic ones. Nonadiabatic pumping currents can flow even in some systems in which adiabatic pumping currents are forbidden by their special symmetries. It has been also elucidated that we can expect a finite pure spin current in a nonadiabatically driven system even exhibiting no chaotic character. This is due to complicated interferences between plural sideband states. Taking into account the fact that a single nonadiabatically oscillating potential can generate a finite pumping current, there is a possibility to have a pure spin current induced by simple molecular devices.

Acknowledgments

This work has been supported by the 21st Century COE program on "Topological Science and Technology" and from the Ministry of Education, Culture, Sport, Science and Technology of Japan. Numerical calculations in this work have been mainly performed on the facilities of the Supercomputer Center, Institute for Solid State Physics, University of Tokyo.

References

1. M. Switkes, C. Marcus, K. Campman and A. C. Gossard, *Science* **283**, 1905 (1999).
2. P. W. Brouwer, *Phys. Rev. B* **58**, R10135 (1998).
3. D. J. Thouless, *Phys. Rev. B* **27**, 6083 (1983).
4. S. K. Watson, R. M. Potok, C. M. Marcus and V. Umansky, *Phys. Rev. Lett.* **91**, 258301 (2003).

CHARGE DENSITY WAVE STATE IN TOPOLOGICAL CRYSTAL

T. NOGAWA* and K. NEMOTO

Division of Physics, Graduate School of Science, Hokkaido University, Kitaku, Kita 10-jo Nishi 8-chome, Sapporo 060-0810, Japan
**E-mail: nogawa@statphys.sci.hokudai.ac.jp*

The charge density wave state in a ring-shaped crystal is studied by mapping to the three dimensional uniformly frustrated XY model with quasi-one-dimensional anisotropy in connectivity. Cylindrical bending results frustration between intra- and inter-chain couplings then phase vortex lines are generated even in the ground state. As temperature becomes lower, the system takes a phase transition to the ordered state, which is characterized by the vortex lattice.

The effect of crystal topology on physical property is a new and attractive topic in condensed matter physics. Tanda *et al.* successfully synthesize single crystals with various closed loop shapes of some transition metal chalcogenides, MX_3.[1] It is expected that these materials bring new kind of physical properties and applications.

MX_3 materials are known for their quasi-one-dimensional chain structure, *i.e.*, electrons have strong binding along the b axis compared with the a and c axes. In the ring-shaped crystal, these chains form concentric circles as illustrated in Fig. 1. The charge density wave (CDW) state at low temperature is observed in a ring-shaped crystal as well as in conventional whisker crystals.[2] Shimatake *et al.* investigated transient dynamics

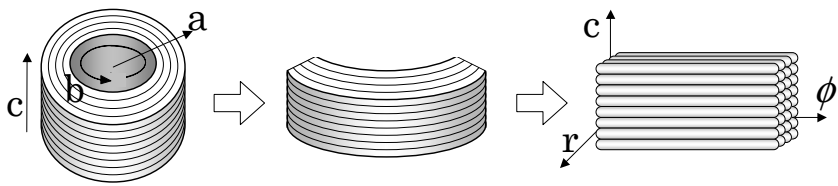

Fig. 1. Schematic diagram of ring-shaped crystal.

of a ring-shaped $NbSe_3$ crystal using an ultra-fast laser and found the suppression of relaxation time divergence at the CDW transition temperature which is observed in a whisker crystal.[3] They also indicate the possibility that the ring crystal shows slow relaxation which is qualitatively different from that of a whisker crystal. In order to understand the unique property of ring-shaped crystals, we propose a model for CDWs in ring-shaped crystals, which depicts frustration between inter- and intra-chain interactions mentioned as follows.

Initially we consider whisker crystals before ring-shaped crystals. The modulated part of charge density in a single chain is expressed as $\rho(x_b) = \rho_0 \cos[Q_0 x_b + \theta_i(x_b)]$. Here, Q_0 is twice of the Fermi wave number and $\theta_i(x_b)$ is a phase fluctuation variable of the i-th chain at the position x_b. If θ is uniform in space, the periodic order exists. Purely one dimensional systems, however, have only short range order. The Coulomb interaction between chains enables the three dimensional long range order. Supposing screening effect, the interaction energy of two chains can be expressed as $\int dx_b \rho_1(x_b)\rho_2(x_b) \propto \int dx_b \cos[\theta_1(x_b) - \theta_2(x_b)]$. This is equivalent to the anti-ferromagnetic coupling of the XY spin model, which can be transformed into the ferromagnetic one by alternating phase shift for chains. Then the three dimensional CDW order is regarded as a uniform phase state.

Next, we consider two chains in a ring-shaped crystal which neighbor on the radius direction. In this case, we should work with cylindrical coordinates, $\phi = x_b/r \in (0, 2\pi)$ as shown in Fig. 1. The radius direction is identified with the a axis and then r equals $a_0 i_a$. The interaction energy is evaluated from the difference of the total phase, $Q_0 r\phi + \theta_i(x_b)$, then

$$\int d\phi \cos[\theta_{\rm in}(\phi) - \theta_{\rm out}(\phi) - Q_0 a_0 \phi]. \tag{1}$$

What happens in the presence of the additional term $Q_0 a_0 \phi$? Synchronization of the spatial modulation of charge density (*e.g.*, it is given by $\theta = -Q_0 a_0 i_a \phi$) lowers the Coulomb interaction energy in the same way for the whisker crystal. Such synchronization, however, results the deviation of wave length from the natural one realized in whisker crystals, *i.e.*, there is compression inside or stretching outside. It yields an elastic distortion energy of CDW inside the chain, $\int dx_b (\partial\theta/\partial\phi)^2$. The wave length becomes larger with the radius then three dimensional charge density order same with the whisker crystal can not be realized for sufficiently thick rings. We consider this frustration between the interactions along the a and b axes is the essential difference from the whisker crystals. Note that the c axis is

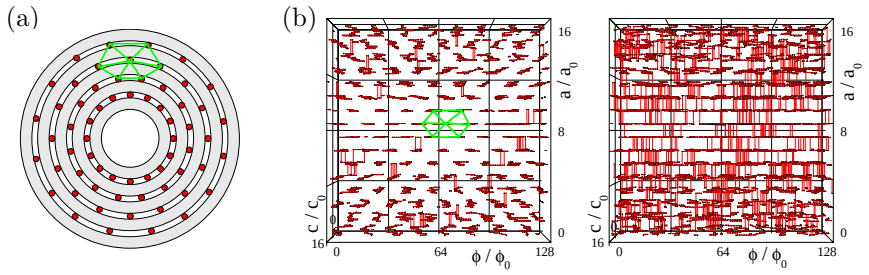

Fig. 2. (a) Schematic diagram of the vortex lattice embedded on a ring-shaped crystal. (b) Vortex configurations viewing from the c axis at $T = 0.8T_c$ and $1.2T_c$. Here $J_\phi/J_a = 64$ and $f = 1/16$. Note that the b axis is compressed by 1/8 compared with the a axis.

not concerned with the frustration.

According to the idea above, we consider a phase field model similar to the Fukuyama-Lee-Rice model.[4,5] The obtained lattice Hamiltonian is written as follows.

$$H = -\sum_{\mathbf{i}} \left[J_a \cos(\theta_{\mathbf{i}} - \theta_{\mathbf{i}+\hat{\mathbf{a}}} - 2\pi f i_\phi) + J_\phi \cos(\theta_{\mathbf{i}} - \theta_{\mathbf{i}+\hat{\phi}}) + J_c \cos(\theta_{\mathbf{i}} - \theta_{\mathbf{i}+\hat{\mathbf{c}}}) \right].$$

Here $\mathbf{i} = (i_a, i_\phi, i_c)$ indicates the discretized position in three dimensions. The term $2\pi f i_\phi$ describes the frustration between the couplings along the a and b axes and f is proportional to $Q_0 a_0$. Dropping this term results a usual XY model, which is proper for CDWs in a whisker crystal, appears. The present model is equivalent to the uniformly frustrated XY spin model[6,7] for the melting transition of flux line lattices in superconductors. In the present case of CDWs, however, the coupling constants have quasi-one-dimensional anisotropy, $J_b \gg J_a \approx J_c$ instead of the two dimensional one $J_c \ll J_a = J_b$ of high T_c layer superconductors.

By simulated annealing with the Monte Carlo method, we investigate the ground state of the system. Even in the ground state, the system contains a number of phase vortex lines, which are topological defects of CDWs, parallel to the c-axis. They are inevitable for not so thin ring-shaped crystals. The mean density of phase vortex lines is equivalent to f. Each vortex line is straight along the c axis and the lines form a two dimensional lattice in the ab-plane due to the effective repulsive interaction between vortex lines. The configuration in the ab plane is shown in Fig. 2(a). For sufficiently strong anisotropy, the lattice is a triangular lattice stretched along the b direction. The unit lattice vectors are given by $(\pm 2a_0, (1/2f)\phi_0, 0)$.

As temperature becomes higher, the system takes a phase transition at the critical temperature T_c and enters the disordered phase, where vortex lines wind and entangle with each other. Typical configurations of vortex lines both in the low and high temperature phases are shown in Fig. 2(b).

In order to investigate the difference of transient behavior near T_c between whisker and ring-shaped crystals, we investigate the relaxation dynamics to equilibrium.[8] The system shows power law relaxation without characteristic time scale in the ordered phase not only at the transition temperature while finite relaxation time and its divergence is observed above T_c. This is considered to be due to the two dimensional long range order of phase variable.[7,8] By the nonequilibrium relaxation analysis,[9] we find a phase transition, which is quite different from that of a usual whisker crystal. The Fourier transformation of vortex density field has a Bragg peak, whose intensity is regarded as an order parameter. Its continuous behavior at the critical temperature indicates a second order phase transition. This is in contrast to the first order transition of the superconductors under the magnetic field parallel to the c-axis.[6]

In conclusion, we studied the charge density wave state of a ring-shaped crystal based on the frustrated XY model. Both the ground state and phase transition is qualitatively different from the ferromagnetic transition of whisker crystals. Bending of three dimensional material destroy the original CDW order. Instead, there appears a longer scale periodic structure of topological defects. Although both of theoretical and experimental studies are in progress and direct comparison of them is difficult, the power law relaxation, which means no characteristic timescale in relaxation, and two dimensional phase order at low temperature is qualitatively consistent with experimental observations; slow relaxation and no divergence of relaxation time.

References

1. S. Tanda *et al.* , *Nature*, **417**, 397 (2002).
2. S. Tsuneta *et al.* , *Physica B*, **329**, 1544 (2003).
3. K. Shimatake, Y. Toda and S. Tanda, *Phys. Rev. B*, **73**, 153403 (2006).
4. H. Fukuyama and P. A. Lee, *Phys. Rev. B*, **17**, 535 (1978).
5. P. A. Lee and T. M. Rice, *Phys. Rev. B*, **19**, 3970 (1979).
6. X. Hu, S. Miyashita and M. Tachiki, *Phys. Rev. Lett.*, **79**, 3498 (1997).
7. X. Hu and M. Tachiki, *Phys. Rev. B*, **70**, 064506 (2004).
8. T. Nogawa and K. Nemoto, *Phys. Rev. B*, **73**, 184504 (2006).
9. Y. Ozeki, K. Ogawa and N. Ito, *Phys. Rev. E*, **67**, 026702 (2003).

SPATIOTEMPORAL MAPPING OF SYMMETRICAL SURFACE ACOUSTIC FIELDS ON CRYSTALS AND PERIODIC MICROSTRUCTURES

T. TACHIZAKI, O. B. WRIGHT and O. MATSUDA

Department of Applied Physics, Graduate School of Engineering
Hokkaido University,
Sapporo, 060-8628, Japan
E-mail: assp@kino.eng.hokudai.ac.jp

Y. SUGAWARA

Department of Physics and Astronomy, University Southampton, Southampton, UK

Spatiotemporal acoustic field imaging on the (100) plane of the cubic crystal LiF and on a square array of gold pyramids on a glass substrate is performed with an ultrafast optical technique. In both cases wave fronts exhibiting fourfold symmetry are obtained. The results of these two experiments on naturally and artificially anisotropic materials are compared.

1. Introduction : Surface acoustic waves and its imaging

Surface acoustic waves (SAW's) are of interest in both physics and engineering. In physics, SAW's are useful for investigating the elastic constant tensor of solids or for studying acoustic modes localized at surfaces or interfaces.[1–4] In engineering, SAW's underpin the operation of GHz frequency filters.[6] In contrast to case for surface waves on liquids, SAW wave fronts exhibit a complex symmetry reflecting the nature of the 4th rank elastic constant tensor and the crystal cut.

Another way of introducing acoustic anisotropy is to use artificially-made periodic structures, otherwise known as phononic crystals.[7] These have been shown to exhibit acoustic band gaps for both bulk and surface wave propagation.

In this paper, we investigate SAW generation and detection in the (100) plane of a cubic crystal as well as in a phononic crystal in the form of a periodic square array by means of an ultrafast optical imaging technique. We discuss and compare the form of the observed acoustic wave fronts.

2. Experiments

Ultrashort light pulses in the blue (415 nm) are used to excite the SAW's in the frequency range 100 MHz to 1 GHz (acoustic wavelength $\sim 10\ \mu$m) through thermoelastic generation at a micrometer-sized spot on the sample. The experimental method is described in detail elsewhere.[4] Detection of surface motion is achieved with an optical interferometer that also makes use of ultrashort light pulses (in the infrared at 830 nm). These are scanned over the sample to form an image. The repetition rate of the light pulses is 80 MHz. By varying the delay between the generation and detection light pulses, we obtain a spatiotemporal record of the SAW's. The imaged quantity is the out-of-plane surface particle velocity. The observed wave front shapes are closely related to the acoustic group velocity surfaces.

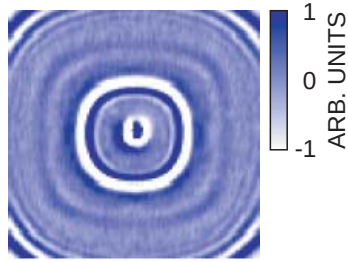

Fig. 1. An experimental image of the out-of-plane surface particle velocity for surface acoustic waves on LiF (100). This data corresponds to a time 6.4 ns after excitation. The scanned area corresponds to a 100-micrometer-square region.

Figure 1 shows a typical SAW image for a 100-micrometer-square region of the (100) surface of a LiF single crystal coated with a 50 nm polycrystalline gold thin film. The wave fronts show fourfold symmetry, characteristic of the underlying substrate. The central ring corresponds to a combination of SAW's and pseudo-SAW's,[4] whereas the weak dark ring lying outside it corresponds to a leaky longitudinal mode. Acoustic velocity dispersion is negligible here because the gold thin film is sufficiently thin.[4,5] This fourfold symmetry of the SAW wave fronts is characteristic of the elastic constant tensor of LiF and the chosen crystal cut. In contrast, in the case of *optical* propagation in a crystal of cubic symmetry for this cut, the wave fronts would be circular. Unlike the 4th-rank elastic constant tensor, the dielectric constant tensor is 2nd rank, and crystals of cubic symmetry result in isotropic optical properties (in the linear optics case).

To compare crystalline and structural anisotropy for SAW's we prepared a surface phononic crystal consisting of a square array of polycrystalline gold pyramids, as shown in Fig. 2. The 210-nm-thick pyramids and 30 nm gold buffer layer are sputtered on to a crown glass substrate of thickness 1 mm (see Fig. 2(A)). The 25 μm period of the gold pyramids is long enough to avoid any phononic band gap effects in this sample for our acoustic frequency range.

Figure 3 shows a SAW image of a 110-micrometer-square region (corresponding to the same region as the optical reflectance image of Fig. 2(B)). The SAW wave fronts again show fourfold symmetry. All materials making up the phononic crystal are elastically isotropic, so that the observed anisotropy is purely structural in origin. In contrast to the case for LiF, strong acoustic velocity dispersion is observed, particularly in the x, y and diagonal directions. This arises from a combination of scattering and thin-film velocity dispersion[5] (the thickness of the gold pyramids being sufficient to introduce considerable velocity dispersion). In these data leaky longitudinal modes are not easy to distinguish from the background noise.

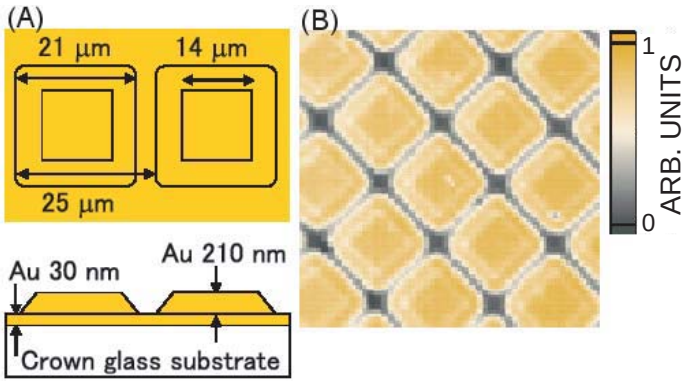

Fig. 2. (A) Schematic diagram of the cross section of a phononic crystal composed of gold pyramids. (B) Optical reflectance image for a 110-micrometer-square region.

3. Conclusion

In conclusion, we have investigated SAW generation and detection in two samples, one exhibiting crystalline anisotropy and one exhibiting structural anisotropy. Fourfold symmetry of the SAW wave fronts is observed for both

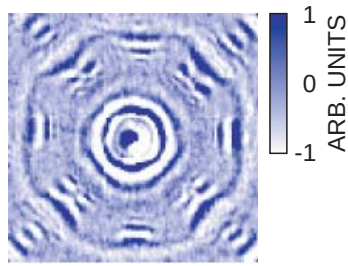

Fig. 3. An experimental image of the out-of-plane surface particle velocity for surface acoustic waves on the phononic crystal. This data corresponds to a time 6.8 ns after excitation. The scanned area corresponds to a 110-micrometer-square region.

samples. We hope that this study will encourage further experiments to investigate the form of wave fronts in complex surface phononic structures.

Acknowledgements

This work is partially supported by the 21st century COE (Centre of Excellence) program on "Topological Science and Technology" from the Ministry of Education, Culture, Sports, Science and Technology of Japan. One of the authors (T.T.) is a JSPS Research Fellow.

References

1. J. P. Wolfe, *Imaging Phonons: Acoustic Wave Propagation in Solids* (Cambridge University Press, Cambridge, 1998).
2. J. P. Wolfe, *Phys. Today* **48**(9), 34 (1995).
3. P. Hess, *Phys. Today* **55**(3), 42 (2002).
4. Y. Sugawara, O. B. Wright, O. Matsuda, M. Takigahira, Y. Tanaka, S. Tamura and V. E. Gusev, *Phys. Rev. Lett.* **88**, 185504 (2002).
5. G. W. Farnell and E. L. Adler, in *Physical Acoustics*, edited by W. P. Mason and R. N. Thurston (Academic, New York, 1972), Vol. 9, p. 35.
6. F. S. Hickernell, in *Physical Acoustics*, edited by R. N. Thurston, A. D. Pierce and E. P. Papadakis (Academic, London, 1999), Vol. 24, p. 135.
7. M. Sigalas, M. S. Kushwaha, and E. N. Economou, *Z. Kristallogr.* **220**, 765 (2005).

CLEAN OPTICAL VORTEX BEAM GENERATION FOR LARGE TOPOLOGICAL CHARGE

J. HAMAZAKI*, Y. MINETA, and R. MORITA†

Department of Applied Physics, Hokkaido University
Kita-13, Nishi-8, Kita-ku, Sapporo 060-8628, Japan
* *E-mail: hamazaki@topology.coe.hokudai.ac.jp*
† *E-mail: morita@eng.hokudai.ac.jp*

By improving the spatial-light-modulator pattern, a clean optical vortex beam for large topological charge was obtained without mixing of nondesired modes or forming an anamorphic circle.

1. Introduction

The Laguerre-Gaussian (LG) mode LG_p^m is an eigenmode of the paraxial wave equation. Its beam has phase distribution of $\exp(im\varphi)$ (m; integer), providing a helical shape for the wavefronts which is a common topological defect. Here, m is the azimuthal index that represents topological charge, that is, the number of 2π cycles in phase about circumference, p is the radial index that represents p nodes along the radial direction, and φ is the azimuthal angle. A peculiarity of beams with helical wavefronts lies in the presence of transverse energy circulation, which is termed an optical vortex. The optical vortex carries a well-defined orbital angular momentum (OAM) per photon.[1] The propagating complex electric field E_{mp} and its slowly-varying envelope u_{mp} of the LG_p^m mode with frequency ω at time t are given by

$$E_{mp}(\rho, \varphi, z, t) = u_{mp}(\rho, \varphi, z) \exp[i(kz - \omega t)], \tag{1}$$

$$u_{mp}(\rho,\varphi,z) = \sqrt{\frac{2p!}{\pi(p+|m|)!}}\left[\frac{\sqrt{2}\rho}{w(z)}\right]^{|m|} L_p^{|m|}\left(\frac{2\rho^2}{w(z)^2}\right)\frac{w_0}{w(z)} \times \exp\left[-\frac{\rho^2}{w(z)^2} - i\frac{k\rho^2}{2R(z)}\right]\exp\left[+im\varphi\right] \times \exp\left[-i(2p+|m|+1)\arctan\left(\frac{z}{z_R}\right)\right], \quad (2)$$

respectively, where ρ and z denote cylindrical polar coordinates, k is wave number in vacuum, and $L_p^{|m|}(x)$ is the generalized Laguerre polynomial defined by

$$L_p^{|m|}(x) = \sum_{r=0}^{p}(-1)^r \begin{pmatrix} p+|m| \\ p-r \end{pmatrix}\frac{x^r}{r!}. \quad (3)$$

Parameters $R(z)$ and $w(z)$ denote the radius of curvature of wavefronts and the beam size at a propagation distance z, as expressed by

$$R(z) = (z_{\mathrm{R}}^2 + z^2)/z, \qquad w(z) = w_0\sqrt{1 + z^2/z_{\mathrm{R}}^2}. \quad (4)$$

with the Rayleigh range

$$z_{\mathrm{R}} = kw_0^2/2. \quad (5)$$

The constant w_0 is the beam waist.

Recently, development of a spatial light modulator (SLM) enables us to generate an LG beam with large m easily. A beam with the OAM attracted significant research interest because of its increasing applications, such as high-efficiency laser trapping,[2] microstructure rotation in laser tweezers and spanners,[3] and quantum information using multidimensional quantum entangled states.[4] From the standpoint of the interaction of the OAM with matter, generation of a clean LG without m- and p-value mixture is required. In the present study, we improved the SLM pattern to obtain the clean LG beams.

2. Generation of optical vortex by SLM

An optical vortex was generated using two-dimensional-programmable SLM (HOLOEYE LC-R 2500, pixel number of 1024×768, pixel size of 19 μm×19 μm) as shown in Fig. 1(a). The light source used was a linearly-polarized cw He-Ne laser (632.8 nm). The beam from the laser was reflectively diffracted by a hologram patterned on the SLM.

Generally, a fork-like pattern shown Fig. 1(b) was used in SLM to generate a well-defined LG beam.[5] Conventionally the fork-like pattern has

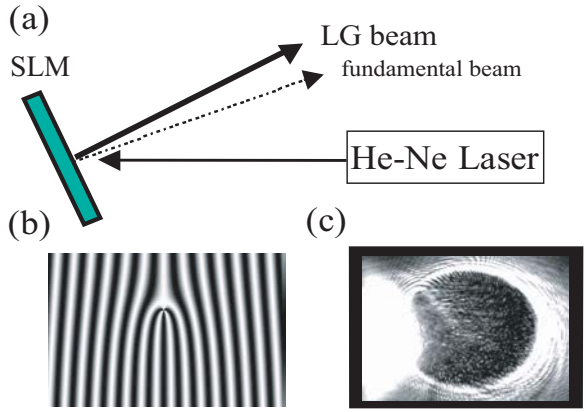

Fig. 1. (a)Experimental setup for optical vortex generation by SLM. (b)Fork-like pattern in SLM for m=3. (c)Intensity profile of generated LG beam for m=100.

been often used for generate LG beams. To confirm properties of optical vortices, we observed the interference patterns with generated beam and sphere wave. Figures 2(a)-(c) correspond to the interference patterns for $m = +1, +2$, and -1, respectively. The number of spiral arms equals the number m of intertwined helical phase fronts, as shown in Figs. 2(a) and (b). Moreover, spiral rotation direction becomes inverse as shown in Fig. 2(c). These patterns well indicate that the generated beam is the well-defined LG beam.

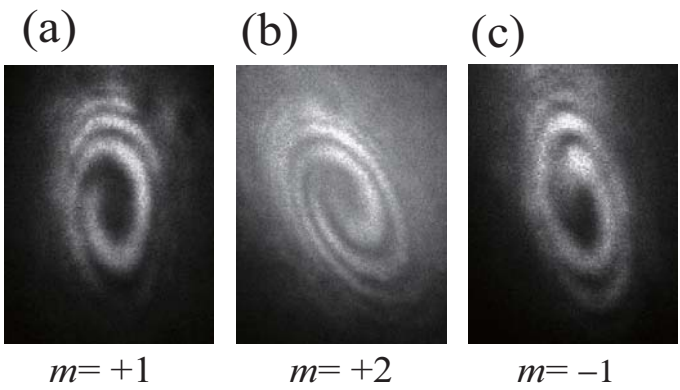

Fig. 2. Interference patterns for (a)m=+1,(b)m=+2, and (c)m=-1.

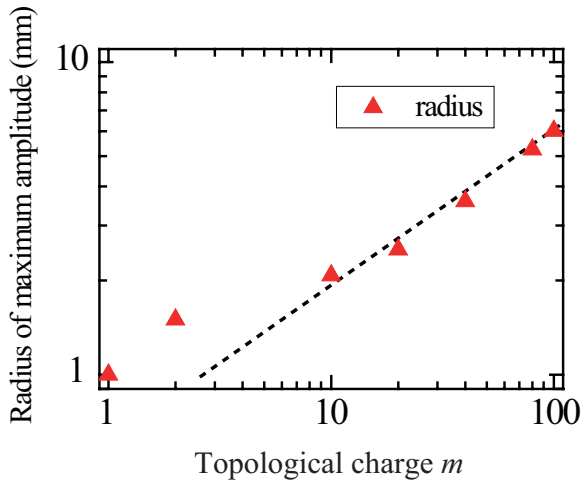

Fig. 3. Measured radius of maximum amplitude of the LG beams as a function of the topological charge m. The dotted line is a line of the slope 0.5.

However, this conventional pattern is not useful for large m LG beam. Because of finite size of pixels, the maximum diffraction angle is limited ($\sim 1^\circ$ for 19-μm pixel size). Figure 3 shows the measured radius of maximum amplitude of the LG beams as a function of the topological charge m up to 100. It is clear that the effective beam waist becomes broad, since the beam waist is proportional to $\sqrt{m}$.[6] Thus the fundamental beam tends to overlap the generated LG beam (see Fig. 1(c)). Moreover the intensity profile of the generated LG beam forms an anamorphic circle, which is given by superposition of various p and m states. By improving the SLM pattern to overcome these, we obtained a clean LG beam without m- and p-value mixture for large topological charge m, which will be discussed in the next section.

3. Clean vortex generation by improved SLM pattern

Since the LG beam with large topological charge m has a wide effective waist, the beam deformation results mainly from (1) the anamorphicity of intensity profile of the fundamental He-Ne beam, and (2) the fundamental beam overlaps with the generated LG beam profile. To overcome the problem (1), we made the fundamental beam waist wider enough to be considered as a plane wave; to solve the problem (2), we used a spiral pattern as shown in Fig. 4(a), instead of the conventional fork-like pattern. Thus

we obtained the clean optical vortex for m=10 and m=100 in Figs. 4(b) and (c), respectively. Clearly, the generated LG beam is well improved, in good contrast to the beam shown Fig. 1(c). The advantage of the spiral pattern is that the reflectively diffracted LG beam can be focused, and the focal length is variable by the SLM pattern. Moreover, the pattern can be limited in a finite circle region, keeping a circular symmetry (as shown in Fig. 4(a)). Hence, it enables us to avoid the contribution of marginal or edge part of the pattern resulting in anamorphicity of the generated beam.

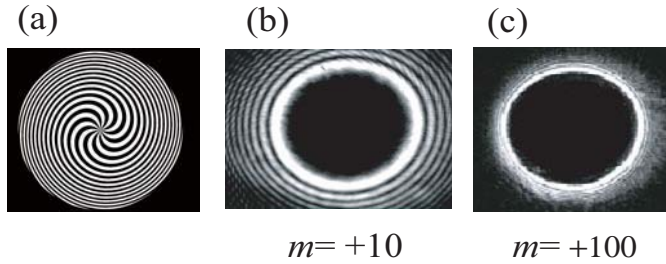

Fig. 4. (a)Spiral pattern in SLM for m=10. Intensity profiles of clean optical vortex for (b)m=10 and (c)m=100.

Acknowledgments

This work has been partly supported by Grant-in-Aid for the 21st Century COE program on "Topological Science and Technology" and Grant-in-Aid for Exploratory Research, 2005-2006, No. 17656020, from the Ministry of Education, Culture, Sports, Science and Technology of Japan.

References

1. L. Allen, M. W. Beijersbergen, R. J. C. Spreeuw, and J. P. Woerdman, *Phys. Rev. A* **45**, 8185 (1992).
2. A. D. Mehta, M. Rief, J. A. Spudich, D. A. Smith, and R. M. Simmons, *Science* **283**, 1689 (1999).
3. V. Garcés-Chávez, D. M. Mcgloin, M. J. Padgett, W. Dultz, H. Schmitzer, and K. Dholakia, *Phys. Rev. Lett.* **91**, 093602 (2003).
4. A. Vaziri, G. Weihs, and A. Zeilinger, *Phys. Rev. Lett.* **89**, 240401 (2002).
5. H. He, N. R. Heckenberg, and H. Rubinsztein-Dunlop, *J. Mod. Opt.* **42**, 217-223 (1995).
6. M. J. Padgett and L. Allen, *Opt. Comm.* **121**, 36-40 (1995).

SPHERICALLY SYMMETRIC BLACK HOLE IN A TOPOLOGICAL UNIVERSE: A TOY MODEL

K. KONNO, T. MATSUURA and S. TANDA

Department of Applied Physics, Hokkaido University, Sapporo 060-8628, Japan

T. MATSUYAMA

Department of Physics, Nara University of Education, Nara 630-8528, Japan

An influence of cosmic topology on a black hole solution is discussed. The solution of a spherically symmetric black hole located at the center of a topological universe is obtained as a toy model. Trajectories of a massive particle around the black hole is found to deviate remarkably from those for the usual Schwarzschild solution at a larger distance from the black hole.

1. Introduction

Recently, the Wilkinson microwave anisotropy probe (WMAP)[1] revealed cosmic microwave background (CMB) fluctuations more accurately, which has determined the best fit of the cosmological parameters.[2] However, a discrepancy between the observation and the theoretical prediction remains at lower orders of azimuthal quantum number l in the expansion of the CMB anisotropy into spherical harmonic functions. The observed quadrupole and octopole components are strikingly below the best fit from theoretical calculations.[2] Surprisingly, such a feature suggests a nontrivial cosmic topology with a finite volume,[3–5] although various factors like astrophysical uncertainties may not be excluded. According to Luminet *et al.*,[3] the suppression of the quadrupole and octopole components can be explained by dodecahedral space topology, in which opposite faces of pentagons are glued together.

Motivated by recent studies on the cosmic topology,[3–5] we investigate a black hole solution in a topological universe. The well-known black hole solutions like the Schwarzschild black hole and the Kerr black hole, which are frequently utilized for astrophysical applications, are obtained under

the boundary condition in which the metric reduces to the Minkowski metric at infinity. However, in a topological universe with a finite volume, the ordinary boundary condition at infinity is not valid. The aim of this paper is to shed light on boundary conditions of black hole solutions, which should be determined by topology of the universe. To our best knowledge, such a problem has not yet been discussed in literature. In this paper, we investigate a spherically symmetric black hole located at the center of a spherical space as a toy model. Our model is far from realistic situations, but will give intuition for more realistic cases. We are particularly interested in the influence of global topology of the universe on the gravitational field of compact objects.

This paper is organized as follows. In Sec. 2, we obtain a spherically symmetric black hole solution in the topological universe. The motion of a test particle around the back hole is investigated in Sec. 3. Finally, we give a conclusion in Sec. 4. In this paper, we use the unit in which $G = c = 1$.

2. Derivation of a black hole solution in a topological universe

We discuss a spherically symmetric black hole located at the center of a spherical space with radius R, which is assumed to be static. In this case, the metric in the polar coordinates has the form

$$ds^2 = g_{\mu\nu}dx^\mu dx^\nu = -e^{2\Phi(r)}dt^2 + e^{2\Psi(r)}dr^2 + r^2 d\theta^2 + r^2 \sin^2\theta d\phi^2. \quad (1)$$

The (tt)- and (rr)-components of the Einstein equation, which determine the functions $\Phi(r)$ and $\Psi(r)$, are written, respectively, as

$$\frac{2}{r^2}\frac{dm(r)}{dr} - \Lambda = 0, \quad (2)$$

$$\frac{2}{r}\frac{d\Phi(r)}{dr} + \left(1 - \frac{2m(r)}{r}\right)^{-1}\left(-\frac{2}{r^3}m(r) + \Lambda\right) = 0, \quad (3)$$

where the mass function $m(r)$ is defined by $m(r) \equiv r\left(1 - e^{-2\Psi}\right)/2$. Here we take into account the cosmological constant Λ in the Einstein equation, owing to the reason mentioned below.

The solution of equations (2) and (3) is obtained as

$$m(r) = M + \frac{\Lambda}{6}r^3, \quad \Phi(r) = \frac{1}{2}\ln C\left(1 - \frac{2M}{r} - \frac{\Lambda}{3}r^2\right), \quad (4)$$

where M and C are constants of integration. The mass of the black hole is given by M. The constant C can be eliminated by taking the scale of the coordinate t as $t \to t/\sqrt{C}$. Thus we take $C = 1$ hereafter.

Next, let us discuss the boundary condition in a topological universe. We now consider the spherical space of radius R with RP^2 boundary condition at the surface as a toy model. The boundary condition for a spherically symmetric black hole is described as $\frac{d\Phi}{dr}\big|_{r=R} = \frac{d\Psi}{dr}\big|_{r=R} = 0$. By this condition, the metric is smoothly connected at the boundary.

In the case of the vanishing cosmological constant, the above condition is not satisfied for any positive value of M. Therefore, we find that the non-zero cosmological constant is necessarily required for constructing static space-time with a black hole satisfying the boundary condition. Namely, we fix the cosmological constant so that the boundary condition is satisfied. Thus the boundary condition leads to $\Lambda = 3M/R^3$. The necessity of the cosmological constant essentially arises from the fact that the universe is finite. In the absence of the cosmological constant, the space-time falls down to a point. Hence we need a cosmological constant to keep the space-time static.

Finally we obtain the metric for the black hole solution

$$ds^2 = -\left(1 - \frac{2M}{r} - \frac{\Lambda}{3}r^2\right)dt^2 + \left(1 - \frac{2M}{r} - \frac{\Lambda}{3}r^2\right)^{-1} dr^2 + r^2\left(d\theta^2 + \sin^2\theta d\phi^2\right). \tag{5}$$

When the radius of the universe becomes infinity, *i.e.* $R \to \infty$, the metric reduces to the ordinary Schwarzschild metric.

The event horizon is specified by $g_{tt} = (g_{rr})^{-1} = 0$. The radius of the event horizon is approximately written as $r_{\rm H} \simeq 2M + \frac{8}{3}M^3\Lambda$. Therefore, the radius of the event horizon becomes larger than the ordinary Schwarzschild radius $r = 2M$.

3. Motion of a test particle around the black hole

3.1. *Trajectories of a massive particle*

First, we discuss the case of a massive particle with mass m. The space-time has the symmetry of translation in the direction of time and the symmetry of space rotation around the black hole. Thus, the energy and the angular momentum of the particle are conserved. The conserved quantities are defined as $E \equiv -p_0/m, L \equiv p_\phi/m$ using the 4-momentum p_μ. Without loss of generality, we can consider the plane of $\theta = \pi/2$. Then, from the equation

$p^\mu p_\mu = -m^2$, we obtain for the trajectories of the particle

$$\left(\frac{dr}{d\tau}\right)^2 = E^2 - V(r)^2, \quad V(r)^2 = \left(1 - \frac{2M}{r} - \frac{\Lambda}{3}r^2\right)\left(1 + \frac{L^2}{r^2}\right), \qquad (6)$$

where τ is the proper time. The particle trajectories are permitted only for the condition of $E^2 \geq V(r)^2$. For this potential, there are two circular orbits at most, which can be derived from the condition of $d\left(V(r)^2\right)/dr = 0$. One is the stable orbit, and the other is the unstable orbit. These are approximately given by

$$r_\pm \simeq r_0^\pm + \frac{\Lambda (r_0^\pm)^5}{3(2Mr_0^\pm - L^2)}, \quad r_0^\pm = \frac{L^2}{2M}\left(1 \pm \sqrt{1 - \frac{12M^2}{L^2}}\right). \qquad (7)$$

Figure 1 shows the effective potential $V(r)^2$. As seen from Fig. 1, the difference between finite R and infinite R is striking at a larger distance from the black hole. The effect of the boundary condition lowers the potential at a larger distance. This is because the last term in the first parenthesis of $V(r)^2$ is negative and proportional to r^2. Hence, the region in which the trajectory is permitted is changed owing to the boundary condition in the topological universe.

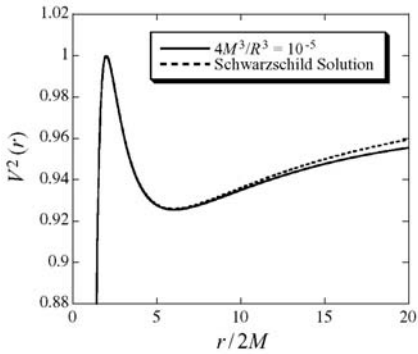

Fig. 1. Effective potential $V(r)^2$ for a massive particle, in the case of $L^2/4M^2 = 4$. The case of $4M^3/R^3 = 10^{-5}$ is compared with that of the Schwarzschild solution.

The trajectories of the particle can be numerically calculated by integrating the equation of motion, which can be derived by differentiating Eq. (6) again. Figure 2 shows trajectories for different R. As inferred from the shape of the potential, the trajectory for finite R clearly deviates from the trajectory for $R \to \infty$ at a larger distance from the center of the black

hole. Therefore, the difference from the result for the ordinary Schwarzschild black hole is striking at a larger distance from the black hole.

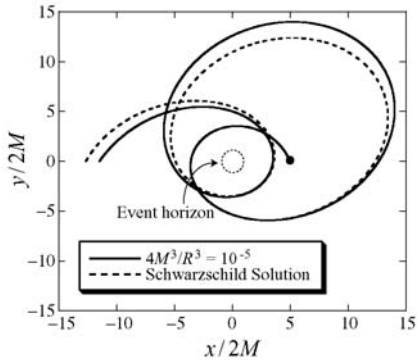

Fig. 2. Trajectories for $L^2/4M^2 = 4$ and $E^2 = 0.95$ in x-y plane, where $(x, y) = (r\cos\phi, r\sin\phi)$. The case of $4M^3/M^3 = 10^{-5}$ is compared with that of the Schwarzschild solution. The stating point is depicted by a filled circle. The event horizon of the black hole is also depicted by a circle.

3.2. *Trajectories of a massless particle*

Next, we discuss a massless particle with 4-momentum p_μ. In the same way as in the case of the massive particle, the conserved quantities for the massless particle are defined as $\tilde{E} \equiv -p_0$, $\tilde{L} \equiv p_\phi$. From the equation $p^\mu p_\mu = 0$, we obtain

$$\left(\frac{dr}{d\lambda}\right)^2 = \tilde{E}^2 - \tilde{V}(r)^2, \quad \tilde{V}(r)^2 = \left(1 - \frac{2M}{r} - \frac{\Lambda}{3}r^2\right)\frac{\tilde{L}^2}{r^2}, \tag{8}$$

where λ is the affine parameter. In this case, there is one unstable circular orbit given by $r = 3M$ for any different values of L and R. Figure 3 shows the effective potential $\tilde{V}(r)^2$. From this figure, we can find that for the same value of R as in the case of the massive particle, the deviation from the result for the Schwarzschild black hole is very much small compared with the case of the massive particle. This is because the last factor in the expression of $\tilde{V}(r)^2$, which decreases to 0 as r increases, strongly suppresses the influence of the topological boundary condition. Therefore, it is difficult to find the effect of the topological boundary condition on trajectories for a massless particle in comparison with the case of the massive particle.

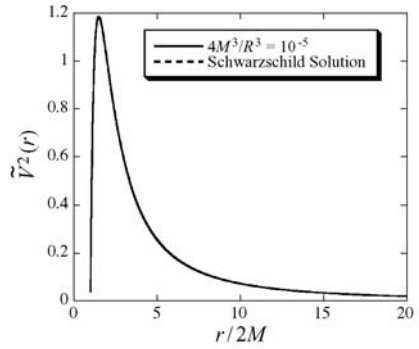

Fig. 3. Effective potential $\tilde{V}(r)^2$ for a massless particle, in the case of $\tilde{L}^2/4M^2 = 8$. The case of $4M^3/R^3 = 10^{-5}$ is compared with that of the Schwarzschild solution. The two curves almost coincides.

4. Conclusion

Inspired by the recent report for the cosmic topology,[3,4] we have investigated a black hole solution in a spherical, topological universe. In particular, we obtained the solution for a spherically symmetric black hole located at the center. Using the solution, we have investigated trajectories of a test particle around the black hole, and discussed the modifications from the results for the usual Schwarzschild black hole solution due to the influence of the global topology of the universe. From the result, we found that the effect is most significant at a larger distance from the center of the black hole just for massive particle's trajectories. Our model is still a toy model. In order to extend the present work to more realistic cases, we have to consider an expanding universe with rigid topology. The black hole solutions which are embedded in a universe were investigated in Refs. 6–8 without the discussion of cosmic topology. The extension to black hole solutions in a topological, expanding universe will be future work.

References

1. See http://Lambda.gsfc.nasa.gov/product/map/
2. C. L. Bennett *et al.*, *Astrophys. J. Suppl. Ser.* **148**, 1 (2003).
3. J.-P. Luminet, J. R. Weeks, A. Riazuelo, R. Lehoucq and J.-P. Uzan, *Nature* **425**, 593 (2003).
4. J. Weeks, J.-P. Luminet, A. Riazuelo and R. Lehoucq, *Mon. Not. R. Astron. Soc.* **352**, 258 (2004).
5. J.-P. Luminet, *Preprint* astro-ph/0501189.
6. K. R. Nayak, M. A. H. MacCallum and C. V. Vishveshwara, *Phys. Rev. D*

63, 024020 (2000).
7. B. S. Ramachandra and C. V. Vishveshwara, *Classical and Quantum Gravity* **19**, 127 (2002).
8. B. S. Ramachandra, K. R. Nayak and C. V. Vishveshwara, *Gen. Rel. Grav.* **35**, 1977 (2003).

AUTHOR INDEX

Amitsuka, H. 151, 178, 184

Bando, H. 172
Bergemann, C. 159
Bernal, O. O. 135

Castro Neto, A. H. 125
Christian Silva, A. 49

Daou, R. 159
Deguchi, K. 178

Fujii, H. 106
Fujita, K. 172
Fukunaga, M. 101
Furukawa, Y. 190

Gong, J. P. 101

Hadač, O. 67
Haga, H. 82
Hamazaki, J. 253
Harrison, N. 151
Hasegawa, I. 226
Hasegawa, T. 208
Hiraoka, Y. 18

Ichinomiya, T. 18, 24
Ishii, A. 178

Jaime, M. 151
Jones, B. A. 125
Julian, S. R. 159

Kanadani, C. 166
Kawabata, K. 82
Kawanaka, H. 172
Kawarazaki, S. 166
Kawasaki, I. 184
Kichiji, N. 59
Kim, K. H. 151
Kobayashi, N. 40
Kobayashi, R. 94
Kögerler, P. 190
Kohyama, K. 40
Konno, K. 258
Konno, N. 11
Kubíček, M. 67
Kumagai, K. 190
Kuwadara, R. 101

Lahtinen, J. 33
Lai, C. H. 3
Lai, Y.-C. 3

Maeno, Y. 178
Marek, M. 67
Masuda, N. 11
Matsuda, K. 184

Matsuda, O. 249
Matsushita, M. 40
Matsushita, S. 40
Matsuura, T. 258
Matsuyama, T. 258
Mayama, H. 195
Mineta, Y. 253
Mitobe, M. 220
Morikawa, M. 239
Morishita, A. 184
Morita, R. 253
Moriyama, O. 40
Mydosh, J. A. 151

Nakagaki, T. 86, 94
Nemoto, K. 208, 245
Nishibe, M. 59
Nishihara, Y. 172
Nishisaka, Y. 190
Nishiura, Y. 86
Nogawa, T. 245

Oh, Y. S. 151
Ohara, J. 202
Ohtsuki, T. 214
Onodera, A. 101
Osada, Y. 101

Süllow, S. 143
Saigusa, T. 94
Saito, W. 106
Saito, Y. 184
Sakaniwa, Y. 226
Sasaki, Y. 40
Satoh, C. 172
Schejbal, M. 67
Schreiber, I. 67
Sharma, P. A. 151
Shima, H. 226, 233
Slevin, K. M. 214
Sugawara, Y. 249

Tabata, Y. 166
Tachizaki, T. 249
Taira, H. 233
Takagi, S. 86
Takesada, M. 101
Tanda, S. 258
Taniguchi, T. 166
Tenya, K. 178, 184
Tero, A. 94
Tsujii, K. 195

Ueda, K.-I. 86
Ueda, T. 86

Wakabayashi, T. 184
Wand, X. 3
Wright, O. B. 249

Yagi, T. 101
Yakovenko, V. M. 49
Yakubo, K. 106, 114, 220, 239
Yamada, H. 114
Yamahana, R. 178
Yamaki, R. 166
Yamamoto, S. 202
Yokoyama, M. 172 , 178
Yoshida, K. 106